

NATIONAL UNIVERSITY OF IRELAND MAYNOOTH



NUI MAYNOOTH

Ollscoil na hÉireann Má Nuad

Real-time Forecasting and Control for Oscillating Wave Energy Devices

Francesco Fusco

A thesis submitted in partial fulfillment for the degree of
Doctor of Philosophy

in the
Faculty of Science and Engineering
Electronic Engineering Department

Supervisor: Prof. John Ringwood
Head of Department: Dr. Sean McLoone

July 2012

Declaration of Authorship

I, Francesco Fusco, declare that this thesis titled ‘Real-time Forecasting and Control for Oscillating Wave Energy Devices’ and the work presented in it are my own. I confirm that:

- This work was done wholly or mainly while in candidature for a research degree at this University.
- Where any part of this thesis has previously been submitted for a degree or any other qualification at this University or any other institution, this has been clearly stated.
- Where I have consulted the published work of others, this is always clearly attributed.
- Where I have quoted from the work of others, the source is always given. With the exception of such quotations, this thesis is entirely my own work.
- I have acknowledged all main sources of help.
- Where the thesis is based on work done by myself jointly with others, I have made clear exactly what was done by others and what I have contributed myself.

Signed:

Date:

ABSTRACT

Ocean wave energy represents a significant resource of renewable energy and can make an important contribution to the development of a more sustainable solution in support of the contemporary society, which is becoming more and more energy intensive. A perspective is given on the benefits that wave energy can introduce, in terms of variability of the power supply, when combined with offshore wind.

Despite its potential, however, the technology for the generation of electricity from ocean waves is not mature yet. In order to raise the economic performance of Wave energy converters (WECs), still far from being competitive, a large scope exists for the improvement of their capacity factor through more intelligent control systems. Most control solutions proposed in the literature, for the enhancement of the power absorption of WECs, are not implemented in practise because they require future knowledge of the wave elevation or wave excitation force. The non-causality of the unconstrained optimal conditions, termed complex-conjugate control, for the maximum wave energy absorption of WECs consisting of oscillating systems, is analysed. A link between fundamental properties of the radiation of the floating body and the prediction horizon required for an effective implementation of complex-conjugate control is identified.

An extensive investigation of the problem of wave elevation and wave excitation force forecasting is then presented. The prediction is treated as a purely stochastic problem, where future values of the wave elevation or wave excitation force are estimated from past measurements at the device location only. The correlation of ocean waves, in fact, allows the achievement of accurate predictions for 1 or 2 wave periods into the future, with linear Autoregressive (AR) models. A relationship between predictability of the excitation force and excitation properties of the floating body is also identified.

Finally, a controller for an oscillating wave energy device is developed. Based on the assumption that the excitation force is a narrow-banded harmonic process, the controller is effectively tuned through a single parameter of immediate physical meaning, for performance and motion constraint handling. The non-causality is removed by the parametrisation, the only input of the controller being an on-line estimate of the frequency and amplitude of the excitation force. Simulations in (synthetic and real) irregular waves demonstrate that the solution allows the achievement of levels of power capture that are very close to non-causal complex-conjugate control, in the unconstrained case, and Model predictive control (MPC), in the constrained case. In addition, the hierarchical structure of the proposed controller allows the treatment of the issue of robustness to model uncertainties in quite a straightforward and effective way.

Acknowledgements

It is a pleasure to thank my PhD supervisor Professor John Ringwood, who has provided great support and stimulating conversations over the course of this research. John has always been helpful and ready to advice me on any matter relating not only my research work, but also my technical writing, presentation skills and teaching experience.

Thanks to the Irish Marine Institute for providing wave measurements data and to the Irish research council for science and engineering (IRCSET) for funding my research.

Thanks to the former and current members of the Center for Ocean Energy Research at NUI Maynooth, Giorgio Bacelli, Jean-Cristophe Gilloteaux, Ronan Costello, Jan Westphalen, Boris Teillant, Phillip Balistky and Iain Keaney, for the productive collaboration and for the invaluable friendship over the years.

Many thanks to all of the staff in the Electronic Engineering Department in Maynooth, for making the department a friendly place, and to all other NUIM postgrads and colleagues in the Engineering Department, Shane Lynn, Kevin Sweeney, Shane Butler, Niall Cahill, Violeta Mangourova, Trong Tue Vu. Thanks to all the football mates in the Engineering Department for sharing exciting and competitive lunch-time matches.

Thanks to my parents, Lina and Peppino, and my brother, Vito, for their encouragement and belief throughout the years, and also their invaluable support during the more challenging times.

Contents

Acronyms	viii
List of symbols	x
List of Figures	xi
List of Tables	xix
1 Introduction	1
1.1 Scope	1
1.2 Motivation	2
1.3 Main contribution	4
1.4 Thesis layout	6
2 Wave energy: A perspective on the variability reduction of power supply	8
2.1 Introduction	9
2.2 Methodology	11
2.2.1 Available data and locations	11
2.2.2 Raw data analysis methodology	12
2.2.3 Power extracted from hypothetical mixed farms	14
2.2.4 Error analysis	16
2.3 Results	17
2.3.1 Raw wind and wave power analysis	17
2.3.2 Benefits of wind/wave combined farms	21
2.4 Conclusion and perspectives	25
3 Ocean waves and oscillating systems for wave energy conversion	27
3.1 Modelling ocean waves	27
3.1.1 Regular waves	28
3.1.2 Irregular waves	33
3.2 Mechanical oscillators	38
3.2.1 Free vibration with no dissipation	39
3.2.2 Free vibration with linear damping	39
3.2.3 Undamped oscillator with harmonic forcing	41
3.2.4 Forced oscillations with damping	42
3.2.5 Transient phenomena	44

3.2.6	Power absorbed by an oscillator	45
3.3	Oscillating bodies interacting with waves	48
3.3.1	Hydrodynamic model	48
3.3.2	Frequency-domain analysis	53
3.3.3	Finite-order approximation and time-domain analysis	56
3.4	Wave power absorption	59
3.4.1	Mechanisms for power take-off	60
3.4.2	Dynamics of an oscillating body Power take-off (PTO) system	63
4	Real-time control of wave energy converters: A literature review	66
4.1	Conditions for maximum wave energy absorption	67
4.1.1	Unconstrained optimum: complex-conjugate control	67
4.1.2	Maximum wave energy absorption subject to physical constraints	71
4.1.3	Non-causality of optimal conditions in the time domain	75
4.2	Real-time control	76
4.2.1	Real-time complex-conjugate control	77
4.2.2	Discrete control: Latching and Declutching	83
4.2.3	Optimisation-based control	86
4.2.4	Control of the PTO impedance	89
4.2.5	Solutions for the active control of sound and vibrations	92
4.3	Discussion and perspectives	93
5	Wave prediction requirements	96
5.1	Introduction	96
5.2	Analysis of non-causality	97
5.2.1	Calculation of the non-causal kernel $h_{opt}(t)$	100
5.3	Quantification of the prediction requirements	107
5.3.1	Manipulation of control for reduction of requirements	109
5.3.2	Causal approximation with a second-order model	112
5.4	Results	115
5.4.1	Wave data and systems geometry	115
5.4.2	Prediction requirements	116
5.4.3	Prediction requirement reduction	122
5.4.4	Causal approximation	123
5.5	Conclusion	126
6	Short-term forecasting of wave elevation and wave excitation force	128
6.1	Introduction	128
6.2	State of the art of short-term wave prediction	130
6.2.1	Wave pressure estimation by the Kalman filter	130
6.2.2	Deterministic sea wave prediction and quiescent period predictive control (QPPC)	132
6.2.3	Digital filters for wave forecasting	134
6.2.4	Spatial wave forecasting through a linear harmonic model	135

6.2.5	Autoregressive models for wave forecasting	136
6.2.6	Non-linear next wave estimation	137
6.3	Wave data analysis	139
6.3.1	Wave spectrum	140
6.3.2	Non-stationarity and the Wavelet transform	142
6.3.3	Linearity analysis	143
6.3.4	Predictability measure	147
6.3.5	Effect of the sampling frequency on the predictability	151
6.4	Forecasting models	152
6.4.1	Cyclical models	152
6.4.2	Auto Regressive (AR) models	155
6.4.3	Sinusoidal extrapolation and the Extended Kalman filter (EKF)	158
6.4.4	Neural networks	160
6.4.5	Further possibilities	161
6.4.6	Confidence intervals	165
6.5	Results	167
6.5.1	Cyclical models	169
6.5.2	Auto-Regressive models	170
6.5.3	Sinusoidal extrapolation through EKF	176
6.5.4	Neural networks	177
6.5.5	Effects of sampling frequency on prediction	180
6.5.6	Discussion	181
6.6	Prediction of the excitation force	183
6.6.1	The wave excitation force	184
6.6.2	Prediction model	185
6.6.3	Results for a range of floating systems	186
6.7	Conclusion	190
7	A real-time controller for wave energy converters	191
7.1	Introduction	191
7.2	The system	193
7.3	Unconstrained controller	195
7.3.1	Non-causal realisation through predictions	195
7.3.2	Causal approximation	198
7.4	Handling constraints	199
7.4.1	Handling motion constraints with the proposed controller	200
7.4.2	Handling motion constraints with model predictive control	203
7.5	Real-time estimate of amplitude, frequency and phase of the excitation force	205
7.6	Low-level controller: a basic approach	206
7.7	Results	209
7.7.1	Unconstrained controller	210
7.7.2	Constrained controller	213
7.7.3	Performance with real waves	215

7.7.4	Robustness to parameter variations	218
7.8	Conclusion	220
8	Robust design of the low-level controller for velocity-tracking	223
8.1	Control specifications	224
8.2	Design of the controller	225
8.2.1	WEC model and uncertainty	226
8.2.2	Controller design	228
8.3	Results	234
8.4	Conclusion	236
9	Conclusion	238
9.1	Overall conclusions	238
9.2	Notes on possible future research	241
A	Model-order reduction based on Hankel singular values	243
A.1	State-space balanced realisation and Hankel singular values	243
A.2	Model reduction based on Hankel singular values	244
B	State estimation with the Kalman filter	245
B.1	The Kalman filter	245
	Bibliography	247

Acronyms

Notation	Description
AIC	Akaike information criterion.
AR	Autoregressive.
ARMA	Autoregressive moving average.
ARX	Autoregressive with exogenous term.
AWS	Archimedes Wave Swing.
BEM	Boundary element method.
BIBO	Bounded-input bounded-output.
BIC	Bayesian information criterion.
CFD	Computational fluid dynamics.
DFT	Discrete-time Fourier transform.
DHR	Dynamic harmonic regression.
DSWP	Deterministic sea-wave prediction.
EKF	Extended Kalman filter.
GA	Genetic algorithm.
GP	Gaussian process.
GRW	Generalised random walk.
IDFT	Inverse discrete-time Fourier transform.
IMC	Internal model control.
LQ	Linear quadratic.
LQG	Linear quadratic Gaussian.
LRPI	Long-range predictive identification.
LS	Least squares.
MA	Moving average.

Notation	Description
MPC	Model predictive control.
NN	Neural network.
OWC	Oscillating water column.
P	Proportional.
PDF	Probability density function.
PF	Particle filter.
PI	Proportional integral.
PID	Proportional integral derivative.
PTO	Power take-off.
QPPC	Quiescent period predictive control.
RCW	Relative capture width.
RLS	Recursive least squares.
RW	Random walk.
SISO	Single-input single-output.
STFT	Short-term Fourier transform.
WEC	Wave energy converter.

List of symbols

Notation	Description
η	free-surface wave elevation.
H_s	significant wave height.
T_e	energy period.
T_p	peak period.
f_r	Radiation force.
f_{ex}	Excitation force.
f_u	Power-take off force.
m	Mass of floating body.
$Z_r(\omega)$	Radiation impedance.
$Z_u(\omega)$	Power take-off impedance.
$Z_i(\omega)$	Intrinsic impedance.
$B(\omega)$	Radiation resistance.
$M_a(\omega)$	Added mass.
m_∞	Added mass at infinite frequency.
$H_r(\omega)$	Radiation impedance without added mass at infinite frequency, $H_r(\omega) = Z_r(\omega) - j\omega m_\infty$.
$H_{ex}(\omega)$	Excitation filter.
K_b	Buoyancy coefficient.
K_v	Viscosity coefficient.
$R^2[l]$	l -step-ahead predictability.
$\mathcal{F}[l]$	Goodness-of-fit of l -steps-ahead prediction.
$\hat{x}[k+l k]$	l -step-ahead prediction of $x(k)$.
$\hat{\sigma}_l^2$	Variance of l -step-ahead prediction error.
$1/H$	Main parameter of proposed causal control, representing the ratio of the reference velocity to the excitation force.
$E\{\cdot\}$	Expected value.
$X(\omega) = \mathcal{F}\{x(t)\}$	Fourier transform.
$X(s) = \mathcal{L}\{x(t)\}$	Laplace transform.
$x(t) = \mathcal{L}^{-1}\{X(s)\}$	Inverse Laplace transform.

List of Figures

1.1	Wave energy resource around the world, expressed as average power per unit metre of wave front [kW/m] [2].	2
1.2	Main categories of the principles for wave energy conversion [3].	3
2.1	Wind capacity credit in Ireland, with respect to installed wind capacity [29]. . . .	10
2.2	Locations of the Irish Marine Institute data buoys.	12
2.3	(a) Power curve for a Vestas V90 3.5 MW wind turbine. (b) Power matrix for the Pelamis 750 kW wave energy converter.	14
2.4	Distribution of the power extracted by an hypothetical off-shore wind turbine V90 and a hypothetical Pelamis wave energy converter, based on observations from the data buoy M1, West Coast of Ireland.	15
2.5	Seasonal average of the instantaneous correlation, $c(0)$, between raw wind and wave power at different locations.	18
2.6	Raw wind and wave power, with their estimated temporal correlation, for a sample collected in Winter 2004 from the M1 data buoy, West Coast.	18
2.7	Raw wind and wave power, with their estimated temporal correlation, for a sample collected in Summer 2004 from the M2 data buoy, East Coast.	19
2.8	Correlation between observed wave periods and significant wave heights, and their estimations based on the wind speed measurements.	20
2.9	A sample comparison between observed significant wave height and its estimation from wind speed measurements at the West and East Coast of Ireland.	20
2.10	A sample comparison between observed wave period and its estimation from wind speed measurements at the West and East Coast of Ireland.	21
2.11	Estimated absolute variations of the extracted power from hypothetical combined wind and wave farms, all delivering approximately an yearly average of 50 MW power output, at different locations.	22
2.12	Estimated standard deviation of the extracted power from hypothetical combined wind and wave farms, all delivering approximately an yearly average of 50 MW power output, at different locations.	22
2.13	Time distribution of the power extracted by an hypothetical off-shore wind turbine V90 and an hypothetical Pelamis wave energy converter, based on observations from the data buoy FS1, South Coast of Ireland.	23
2.14	Distribution of the power extracted by hypothetical combined wind and wave farms off the West and East Coast of Ireland.	24

2.15 Predictability of the power extracted from hypothetical combined wind and wave farms off the West and East Coast of Ireland.	24
2.16 Predictability of the power extracted from hypothetical combined wind and wave farms off the SouthWest and South Coast of Ireland.	25
3.1 Fluid domain and conditions for the solution of harmonic waves on water of constant depth.	29
3.2 Amplitude and phase response of the position of an undamped mechanical oscillator to an external harmonic force.	42
3.3 (a) Position and (b) Velocity frequency response of a damped mechanical oscillator to an external harmonic force.	44
3.4 Average power transferred to a damped mechanical oscillator from an external harmonic force [55].	47
3.5 Typical oscillating bodies for wave energy conversion: (a) Bottom-referenced floating body; (b) Self-reacting bodies.	48
3.6 Hydrodynamic parameters of a cylinder with radius $R = 5$ m, draught $h = 20$ m, height $H = 25$ m and mass $M = 1.62 \times 10^6$ Kg: (a) radiation resistance, $B(\omega)$, and added mass, $M_a(\omega)$; (b) excitation filter $H_{ex}(\omega)$	52
3.7 Impulse responses calculated from Inverse discrete-time Fourier transform (IDFT) of hydrodynamic parameters of Fig. 3.6: (a) radiation, $h_r(t)$; (b) excitation, $h_{ex}(t)$	52
3.8 Velocity response of two floating cylinders in heave: (a) radius $R = 5$ m, draught $h = 20$ m, mass $M = 1.62 \times 10^6$ Kg; (b) radius $R = 6$ m, draught $h = 2$ m, mass $M = 0.28 \times 10^6$ Kg.	55
3.9 Finite-order approximation of the model of the heaving cylinder in Fig. 3.6: (a) Radiation identification with model of order; (b) Finite-order approximation of force-to-velocity system.	58
3.10 Typical oscillating bodies for wave energy conversion: (a) Bottom-referenced floating body; (b) Self-reacting bodies.	60
3.11 Direct-drive linear generator [1].	61
3.12 Typical topologies for hydraulic PTOs [87]: (a) variable pressure and bi-directional flow; (b) constant pressure and uni-directional flow.	62
4.1 Power absorption versus excitation power and power lost in radiation [6].	68
4.2 Power absorption when PTO impedance is the complex-conjugate of the intrinsic impedance, compared to the case of a constant PTO resistance, $\overline{R_u}$	70
4.3 Power absorption when PTO is purely resistive and it is tuned to optimal value.	71
4.4 Budal diagram giving upper bound of power absorption based on maximum physical displacement of single body in heave [6]. Incident wave amplitude is $ \hat{\eta} = 1$ m.	72
4.5 Power absorption under motion constraints [7]. The dotted line represents the unconstrained maximum.	74
4.6 Feedforward realisation of complex-conjugate control. The optimal PTO force is calculated from estimates and/or predictions of the excitation force.	77
4.7 Feedback implementation of complex-conjugate control. The optimal PTO force calculated from measurements and/or predictions of the excitation force.	77

4.8	Velocity-tracking architecture for the realisation of complex-conjugate control. Optimal velocity calculated from estimates of excitation force and from optimal condition of complex-conjugate control. A low-level controller, $K(\omega)$, imposes the desired velocity on the WEC by acting on the PTO force.	78
4.9	Latching control: (a) Block diagram; (b) Typical behavior of velocity and PTO force compared against excitation force [8].	84
4.10	Performance of latching and declutching control strategies applied to a heaving WEC, in regular waves, compared against constant linear damping [112].	86
4.11	Typical block diagram for control strategies that set the damping and stiffness coefficients realised by the PTO to adapt the response of a WEC to the prevailing sea state.	90
5.1	General structure for a non-causal controller of a WEC [15]. A high-level controller (HLC) generates the velocity reference, $v_{ref}(t)$, from predictions of the excitation force. The low-level controller (LLC) implements a velocity-tracking feedback loop.	99
5.2	Radiation impedance, after the singularity at infinite frequency is removed, namely $H_r(j\omega) = Z_r(j\omega) - j\omega M_\infty$, of a heaving cylinder with radius $R = 5$ m, draught $h = 20$ m, height $H = 25$ m and mass $m = 1.62 \times 10^6$ Kg.	104
5.3	Finite-order approximation of the radiation of the floating cylinder, shown in Fig. 5.2. The order of the approximation is $n = 4$	105
5.4	Error produced by finite-order approximation of the optimal, non-causal function $H_{opt}(\omega)$	106
5.5	Discrete-time Fourier transform (DFT) of $K_{opt}(\omega) = H_{opt}(\omega) - 1/2K_v$, zero-padded up to 100π so to obtain a time resolution $T_s = 0.01$ s. For illustration purposes, only values up to 4 rad/s are shown here.	106
5.6	Approximations of the non-causal kernel function corresponding to $H_{opt}(\omega)$, using system identification and Laplace inversion, as opposed to numerical IDFT.	107
5.7	Non-causal transfer function, $H_{opt}(\omega)$, between excitation force and optimal velocity. It is a real and even function of the frequency.	109
5.8	Relation between lowest frequency pole and non-causality of the impulse response. $K_{opt}(\omega)$ and $k_{opt}(t)$ are calculated for two heaving cylinders.	110
5.9	Manipulation of $H_{opt}(\omega)$, resulting in $H_{red}(\omega)$, such that the lowest frequency pole is moved rightward, thus decreasing the dominant time constant of the correspondent impulse response.	111
5.10	Comparison of real frequency response, $1/Z_i(\omega)$ against second-order approximation, for cylinder 1 of Table 5.1.	113
5.11	Velocity-generation law, $V(\omega)/F_{ex}(\omega)$, for reactive control calculated for the full system and a second-order approximation model (constant over frequency). The system is cylinder 2 of Table 5.1.	114
5.12	Real-time implementation of reactive control as a velocity-follower. For a second-order system, the reference generation is a purely proportional block, which is <i>causal</i> and realisable.	115

5.13	Distribution of peak (of energy) frequency, ω_p , and significant wave height, H_s , collected from a data buoy in Belmullet (54° 13' N, 10° 8' W) over the year 2010. The data sets selected for the numerical simulations are highlighted.	116
5.14	Performance of different spheres, achievable through complex-conjugate control when information of future excitation force, at different leading times, is included in the reference velocity calculation.	118
5.15	Average prediction horizon required by spheres with different values of τ_1 for the achievement of a positive <i>RCW</i> with complex-conjugate control.	118
5.16	Performance of different cylinders, achievable through complex-conjugate control when information of future excitation force, at different leading times, is included in the reference velocity calculation: (a) constant height and changing radius; (b) constant radius and changing height.	120
5.17	Average prediction horizon required by cylinders with different values of τ_1 for the achievement of a positive <i>RCW</i> with complex-conjugate control.	121
5.18	Average prediction horizon required by spheres with different values of the <i>Q</i> factor for the achievement of a positive <i>RCW</i> with reactive control.	121
5.19	Modification of the velocity reference generation transfer function $H_{opt}(\omega)$ for reduced prediction requirements. Behavior of two systems in a sea state with peak frequency $\omega_p = 0.5 \text{ rad/s}$	122
5.20	Modification of the velocity reference generation transfer function $H_{opt}(\omega)$ for reduced prediction requirements.	123
5.21	Maximum <i>RCW</i> that is achievable when using $H_{red}(\omega)$, as a percentage of the ideal <i>RCW</i> , obtained with $H_{opt}(\omega)$	123
5.22	Causal approximation of complex-conjugate control against performance of ideal, non-causal controller.	124
5.23	Average Relative capture width (<i>RCW</i>) obtained with causal approximation, as a percentage of ideal maximum achievable with non-causal complex-conjugate control.	125
6.1	Two main approaches to wave forecasting	129
6.2	Correspondence between significant wave height H_s , peak frequency ω_p and energy frequency ω_e at the locations: (a) Galway; (b) Pico.	141
6.3	Typical wave spectra at the locations: (a) Galway Bay; (b) Pico Island.	141
6.4	Wavelet transform for three different data sets from Galway Bay.	144
6.5	Wavelet transform for two different data sets from the Pico Island.	145
6.6	Gaussianity analysis at the Galway Bay.	146
6.7	Gaussianity analysis at the Pico Island.	147
6.8	Bispectrum of some data sets from Galway Bay: (a) G_1 ; (b) G_2 ; (c) G_3	148
6.9	Bispectrum of some data sets from the Pico Island: (a) P_2 ; (b) P_1	148
6.10	Predictability index, $R^2[l]$, estimated for the selected wave records.	150
6.11	Predictability of some wave elevation data sets from the Galway Bay, when low-pass filtering with different cut-off frequencies, ω_c , is applied.	150
6.12	Predictability of some wave elevation data sets from the Pico Island, when low-pass filtering with different cut-off frequencies, ω_c , is applied.	151

6.13	Estimated predictability for a wave elevation time series from the Pico Island, when different sampling frequencies are adopted.	151
6.14	Data sets utilised to test the models of Section 6.4: (a) Galway Bay; (b) Pico Island.	168
6.15	Prediction accuracy of cyclical models on wave data from the Galway Bay	169
6.16	Prediction accuracy of cyclical models on wave data from the Pico Island	169
6.17	Some time-series details of the multi-steps-ahead wave prediction, using cyclical models. The 90% confidence interval is also shown.	171
6.18	Distribution of skewness and kurtosis of the l -steps-ahead prediction error, for different l and for different cyclical models, over all the considered data sets from both the Pico Island and the Galway Bay.	172
6.19	AIC_l (continuous line) and BIC_l (dashed line), for some l , evaluated for the Galway Bay and Pico Island data sets, low-pass filtered with cut-off frequency ω_c	172
6.20	Prediction accuracy of AR models of different orders, n , over the wave data from the Galway Bay and the Pico Island.	173
6.21	Some time-series details of the multi-steps-ahead wave prediction, and its 90 % confidence, using AR models.	174
6.22	Distribution of skewness and kurtosis of the l -steps-ahead prediction error, for several l and for different AR models, over all the considered data sets from the Pico Island and from the Galway Bay.	175
6.23	Spectrum of the AR model compared to wave spectra of training and validation data, which are amplified accordingly for clarity of exposition. The data correspond to set P_3 of Fig. 6.14(b).	175
6.24	Prediction accuracy of single-component cyclical models with a variable frequency, estimated through the EKF.	176
6.25	Frequencies of a two-components cyclical model, with variable frequencies, estimated through the EKF. The data set utilised is P_2	177
6.26	Prediction accuracy of neural networks.	178
6.27	Some screenshots of the multi-steps ahead wave prediction, and its 90% confidence, with neural networks.	179
6.28	Distribution of skewness and kurtosis of the l -steps-ahead prediction error, for several l and for different neural networks over all the considered data sets from the Pico Island and from the Galway Bay.	179
6.29	Prediction accuracy of AR models and neural networks when the sampling frequency of the data is decreased.	180
6.30	Magnitude of excitation filter, $H_{ex}(\omega)$, of two heaving cylinder with the same mass distribution and radius, $R = 3$ m, but different draught, $h = 4$ and $h = 20$ m, resulting in different bandwidth, $\Delta\omega \approx 0.7$ and $\Delta\omega \approx 0.5$ rad/s, respectively. The bandwidth is calculated as the frequency at which the magnitude is -3 dB, compared to the value at $\omega = 0$	184
6.31	Distribution of peak frequency, ω_p , and significant wave height, H_s , collected from a data buoy in Belmullet ($54^\circ 13' N$, $10^\circ 8' W$) over the year 2010. The data sets selected for the numerical simulations are highlighted.	187

6.32	Accuracy of the the prediction of the wave excitation force acting on three cylinders, and produced by three different sea states. The prediction is calculated with AR models.	188
6.33	Average horizon for which the excitation force acting on a system can be predicted with more than 60% of accuracy.	189
7.1	One-degree of freedom (heave) floating system for wave energy conversion.	193
7.2	Radiation and excitation frequency responses for a floating cylinder with radius $R = 3$ m, height $H = 5$ m, draught $h = 4$ m, mass $M = 3.2 \times 10^5$ Kg, calculated using the hydrodynamic software Wamit [59].	194
7.3	Finite-order approximation of the response of the WEC, calculated in the frequency domain, using the toolbox developed in [66].	195
7.4	Non-causal approximation of complex-conjugate control.	196
7.5	Non-causal reference generation, manipulated for the reduction of the prediction requirements.	197
7.6	Optimal relation between excitation force and oscillation velocity. The phase is zero.	198
7.7	Causal approximation of complex-conjugate control.	199
7.8	Causal controller with adaptive tuning of velocity amplitude for motion-constraints handling.	201
7.9	Magnitude of velocity reference, with respect to amplitude of incident wave elevation, based on (7.21). The magnitude of the excitation force, F_{ex} , is translated in amplitude of the incident wave elevation, $ \hat{\eta} = H_{ex}(\omega)F_{ex} $, as from (7.3).	201
7.10	Ideal optimal value and upper limit, for a constraint $X_{lim} = 0.8$ m, of the adaptive constant $1/H$, as from (7.21). The magnitude of the excitation force, F_{ex} , is translated in amplitude of the incident wave elevation, $ \hat{\eta} = H_{ex}(\omega)F_{ex} $, as from (7.3).	202
7.11	Real-time estimate of the amplitude and frequency of the wave excitation force with the EKF: (a) amplitude estimate; (b) frequency estimate; (c) Power spectral distribution of the wave excitation force utilised for the simulation (peak frequency is $\omega \approx 5.15$ rad/s.	207
7.12	Low-level controller as a feed-forward with direct disturbance rejection.	208
7.13	Open-loop transfer function $K(s)/Z_i(s)$	209
7.14	Some spectral shapes utilised for the simulation of the waves. Spectra centred around different peak frequencies are also utilised.	210
7.15	Performance of unconstrained controllers.	211
7.16	Performance of (a) non-causal and (b) causal control, as a percentage of ideal complex-conjugate control, with double-peaked spectra: $H_{s,1}/H_{s,2}$ is the relative energy between the two sea states; $\Delta\omega$ is the frequency spacing.	212
7.17	Ratio of average negative power to average absorbed power.	212
7.18	Performance of proposed non-optimal causal control, compared with optimal MPC.	214

7.19	Behavior of the proposed causal and non-optimal controller against MPC, for a given excitation force, produced by an irregular wave simulated from a single-peaked Ochi spectrum with $H_s = 2$ m, $\omega_p = 0.7$ rad/s and $\lambda = 1$. Overall performance over the sea state is $RCW \approx 0.37$ for the causal controller and $RCW \approx 0.44$ for the MPC. .	216
7.20	Performance of proposed controller, as a percentage of MPC, with double peak spectra: $H_{s,1}/H_{s,2}$ is the relative energy between the two sea states; $\Delta\omega$ is the frequency spacing.	217
7.21	Ration of average negative power to average absorbed power.	217
7.22	Wave spectrum of real wave data used to test the performance of the proposed controller. The data comes from the Belmullet wave energy test site ($54^\circ 13'$ N, $10^\circ 8'$ W) and it consists of 30-minutes wave-elevation records sampled at 1.28 Hz.	217
7.23	Variation of system's frequency response caused by variation in mass, ΔM , and stiffness, ΔK	218
7.24	Performance of the proposed controller and of MPC with parametric variations in mass, ΔM , and stiffness, ΔK . The incident wave is simulated from an Ochi spectral distribution with significant wave height $H_s = 1$ m, peak frequency $\omega_p = 1.25$ rad/s (around the resonance frequency of the device) and spectral sharpness $\lambda = 0.5$	220
7.25	Performance of the proposed controller and of MPC with parametric variations in mass, ΔM , and stiffness, ΔK . The incident wave is simulated from an Ochi spectral distribution with significant wave height $H_s = 2$ m, peak frequency $\omega_p = 0.7$ rad/s and spectral sharpness $\lambda = 0.5$	220
7.26	Detail of the distribution of the heaving position of some of the points of Fig. 7.25(b). The increase in performance is due to a violation of the constraints.	221
8.1	General structure of a feedback control that imposes a desired velocity of oscillation on a floating body, under the influence of the wave excitation force.	224
8.2	Block diagram of the Internal model control (IMC) [192].	225
8.3	Uncertainty in the model. Largest parametric variation is $\Delta K = \pm 10\%$	227
8.4	Equivalent block diagram of the IMC [192].	228
8.5	Sensitivity, $S_n(s)$, and complementary sensitivity, $T + n(s)$, in the case of nominal plant.	231
8.6	The condition for robust stability is not verified by $Q(s)$ chosen at step 1, from (8.13).	232
8.7	The complementary sensitivity function is lowered down with a notch filter so that the robust stability condition is satisfied: (a) Notch filter (magnitude expressed in dB to highlight the notch); (b) Modification of complementary sensitivity.	233
8.8	Complete control architecture. The high-level controller, designed in Chapter 7, produces a reference velocity, that is imposed on the system by a robust feedback controller, $K(s)$, designed in the present Chapter.	234
8.9	Performance of proposed robust controller against feedforward controller when the largest parametric variation, $\Delta K = \pm 10\%$, is applied: (a)-(b) Relative capture width; (c)-(d) Percentage of occurrence of motion constraints violation, due to the model inaccuracy.	235

8.10 Sensitivity of robust control and feedforward control to variations in the buoyancy coefficient, ΔK . The incident wave is centred at a frequency $\omega_p = 1.22$ rad/s, that is the resonance frequency of the device, where the uncertainty is the largest. . . .	236
9.1 Logic structure of the thesis.	239

List of Tables

5.1	Reduction to second-order model, applied to some heaving cylinders. R is the radius, h is the draught and m is the submerged mass.	113
5.2	Number of data sets available per each peak frequency, as from Fig. 5.13.	116
5.3	Geometry of heaving buoys. C : cylinder; S : sphere.	117
6.1	(<i>a</i>) The current quadrant is individuated on the basis of the sign of the excitation force, f_{ex} , and of its first derivative with respect to time. (<i>b</i>) The n parameter, in (6.18), is chosen on the basis of the current quadrant.	139
6.2	Goodness-of-fit $\mathcal{F}(l)$ of different forecasting models on the Galway bay data sets of Fig. 6.14(a)	181
6.3	Goodness-of-fit $\mathcal{F}(l)$ of different forecasting models on the Pico island data sets of Fig. 6.14(b)	181
6.4	Number of data sets available per each peak frequency, as from Fig. 5.13.	186
6.5	Geometry of heaving buoys. C : cylinder	188
7.1	Details of real wave records, whose spectrum is shown in Fig. 7.22, where H_s : significant wave height; ω_p : peak frequency; ω_e : energy frequency.	217
7.2	Performance of the proposed non-optimal and causal controller against MPC, with real wave data, whose spectrum is shown in Fig. 7.22.	218

Dedicated to my parents, Lina and Peppino... without their support, encouragement and love this thesis would have not been possible.

Chapter 1

Introduction

1.1 Scope

The energy carried by ocean waves represents a major source of renewable energy that could make an important contribution toward tackling the world's energy problem. Wave energy represents a stored form of solar energy, part of which is converted to wind, as a result of temperature gradients in the air, and ultimately to waves, as a result of the action of the wind on the oceans. In the conversion process, the density of the energy increases, going from an average 0.15 kW/m^2 for the solar radiation to 0.4 kW/m^2 for the wind and, finally, to 2.5 kW/m^2 for ocean waves. The overall wave energy is estimated to around 2 TW, which is of the same order of magnitude as the world's electricity consumption (less than 10 TW) [1].

Figure 1.1 indicates the world distribution of wave energy transport, that is the power carried over a metre of wave front. Depending on the location, the wave energy transport goes from as low as 10 kW/m to as high as $70\text{-}90 \text{ kW/m}$. Large swell waves produced by north-easterly (in the northern hemisphere) and south-easterly winds (in the southern hemisphere) can travel very long distances with almost no loss of energy. As a result, high levels of wave energy are typically experienced off the Western coast of the continents, which are exposed to the open ocean. Among the locations with the largest potential are the Western coasts of Europe, North-America and Australia.

Despite the large potential, however, many systems for wave energy conversion, namely Wave energy converters (WECs), are at quite an immature stage of development, while only a few have made it to a pre-commercial stage. Harnessing the highly-concentrated wave power does not come, in fact, without challenge. The main difficulties are related to the hostile environment constituted by the sea, which puts enormous stress on the technical requirements of survivability and longevity of WECs, also considering the scarce accessibility of the devices for maintenance, with negative effects on the overall economical performance.

An indication of the relative immaturity of wave energy technology can also be taken from the large number of device types and energy extraction concepts currently being developed or researched. In 1992, Hagerman [3] proposed the categorisation shown in Fig. 1.2, that still applies to the majority of the systems currently under development. Most WECs consist of oscillating systems, that can be either *oscillating bodies* (relative motion between flexible/rigid structures) or *Oscillating water columns (OWCs)* (relative motion between a mass of water and a structure),

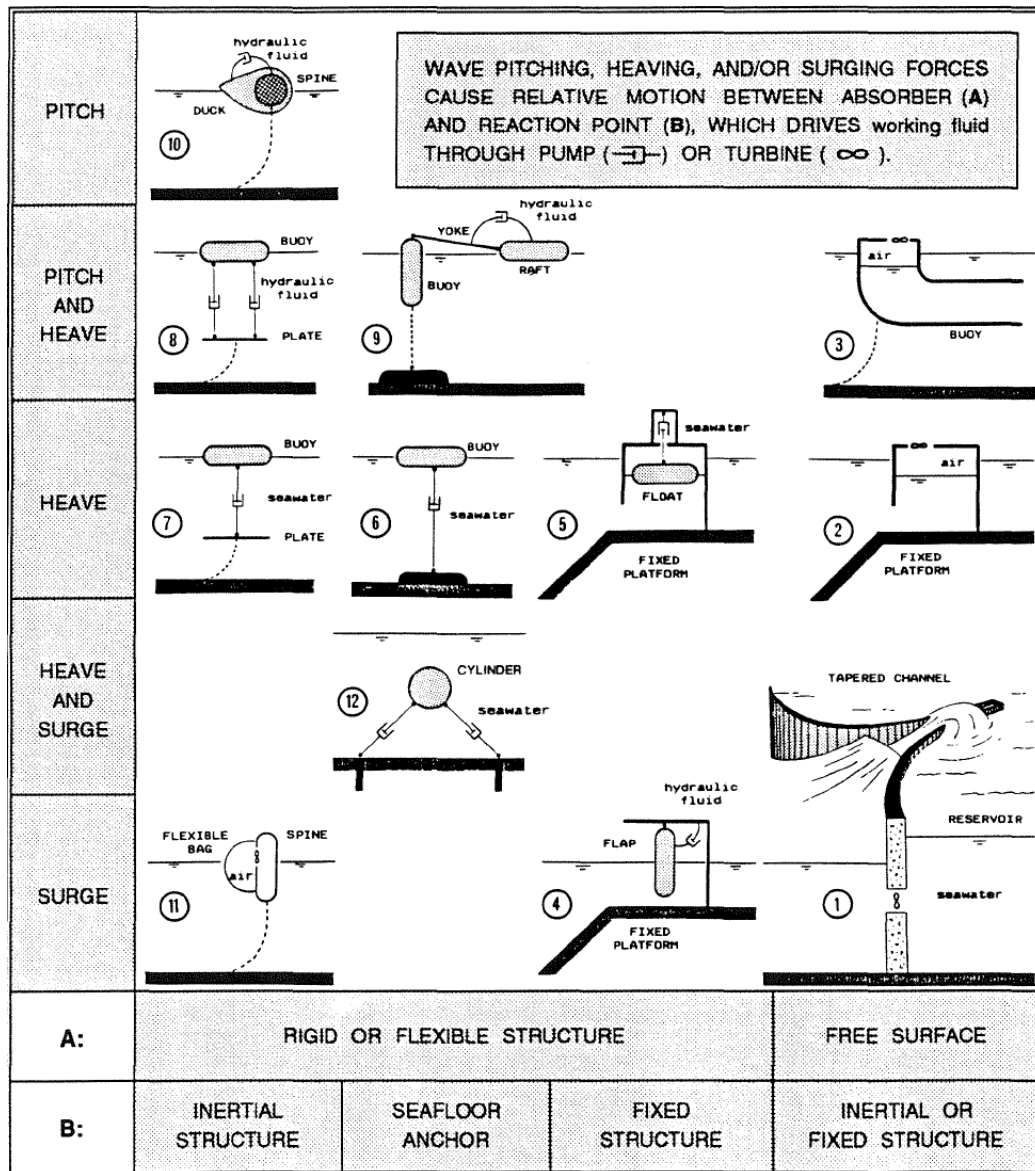


Figure 1.2: Main categories of the principles for wave energy conversion [3].

consequence, it is believed that real-time control of WECs can play a major role in making wave energy an economically viable alternative to other renewable energy technologies.

A recurrent issue that is encountered in most strategies that have been proposed for the control of wave energy devices [12, 6, 13], is the need of future knowledge of the incident wave elevation (or of the force produced by the wave on the device). This need for prediction derives by the translation of complex-conjugate control into the time domain, which produces non-causal relationships involving the wave excitation force or the incident wave elevation [6]. Although acknowledged, however, the need for predictions has never been quantified and, as a consequence, the problem of wave forecasting, for use in the control of WECs, was never addressed with sufficient depth.

With the work presented in this thesis, the author tries to provide more insight in the non-causality of the existing control strategies for wave energy devices. An attempt is made toward the clarification and quantification of the prediction requirements of the control. The problem of wave forecasting is then dealt with and put in perspective with the prediction requirements. The integration of the wave predictions within the control design also constitutes the focus of this thesis. When dealing with the control, attention is also given to a formulation that can accommodate motion constraints and model uncertainties.

1.3 Main contribution

The main novel contributions of this thesis are summarised as follows:

1. In Chapter 2, it is shown that wave energy can play an important role as part of a mixed portfolio of renewable energy farms. In particular, appropriate combinations of offshore wave and wind energy devices offer major benefits in terms of reduced variability and improved predictability of the generated power.
2. A quantitative analysis of the non-causality of complex-conjugate control is proposed in Chapter 5. In particular, it is shown that the required prediction horizon for the wave excitation force is directly related to certain fundamental properties of the geometry of the WEC. The possibility to reduce the prediction requirements, based on *a priori* knowledge of the operating conditions of the system, is also demonstrated.
3. In Chapter 6, it is shown that the short-term wave forecasting problem, for use in the implementation of non-causal real-time controllers of a WEC, can effectively be solved as a univariate time-series problem, with no need of distant wave elevation measurements, resulting in a cheaper and simpler design. Linear AR models are able to provide accurate predictions for up to 2 wave periods into the future, in the case of low-frequency swell (high-energetic) waves.
4. The achievable prediction of the wave excitation force, that is the effect of the wave elevation on the wave energy device, is related to some fundamental properties of the geometry of the WEC, in Chapter 6. Comparison of the achievable prediction with the prediction requirements shows that the non-causality of complex-conjugate control can be overcome with the

proposed AR forecasting models. In Chapter 7, it is demonstrated how the implementation of complex-conjugate control using predictions allows the achievement of a performance that is very close to the ideal, in a variety of irregular waves.

5. A simple and effective real-time control system for the maximisation of the energy capture of a WEC is developed, in Chapter 7. The controller is based on a non-stationary, narrow-banded approximation of the wave excitation force that, while sub-optimal in terms of prediction, introduces certain advantages:
 - The controller is easily tunable with a single parameter of direct physical meaning, for performance and constraint handling.
 - The parametrisation is such that the non-causality is removed, since the wave excitation force is assumed to be a non-stationary and narrow-banded harmonic process.
 - The achieved performance, in real waves, is comparable with non-causal complex-conjugate control, in the unconstrained case, and with MPC in the presence of motion constraints.
6. The structure of the proposed controller can incorporate robustness to model uncertainties in quite a straightforward way, as is demonstrated in Chapter 8.

The contributions of this thesis resulted in the publication of a number of publications, outlined as follows:

- [14] Fusco, F. and Ringwood, J. A Simple and Effective Real-time Controller for Wave Energy Converters. *IEEE Transactions on Sustainable Energy*. In press.
- [15] Fusco, F. and Ringwood, J. A Study on the Prediction Requirements in Real-Time Control of Wave Energy Converters. *IEEE Transactions on Sustainable Energy*, vol. 3, no. 1, pp. 176-184, 2012.
- [16] Fusco, F. and Ringwood, J.V. Short-Term Wave Forecasting for Real-Time Control of Wave Energy Converters. *IEEE Transaction on Sustainable Energy*, vol 1, no. 2, pp. 99-106, 2010.
- [17] Fusco, F, Ringwood, J. Variability Reduction through Combination of Wind and Waves: A Irish case study. *Energy*, vol. 35, pp. 314-325, 2010.
- [18] Fusco, F. and Ringwood, J. A Model for the Sensitivity of Non-Causal Control of Wave Energy Converters to Wave Excitation Force Prediction Errors. *Proceedings of the 9th European Wave and Tidal Energy Conference (EWTEC)*, Southampton, UK, 2011.
- [19] Fusco, F. and Ringwood, J. Quantification of the Prediction Requirements in Reactive Control of Wave Energy Converters. *Proceedings of the 18th World Congress of the International Federation of Automatic Control (IFAC)*, Milano, Italy, pp. 11483-11488, 2011.
- [20] Fusco, F. and Ringwood, J. Suboptimal Causal Reactive Control of Wave Energy Converters Using a Second Order System Model. *Proceedings of the 21st International Offshore (Ocean) and Polar Engineering Conference (ISOPE)*, Maui, USA, pp. 687-694, 2011.

- [21] Fusco, F., Gilloteaux, J-C., Ringwood, J. A Study on Prediction Requirements in Time-domain Control of Wave Energy Converters. *Proceedings of Control Applications in Marine Systems (CAMS)*, Warnemunde, Germany, pp. 405-410, 2010.
- [22] Fusco, F. and Ringwood, J.V. Short-term wave forecasting with AR models in real-time optimal control of wave energy converters. *Proc. IEEE International Symposium on Industrial Electronics*, Bari, Italy, pp. 2475-2480, 2010.
- [23] Fusco, F., Ringwood, J. A Study on Short-Term Sea Profile Prediction for Wave Energy Applications. *Proceedings of the 8th European Wave and Tidal Energy Conference (EWTEC)*, Uppsala, Sweden, 2009.

1.4 Thesis layout

The thesis is organised as follows.

In Chapter 2, wave energy is put in perspective with other renewable energy sources. The uncontrollable and intermittent nature of renewable energy sources introduces major problems in the management of the power grid, when significant levels of penetrations are reached. The potential benefits of including wave energy into a renewable energy mix is, therefore, investigated, in terms of variability reduction and predictability improvement.

The basic theory of ocean waves is then introduced in Chapter 3. In the same chapter, the typical model of a WEC consisting of an oscillating system, for use in control design, is detailed. Similarities with mechanical mass-spring-damper oscillators are also outlined to clarify some properties of WECs.

The major theoretical studies about the conditions for maximum wave energy extraction from an oscillating body, in the unconstrained and constrained case, are summarised in Chapter 4. This is followed by an extensive review of the control methods proposed in the literature, for the improvement of the energy capture of WECs.

The non-causality of the ideal complex-conjugate control is investigated in detail in Chapter 5. The prediction requirements, in terms of forecasting horizon, are quantified and related to fundamental properties of the geometry of the WEC.

The wave forecasting problem is then dealt with in Chapter 6. After a detailed analysis of the properties of real ocean waves, and after a review of the major techniques proposed in the literature, several forecasting models are tested with real wave data. The extension of the proposed forecasting models to the prediction of the wave excitation force, that is the effect of the wave elevation on a floating system, is also investigated. The achievable prediction horizon of the excitation force is then related to fundamental properties of the geometry of the WEC and is compared to the prediction requirements.

In Chapter 7, a simple and effective real-time controller for the improvement of the energy capture of a WEC is proposed. The control system follows a hierarchical structure, where a high-level controller produces a desired oscillation velocity, which is then imposed on the WEC by a low-

level controller. While Chapter 7 is focused on the high-level controller, Chapter 8 demonstrates how the low-level controller can be designed such that robustness to model uncertainties is achieved.

Finally, conclusions and possible future directions of this research work are documented in Chapter 9.

Chapter 2

Wave energy: A perspective on the variability reduction of power supply

Abstract

With the widespread awareness that a more sustainable energy strategy is required to our society, most countries worldwide (at least developed and developing ones) are pursuing policies for improved energy efficiency and wide exploitation of renewable energy sources. High levels of penetrations of intermittent energy sources, however, strongly increase the requirement of surplus capacity from conventional and controllable thermal plants, that, as a cause, are operated at much lower efficiencies to ensure the stability of power systems.

The adoption of storage facilities being a costly alternative, and the implementation of intelligent strategies for adapting the load to the generation (so-called *smart* grids) not seeming achievable in the immediate future, there exist a third possibility of exploiting the non-correlation between different (could be geographic diversity) variable sources such that variability of the generated power is reduced.

This chapter presents a methodology to assess the possible benefits of the combination of wind energy with the still unexploited, but quite significant in Ireland, wave energy. An analysis of the raw wind and wave resource at certain locations around the coasts of Ireland shows how they are very low correlated on the South and West Coast, where the waves are dominated by the presence of high energy swells generated by remote westerly wind systems. As a consequence, the integration of wind and waves in combined farms, at these locations, allows the achievement of a more reliable, less variable and more predictable electrical power production.

2.1 Introduction

In response to the relatively urgent need to reduce the dependence from fossil fuels, particularly in the sectors of energy supply, industry and transport, many legislative organs worldwide have set some targets to constrain the turning towards renewables. In particular, the European Union stated that a 20% target for the overall share of energy from renewable sources and a 10% target for energy from renewable sources in transport would be appropriate and achievable objectives, and that a framework that includes mandatory targets should provide the business community with the long-term stability it needs to make rational, sustainable investments in the renewable energy sector which are capable of reducing dependence on imported fossil fuels and boosting the use of new energy technologies [24]. Along with these mandatory targets for the EU member countries, many of the nations set their own targets locally. In the specific case of Ireland, on which this study is focused on, the target to be achieved in 2010 from the EU Directive was 13.2% of gross electricity consumption from renewable sources, but nationally Ireland set a more ambitious target of 15% by 2010 and 33% (moved to to 40%) by 2020. According to the last report from the Sustainable Energy Authority of Ireland (SEAI), the share of electricity generated from renewable energy sources in 2009 was 14.4% (provisional), exceeding the interim EU target of 13.2% by 2010 and placing Ireland firmly on track to meet the Government target of 15% of all electricity generation to be from renewable energy sources by 2010 [25].

In the most recent study from the independent electricity transmission system operator in Ireland, Eirgrid, it was reported that, by the end of September 2010, the installed conventional generation capacity is 6829 MW and that the installed renewable capacity is greater than 1700 MW, mainly deriving from wind (1466 MW) and hydro (nearly 240 MW). The demand for electrical energy, showing a all-time peak of 5090 MW in 2010, was growing at a rate of approximately 3% per annum for midyear data, and at an estimated rate in the range of 24% per annum for the peak demand, before the slowing down of the economy (0.9% increase in demand from 2009 to 2010) [26]. In order to realise the 2020 target of 40% of electricity demand to be met by renewables, Ireland is putting particular reliance on wind, so that connection of additional 3100 MW in the next years will be required [25].

Such a high level of wind penetration, however, does not come without difficulties, as was reported in [27]. It requires higher surplus capacity for supply security reasons (reliability impact), due to the source variability and difficulty of prediction, and it causes a much lower capacity factor for conventional plants (balancing impact). More frequent on/off and output variations for thermal plants significantly affects their efficiency with resulting higher electricity production costs and CO₂ emissions. So, for example, considering a system with peak demand of 5000 MW, while the expected CO₂ emission savings would be nearly 5.4% for an installed wind capacity of 500 MW, an increase to 1500 MW would cause the emission savings to raise only up to 12.9% (and not up to an expectable 16.2%) [28]. The capacity credit, measuring the amount of load that can be provided by a variable plant with no change in the reliability of supply (and so effectively the actual amount of conventional plants that can be displaced by variable renewable plants) is heavily affected as well. An Irish study from Eirgrid, based on 2006 wind data, established that this capacity credit is reasonably significant at low levels of wind penetration, but the benefit tends towards saturation as wind penetration levels increase, as illustrated in Fig. 2.1. This is because

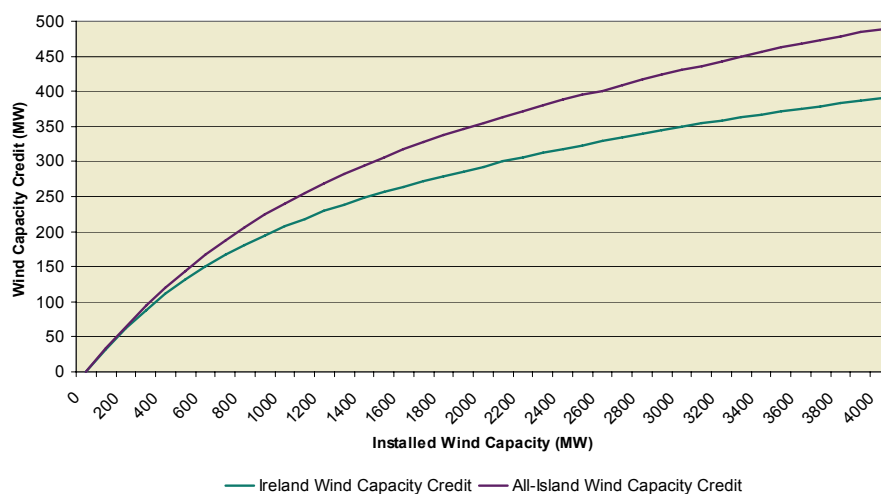


Figure 2.1: Wind capacity credit in Ireland, with respect to installed wind capacity [29].

there is a significant risk that a single source of failure (i.e. very low or very high wind speeds across the country) will result in all wind farms producing practically no output for a number of hours, even allowing for geographic diversity [27].

These effects are particularly stark in the specific case of Ireland, which has little scope to smooth out the intermittent production pattern of wind through interconnection on scale. Consider, in fact, that the power system in the Republic of Ireland and Northern Ireland acts as a single power system of about 8500 MW, considerably smaller than the United Kingdoms (76000 MW) and not comparable at all to the continental Europe UCTE power system (600000 MW). Note that the inter-connector between Northern Ireland and Scotland, and the planned interconnections between Ireland and UK and France are non-synchronous DC connections and do not contribute to create a single system. The wind penetration over the global power system, therefore, will be significantly higher than in other countries, making the cited difficulties of reliability impact, balancing impact and saturation of the capacity credit particularly significant in the attempt to achieve the stated 40% target. This issue of the integration of a high share of intermittent resources into the energy system, especially the electricity supply, is considered as one of the main challenges of renewable energies for sustainable development [30, 31].

The main reason why the value of wind energy declines (indeed this is true for any renewable source) lies in the fact that the output from successive increments of capacity is correlated with that already in the system [32]. In contrast, combining capacity from renewables with uncorrelated or complementary outputs can be of considerable benefit, so that the potential synergies among different renewable sources are clearly much too important to ignore, as they may often make the combined exploitable potential larger than the sum of the parts considered in isolation [33]. A number of studies have been carried out on the large-scale integration of power from renewable into the electricity supply [34, 35, 36, 37, 38]. Ireland, together with the considerable wind potential, offers an enormous ocean wave resource, which is expected to make a significant contribution towards Irelands future energy requirements (note that innovative combined wind and wave energy

conversion systems are being developed [39]). Moreover, it offers the possibility of introducing that diversity in the renewable sources mix that may help to reduce the variability and uncertainty in the produced power, so to improve its reliability, at high level of intermittent source penetration in the power system. This study, fully reported in [17], will assess that the correlation between the wind and wave resource can be quite low over significant parts of the year, particularly at some locations, so that their aggregation and combination can reduce the overall variability of the power produced, with all the resulting benefits in terms of improved capacity credit and improved effectiveness in the reduction of green house emissions. A similar analysis, focused on the coast of California, is given in [40].

Unfortunately wave energy is still far from being a developed and well tested technology, so that it is not expected to make a significant contribution to a more renewable-oriented power supply system before the year 2020. The results of this study, however, will hopefully make a significant contribution to eventual attempts to the achievement of further targets that may be set in the following decades, consisting of much higher levels of penetration of renewable sources in the power system.

2.2 Methodology

The key benefit, deriving from the diversification of the mix of renewable technologies, lies in the possibility of reducing the variability of the produced power. When adopting a single variable source (for example wind) the only way to reduce variability is by geographical diversity and displacement of the farms. When considering different variable sources, if they are uncorrelated, their combination is a powerful alternative in order to obtain a reduction of the overall variability of the produced power. The methodology will therefore focus, firstly, on the assessment of the correlation between raw wave and wind power, as discussed in Section 2.2.2, available at different significant off-shore locations around Ireland, which are documented in Section 2.2.1. The variability and the predictability of the power produced by hypothetical wind and wave farms are then quantified according to the methodology described in Section 2.2.3. Finally, Section 2.2.4 presents the error analysis of the adopted methodology for this study.

2.2.1 Available data and locations

The data utilised for this study was provided by the Irish Marine Institute in the form of hourly spaced observations collected around the coast of Ireland by means of weather data buoys. The 4 buoys which will be considered are located as in Fig. 2.2, with some other locations neglected due to the lack of a complete set of observations, because of long periods of operational problems. These sites represent, however, a significant enough set in order to cover the main diversities in the Irish windwave climates. The observations consist of wind speed v_w , average zero-crossing wave period T_z and significant wave height H_s time series collected in the period from January 2002 to January 2005. Due to technical problems experienced by the different data buoys, the time series are affected by several sets of missing measurements (single points to entire days).

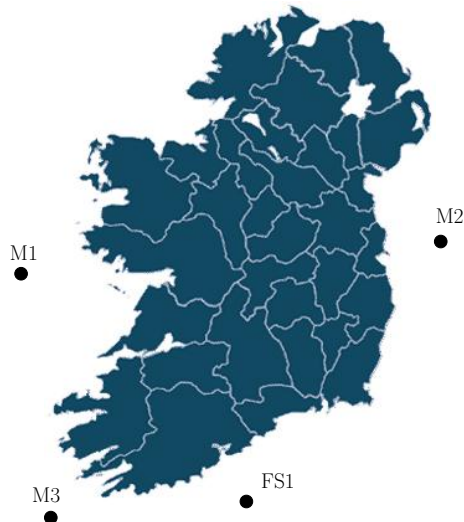


Figure 2.2: Locations of the Irish Marine Institute data buoys.

A preprocessing procedure was then implemented in order to reconstruct some of them. Up to 2 missing samples were interpolated through cubic splines [41], while more than 2 samples-long holes were discarded. This still allowed the availability of significant portions of the observations (minimum 168 samples-long, corresponding to 3 weeks) for at least two months of every season in each year considered.

2.2.2 Raw data analysis methodology

The variability of the power produced from a mixed farm is only reduced if the different variable sources appear in different moments so that they balance each others variations. This property can be quantified through the cross-correlation, given by the following expression, for two generic signals, $x(k)$ and $y(k)$:

$$c(\tau) = \frac{1}{N} \sum_{k=1}^{N-\tau} \frac{[x(k) - \mu_x][y(k + \tau) - \mu_y]}{\sigma_x \sigma_y}, \quad (2.1)$$

where μ_x , μ_y and σ_x , σ_y are the mean and the standard deviation of x and y . The quantity $c(\tau)$ gives the correspondence between two signals, at a time lag τ . In our study, we are particularly interested in assessing the instantaneous correspondence between wind and wave power at the different locations, so $c(0)$ is of particular interest, with the following interpretation:

- $c(0) = 1$: The resources correspond perfectly, they are present at the same moments.
- $c(0) = 0$: The resources have absolutely no correspondence, there is no common pattern in their evolution.
- $c(0) = -1$: The resources have a perfect inverse correspondence, they are at the opposite of their mean level in every instant.

In order to obtain the available raw power, the time series of v_w , T_z and H_s must be converted into units of power. In this respect, the wind power density (power per unit area) is calculated by means of the following expression [33]:

$$P_{wind} = \frac{1}{2} \rho_a v_w^3 \quad \left[\frac{W}{m^2} \right], \quad (2.2)$$

where ρ_a is the air density and v_w the wind speed. The wave power density (power per unit of crest width) is based on the following formula, valid in a deep water condition (water depth much greater than wave length), which is verified at the considered off-shore locations [4]:

$$P_{wave} = \frac{\rho_w g^2 H_s^2 T_e}{32\pi} \quad \left[\frac{W}{m} \right], \quad (2.3)$$

where ρ_w is the water density, g is the gravity acceleration, H_s is significant wave height and T_e is the energy period. Since only the zero-crossing period, T_z , available from the measurements, this is utilised in (2.3), instead of the energy period. More details about the definition of summary statistics for the description of real ocean waves, such as significant wave height and energy period, will be given in Chapter 3, Section 3.1.

Correlation is a purely statistical measure and it is therefore important to provide some physical justification in order to support whatever conclusion might emerge from the analysis. A methodology will then be proposed, based on the knowledge about the process of wave generation from wind. It was experimentally shown how a wind speed $U_{19.5}$, measured at 19.5 m above the sea level, produces, if blowing over a sufficient fetch and for enough time, a sea state defined by the following significant wave height H_s and period T_z [42]:

$$H_s \approx 0.21 \frac{U_{19.5}^2}{g} \quad (2.4)$$

$$T_z = \frac{2\pi}{0.4} \sqrt{\frac{H_s}{g}}. \quad (2.5)$$

This allows the calculation of the expected wave height and period, based on the wind speed measurements, and the comparison with the values actually observed. A significant disagreement would encourage the hypothesis of a low correlation between wind and wave power, probably due to the presence of remotely generated waves (generally a low frequency swell), which would be very likely to be observed off the West and SouthWest coast of Ireland, particularly exposed to the Atlantic Ocean.

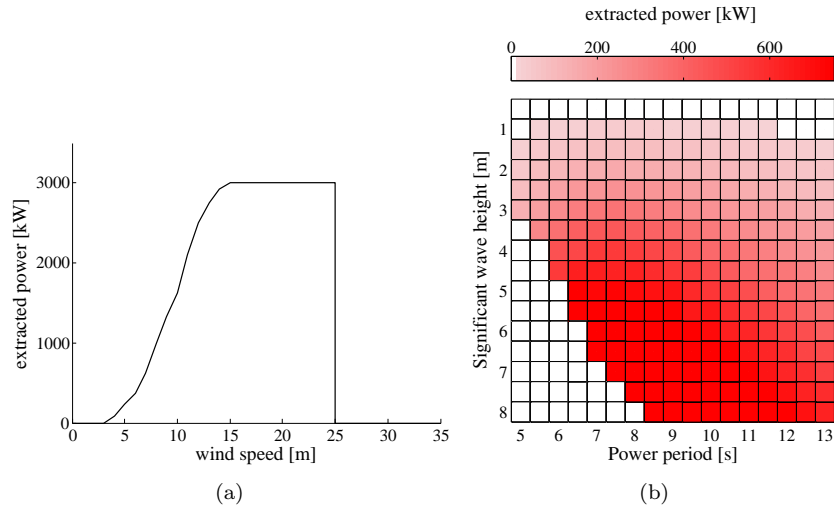


Figure 2.3: (a) Power curve for a Vestas V90 3.5 MW wind turbine. (b) Power matrix for the Pelamis 750 kW wave energy converter.

2.2.3 Power extracted from hypothetical mixed farms

Initially, the available raw power must be converted into actual extracted power from hypothetical wind and wave farms. Regarding the power extracted from wind, the relatively mature state of wind turbine technology permits the use of well established power curves. A typical 3.5 MW off-shore wind turbine was chosen for this study, whose power curve is shown in Fig. 2.3(a). Computing the extracted power from wave energy devices, on the other hand, is not as straightforward, mainly because of the fact that there is little established wave technology and the operating principles of the available devices are very diverse, so that it is difficult to find a standardised measure of the extracted power in the case of waves. For this study, the 750 kW Pelamis wave energy converter is chosen, because of the well documented characteristics of its power production, which is articulated through the published power matrix, as in Fig. 2.3(b).

In order to determine the power extracted from a farm, the power from single devices must be projected to the corresponding number of wind turbines and wave energy converters, depending on the considered mix. For this study 50 MW farms have been considered, where the number of devices are calculated so that their combined yearly average power output level is 50 MW and the considered mix is respected. The reason why the rated capacity is not used is that the capacity factors for wind turbines and the Pelamis are not the same, due to the significant differences in the probability distribution of their produced power, as it can be appreciated from Fig. 2.4. Wind turbines, most of the time, work either at low level or at full capacity, whereas the Pelamis power output is mostly concentrated at average levels, so that a comparison based solely on the capacity and not taking into account the capacity factor, would be quite unjust and might return misleading results.

A more precise estimation of a farm power output would involve the introduction of a smoothing effect due to the spatial diversity of the individual turbines/WECs, whereas only single point measurements are being utilised in this study. While the problem for wind farms has been well studied and some methodologies were developed (e.g. refer to [42, 43]), the state of the art for

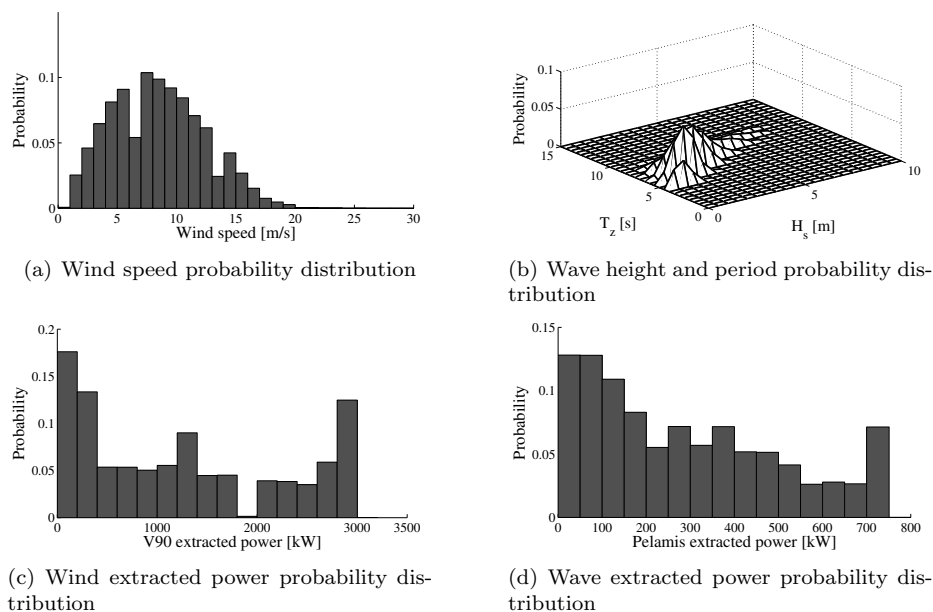


Figure 2.4: Distribution of the power extracted by an hypothetical off-shore wind turbine V90 and a hypothetical Pelamis wave energy converter, based on observations from the data buoy M1, West Coast of Ireland.

wave energy is still too immature to allow such a methodology to be developed for wave energy converter arrays. This is the reason why this smoothing effect has been discarded in the present study.

Once the measurement time series from the data buoys at the different locations are converted in hypothetical power outputs from mixed wind and wave farms, their characteristics of variability and predictability are compared in order to evaluate the eventual benefits that a heterogeneous mix can introduce with respect to a single resource and the differences in characteristics with respect to the location.

The variability is analysed on the basis of three significant quantities.

1. An *absolute variability* index, Δ , is calculated as the cumulative sum of the variations over all the considered data set:

$$\Delta = \sum_{k=1}^{N-1} |x_{k+1} - x_k|, \quad (2.6)$$

where x_i is the estimated power extracted at hour i .

2. The *standard deviation* σ [44] is a useful measure, indicating a typical range of variability, in kW or MW, around the average level for the produced power. With a 95% probability, the power output were within a $\pm 2\sigma$ range from the average level if the distribution was Gaussian. However, based on Fig. 2.4, the distribution of the extracted power can be far from Gaussian, in the case of wind and waves.
3. The third variability measure proposed quantifies the number of hours (as a percentage over the total hours considered) the farms produce a certain power output level. This is

particularly interesting, in that one of the main problems of wind farms is that they show considerable periods of time with zero power produced, so that it is very important to verify if the situation changes and to what extent when considering mixed farms.

Regarding the predictability, a very useful quantity is proposed, which is independent of any specific algorithm that may be used to produce the actual prediction, defined as the ratio of the variance of the optimal k -step-ahead prediction, $\sigma_{\hat{x}_k}^2$, to the variance of the real signal, σ_x^2 :

$$R^2(k) = \frac{\sigma_{\hat{x}_k}^2}{\sigma_x^2}. \quad (2.7)$$

The predictability index in (2.7) is bounded between 0 (signal completely unpredictable, white noise) and 1 (signal perfectly predictable, deterministic). An efficient algorithm for its computation was proposed in [45] and it is adopted for this study. Note that $R^2(k)$ is a simplification of a more general predictability notion based on mutual information theory [46], where only the linear interactions in the time series are considered. It is, however, enough for the comparison purposes of this study.

2.2.4 Error analysis

In order to properly evaluate and consider the results presented in this study, the basic hypothesis, assumptions and errors are outlined here.

The wind and wave measurements collected by the data buoys have an accuracy specified as follows:

- Hourly wind speed is with an accuracy of $\pm 2kn$, in the interval $[0, 40] kn$, and of $\pm 5\%$ in the interval $[40, 200] kn$.
- The wave height is calculated as four times the root mean square (RMS) value of the wave elevation observed for 17.5 min every hour, and the accuracy is $\pm 2 - 5\%$.
- The wave period is recorded on the basis of the number of times the wave elevation, observed for 17.5 min every hour, passes through the mean water level in upward direction. It is quantized so that the accuracy is $\pm 0.5 s$.

As explained in section 2.2.1, over the data collection period considered (January 2002 to January 2005), both long (several days) and short (a few samples) data segments are missing from the records. In order to extract large continuous portions of useful data a preprocessing procedure was applied where up to two consecutive missing samples were interpolated with cubic splines. For the presented results only contiguous segments at least 3 weeks long (168 samples) were considered.

The evaluation of the extracted power from the time series is based on certain assumptions over the particular device. In the case of wind, the well advanced state of the technology produced a certain convergence of the performance of the off-shore wind turbines available on the market, so that their power curves are quite comparable. The field of wave energy, on the other hand, is still an assortment of different devices, based on rather diversified operating principles, so that their power curves are very different among each other and can also be very site specific. The

proposed device for this study is the Pelamis, because it is the one of the few devices which is well documented, as regard its power matrix characteristics, thanks to its relatively advanced state of testing and development. It is based on a robust concept designed for off-shore applications and high energy sea states, so that the results regarding wave energy are slightly West and South coast biased, in that the predominant sea states, in contrast to the East coast, occupy the central part of the Pelamis power matrix.

2.3 Results

According to the methodology outlined in Section 2.2, the results are collected into a preliminary analysis of the raw wind and wave resource available at the considered off-shore locations, in section 2.3.1. The evaluation of the possible benefits that heterogeneous farms can bring about, in terms of reduced variability and improved predictability of the power injected into the grid, are then discussed in section 2.3.2.

2.3.1 Raw wind and wave power analysis

The instantaneous correlation coefficient $c(0)$ between wind and wave power, estimated on the basis of data collected through year 2002 to early 2005, is shown in Fig. 2.5 for the different locations and for different seasons. There is a clear difference between the East Coast, where the correlation between the wave and wind resource is quite strong, and the West and South coasts of Ireland, where wind and waves seem to be less correlated. This result was to be expected, as the West and South coasts of Ireland are completely exposed to the Atlantic Ocean and therefore to waves remotely generated by westerly wind systems, which have little correlation with the local weather conditions closer to the Irish coast and which are known to contain most of the wave energy (they are the so-called swells). The East Coast, on the other hand, due to the presence of Ireland itself as a shelter from the SouthWest prevailing swell waves, experiences mostly wind waves generated by local winds (either north easterlies or attenuated westerlies) so that the correlation is much higher.

The instantaneous correlation, however, gives only a limited view of a bigger picture, as it is clearer from the temporal correlation details of Figs. 2.6 and 2.7, where the wind and wave power time series behavior is shown. The portion of data from the East Coast shows that wave and wind power, apart from a scaling factor, evolve according to the same dynamics and this confirms the hypothesis of the presence of mainly wind waves, generated by local winds. The slight delay, about 2-3 h (it can be determined as the maximum point of the temporal correlation), is due to the time required for the waves to develop, which is relatively short for low energies. Fig. 2.6, documenting the West Coast correlations, reveals a poor correspondence between waves and wind patterns, where there might be an independent swell superimposed on the local wind waves, which are evolving according to the local wind pattern.

A further confirmation that the low correlation at some locations is mainly due to the presence of a swell superimposed on local wind waves can be had by comparing the observed sea state

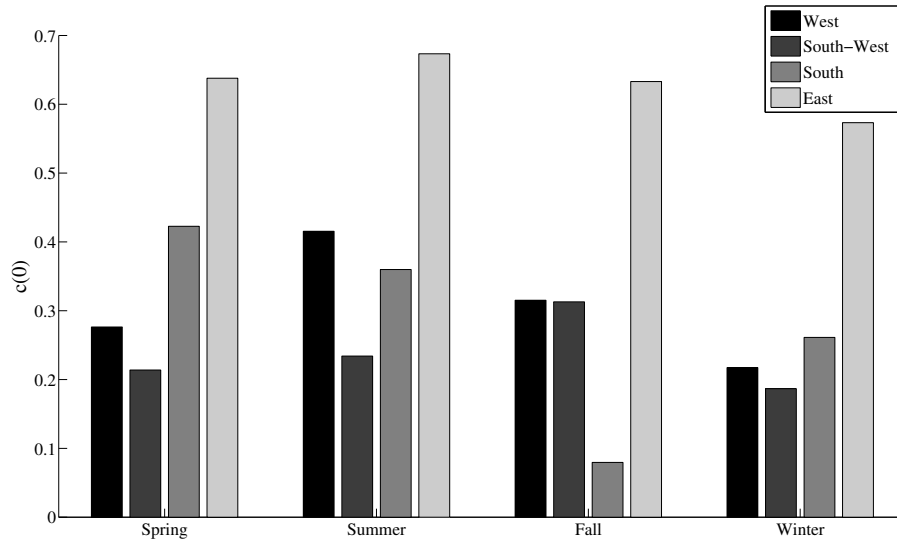


Figure 2.5: Seasonal average of the instantaneous correlation, $c(0)$, between raw wind and wave power at different locations.

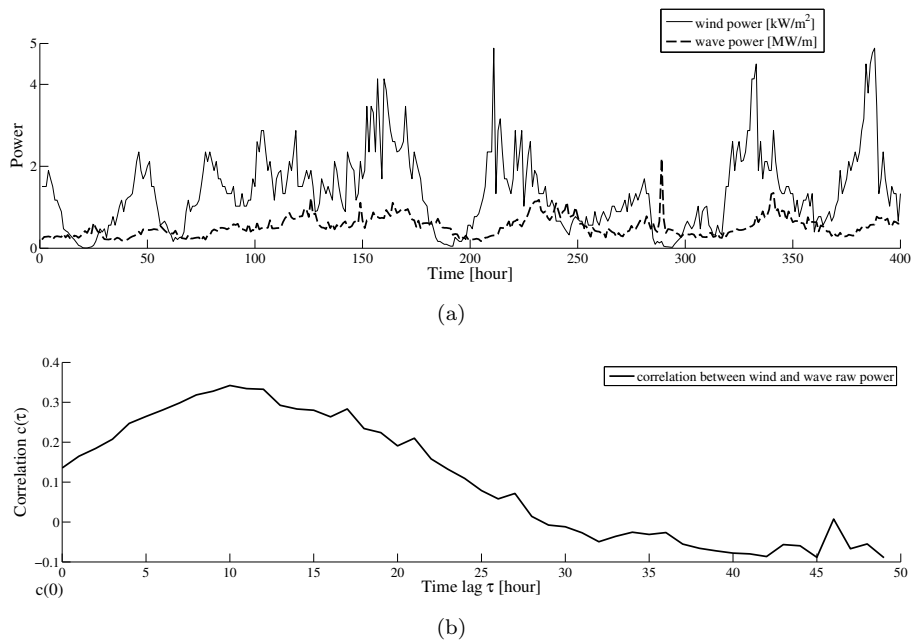


Figure 2.6: Raw wind and wave power, with their estimated temporal correlation, for a sample collected in Winter 2004 from the M1 data buoy, West Coast.

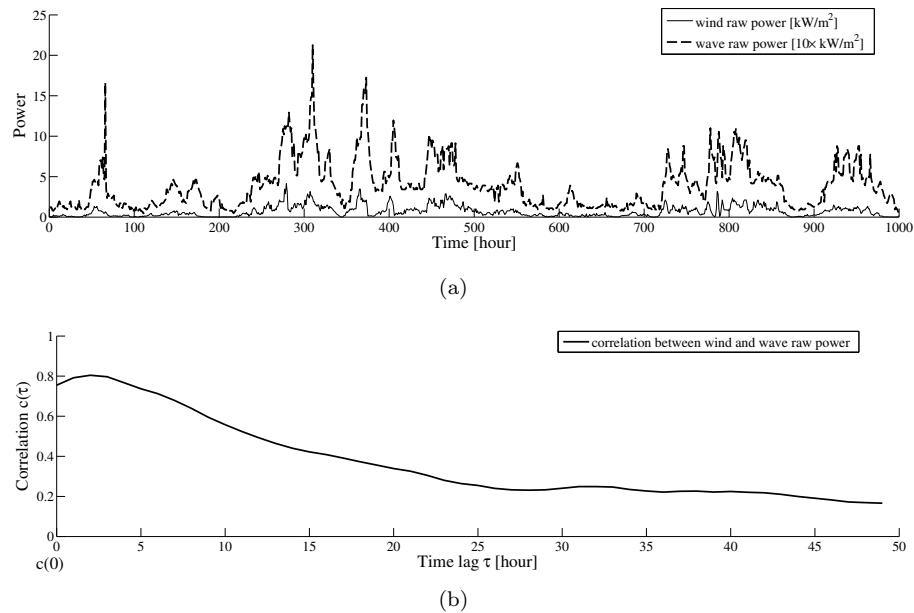


Figure 2.7: Raw wind and wave power, with their estimated temporal correlation, for a sample collected in Summer 2004 from the M2 data buoy, East Coast.

with that expected due to the local wind conditions, according to the method outlined in Section 2.2.2. This comparison is expressed once again with the correlation and the results plotted in Fig. 2.8, both for the wave period and the significant wave height. A much stronger agreement is found for the East Coast location, particularly regarding the wave period, whose estimation is quite uncorrelated (or even slightly anti-correlated) with the real observations at the South and West locations. In order to have a clearer comprehension of the reasons for these results, Fig. 9 presents a detailed representation of the comparison of expected wave height and observed wave height at the West and East locations. While for the East Coast data, the agreement is quite good, the situation of the West Coast denotes an estimated wave height which is most of the time much lower than the observed one. The latter, in fact, contains waves that are not generated by local winds and that are completely neglected by this method. The same conclusion can be drawn from a detailed comparison of the estimated and observed wave periods, shown in Fig. 10. On the West Coast the expected wave period, most of the time, is much lower than the observed one, because the local wind conditions give rise to high frequency wind waves. The predominant sea state, however, is generally concentrated around the high period swells which are travelling from remote locations where they were developed. This situation would be very clear if wave spectra were available for the considered locations, but unfortunately they require higher sampling rates than those available from the meteorological data buoys utilised in this study.

In the view of this study's purposes the results presented in Figs. 2.5 to 2.10 are more than enough to provide a clear picture of the global situation of the wind and wave energy resource around the West, South and East coasts of Ireland. In particular, the high energy swells, at the South and West locations, are independent from the local wind conditions, so that mixed wave and wind farms, at these locations, are a concrete opportunity to generate less variable and more

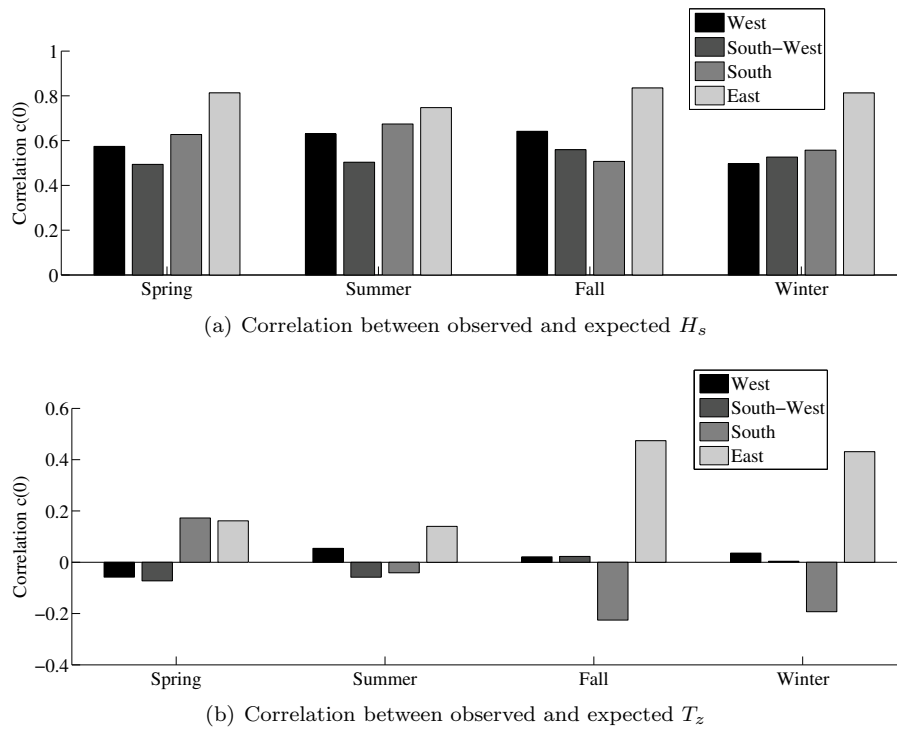


Figure 2.8: Correlation between observed wave periods and significant wave heights, and their estimations based on the wind speed measurements.

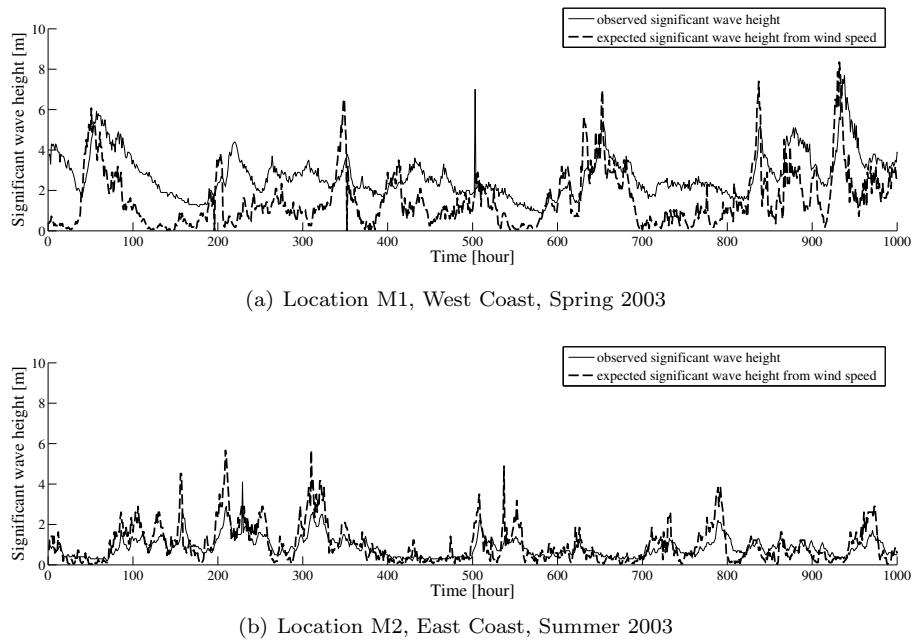
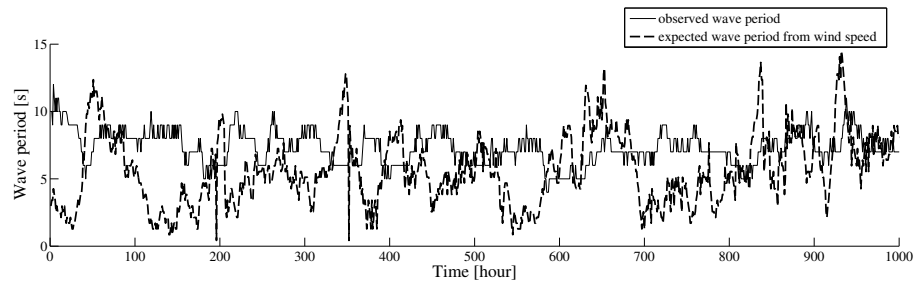
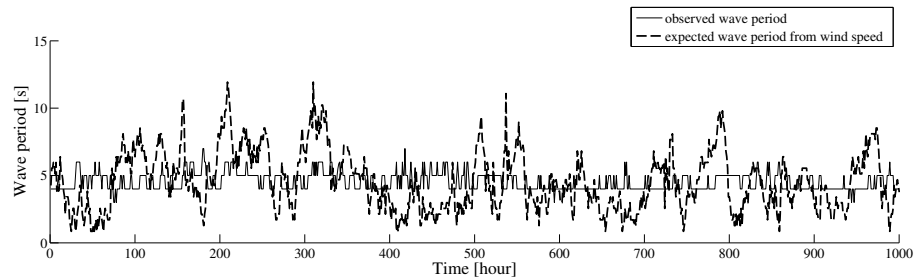


Figure 2.9: A sample comparison between observed significant wave height and its estimation from wind speed measurements at the West and East Coast of Ireland.



(a) Location M1, West Coast, Spring 2003



(b) Location M2, East Coast, Summer 2003

Figure 2.10: A sample comparison between observed wave period and its estimation from wind speed measurements at the West and East Coast of Ireland.

consistent electrical power.

2.3.2 Benefits of wind/wave combined farms

The most obvious benefit that can be expected from a diversification of the renewable mix for the electricity production is the reduced variability, which directly reduces the required surplus capacity from traditional thermal plants and the frequency of their startups/shutdowns, thus improving the capacity credit deriving from the renewable farm.

Fig. 2.11 shows the absolute variation of power, at different locations, produced from farms composed of different mixes of wind energy and wave energy devices. The trend is quite clear for the West locations, where the variability reduces while moving to mostly wave-oriented solutions, and for the East coast, where the situation is reversed. A less clear trend can be observed for the South FS1 location, where the best mix is somewhere in between. A quite similar picture can be derived from the standard deviation analysis, which is shown in Fig. 2.12. Only for the South Coast location, the situation is different, in that it presents a better performance for mostly wind composed farms. This different situation for the two indices at the South location may be explained by the fact that, although there is a low correlation between the wind and wave resources, so that the global variability is reduced through combination, the wave energy devices would most of the time produce low power outputs (refer to Fig. 2.13), so that the extracted power excursion from the average level, measured by the standard deviation, would still be large.

One more important property to be considered is the time distribution of the power output from a farm, that is for how long a certain power output is experienced. Fig. 2.14 shows the

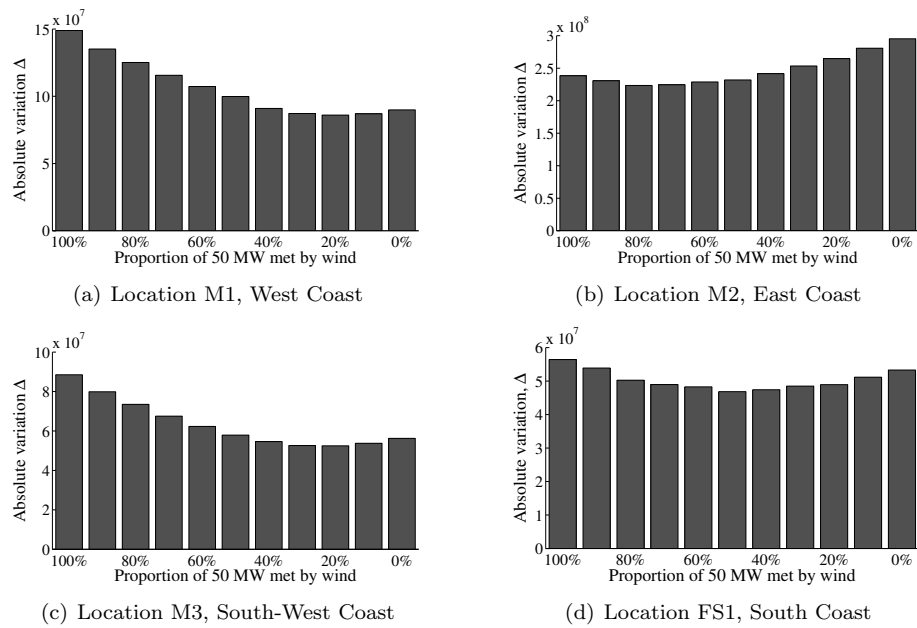


Figure 2.11: Estimated absolute variations of the extracted power from hypothetical combined wind and wave farms, all delivering approximately an yearly average of 50 MW power output, at different locations.

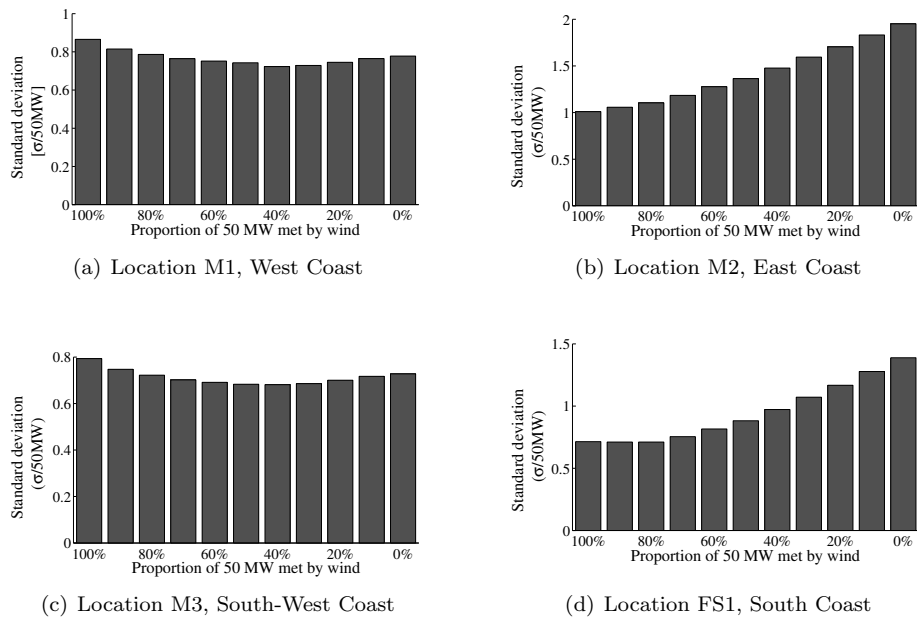


Figure 2.12: Estimated standard deviation of the extracted power from hypothetical combined wind and wave farms, all delivering approximately an yearly average of 50 MW power output, at different locations.

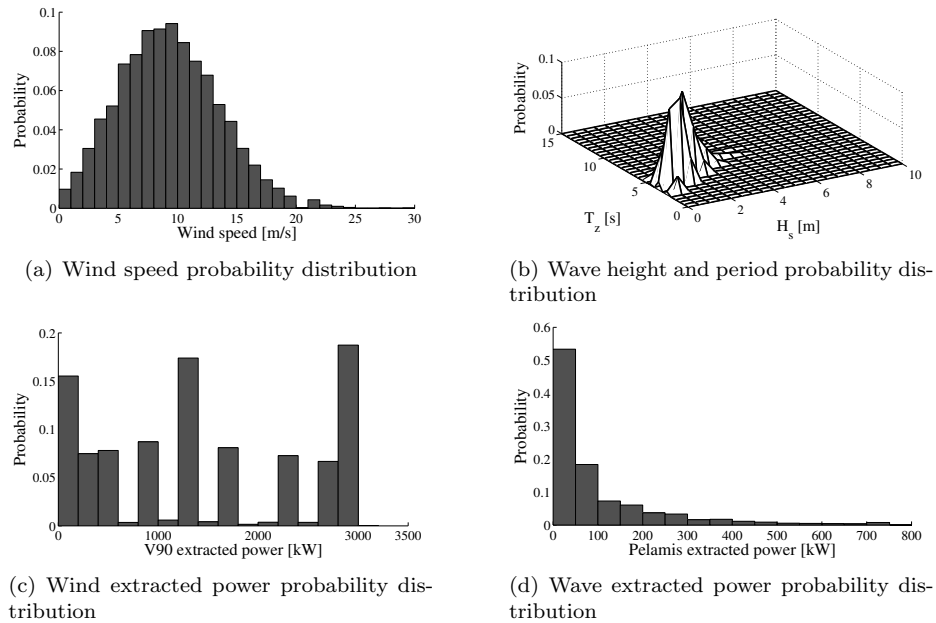
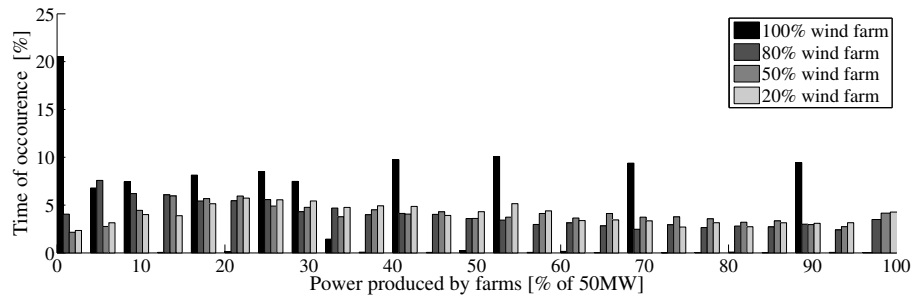


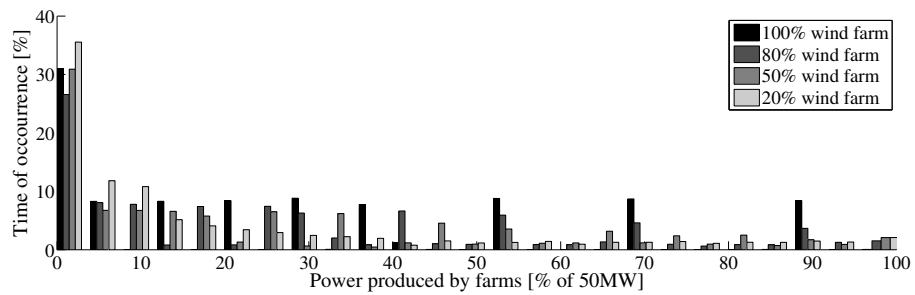
Figure 2.13: Time distribution of the power extracted by an hypothetical off-shore wind turbine V90 and an hypothetical Pelamis wave energy converter, based on observations from the data buoy FS1, South Coast of Ireland.

two extreme situations of the West coast and East coast (South and SouthWest are somewhere in-between). Whereas the introduction of even a small percentage of wave energy, e.g. 20%, in the mixed farms on the West Coast allows for a strong reduction of very low (or null) power production periods, the situation on the East Coast is not that appealing, as expected.

The final property considered in this study is the predictability of the power produced by combined wind and wave farms. Before presenting the results, it is worth noting that the power time series we are considering here have been statically mapped from wind speed and wave conditions time series, which means that their dynamics do not change. In reality, a filtering effect would be present, which would modify their dynamics, making the power time series smoother. Considering the wind, in particular, reasonable predictions of the wind power output from off-shore farms can be obtained for up to 48 h ahead (refer to [47, 48]), but the actual wind speed is much harder to predict because of its rather erratic behavior. Waves, on the other hand, have much smoother dynamics, particularly the high energy swells, so that they are easier to predict. The smoothing effect introduced by wave farms cannot be reasonably estimated, as already said, so that for a more just comparison, the effect is discarded for the wind power as well. It emerges, therefore, from the results in Figs. 2.15 and 2.16, that there is an improvement when moving to more wave-oriented solutions on the West and South coasts, whereas no real change is experienced for the East location. Wind waves, predominant on the East are, in fact, more irregular than the big swells present off the South and West coast, so that their predictability is negatively affected.

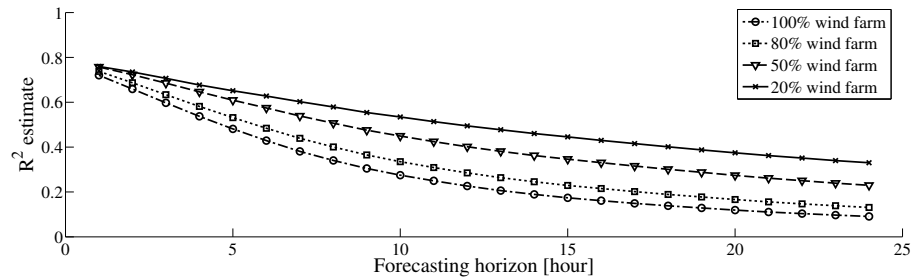


(a) Location M1, West coast

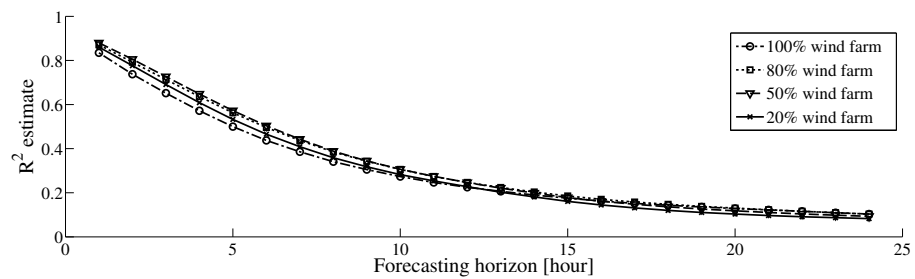


(b) Location M2, East coast

Figure 2.14: Distribution of the power extracted by hypothetical combined wind and wave farms off the West and East Coast of Ireland.



(a) Location M1, West Coast



(b) Location M2, East Coast

Figure 2.15: Predictability of the power extracted from hypothetical combined wind and wave farms off the West and East Coast of Ireland.

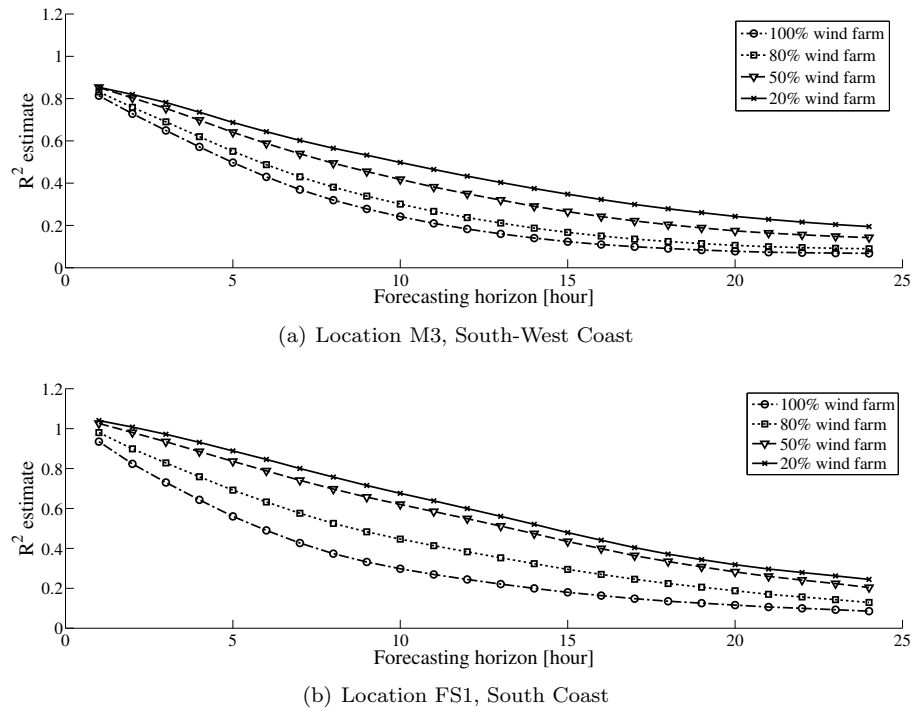


Figure 2.16: Predictability of the power extracted from hypothetical combined wind and wave farms off the SouthWest and South Coast of Ireland.

2.4 Conclusion and perspectives

The variability of the power produced from renewable sources and its uncontrollable nature negatively affects their effectiveness in reducing the requirement for thermal plants (it reduces their capacity credit) and makes them a less attractive and a potentially more expensive alternative.

Ireland, together with its great wind potential, also offers an important and enviable wave resource. This study is therefore focused on the assessment of the correlation between the two resources, at different locations around Ireland, and the possibility to reduce the variability of the power extraction if mixed wind and wave off-shore farms are adopted, with respect to the exploitation of solely one resource.

It is shown how the West and South coasts experience, most of the time, waves where the predominant (from an energy point of view) part is composed of large swell systems, generated by remote wind systems, which have little correlation with the local wind conditions. This means that the two resources can appear at different times and their integration in combined farms allows a more reliable, less variable and more predictable electrical power production. The reliability is improved thanks to a significant reduction of the periods of null or very low power production (which is a problem with wind farms). The variability and predictability improvements derive from the smoothing effect due to the integration of poorly correlated diversified sources.

On the other hand the combination of wind and waves off the East Coast does not appear to be an attractive solution, due to a quite limited wave energy resource, which is strongly correlated to the local wind conditions. The results here were also coloured by the choice of a wave energy device, the Pelamis, which is more suitable to the sea states typical of the West coast. But it

is reasonable to expect that even the choice of a different wave energy converter, for smaller sea states, would not improve significantly the properties of variability, reliability and predictability at this location, due to the strong correlation between the two resources.

The conclusion is, then, that the potential benefits of the integration of wind and wave resources, where the climate of the location is appropriate, are too important to be neglected. This Chapter establishes the groundwork to allow the quantification of these benefits, particularly from a raw resource assessment point of view. With wave energy technology becoming more mature, it will then be possible to develop a more complete analysis where these benefits are integrated, together with the actual costs of the different wave and wind technologies, in a global functional, whose optimisation shall lead to a proper dimensioning and design of offshore combined farms, given the climate of a certain location.

Chapter 3

Ocean waves and oscillating systems for wave energy conversion

Abstract

The present thesis focuses on wave energy conversion systems consisting of floating bodies that oscillate in water due to the force induced by incident waves. Such systems, typically, are most conveniently thought of as oscillators, so that standard terminology and modelling techniques typical of oscillation and vibration analysis can apply. After a brief introduction about the typical models utilised for the description of ocean waves, in Section 3.1, the standard theory and basic terminology associated with mechanical oscillators is introduced in Section 3.2. The interaction between bodies floating in water and ocean waves, and the typical model of a WEC that will be utilised throughout the thesis, are then discussed in Section 3.3. Principles and basics about the conversion of the mechanical energy transmitted from the wave to the oscillation, into other forms of mechanical or electrical energy, are finally discussed in Section 3.4.

3.1 Modelling ocean waves

Ocean waves propagate along the water surface as a result of an exchange between potential and kinetic energy. The type of water waves that are of interest in wave energy (wavelengths exceeding 0.25 m) are the so-called *gravity waves*, where the potential energy is essentially due to gravity. Section 3.1.1 discusses the analytical solution of harmonic (or regular) gravity waves, that can be derived under certain assumptions about the fluid domain. Such a solution is useful for the definition of the basic terminology and for the understanding of the fundamental characteristics of water gravity waves. Please refer to [6] and [49] for a comprehensive coverage of the topic. The typical model of real (*irregular* or *random*) waves is then proposed in Section 3.1.2.

3.1.1 Regular waves

The general hydrodynamic interactions within the volume of a fluid, defined by the density, $\rho(x, y, z, t)$, and by the particles velocity, $\vec{v}(x, y, z, t)$, are regulated by the following two relationships:

$$\frac{\partial \rho}{\partial t} + \nabla \cdot (\rho \vec{v}) = 0 \quad (3.1)$$

$$\frac{\partial \vec{v}}{\partial t} + (\vec{v} \cdot \nabla) \vec{v} = -\frac{1}{\rho} \nabla p_{tot} + \nu \nabla^2 \vec{v} + \frac{1}{\rho} \vec{f}. \quad (3.2)$$

The continuity equation, in (3.1), expresses the conservation of mass. In (3.2), reporting the Navier-Stokes equation, which expresses the conservation of momentum, p_{tot} is the pressure of the fluid, ν is the coefficient of kinematic viscosity and $\vec{f} = \vec{f}(x, y, z, t)$ is an external force.

For the analysis of harmonic gravity waves in water the fluid is assumed to be ideal, that is inviscid, $\nu = 0$, and incompressible, $\rho = const.$ Moreover, the only external force is gravity, so that $\vec{f} = \rho \vec{g}$. Equations (3.1) and (3.2), therefore, simplify to:

$$\nabla \cdot (\rho \vec{v}) = 0 \quad (3.3)$$

$$\frac{\partial \vec{v}}{\partial t} + (\vec{v} \cdot \nabla) \vec{v} + \frac{1}{\rho} \nabla p_{tot} - \vec{g} = 0. \quad (3.4)$$

The additional assumption of irrotational fluid is taken, that is $\nabla \times \vec{v} = 0$. As a consequence, a scalar quantity, namely the velocity potential $\varphi(x, y, z, t)$, can be defined such that its gradient yields the velocity:

$$\vec{v} = \nabla \varphi. \quad (3.5)$$

From the condition of an irrotational field, the two vectorial equations, (3.3) and (3.4), can be expressed as two scalar equations, which are a function of the velocity potential, φ :

$$\nabla^2 \varphi = 0 \quad (3.6)$$

$$\nabla \left(\frac{\partial \varphi}{\partial t} + \frac{\nabla \varphi \cdot \nabla \varphi}{2} + \frac{p_{tot}}{\rho} + gz \right) = 0, \quad (3.7)$$

where, in (3.7), the constant term due to the gravity force was integrated with respect to space, $\vec{g} = -\nabla(gz)$ (z is the vertical coordinate, positive above the water surface). Note that, in going from (3.4) to (3.7), the vectorial identity $\vec{v} \times (\nabla \times \vec{v}) = \frac{1}{2} \nabla \vec{v} \cdot \nabla \vec{v} - \vec{v} \cdot \nabla \vec{v}$ was utilised which, based on the condition of irrotational fluid, simplifies to $\vec{v} \cdot \nabla \vec{v} = \frac{1}{2} \nabla \vec{v} \cdot \nabla \vec{v}$.

In order to specify a solution of the Laplace equation, in (3.6), a fluid domain needs to be identified, and the behavior of the velocity potential at the boundaries has to be specified. Consider the particular domain in Fig. 3.1, which is defined by a constant water depth h and by a free surface (interface between water and air), and that is unlimited along the other dimensions. The z -axis is perpendicular to the free-surface and points upwards. The x - and y - axes identify the water surface and are oriented such that the triple xyz specifies a right-handed, three-dimensional system of coordinates. The mean water level is at $z = 0$ and the free-surface excursion from the average

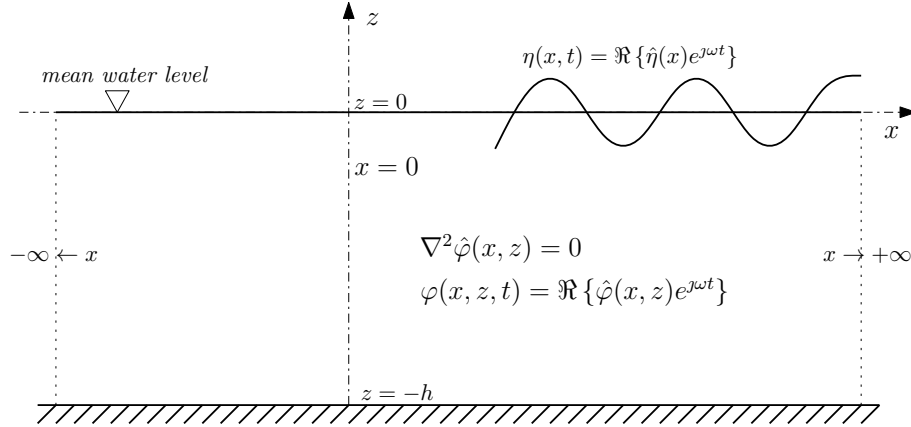


Figure 3.1: Fluid domain and conditions for the solution of harmonic waves on water of constant depth.

level is denoted as $\eta = \eta(x, y, t)$.

The boundary condition at the sea bottom specifies that the vertical velocity of the water particles has to be zero:

$$\left[\frac{\partial \varphi}{\partial z} \right]_{z=-h} = 0. \quad (3.8)$$

As regards the free-surface, two different boundary conditions can be specified. The dynamic boundary condition expresses the equality between air pressure and fluid pressure at their interface, which is true for gravity waves, where forces other than gravity, such as surface tension giving rise to capillary forces, are neglected. From (3.7), the following dynamic boundary condition can be derived [6]:

$$g\eta + \left[\frac{\partial \varphi}{\partial t} + \frac{1}{2} \nabla \varphi \cdot \nabla \varphi \right]_{z=\eta} = 0, \quad (3.9)$$

that, for small velocities and small surface elevations $\eta(x, y, t)$, can be linearised to:

$$g\eta + \left[\frac{\partial \varphi}{\partial t} \right]_{z=0} = 0. \quad (3.10)$$

An additional kinematic condition is found by imposing that the water particles on the free-surface follow the evolution of the wave elevation: that is, their vertical velocity is the same as the vertical variation of the free-surface elevation η . By imposing such a condition in the Navier-Stokes equation, (3.7), the linearised expression for the kinematic boundary condition is derived [5] as:

$$\left[\frac{\partial \varphi}{\partial z} \right]_{z=0} = \frac{\partial \eta}{\partial t} \quad \Longleftrightarrow \quad \left[\frac{\partial^2 \varphi}{\partial t^2} + g \frac{\partial \varphi}{\partial z} \right]_{z=0} = 0. \quad (3.11)$$

Steady-state solutions of the Laplace equation, (3.6), are harmonic. The notation can, therefore, be simplified by expressing each physical quantity in terms of its complex amplitude, $\hat{\varphi}(x, y, z)$,

and frequency, ω , where the time-dependence is removed:

$$\varphi(x, y, z, t) = \Re \{ \hat{\varphi}(x, y, z) e^{j\omega t} \}. \quad (3.12)$$

The Laplace equation, (3.6), and the boundary conditions, (3.8), (3.10) and (3.11), can therefore be simplified to:

$$\nabla^2 \hat{\varphi} = 0 \quad (3.13)$$

$$\left[\frac{\partial \hat{\varphi}}{\partial z} \right]_{z=-h} = 0 \quad (3.14)$$

$$g\hat{\eta} + j\omega[\hat{\varphi}]_{z=0} = 0 \quad (3.15)$$

$$\left[-\omega^2 \hat{\varphi} + g \frac{\partial \hat{\varphi}}{\partial z} \right]_{z=0} = 0. \quad (3.16)$$

By taking the further assumption of plane waves propagating along the x direction, as shown in Fig. 3.1, an analytical solution of equations (3.13) to (3.16) can be found for the complex amplitude of the velocity potential. Note that additional radiation conditions for $x \rightarrow \pm\infty$ need to be utilised for the uniqueness of the solution. The physical meaning of radiation conditions consists of the selection of the solution of the boundary value problem describing divergent waves with sources (real or fictitious) situated in a bounded domain [50].

Without delving too much into procedural details, which is beyond the scope of this thesis, the solution for the velocity potential, when neglecting evanescent waves and only considering propagating waves, is a superposition of harmonic solutions of the type:

$$\hat{\varphi}(x, z) = \frac{1 + e^{-2k(z+h)}}{1 + e^{-2kh}} e^{kz} (ae^{-jkx} + be^{+jkx}), \quad (3.17)$$

where $a, b \in \mathbb{C}$ and the angular wave number k is related to the angular frequency ω through the following dispersion relationship:

$$\omega^2 = gk \tanh(kh). \quad (3.18)$$

An explicit expression for the free surface elevation can be derived directly from (3.17) and (3.15):

$$\hat{\eta}(x) = -\frac{j\omega}{g} \hat{\varphi}(x, z=0) = -\frac{j\omega a}{g} e^{-jkx} - \frac{j\omega b}{g} e^{+jkx}, \quad (3.19)$$

where the terms $e^{\mp jkx}$ denote a wave propagating, respectively, in the positive and negative x direction. A time-domain expression for a wave propagating in the positive x direction only, can easily be derived from (3.19), by setting $b = 0$:

$$\eta(x, t) = \Re \{ \hat{\eta}(x) e^{j\omega t} \} = A \cos(\omega t - kx + \alpha), \quad (3.20)$$

where the amplitude and phase $A, \alpha \in \mathbb{R}$, related to the complex number $j\omega a/g$, are introduced for ease of notation. In particular, it can be verified that $A = |j\omega a/g|$ and $\alpha = \angle(j\omega a/g) + \pi/2$.

Equation (3.20) represents the steady-state solution for a harmonic ocean gravity wave propagating in water of constant depth h , under the assumptions of ideal and irrotational fluid. The wavelength $\lambda = 2\pi/k$ is related to the frequency ω through the dispersion relationship, (3.18). The phase velocity of the wave, due to the non-linearity of the dispersion relationship, also depends on the frequency:

$$v_p \triangleq \frac{\omega}{k} = \frac{g}{\omega} \tanh(kh), \quad (3.21)$$

which means that ocean waves are dispersive. Waves at different frequencies propagate at different velocities.

Note that the dispersion relationship (3.18), can be simplified when $kh \gg 1$, which is termed the *deep water* condition. Then,

$$\omega^2 \approx gk \quad \iff \quad kh \gg 1. \quad (3.22)$$

The error of the approximation $\tanh(kh) \approx 1$, in particular, is less than 1% for $h > 0.5\lambda$ (note that $k = 2\pi/\lambda$), that is when the water depth is greater than half the wavelength.

It can be shown that the small amplitude and small velocity assumptions, utilised for the linearisation of the kinematic and dynamic boundary conditions, (3.10) and (3.11), are a good approximation in deep water. In shallow water conditions, when $kh \ll 1$, the harmonic model of the waves, given in (3.20), gives infinite velocities along the x direction, and is no longer valid [6].

Energy and power of regular waves

The propagation of mechanical waves, such as waves on water, is always associated with an exchange between kinetic and potential energy. In the specific case of a gravity wave on water, $\eta(x, y, t)$, the potential energy, per unit area on the horizontal plane xy , is given by:

$$E_p(x, y, t) = \rho g h \eta(x, y, t) + \frac{\rho g}{2} \eta(x, y, t)^2, \quad (3.23)$$

that is the product of the mass of water per unit area, $\rho g(h + \eta)$, times the position of the centre of mass, $(h + \eta)/2$. The reference level is set to the mean water level, $z = 0$.

The time-average of (3.23) is given by:

$$E_p(x, y) = \overline{E_p(x, y, t)} = \frac{\rho g}{2} \overline{\eta^2(x, y, t)}, \quad (3.24)$$

and, for the particular case of a progressive harmonic wave, expressed in (3.20):

$$E_p(x) = \frac{\rho g}{4} A^2 \triangleq E_p \quad \left[\frac{J}{m^2} \right], \quad (3.25)$$

that is the time-average potential energy, per unit area, is constant and proportional to the square of the wave amplitude A .

The kinetic energy per unit volume is half the mass per unit volume multiplied by the velocity

squared:

$$E_k(x, y, z, t) = \frac{1}{2}\rho|\vec{v}(x, y, z, t)|^2. \quad (3.26)$$

Assuming a progressive harmonic wave, in deep water, the complex amplitude of the velocity is directly derived, from the solution of the velocity potential (3.17), as:

$$\hat{v}(x, z) = \frac{\partial \hat{\phi}}{\partial x} \hat{i} + \frac{\partial \hat{\phi}}{\partial z} \hat{z} = -jkae^{kz} e^{-jkx} \hat{x} + kae^{kz} e^{-jkx} \hat{z}, \quad (3.27)$$

where \hat{x} and \hat{z} represent the unitary vectors in the direction of the x - and z -axis, respectively. The time-average kinetic energy, per unit volume, is therefore given by:

$$E_k(x, z) = \overline{E_k(x, z, t)} = \frac{1}{2}\rho \cdot \frac{1}{2}|\hat{v}(x, z)|^2 = \frac{1}{2}\rho \cdot e^{2kz} k^2 |a|^2, \quad (3.28)$$

and, by introducing the wave amplitude $A = |j\omega a/g|$:

$$E_k(x, z) = \frac{1}{2}\rho \frac{k^2 g^2}{\omega^2} e^{2kz} A^2 = \frac{\rho\omega^2}{2} A^2 e^{2kz}, \quad (3.29)$$

where, in (3.30), the dispersion relation in deep water, (3.22), was utilised. By integrating eq. (3.30) from $z = -\infty$ to $z = 0$:

$$E_k(x) = \int_{-\infty}^0 E_k(k, z) dz = \frac{\rho\omega^2}{4k} A^2 = \frac{\rho g}{4} A^2 \triangleq E_k \quad \left[\frac{J}{m^2} \right], \quad (3.30)$$

the time-average kinetic energy per unit area is obtained. Note that $E_k(x) = E_k$ is constant along the direction of propagation and equals the time-average *potential* energy per unit area, E_p , as from (3.24).

The total average energy, per unit area, of a progressive harmonic wave, is finally given as sum of potential and kinetic energy:

$$E = E_p + E_k = \frac{\rho g}{2} A^2 \quad \left[\frac{J}{m^2} \right]. \quad (3.31)$$

Regarding the power associated with a travelling wave, it can be expressed as wave-energy transport, or wave power per metre of wave front. In particular, it can be shown that, for a progressive harmonic wave, the power carried by one metre of wave front may be written as [6]:

$$P = E \cdot v_g \quad \left[\frac{W}{m} \right], \quad (3.32)$$

where E is the average energy per metre squared, given in (3.31), and v_g is the group velocity, defined as:

$$v_g \triangleq \frac{d\omega}{dk} = \frac{g}{2\omega} \cdot \left[1 + \frac{2kh}{\sinh(2kh)} \right] \tanh(kh). \quad (3.33)$$

While harmonic waves travel at the phase speed, the result in (3.32) may be interpreted as if the

wave energy travels at the group speed. In the case of deep water, the group velocity approximates half the phase velocity, v_p , defined in (3.21):

$$v_g \approx \frac{g}{2\omega} = \frac{1}{2}v_p \quad \Longleftrightarrow \quad kh \gg 1, \quad (3.34)$$

and it is possible to obtain an explicit expression of the average wave power, P , as a function of the frequency, ω , or period, $T = 2\pi/\omega$, and of the wave amplitude, A :

$$P = \frac{\rho g^2}{4\omega} A^2 = \frac{\rho g^2}{8\pi} A^2 T \quad \left[\frac{W}{m} \right]. \quad (3.35)$$

From (3.35), the average wave power per metre of wave front is proportional to the square of the wave amplitude and linearly proportional to the wave period.

3.1.2 Irregular waves

The analysis of harmonic solutions for gravity waves on water, briefly introduced in Section 3.1.1, provides important insight into the fundamental properties of ocean waves. Real waves, however, are not harmonic or regular and different tools need to be introduced for their analysis. Given their stochastic nature, in particular, ocean wave elevation records are treated as weakly-stationary random processes [44], which means that their first- and second-order statistical properties do not vary with time, at least over the length of an observations set (usually 20 or 30 minutes).

Given a random or irregular wave at a specific point of the sea, $\eta(t)$, its average value is always null, as ocean waves propagate only along the mean water surface, and its auto-correlation function is defined as:

$$r(\tau) = \lim_{T \rightarrow \infty} \frac{1}{2T} \int_{-T}^T \eta(t)\eta(t+\tau)dt. \quad (3.36)$$

Note that $r(\tau)$ does not depend on the specific time t but only on the time-lag τ , due to the fact that $\eta(t)$ is weakly stationary. Also note that the auto-correlation function coincides with the covariance function because of the zero mean. In particular, the value at $\tau = 0$ represents the second-order moment, or variance, of the signal:

$$r(0) \equiv E \{ \eta(t)^2 \} = \lim_{T \rightarrow \infty} \frac{1}{2T} \int_{-T}^T \eta(t)^2 dt. \quad (3.37)$$

Equations (3.36) and (3.37) are averaged over time as they assume that the wave elevation, $\eta(t)$, is a power signal, with infinite energy but finite average power, which is true for harmonic signals such as a regular waves, in (3.20), or combinations of them. The variance, $r(0)$, in particular, also represents the average power of the signal. By extending Parseval theorem to power signals, it is possible to express the variance as a function of the frequency [44]:

$$r(0) = \lim_{T \rightarrow \infty} \frac{1}{2T} \int_{-T}^T \eta(t)^2 dt = \lim_{T \rightarrow \infty} \frac{1}{2T} \cdot \frac{1}{2\pi} \int_{-\infty}^{+\infty} |\Xi_T(\omega)|^2 d\omega, \quad (3.38)$$

where $\Xi_T(\omega)$ is the Fourier transform of $\eta(t)$, truncated at time $\pm T$:

$$\Xi_T(\omega) = \int_{-T}^{+T} \eta(t) e^{-j\omega t} dt. \quad (3.39)$$

By introducing the power spectral density, $S(\omega)$, defined as:

$$S(\omega) = \lim_{T \rightarrow \infty} \frac{1}{2\pi T} |\Xi_T(\omega)|^2, \quad (3.40)$$

the average power of the signal, that equals its variance (since it is a power signal), can finally be written as:

$$r(0) = \frac{1}{2} \int_{-\infty}^{+\infty} S(\omega) d\omega = \int_0^{+\infty} S(\omega) d\omega. \quad (3.41)$$

Note that, in the last equivalence of (3.41), the fact that $S(\omega)$ is a real and even function by definition, (3.40), is utilised.

The power spectral density $S(\omega)$, termed *wave spectrum*, represents the distribution, in the frequency domain, of the average power (or variance) of the wave elevation. From the Wiener-Khinchine theorem, the autocorrelation function, $r(\tau)$, and the power spectral density, $S(\omega)$, for a weakly-stationary random process, like $\eta(t)$, are a Fourier transform pair of the type [44]:

$$r(\tau) = \frac{1}{2} \int_{-\infty}^{+\infty} S(\omega) e^{-j\omega\tau} d\omega, \quad (3.42)$$

where the coefficient 1/2 comes from the equivalence in (3.41). The relation in (3.42) is very useful in the estimation of the spectral density from the data.

Given a random wave $\eta(t)$, the time-averaged wave energy per metre squared, E , is proportional to its variance (note that this is the average power of the signal, but it is physically interpreted as average energy) [6]:

$$E = \rho g \overline{\eta(t)^2} = \rho g r(0) = \rho g \int_0^{+\infty} S(\omega) d\omega \quad \left[\frac{J}{m^2} \right] \quad (3.43)$$

In the case of an harmonic wave of amplitude A , as in (3.20), the total variance is $r(0) = A^2/2$, so that (3.43) gives the same result found for harmonic waves, as in (3.31).

From a statistical analysis of waves in deep water, it was found that the distribution of the wave elevation, $\eta(t)$, is Gaussian around the zero mean [44]. A Gaussian, stationary random process is only specified by its first- and second-order moment, and it can be thought of as a superposition of independent processes at different frequencies. In the particular case of ocean waves, this means that, in deep water, waves can be modelled as a superposition of independent harmonic waves:

$$\eta(x, t) = \int_0^{+\infty} A(\omega) \cos(\omega t - kx + \alpha(\omega)), \quad (3.44)$$

where the amplitude of the components, $A(\omega)$, is related to the magnitude of the spectrum, $S(\omega)$, and to the energy associated with each regular wave.

Under the Gaussian assumption, the average wave power per metre of wave front can be cal-

culated as the integral of the power associated with each regular wave:

$$P = \frac{\rho g^2}{2} \int_0^{+\infty} \frac{S(\omega)}{\omega} d\omega \quad \left[\frac{W}{m} \right], \quad (3.45)$$

where the power of the single harmonic components was calculated from the average energy times the group speed at that frequency, $g/(2\omega)$ in deep water, as defined in (3.32).

In addition to the wave spectrum, some additional parameters have been introduced in order to intuitively specify the main characteristics of an irregular or random wave. Such parameters usually consist of different ways of expressing an *average* measure for the period and amplitude of the wave. A wide variety of definitions exist both for the wave height (root-mean-squared height, significant wave height, etc.) and for the wave period (mean zero-crossing period, energy period, peak period, etc.). Throughout this thesis, the most common measures are adopted, these being the significant wave height, H_s , and the energy period, T_e , defined as:

$$H_s = 4\sqrt{m_0} \quad (3.46)$$

$$T_e = 2\pi \frac{m_{-1}}{m_0}. \quad (3.47)$$

In (3.46) and (3.47), m_0 and m_{-1} are the spectral moments of order 0 and -1 :

$$m_k = \int_0^{+\infty} m^k S(\omega) d\omega, \quad (3.48)$$

with m_0 corresponding to the variance, $r(0)$, of the wave. Another quantity that will be conveniently proposed is the peak period, T_p , defined as the value at which $S(\omega)$ is maximum:

$$T_p : S(\omega = 2\pi/T_p) = \max. \quad (3.49)$$

Note that, more exactly, H_s is defined as the average height (double the amplitude, or peak-to-trough height) of the highest third of the waves and it is only approximated by (3.46) within certain assumptions, namely deep water and narrow-banded wave [44, 51]. However, the definition (3.46), based on the spectral moment, sometimes referred to as H_{m0} , has become more adopted in practice as significant wave height, because it is directly related to the energy and power of the wave. Regarding the energy period T_e , it can be thought of as a weighted, average period, where the energy of each regular waves composing the random wave represents the weight.

Based on (3.46) and (3.47), equivalent expressions for the average energy and power of an irregular wave can be derived from (3.43) and (3.45):

$$E = \frac{\rho g}{16} H_s^2 \quad \left[\frac{J}{m^2} \right] \quad (3.50)$$

$$P = \frac{\rho g^2}{64\pi} H_s^2 T_e \quad \left[\frac{W}{m} \right]. \quad (3.51)$$

Some remarks need to be pointed out about the validity and the completeness of the wave spectrum as a tool to describe real ocean waves. In particular, it was mentioned that waves in deep water are approximately Gaussian, so the the spectral density gives full information about

the harmonic components of the wave, which are assumed to be independent of each other. In intermediate to shallow water, the distribution of the wave elevation tends not to be Gaussian and, at the same time, significant interaction (energy exchanges) between harmonic components may be experienced. In such situations, higher-order (third, fourth order) statistical and spectral analysis is necessary for a complete description of ocean waves [44].

Another assumption that was initially made regarding the weakly-stationarity of waves, at least over the length of an observations record (20 or 30 minutes), requires clarification. Such an assumption means that the wave spectrum is constant, that is the energy associated with each harmonic component does not change with time. In reality the spectral distribution of real waves is not constant, and mathematical tools such as the short-term Fourier transform or the Wavelet transform can be used for a more complete analysis.

Methods for higher-order statistical analysis and for analysis of non-stationarity are not included here, since stationary deep water waves will be assumed throughout most of the following Chapters, and will only be introduced, when needed, in Section 6.3.

A final important point to be made is that the wave spectrum, discussed here, represents an accumulation of the energy of all waves coming from various directions. In reality, wave energy is usually spread over multiple directions of propagation. Information on wave directionality is extremely significant for the design of marine systems, such as ships, ocean structures and wave energy devices. The response of a system in a seaway, computed using a unidirectional wave spectrum, is not only overestimated but the associated coupled responses induced by waves from other directions are also disregarded [44]. The wave spectrum can be extended to the *directional spectrum*, $S(\omega, \theta)$, where an additional parameter, θ , accounts for the direction of the energy. Since the rest of the thesis is focused on axi-symmetric systems, which equally respond to waves coming from different directions, directional spectra are not dealt with any further.

Standard spectral shapes

From wave measurements, much statistical information has been obtained for the spectrum and, in particular, it has been found that wave spectra have some general characteristics which may be approximately described by semi-empirical mathematical relations [44]. Standard spectral formulations relate the spectral shape to the main characteristics of the waves and associated variables, such as average wind velocity, significant wave height, peak or energy period, etc. The use of wave spectral distributions is crucial at the design stage of marine system, when it is important to re-create any type of sea conditions that may occur in real seas, since a complete set of real wave measurements is rarely available.

The simplest representation is the Pierson-Moskovitz spectrum, that represents a typical fully-developed sea, completely specified by the average wind speed, U , at 19 m above the sea surface:

$$S_{pm}(\omega) = \frac{Ag^2}{\omega^5} e^{-B \left(\frac{g/U}{\omega} \right)^4}, \quad (3.52)$$

where $A = 8.10 \times 10^{-3}$ and $B = 0.74$. Equivalent expressions in terms of the significant wave height, $H_s = 0.21U^2/g$, or peak frequency, $\omega_p = 0.87g/U$, can be obtained [44].

In order to represent fully- as well as partially-developed seas, the Bretshneider spectrum was defined in terms of significant wave height, H_s , and peak frequency, ω_p , as:

$$S_{bs}(\omega) = \frac{1.25\omega_p^4}{4\omega^5} H_s^2 e^{-1.25\left(\frac{\omega_p}{\omega}\right)^4}. \quad (3.53)$$

The peak frequency moves from higher to lower frequencies while the waves go from partially- to fully-developed seas [44]. Note that the Bretshneider spectrum converges to the Pierson-Moskovitz spectrum for $\omega_p = 0.4\sqrt{g/H_s}$ and it is sometimes referred to as the two-parameter Pierson-Moskovitz spectrum.

Numerous other standard formulations allow for more complex descriptions of the spectral shapes. As an example, the JONSWAP spectrum [44] is able to describe wind-generated seas with fetch limitations, as well as low-frequency and narrow-banded swells. A quite general formulation, that will be adopted throughout some of the following Chapters, was proposed in [52] and [44]: The 6-parameter Ochi-Hubble spectral distribution gives the possibility of independently specifying the peak frequency, ω_p , the significant wave height, H_s , and the peakedness, λ , of two concurrent waves, usually one at relatively high-frequency (local wind-waves) and one at relatively low-frequency (swell):

$$S_{oh}(\omega) = \sum_{j=1,2} \frac{\left(\frac{4\lambda_j+1}{4}\omega_{p,j}^4\right)^{\lambda_j}}{\Gamma(\lambda_j)} \cdot \frac{H_{s,j}^2}{\omega^{4\lambda_j+1}} e^{-\left(\frac{4\lambda_j+1}{4}\right)\left(\frac{\omega_{p,j}}{\omega}\right)^4}, \quad (3.54)$$

where $j = 1, 2$ are the two components of the spectrum and $\Gamma(\cdot)$ is a Gamma function. The Ochi-Hubble spectrum, therefore, can model double-peaked spectra, as well as single-peaked spectra (if only $j = 1$ is considered), and contains both Bretshneider and Pierson-Moskovitz as specific cases.

Spectral formulations accounting for directional spreading of the wave energy were also proposed [44], but are not considered here, as mentioned, since this thesis is focused on axi-symmetric systems, where directionality of the incident wave is not important. The interested reader is referred to [44] for a comprehensive coverage of standard spectral formulations.

Simulation of irregular waves

From the wave power spectrum, it is possible to simulate a time series of the wave elevation. Standard spectral shapes, in particular, can be utilised for time-domain simulations of offshore systems in any desired wave conditions, when no real data are available.

The problem of simulating time-series defined by its spectral density given in an analytical form has been solved satisfactorily for rational power spectral densities [53, 54]. The time series is simulated as the output of a linear filter excited by white noise, where the magnitude squared of the filter represents the power spectral density. In the case of ocean waves, standard power spectral densities, like (3.52), (3.53) or (3.54), are not rational and can only be *approximated* by a linear transfer function. In [51], a second-order filter is proposed, where it is possible to specify the peak frequency and the peakedness of the spectrum, while the significant wave height is related to the variance of the input white noise and the area of the spectral density.

A more accurate approach to the simulation of time records with any given spectral distribution,

given in parametric or non-parametric form, is proposed in [54], and it was successfully adopted for the simulation of wave elevation time series [51]. The wave spectrum is approximated by a periodogram of multi-sine time-series with deterministic amplitudes chosen so that, for a given number of equally spaced frequencies in the range $[0, 2\pi)$, the periodogram equals the original power spectral density. It is demonstrated that, in order to get a stationary ergodic random process, the phase shifts should be chosen with some well defined random properties [54]. Following such an approach, a wave elevation record of N points, sampled at f_s Hz, is generated as a superposition of harmonic signals:

$$\eta(kT_s) = \sum_{j=0}^{N/2} A_j \sin(\omega_j k + \alpha_j), \quad (3.55)$$

where the amplitudes A_j are specified by the spectral shape $S(\omega_j)$, the phases α_j , for $j = 1, \dots, \frac{N}{2} - 1$, are randomly chosen from a uniform distribution in the interval $[0, 2\pi)$, with $\alpha_{N/2}$ random, Bernoulli distributed $\mathfrak{B}(\frac{1}{2}, \{\pi/2, 3\pi/2\})$ (i.e. $\pi/2$ or $3\pi/2$ with probability $1/2$). [54]. The minimum number of frequencies, N , equally spaced in the interval $[0, \pi f_s]$, is chosen such that the statistical properties of random waves are maintained, which is related to the time lag after which the auto-correlation $r(\tau)$, defined in (3.36), is approximately zero [54]. For real waves, because the minimum N can be quite small (correlation usually falls to zero after 1 or 2 wave periods), a much bigger value is chosen, $N = T \cdot f_s$, so that the generated signal does not repeat itself over the simulation time T .

3.2 Mechanical oscillators

In this Section, the basics of mechanical oscillating systems are presented. In particular, the mathematical tools for the analysis of vibrations are described in the case of linear systems, and the total effect of oscillations at different frequencies over the system are assumed to correspond to the superposition of single effects. Sections 3.2.1 to 3.2.4 describe some basic oscillating systems with their important features and introduce the analysis in the frequency domain. Section 3.2.5 focuses on the transient phenomena which are neglected by the frequency domain description. Finally, some considerations about the power absorbed by oscillators are given in Section 3.2.6. For a more detailed discussion about oscillators, the reader is directed to [55] and [6].

3.2.1 Free vibration with no dissipation

A mass, m , subjected uniquely to an elastic force and constrained to a move along a single direction, x , obeys the following dynamic equation:

$$m\ddot{x}(t) + kx(t) = m\dot{v}(t) + k \int_{-\infty}^t v(\tau)d\tau = 0, \quad (3.56)$$

where k is the stiffness of the restoring elastic force and $v(t) = \dot{x}(t)$ is the velocity.

Equation (3.56) can also be rewritten as:

$$\ddot{x}(t) + \omega_0^2 x(t) = 0, \quad (3.57)$$

where the *natural frequency*, ω_0 , is defined as:

$$\omega_0 = \sqrt{\frac{k}{m}} \quad (3.58)$$

The equation of motion in (3.57) is a second-order homogeneous differential equation with constant coefficients, and its general solution is given by:

$$x(t) = C_1 e^{j\omega_0 t} + C_2 e^{-j\omega_0 t}, \quad (3.59)$$

where the constants $C_1, C_2 \in \mathbb{C}$ are determined by the initial conditions on $x(t)$ and its derivatives.

Clearly, $x(t)$, according to the solution (3.59), shows a purely oscillatory movement at a frequency ω_0 that has been called, on purpose, the natural frequency of the system.

Note that the solution in (3.59) can also be expressed in complex-amplitude notation:

$$\hat{x}(\omega_0) = A e^{j\alpha} \quad \Longleftrightarrow \quad x(t) = \Re \{ \hat{x} e^{j\omega_0 t} \}, \quad (3.60)$$

where amplitude and phase $A, \alpha \in \mathbb{R}$ are related to C_1 and C_2 and, therefore, to the initial conditions of the system.

3.2.2 Free vibration with linear damping

Now, consider the case of an oscillating system when it is subjected to an additional damping. In particular, the damping force is supposed to be proportional to the oscillation velocity, via a damping constant, b . The dynamics of such a system are described by:

$$m\ddot{x}(t) + b\dot{x}(t) + kx(t) = m\dot{v}(t) + bv(t) + k \int_{-\infty}^t v(\tau)d\tau = 0, \quad (3.61)$$

Equation (3.61) can also be rewritten as:

$$\ddot{x}(t) + \gamma\dot{x}(t) + \omega_0^2 x(t) = 0, \quad (3.62)$$

where the *natural frequency*, ω_0 , is defined as in (3.58) and the following parameter is introduced:

$$\gamma = \frac{b}{m} \quad (3.63)$$

The general solution of the differential equation in (3.62) assumes the following form:

$$x(t) = C_1 e^{\lambda_1 t} + C_2 e^{\lambda_2 t}, \quad (3.64)$$

where $\lambda_{1,2}$ are the solutions of:

$$\lambda^2 + \gamma\lambda + \omega_0^2 = 0, \quad (3.65)$$

calculated as:

$$\lambda_{1,2} = -\frac{\gamma}{2} \pm j\sqrt{\omega_0^2 - \frac{\gamma^2}{4}}. \quad (3.66)$$

If $\gamma^2/4 < \omega_0^2$, the motion is represented by a damped oscillation:

$$x(t) = A e^{-\frac{\gamma}{2}t} \cos\left(\sqrt{\omega_0^2 - \frac{\gamma^2}{4}}t + \alpha\right), \quad (3.67)$$

where the constants A and α depends on the initial conditions and are strictly related to constants C_1 and C_2 of equation (3.64).

The oscillating system, if left in a position different from rest, will experience some damped oscillation at a frequency lower than the natural frequency. The higher the damping the faster the response decays to zero and the further the frequency of the oscillation is from the natural frequency.

For an oscillating system it is useful to define the *quality factor*:

$$Q \triangleq \frac{\omega_0}{\gamma}, \quad (3.68)$$

closely related, from (3.67), to the number of oscillations after which the amplitude of the oscillation falls off to $1/e$ -th of the initial amplitude. According to the range of values assumed by Q , different situations can be identified:

- $Q \gg 1$: Slow rate of dissipation of energy, relatively small damping.

$$\sqrt{\omega_0^2 - \frac{\gamma^2}{4}} = \omega_0 \sqrt{1 - \frac{1}{4Q^2}} \sim \omega_0, \quad \text{for } Q \gg 1 \quad (3.69)$$

- $Q < \frac{1}{2}$: Motion is no longer oscillatory!

$$\omega_0^2 < \frac{\gamma^2}{4} \quad (3.70)$$

- $Q = \frac{1}{2}$: Critical damping or the threshold of oscillation.

$$\omega_0^2 = \frac{\gamma^2}{4} \Rightarrow x(t) = (C_1 + C_2 t) e^{-\frac{\lambda}{2} t} \quad (3.71)$$

3.2.3 Undamped oscillator with harmonic forcing

Consider an undamped oscillating system as described in Section 3.2.1, forced through an harmonic input force:

$$m\ddot{x}(t) = -kx(t) + F_0 \cos(\omega t). \quad (3.72)$$

By introducing the natural frequency, ω_0 , as defined in (3.58):

$$\ddot{x}(t) + \omega_0^2 x(t) = \frac{F_0}{m} \cos(\omega t). \quad (3.73)$$

The periodic driving force, $F_0 \cos(\omega t)$, will try to impose its own frequency, ω , on the oscillator. We have seen, in Section 3.2.1, that an oscillator, driven from its equilibrium position and then left to itself, will oscillate with its natural frequency ω_0 . We must expect, therefore, that the actual motion is a superposition of oscillations at the two frequencies ω_0 and ω .

In steady state, only forced oscillation will be present, but note that an undamped oscillating system never reaches the steady state condition and the natural oscillation never dies out, as from (3.59). It is interesting, however, to start by analysing the steady state solution solely (the transient will be treated in Section 3.2.5). We seek an oscillatory motion with same frequency, ω , as the input force:

$$x(t) = A \cos(\omega t + \alpha), \quad (3.74)$$

or, in complex-amplitude notation:

$$\hat{x} = A e^{j\alpha}. \quad (3.75)$$

The equation of motion, (3.73), can also be written in terms of the complex amplitude:

$$-\omega^2 A e^{j\alpha} + \omega_0^2 A e^{j\alpha} = \frac{F_0}{m}, \quad (3.76)$$

where $\hat{x} = j\omega \hat{x}$. From (3.76), the steady-state motion of the system results as:

$$\hat{x} = \frac{F_0/m}{\omega_0^2 - \omega^2} = A e^{j\alpha}, \quad (3.77)$$

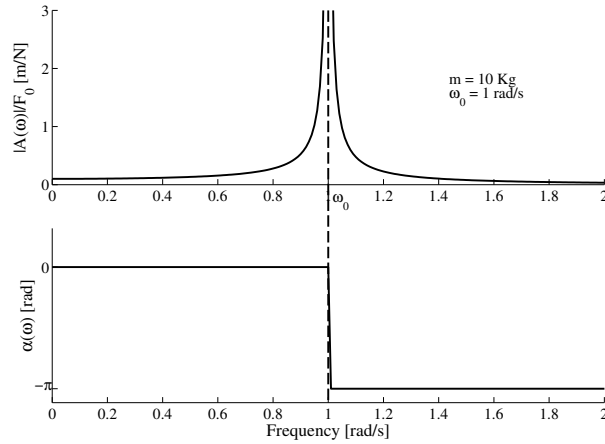


Figure 3.2: Amplitude and phase response of the position of an undamped mechanical oscillator to an external harmonic force.

with

$$A = A(\omega) = \left| \frac{F_0/m}{\omega_0^2 - \omega^2} \right| \quad (3.78)$$

$$\alpha = \alpha(\omega) = \begin{cases} 0, & \omega < \omega_0 \\ -\pi, & \omega > \omega_0 \end{cases} \quad (3.79)$$

Note that $A(\omega)$ and $\alpha(\omega)$ can be interpreted as amplitude and phase response of the system, which determine the amplitude and phase lag of the motion with respect to the input harmonic force. From (3.77) and Fig. 3.2, the amplitude of the motion increases as the excitation frequency ω approaches the natural frequency of the system ω_0 . At *resonance*, i.e. when $\omega \equiv \omega_0$, the amplitude tends to infinity.

3.2.4 Forced oscillations with damping

A damped oscillator, subjected to an external harmonic force, is described by the following dynamics:

$$m\ddot{x}(t) = -b\dot{x}(t) - kx(t) + F_0 \cos(\omega t) \quad (3.80)$$

and, introducing ω_0 and γ , defined in (3.58) and (3.63) respectively, we get:

$$\ddot{x}(t) + \gamma\dot{x}(t) + \omega_0^2 x(t) = \frac{F_0}{m} \cos(\omega t). \quad (3.81)$$

The focus, here, is on steady-state motion, so that a solution in terms of the complex amplitude can be sought:

$$-\omega^2 \hat{x} + j\omega\gamma\hat{x} + \omega_0^2 \hat{x} = \frac{F_0}{m}, \quad (3.82)$$

which is verified if

$$\hat{x} = \frac{F_0/m}{\omega_0^2 - \omega^2 + j\omega\gamma} = A(\omega)e^{j\alpha(\omega)}, \quad (3.83)$$

with

$$A(\omega) = \frac{F_0/m}{\sqrt{(\omega_0^2 - \omega^2)^2 + (\gamma\omega)^2}} \quad (3.84)$$

$$\tan \alpha(\omega) = -\frac{\gamma\omega}{\omega_0^2 - \omega^2}. \quad (3.85)$$

Note that, as also shown in Fig. 3.3, the maximum amplitude of the oscillation is not obtained at resonance $\omega = \omega_0$ but, due to the damping, at a frequency ω_m , such that:

$$A(\omega = \omega_m) = \max, \quad (3.86)$$

which is verified when the denominator is a minimum:

$$\frac{\partial}{\partial \omega^2} \sqrt{(\omega_0^2 - \omega^2)^2 + (\gamma\omega)^2} = 0, \quad (3.87)$$

that simplifies to:

$$\frac{\partial}{\partial \omega^2} [(\omega_0^2 - \omega^2)^2 + (\gamma\omega)^2] = 0 \Leftrightarrow \omega_m^2 = \omega_0^2 - \frac{\gamma^2}{2} \Rightarrow \omega_m = \sqrt{\omega_0^2 - \frac{\gamma^2}{2}} \quad (3.88)$$

Note that the frequency, ω_m , for which the amplitude of the forced oscillation, at steady state, is maximum equals the oscillation of the damped free oscillation, found in (3.67).

At resonance ($\omega = \omega_0$), it can be verified that the velocity is in phase with the input force and its amplitude is a maximum, as shown in Fig. 3.3(b). In fact, from (3.83), the following expression for the oscillation velocity can be derived:

$$\hat{v} = \frac{F_0/m}{\gamma + j\omega \left(1 - \frac{\omega_0^2}{\omega^2}\right)} = \frac{F_0}{b + j\omega \left(m - \frac{k}{\omega^2}\right)} = \frac{\omega F_0/m}{\sqrt{(\omega_0^2 - \omega^2)^2 + (\gamma\omega)^2}} e^{j\frac{\pi}{2} + \alpha(\omega)}, \quad (3.89)$$

and, at resonance:

$$\frac{\pi}{2} + \alpha(\omega = \omega_0) = 0 \quad (3.90)$$

$$\frac{\partial}{\partial \omega^2} \left[\left(\frac{\omega_0^2}{\omega^2} - 1 \right)^2 \omega^2 + \gamma^2 \right]_{\omega=\omega_0} = 0. \quad (3.91)$$

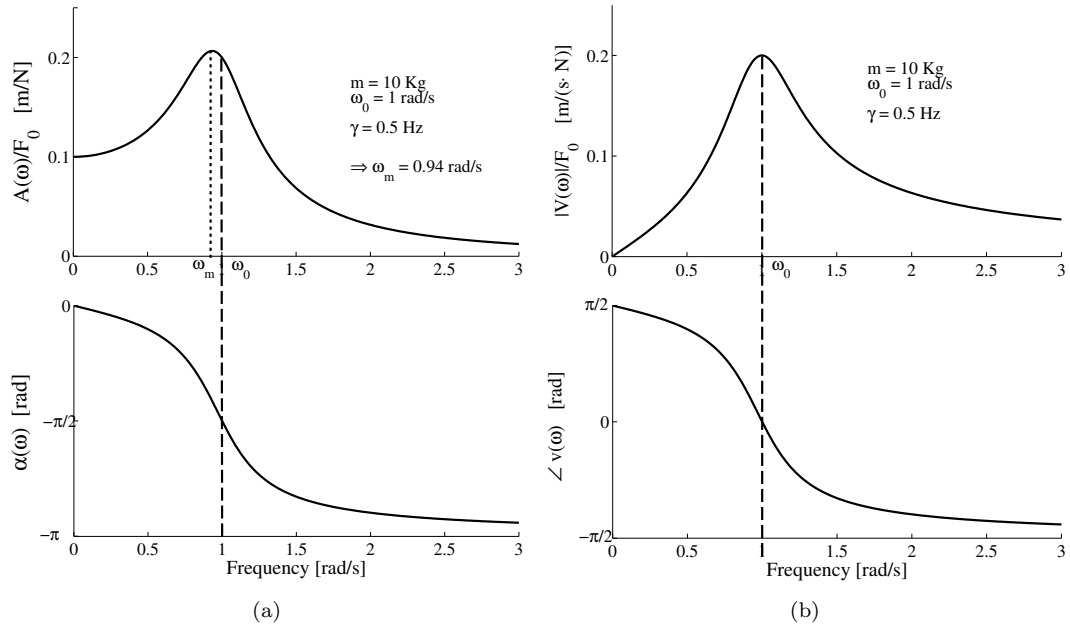


Figure 3.3: (a) Position and (b) Velocity frequency response of a damped mechanical oscillator to an external harmonic force.

3.2.5 Transient phenomena

The solution analysed in Sections 3.2.3 and 3.2.4, for oscillators subjected to an external harmonic excitation, uniquely regards the steady state and neglects anything that may happen during the transient time, defined as difference between full response of the system and steady-state response (note that there is no transient if initial conditions match the steady-state response). The methodology adopted to find the solutions of the motion, in fact, can be generalised as a method in the frequency domain, which is known to take into account only the steady state.

In order to consider the transient motion of the system, it is required that the representative differential equations, (3.73) and (3.81) in this case, are mathematically solved in the time domain.

Consider, first, the undamped oscillator:

$$\ddot{x}(t) + \omega_0^2 x(t) = F_0 \cos(\omega t). \quad (3.92)$$

The general solution of a second order differential equation with constant coefficients is given by

$$x(t) = x_o(t) + x_p(t), \quad (3.93)$$

sum of the general solution of the homogeneous equation, $x_o(t)$, and a particular solution of the complete equation, $x_p(t)$. From the results in (3.59) (free undamped oscillation corresponds to the homogeneous problem) and in (3.77) (particular solution of the non-homogeneous equation):

$$x(t) = A \cos(\omega_0 t + \alpha) + \frac{F_0/m}{\omega_0^2 - \omega^2} \cos(\omega t) \quad (3.94)$$

The solution in (3.94), as expected, is a superposition of a transient (infinitely long in this case) oscillation at the natural frequency, whose parameters A and α depend on the initial conditions, and a steady state oscillation at the excitation frequency ω , independent from the initial conditions and only related to the excitation and the properties of the system.

The damped oscillator is described by the following differential equation:

$$\ddot{x}(t) + \gamma\dot{x}(t) + \omega_0^2 x(t) = F_0 \cos(\omega t) \quad (3.95)$$

and the general solution is directly derived from (3.62) and (3.83):

$$x(t) = B e^{-\frac{\gamma}{2}t} \cos(\omega_m t + \beta) + \frac{F_0/m}{\sqrt{(\omega_0^2 - \omega^2) + (\gamma\omega)^2}} \cos \left[\omega t - \arctan \left(\frac{\gamma\omega}{\omega_0^2 - \omega^2} \right) \right] \quad (3.96)$$

The solution (3.96) is the superposition of a transient oscillation at a frequency $\omega_m = \sqrt{\omega_0^2 - \gamma^2/4}$, specified by the parameters B and β , from the initial conditions, and a steady-state oscillation at the frequency of the excitation, independent of the initial conditions.

Note that for relatively high damping, γ , the system quickly approaches steady-state conditions, although the amplitude and velocity, for a given frequency, tend to be smaller.

3.2.6 Power absorbed by an oscillator

The power, $P(t)$, transmitted to an oscillator through an input force, $f(t)$, is:

$$P(t) = f(t)\dot{x}(t) = f(t)v(t), \quad (3.97)$$

where $v(t)$ is the oscillation velocity.

As for the analysis of forced oscillating systems, in Sections 3.2.3 and 3.2.4, harmonic excitation forces are considered, of the type:

$$f(t) = F_0 \cos(\omega t) \quad (3.98)$$

In the case of the undamped oscillator, the steady-state oscillation velocity can be directly derived from (3.77):

$$v(t) = -\frac{F_0/m}{\omega_0^2 - \omega^2} \omega \sin(\omega t), \quad (3.99)$$

where m is the mass of the system and $\omega_0 = \sqrt{k/m}$ is its natural frequency, dependant on the stiffness k . The correspondent power, in steady state, will be:

$$P(t) = -\frac{\omega F_0^2/m}{\omega_0^2 - \omega^2} \sin(\omega t) \cos(\omega t) = -\frac{1}{2} \frac{\omega F_0^2/m}{\omega_0^2 - \omega^2} \sin(2\omega t) \quad (3.100)$$

Consequently, the average power \bar{P} is:

$$\bar{P} = E\{P(t)\} = 0 \quad (3.101)$$

Energy is fed into the system during 1/4 of cycle and is taken out during the following 1/4 of cycle. No energy is permanently absorbed by the oscillator.

In the case of a damped oscillator, the velocity, by taking the derivation of (3.83), is:

$$v(t) = -\frac{\omega F_0/m}{\sqrt{(\omega_0^2 - \omega^2) + (\gamma\omega)^2}} \sin[\omega t - \alpha(\omega)] = -\frac{F_0\omega_0/k}{\sqrt{\left(\frac{\omega_0}{\omega} - \frac{\omega}{\omega_0}\right) + \frac{1}{Q^2}}} \sin[\omega t - \alpha(\omega)], \quad (3.102)$$

where $\alpha(\omega)$ is given in (3.85) and $Q = \omega_0/\gamma$ is the quality factor, dependant on the damping coefficient γ and on the natural frequency, ω_0 , of the oscillator.

The resulting power, in steady state, is:

$$P(t) = -F_0 v_0 \cos(\omega t) [\sin(\omega t) \cos \alpha - \cos(\omega t) \sin \alpha] = - (F_0 v_0 \cos \alpha) \sin(\omega t) \cos(\omega t) + (F_0 v_0 \sin \alpha) \cos^2(\omega t), \quad (3.103)$$

where the amplitude of the oscillation velocity, v_0 , has been introduced and is a function of the frequency, ω , of the excitation:

$$v_0 = v_0(\omega) = \frac{F_0\omega_0/k}{\sqrt{\left(\frac{\omega_0}{\omega} - \frac{\omega}{\omega_0}\right) + \frac{1}{Q^2}}}. \quad (3.104)$$

The average power delivered to the system over a period is:

$$\bar{P} = \int_0^{2\pi/\omega} P(t) dt = \frac{1}{2} F_0 v_0 \sin \alpha, \quad (3.105)$$

which is a function of frequency and, based on (3.104), can be expanded as follows:

$$\bar{P} = P(\omega) = \frac{F_0^2 \omega_0}{2Qk} \cdot \frac{1}{\left(\frac{\omega_0}{\omega} - \frac{\omega}{\omega_0}\right)^2 + \frac{1}{Q^2}}. \quad (3.106)$$

In this case, some power is permanently delivered to the system, due to the damping, and this is a maximum at resonance, $\omega = \omega_0$. The average power approaches zero for very low and very high frequencies, and except for very low quality factors, Q , it is nearly symmetrical about the maximum. Figure 3.4 shows the behavior of the power curve, $P(\omega)$, for some values of the quality factor Q .

It is convenient to define a bandwidth for the different power curves, as a function of the frequency, by taking the difference between those values of ω for which the power input is half of the maximum value [55]. In order to find a useful expression for it, note that for values of ω close to the natural frequency ω_0 :

$$\frac{\omega_0}{\omega} - \frac{\omega}{\omega_0} = \frac{(\omega_0 + \omega)(\omega_0 - \omega)}{\omega\omega_0} \simeq \frac{2(\omega_0 - \omega)}{\omega_0}, \quad \text{for } \omega \simeq \omega_0. \quad (3.107)$$

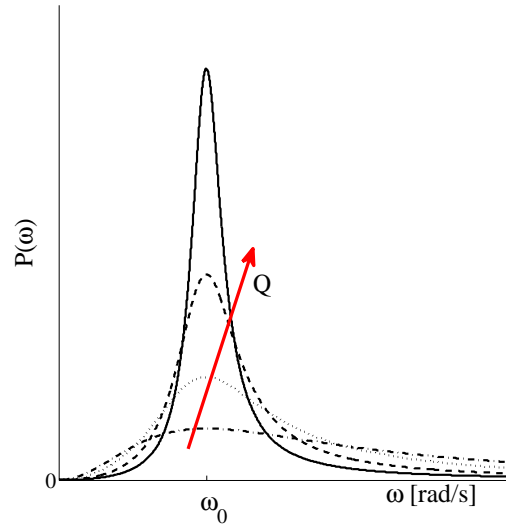


Figure 3.4: Average power transferred to a damped mechanical oscillator from an external harmonic force [55].

The average power, $P(\omega)$, can, therefore, be approximated in the proximity of the natural frequency, as:

$$P(\omega) \simeq \frac{F_0^2 \omega_0}{2kQ} \cdot \frac{\omega_0^2}{4(\omega_0 - \omega)^2 + \frac{\omega_0^2}{Q^2}} = \frac{\gamma F_0^2}{2m} \cdot \frac{1}{4(\omega_0 - \omega)^2 + \gamma^2}, \quad \text{for } \omega \simeq \omega_0. \quad (3.108)$$

It can finally be verified that:

$$P(\omega_0 \pm \Delta\omega) = \frac{1}{2}P(\omega_0) \Leftrightarrow 4(\Delta\omega)^2 \simeq \gamma^2 \Rightarrow 2\Delta\omega \simeq \frac{\omega_0}{Q} \quad (3.109)$$

The width of the resonance curve for the forced damped oscillator is approximately equal to the reciprocal of the time needed for the free oscillations to decay to $1/e$ -th of their initial energy. The higher the quality factor, the narrower the power curve, as shown in Fig. 3.4.

A narrow resonance corresponds to a slow decay of the free oscillations:

$$\frac{2\Delta\omega}{\omega_0} \ll 1 \Leftrightarrow Q \gg 1. \quad (3.110)$$

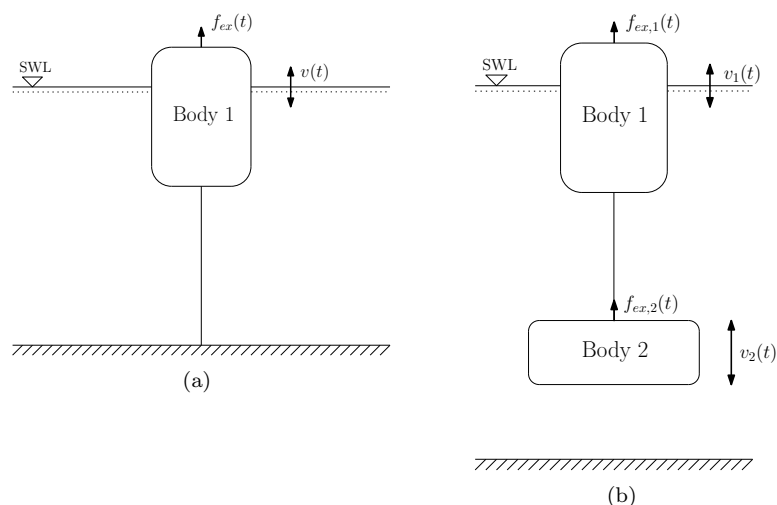


Figure 3.5: Typical oscillating bodies for wave energy conversion: (a) Bottom-referenced floating body; (b) Self-reacting bodies.

3.3 Oscillating bodies interacting with waves

In order to obtain energy conversion, the wave force acting on a WEC, consisting of oscillating bodies, needs to react against an opposition, which can be a fixed point (on the seabed or on the shore) or another body performing a different oscillation [56]. In this Section, the typical linear model of a bottom-referenced floating system, constrained to move in one degree of freedom, as shown in Fig. 3.5(a), is presented. In [56], it was shown how the model of a two-body WEC, of the type in Fig. 3.5(b), can be converted into an equivalent one-body model, whose heaving velocity is the relative velocity between the two bodies and the excitation force is an equivalent excitation force, which is a combination of the wave forces acting on the two bodies. The formal discussion of the present Section can, therefore, be generalised to WECs consisting of two-body systems.

In Section 3.3.1, the hydrodynamic model of the system in Fig. 3.5(a), which will be used throughout the following Chapters, will be introduced. Since the model is linear, a frequency-domain analysis is carried out in Section 3.3.2 to highlight the main characteristics. Section 3.3.3 proposes an analysis in the time-domain that gives more insight into the floating system, which is based on a finite-order approximation.

3.3.1 Hydrodynamic model

The dynamics of a floating rigid body of mass m , constrained to move in the heave direction (normal direction with respect to the water surface) only, and subjected to the external force from incident waves, results from the following balance of forces [6]:

$$m\ddot{x}(t) = f_w(t) + f_b(t) + f_v(t), \quad (3.111)$$

where $x(t)$ the vertical excursion with respect to equilibrium, $f_w(t)$ is the hydrodynamic force due to the interaction with waves, $f_b(t)$ is an hydrostatic force due to the equilibrium between

buoyancy and gravity, and $f_v(t)$ represents losses due to viscosity.

According to linear potential theory [6], the wave-induced force is linearly decomposed into excitation force $f_{ex}(t)$, that is the wave force when the system is supposed to be fixed, and the radiation force $f_r(t)$, due to the wave radiated when the body is moving:

$$f_w(t) = f_{ex}(t) + f_r(t). \quad (3.112)$$

The excitation force is modelled as the output of a Single-input single-output (SISO) system:

$$f_{ex}(t) = \int_{-\infty}^t h_{ex}(\tau)\eta(t - \tau), \quad (3.113)$$

where the input is the incident the wave elevation, $\eta(t)$, and $h_{ex}(t)$ is the impulse-response function, related to the geometry of the floating body. In the frequency domain:

$$F_{ex}(\omega) = H_{ex}(\omega)\Xi(\omega), \quad (3.114)$$

where $H_{ex}(\omega)$ is the excitation filter, the Fourier transform of $h_{ex}(t)$, and $\Xi(\omega)$ is the Fourier transform of the incident wave elevation, $\eta(t)$. It is important to mention that the system in (3.113) is non-causal, so that it cannot be implemented in real-time as the excitation force depends on future values of the incident wave. The reason behind the non-causality is in the selection of incident wave elevation as an input, which is a convenient conceptual simplification. The real cause of the excitation force, in fact, is the hydrodynamic pressure on the body's wet surface, as discussed in [57].

The radiation force, $f_r(t)$, is the force required by the floating body in order to radiate waves as a result of its motion. Within linear potential theory, f_r is the output of a SISO system whose input is the oscillation velocity of the body, $v(t) = \dot{x}(t)$:

$$f_r(t) = - \int_{-\infty}^t z_r(\tau)v(t - \tau). \quad (3.115)$$

In (3.115), the impulse-response function $z_r(t)$ is the inverse-Fourier transform of the radiation impedance, $Z_r(\omega)$, of the floating system:

$$Z_r(\omega) = \mathcal{F}\{z_r(t)\} = B(\omega) + j\omega M_a(\omega), \quad (3.116)$$

usually decomposed into its real part, $B(\omega)$, termed the radiation resistance, and its imaginary part, $\omega M_a(\omega)$, where $M_a(\omega)$ is termed added mass. The added mass, in general, does not go to zero in the limit $\omega \rightarrow \infty$, so that the Fourier transform in (3.116) can only be defined in a generalised sense:

$$z_r(t) = h_r(t) + M_a(\infty)\frac{d}{dt}\delta(t) = \mathcal{F}^{-1}\{B(\omega) + j\omega[M_a(\omega) - M_a(\infty)]\} + \mathcal{F}^{-1}\{j\omega M_a(\infty)\}, \quad (3.117)$$

where the singularity $M_a(\infty) = \lim_{\omega \rightarrow \infty} M_a(\omega)$ is separated from the radiation impedance, $\delta(t)$ is

a Dirac's delta distribution, and:

$$H_r(\omega) = \mathcal{F}\{h_r(t)\} = B(\omega) + j\omega [M_a(\omega) - M_a(\infty)] \quad (3.118)$$

is a well-defined Fourier transform. The radiation force, in the time domain, is therefore alternatively expressed as:

$$f_r(t) = - \int_{-\infty}^t h_r(\tau)v(t - \tau) - M_a(\infty)\dot{v}(t). \quad (3.119)$$

An important property about the radiation is given by the fact that $h_r(t)$ is a real function (velocity and radiation force are real), so that its Fourier transform, $H_r(\omega)$, has a even real part and an odd imaginary part. As a result the radiation resistance, $B(\omega)$, and the added mass after the singularity is removed, $M_a(\omega) - M_a(\infty)$, are both real and even functions in the frequency domain and are related to each other through the Kramers-Kronig relation [6]:

$$B(\omega) = \frac{2\omega^2}{\pi} \int_0^{+\infty} \frac{M_a(\zeta) - M_a(\infty)}{\omega^2 - \zeta^2} d\zeta. \quad (3.120)$$

The imbalance between gravity and buoyancy, that will be called net buoyancy force, f_b , is modelled as a constant proportional to the vertical displacement from equilibrium [6]:

$$f_b(t) = -K_b x(t), \quad (3.121)$$

where K_b is the constant of buoyancy. Equation (3.121) is an approximation that is valid for small displacements and for floating bodies whose horizontal Section is small compared to the wavelength of the incident wave (small-body approximation) [6]. Under the stated assumptions, the constant K_b is related to the average water plane area, S_w , of the floating system [6]:

$$K_b = \rho g S_w, \quad (3.122)$$

although, in reality, the instantaneous water plane area, changing with the vertical displacement but also with the evolution of the incident wave, should be considered.

The remaining force in (3.111) models viscous forces, $f_v(t)$, and is assumed to be linear, through a loss resistance K_v , with the velocity:

$$f_v(t) = -K_v \dot{x}(t). \quad (3.123)$$

Equation (3.123) is a simplification, for small velocities, that keeps the model linear and enables a frequency-domain analysis. Friction losses, however, are more accurately modelled as a quadratic function of the velocity [57, 51].

Inserting expressions (3.115), (3.121) and (3.123) into the general equation of motion, (3.111), the following dynamic equation for the heaving rigid-body is obtained, firstly proposed in [58]:

$$m\ddot{x}(t) + m_\infty\ddot{x}(t) + \int_0^{+\infty} h_r(\tau)\dot{x}(t - \tau)d\tau + K_v\dot{x}(t) + K_b x(t) = f_{ex}(t), \quad (3.124)$$

where $m_\infty = M_a(\infty)$ and the excitation force, defined in (3.113), has been left unspecified so that a causal force-to-displacement SISO system is obtained. Note that (3.124) is very similar to the model of a mass-spring-damper mechanical oscillator driven by an external force, given in (3.81). In the floating body, the damping is given by the radiation convolution term and by the loss-coefficient K_v , while the spring effect is given by the net-buoyancy force and, therefore, by the coefficient K_b . The analogy will be clearer in the frequency-domain analysis discussed in Section 3.3.2.

Identification of the hydrodynamic parameters

The radiation and excitation properties of the floating body, as from (3.114) and (3.116), are defined by the hydrodynamic transfer functions $Z_r(\omega)$ and $H_{ex}(\omega)$. Unfortunately, it is not possible, in general, to avail of an explicit expression of such properties. $Z_r(\omega)$ and $H_{ex}(\omega)$ can only be calculated numerically, for some frequencies, once the geometry of the system is specified.

The parameters of the floating systems that will be utilised in this work are calculated through the hydrodynamic software WAMIT [59]. WAMIT is a computer program based on the linear and second-order potential theory for analysing floating or submerged bodies, in the presence of ocean waves. The calculation of the hydrodynamic coefficients is based on the panel method, where the geometry of the body is represented by an ensemble of flat quadrilateral panels, or facets, and the solutions for the velocity potential are approximated by piecewise constant values on each panel [60]. As an alternative, WAMIT also offers a higher-order method, where the body surface is defined by one or more patches, each one representing a smooth continuous surface in space and such that the ensemble of all patches represents the complete body surface (or one half or quarter of that surface, if one or two planes of symmetry exist) [60].

The higher-order method was developed in order to overcome some of the main limitations of the panel method, some of which are: the need for large numbers of panel for complex geometries (e.g. large volumes, sharp corners) and the difficulties in obtaining accurate point-wise values of the derivatives of the potential on the body [61]. As a result, the higher-order method allows the achievement of accurate results with rapid convergence [61], and will be chosen for the resolution of the hydrodynamics of the systems used as examples throughout this thesis.

Figure 3.6 shows an example of results calculated by WAMIT, using the higher-order method, for a heaving cylinder of radius $R = 5$ m, height $H = 25$ m and mass $M = 1.62 \times 10^6$ Kg. The draught of the cylinder, or height of its submerged part when at equilibrium, is $h = 20$ m. The mass distribution is not uniform and such that the centre of gravity, at equilibrium, is 12 m under the mean water level (below the centre of buoyancy). The radiation impedance, $Z_r(\omega)$, is shown in Fig. 3.6(a) in terms of radiation resistance, $B(\omega)$, and added mass, $M_a(\omega)$. Note that the added mass does not go to zero in the limit $\omega \rightarrow \infty$, as expected. The excitation filter, $H_{ex}(\omega)$, shown in Fig. 3.6(b) in terms of magnitude and phase, is clearly non-causal, as expected, due to its monotonically-increasing phase response.

The IDFT [62] can be utilised to derive the impulse responses of the time-domain model in (3.124). Fig. 3.7 shows the radiation kernel, $h_r(t)$, and the excitation kernel, $h_{ex}(t)$, defined in equations (3.117) and (3.113), and calculated from the frequency-domain results in Fig. 3.6. Note the non-causality of $h_{ex}(t)$, which has non-zero values for $t < 0$. Also note that, because $H_r(\omega)$

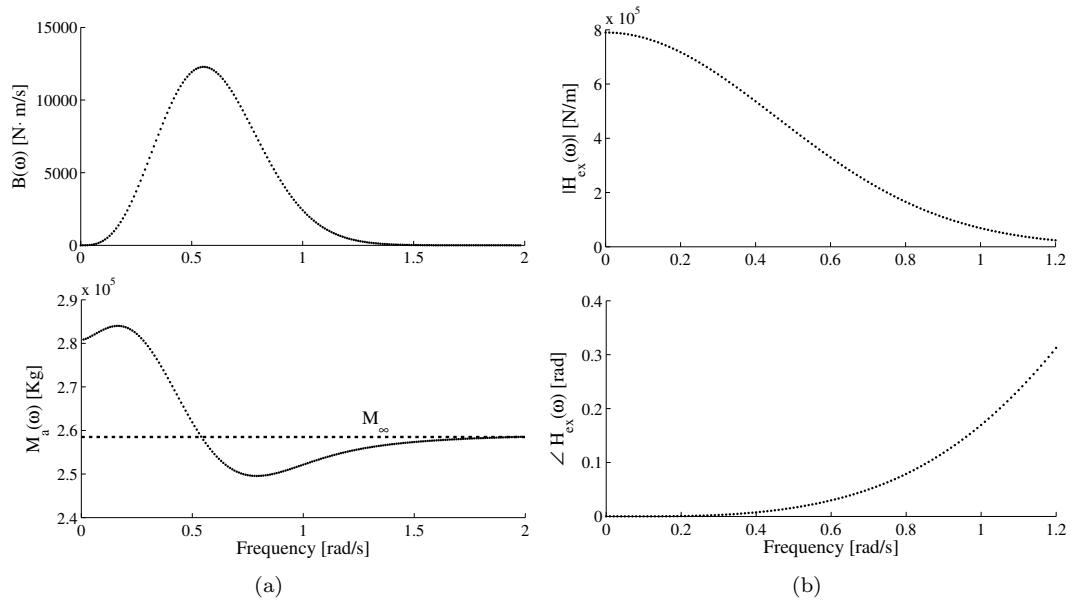


Figure 3.6: Hydrodynamic parameters of a cylinder with radius $R = 5$ m, draught $h = 20$ m, height $H = 25$ m and mass $M = 1.62 \times 10^6$ Kg: (a) radiation resistance, $B(\omega)$, and added mass, $M_a(\omega)$; (b) excitation filter $H_{ex}(\omega)$.

and $H_{ex}(\omega)$ have a limited support in the frequency domain, zero-padding can be applied in order to obtain an impulse response at any desired sampling frequency.

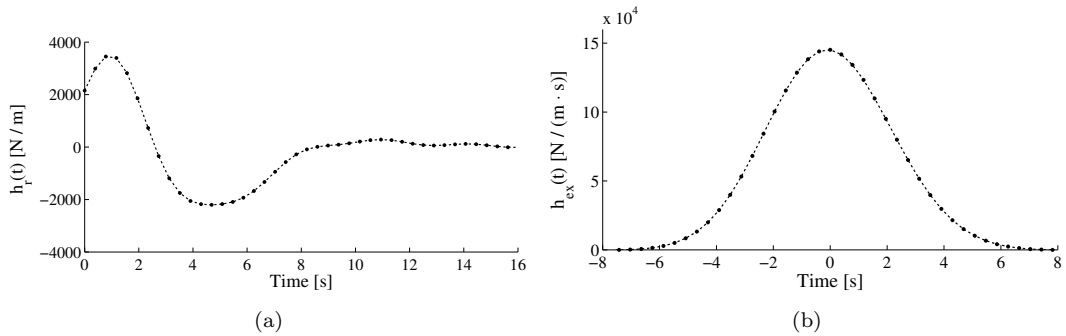


Figure 3.7: Impulse responses calculated from IDFT of hydrodynamic parameters of Fig. 3.6: (a) radiation, $h_r(t)$; (b) excitation, $h_{ex}(t)$.

3.3.2 Frequency-domain analysis

By applying the Fourier transform to (3.124), with zero-initial conditions, $x(0) = v(0) = 0$, the following equation is obtained:

$$-\omega^2(m + m_\infty)X(\omega) + j\omega [H_r(\omega) + K_v] X(\omega) + j\omega K_b \left[\frac{1}{j\omega} + \pi\delta(\omega) \right] X(\omega) = F_{ex}(\omega), \quad (3.125)$$

which can be simplified for $\omega \neq 0$:

$$-\omega^2(m + m_\infty)X(\omega) + j\omega [H_r(\omega) + K_v] X(\omega) + K_b X(\omega) = F_{ex}(\omega) \quad (3.126)$$

In (3.126), $X(\omega) = \mathcal{F}\{x(t)\}$ represents the Fourier transform of the generic time-domain function $x(t)$, namely $X(\omega) = \mathcal{F}\{x(t)\}$. Note that a Dirac delta function, $\delta(\omega)$, has been introduced in (3.125), in the Fourier transform of the buoyancy force, in order to maintain the physical causality of the relationship [57].

By separating the radiation transfer function, $H_r(\omega)$, defined in (3.118), into radiation resistance and added mass, we can express the following relation, from (3.126), between the vertical excursion and the excitation force:

$$\frac{X(\omega)}{F_{ex}(\omega)} = \frac{1}{K_b - \omega^2 [m + m_\infty + m_a(\omega)] + j\omega [B(\omega) + K_v]}, \quad (3.127)$$

where the added mass at infinite frequency is written as $m_\infty \triangleq M_a(\infty)$ and $m_a(\omega) \triangleq M_a(\omega) - M_a(\infty)$.

As a consequence, the velocity response to the excitation force is defined as:

$$\frac{V(\omega)}{F_{ex}(\omega)} \triangleq j\omega \frac{X(\omega)}{F_{ex}(\omega)} = \frac{1}{B(\omega) + K_v + j\omega \left[m + m_\infty + m_a(\omega) - \frac{K_b}{\omega^2} \right]} \quad (3.128)$$

The quantity in the denominator of (3.128) is conveniently defined as the intrinsic mechanical impedance, $Z_i(\omega)$, only related to the properties of the floating body:

$$Z_i(\omega) = B(\omega) + K_v + j\omega \left[m + m_\infty + m_a(\omega) - \frac{K_b}{\omega^2} \right], \quad (3.129)$$

so that the force-to-velocity system can be written as:

$$V(\omega) = \frac{1}{Z_i(\omega)} F_{ex}(\omega). \quad (3.130)$$

Note that (3.128) is very similar to the velocity response of a mechanical oscillator, as from (3.89). In particular, the heaving body in water can be thought of as a mass-spring-damper oscillator where the damping is given by the radiation resistance and the loss-coefficient, $B(\omega) + K_v$, the mass is given by the mass of the body plus some added mass due to the radiation, $m + m_a(\omega) + m_\infty$, and the spring is represented by the constant of buoyancy K_b . The properties of mechanical oscillators, discussed in Section 3.2, can therefore be generalised to a floating body in one degree of freedom.

In particular, a natural frequency of the system can be defined such that at resonance, when the frequency of the excitation equals the natural frequency, the velocity is a maximum and is in phase with the external force, so that also the transmitted power is a maximum, as pointed out in Section 3.2.6. The velocity response, or power, from Fig. 3.4, is more narrow-banded and has a higher peak for decreasing damping. In addition, the natural frequency gives information about the transient response of the system, which is an oscillation close to such frequency (also depending on the damping), superimposed on an oscillation at the frequency of the excitation, as from (3.96) and the discussion in Section 3.2.5.

However, the frequency-dependance of the radiation impedance, and therefore of added mass, $m_a(\omega)$, and radiation resistance, $B(\omega)$, together with the fact that an analytical expression in the frequency-domain is not available in general, complicates the definition of natural frequency and its association to the aforementioned properties. It's easy to deduce that the conditions of maximum velocity, zero-phase with the excitation force, and maximum power may happen, in general, at different frequencies, depending on the shape of $m_a(\omega)$ and $B(\omega)$!

In practice, however, and particularly for floating bodies of interest to the wave energy community, that is bodies that respond well to typical waves, the values of $m_a(\omega)$ and $B(\omega)$ are quite small, when compared to the mass and the spring term of the system. The natural frequency can therefore be well approximated as [49]:

$$\omega_0 \approx \sqrt{\frac{K_b}{m + m_\infty}}, \quad (3.131)$$

very similar to the definition, given in (3.58), for a mechanical oscillator. The approximation (3.131) will be more accurate the smaller the radiation damping is, that is the narrower is the bandwidth of the system's response. Fig. 3.8 compares the velocity response of two heaving cylinders with very different bandwidth. The resonance frequency, calculated from (3.131), is also shown. For the narrow-banded system, Fig. 3.8(a), the velocity is a maximum and in phase with the excitation force approximately at resonance, while for the wider-banded case, shown in Fig. 3.8(b), maximum velocity and zero-phase lag are at a slightly different frequency than ω_0 . The difference is, however, negligible in the latter case as well and the approximation in (3.131) will be valid for any floating system analysed throughout the present thesis.

Transmitted power

As carried out for the mechanical oscillators, in Section 3.2, the average power transmitted to the wave/body system by an external force can be calculated, in the frequency domain, from:

$$P_{ex}(\omega) = \frac{1}{2} \Re \{ F_{ex}(\omega) V(\omega)^* \}, \quad (3.132)$$

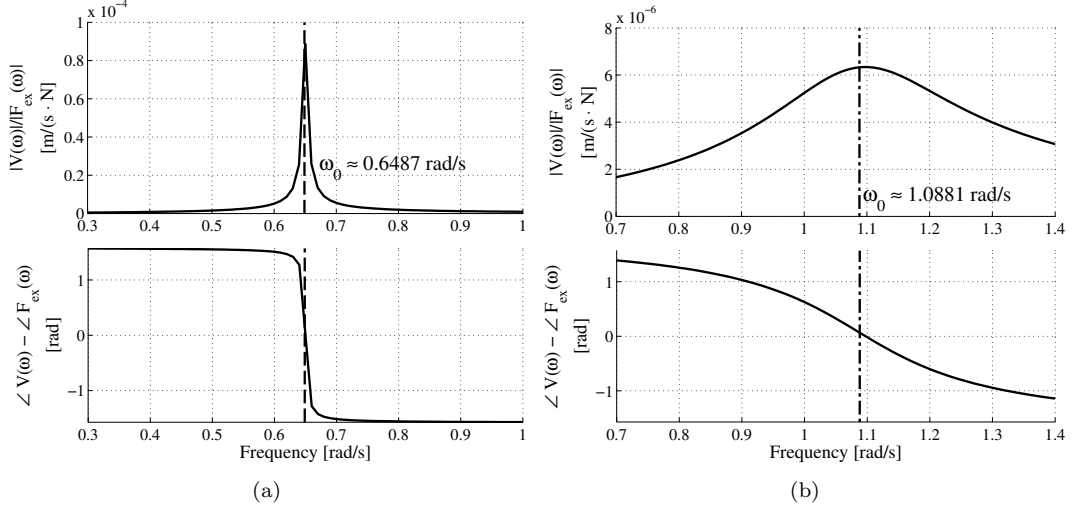


Figure 3.8: Velocity response of two floating cylinders in heave: (a) radius $R = 5$ m, draught $h = 20$ m, mass $M = 1.62 \times 10^6$ Kg; (b) radius $R = 6$ m, draught $h = 2$ m, mass $M = 0.28 \times 10^6$ Kg.

and, by using the dynamic equation (3.130):

$$P_{ex}(\omega) = \frac{1}{2} \Re \left\{ \frac{1}{Z_i(\omega)^*} F_{ex}(\omega) F_{ex}(\omega)^* \right\} = \frac{1}{2} \frac{B(\omega) + K_v}{[B(\omega) + K_v]^2 + \omega^2 \left[m + m_\infty + m_a(\omega) - \frac{K_b}{\omega^2} \right]^2} |F_{ex}(\omega)|^2. \quad (3.133)$$

The power transmitted to the floating system, or excitation power, $P_{ex}(\omega)$, is completely dissipated in radiation and viscous losses, that contribute to the total damping of the system, $B(\omega) + K_v$. It can be verified easily, in fact, that:

$$P_r(\omega) + P_v(\omega) = -\frac{1}{2} \Re \{ F_r(\omega) V(\omega)^* \} - \frac{1}{2} \Re \{ F_v(\omega) V(\omega)^* \} = P_{ex}(\omega), \quad (3.134)$$

where $P_r(\omega)$ is the average power lost in radiation and $P_v(\omega)$ is the power due to viscous losses.

The expression for the excitation power, (3.133), is similar to the power transmitted to a mechanical oscillator, given in (3.32), and has a resonant behavior like the one given in Fig. 3.4; it is maximum at resonance and it gets narrower and more peaked for lower damping (given by viscosity and radiation in this case). Again, due to the frequency-dependence of the radiation impedance, the maximum power is not obtained, in general, at the same frequency for which the velocity is a maximum. But in practice, the peak power is approximately at the frequency ω_0 , as defined in (3.131), where the velocity is (approximately) a maximum and in phase with the excitation force.

It is more useful, in general, to express the power transmitted to the system by the incident wave, rather than by the wave excitation force. From (3.133), and by using (3.114), it is possible

to write:

$$P_{ex}(\omega) = \frac{1}{2} \frac{[B(\omega) + K_v] |H_{ex}(\omega)|^2}{[B(\omega) + K_v]^2 + \omega^2 \left[m + m_\infty + m_a(\omega) - \frac{K_b}{\omega^2} \right]^2} |\Xi(\omega)|^2. \quad (3.135)$$

Note that $|\Xi(\omega)|^2$ can be interpreted as the power spectral density of the wave elevation, given in (3.40), so that (3.135) expresses the power transmitted to the floating system as a function of the wave spectrum.

Note that the maximum of the excitation power with respect to the incident waves, due to the presence of the frequency-dependent filter $H_{ex}(\omega)$, can happen at a frequency different than the maximum of $P_{ex}(\omega)$ with respect to the wave force. This means that, in theory, maximum power transfer from the waves to the system may not happen at resonance. The excitation filter, $H_{ex}(\omega)$, however, is related to the radiation impedance, $Z(\omega)$, in such a way that both maxima occur approximately at the natural frequency, ω_0 , as defined in (3.131). Again, such an approximation is more accurate the smaller the radiation damping or the narrower the bandwidth of the system. Refer to [49, 6] for a detailed analysis about the relation between excitation and radiation properties of a floating structure.

3.3.3 Finite-order approximation and time-domain analysis

The general equation of motion for a floating body in water, expressed in (3.124), is an *integro-differential* equation, due to the presence of the convolution integral modelling the radiation force. The frequency-domain analysis, proposed in Section 3.3.2, is very useful for understanding the main characteristics of the system, but it only gives information about the steady-state response. For a more complete understanding of the behavior of the floating body, a time-domain analysis of equation (3.124) should be carried out.

As also underlined in [58], where the integro-differential equation of motion of a floating system was first proposed, while a valid and complete tool for simulation, the integro-differential time-domain model is not directly suitable for analysis purposes. An explicit solution of the motion of the floating body, in fact, can only be found for specific forms of the convolution integral. However, as explained in Section 3.3.1, the radiation impedance, in general, is only known numerically for some frequencies, and the corresponding kernel function is only known numerically. As a consequence, the full motion of a floating body, in the time-domain, can only be resolved numerically, which makes it difficult to propose an analysis of the type discussed in Section 3.2.5, when dealing with simple mechanical oscillators.

It is possible, however, at least for analysis purposes, to determine a finite-order approximation of the radiation, and therefore to approximate the integro-differential equation of motion with a finite-order differential equation, for which it is always possible to express an analytical solution. The approximation of the model of the floating system with a transfer function is also particularly useful for the design of the controller of a WEC, which is the focus of Chapters 7 and 8.

Radiation identification and modal analysis

The identification of a finite-order system to model the radiation is a well developed topic in the area of offshore and marine structures.

A typical method for the extraction of the natural modes of a system from the transient response was proposed in [63], based on Prony's approximation method [64]. Prony's method was successfully implemented in wave energy and consists of expressing the radiation impulse response as a summation of a finite number of complex exponentials [12]:

$$I(t) \triangleq \int_{-\infty}^t h_r(\tau)v(t-\tau)d\tau \approx \int_{-\infty}^t \sum_{k=1}^n R_k e^{p_k \tau} v(t-\tau)d\tau, \quad (3.136)$$

where $R_k, p_k \in \mathbb{C}$ represent the residuals and poles of the correspondent transfer function [63]. The number of exponentials, n , represents the order of the approximation.

For the specific problem of the identification of the radiation's model of an offshore structure, alternative time-domain methods, based on state-space models, and frequency-domain methods are compared with Prony's method in [65, 66]. Particularly in [66], it is concluded that a direct identification of a transfer function in the frequency domain better suits the problem, as it allows the easy specification of some physical constraints. A frequency-domain identification of the radiation was also proposed in [67] and [68].

The radiation frequency response $H_r(\omega)$, defined in (3.118) and known for some frequencies ω_j , $j = 1, \dots, N$, is approximated by a finite-order transfer function of order n :

$$\hat{H}_r(s) = \frac{b_m s^m + b_{m-1} s^{m-1} + \dots + b_1 s + b_0}{s^n + a_{n-1} s^{n-1} + \dots + a_1 s + a_0} = \frac{B(s)}{A(s)}. \quad (3.137)$$

The $n+m+1$ parameters, $\vartheta = [b_m, b_{m-1}, \dots, b_1, b_0, a_{n-1}, a_{n-2}, \dots, a_1, a_0]$, of the transfer function $\hat{H}_r(s)$ are calculated from the minimisation of the following non-linear cost function, as proposed by Levy [69]:

$$\vartheta = \min_{\vartheta} \sum_{k=1}^N w_k \left| H_r(\omega_k) - \frac{B(s = j\omega_k)}{A(s = j\omega_k)} \right|^2, \quad (3.138)$$

where $H_r(\omega_j)$ are the hydrodynamic data and w_k is some weighting function. The range of possibilities for the structure of the transfer function in (3.137) can be restricted by exploiting some prior knowledge about the radiation. From [66], $\hat{H}_r(s)$ has to have at least one zero at $s = 0$ ($b_0 = 0$), unitary relative degree $m = n - 1$, and has to be Bounded-input bounded-output (BIBO) stable (roots of $A(s)$ have negative real parts). An additional property of the radiation is passivity, that is that $H_r(\omega)$ is a real positive function, or $\Re\{H_r(\omega)\} \geq 0 \forall \omega$. Unfortunately, passivity can only be imposed in the optimisation procedure via a non-linear constraint, that makes the problem non-convex and difficult to be solved. As proposed in [66], a better alternative consists of verifying the passivity after the identification, and eventually enforcing it *a posteriori* by varying some of the parameters [70]. A toolbox, for the solution of the optimisation problem in (3.138), was developed by Perez and Fossen [71].

Once a finite-order approximation of the radiation impedance, namely $H_r(s) \approx H_r(j\omega)$, has

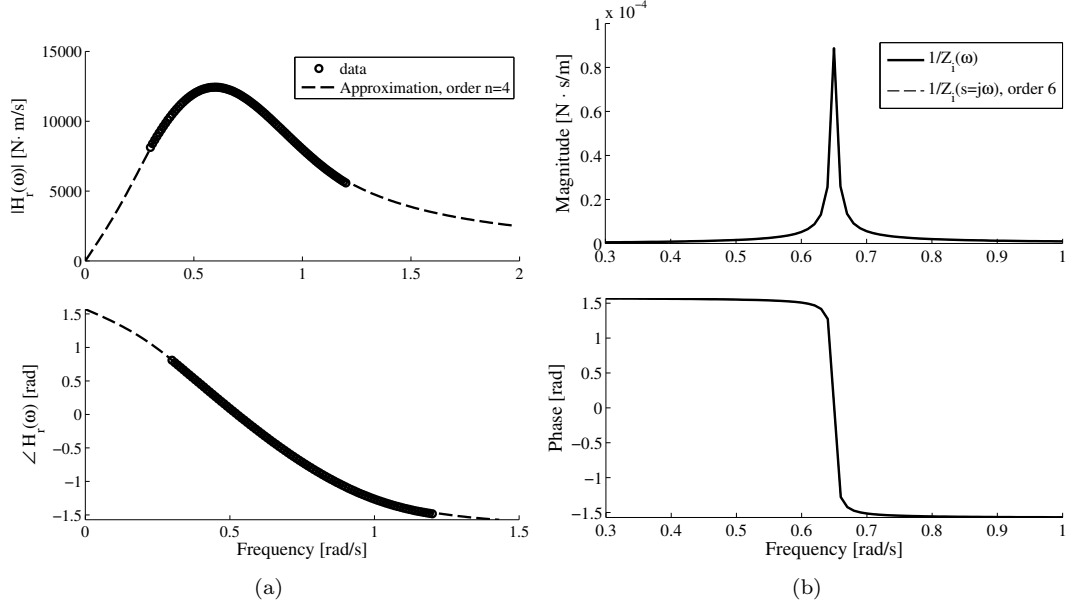


Figure 3.9: Finite-order approximation of the model of the heaving cylinder in Fig. 3.6: (a) Radiation identification with model of order; (b) Finite-order approximation of force-to-velocity system.

been identified, the floating system in (3.124) can be written as the finite-order SISO system:

$$\frac{V(s)}{F_{ex}(s)} = \frac{s}{s^2(m + M_\infty) + sH_r(s) + K_b} \triangleq \frac{1}{Z_i(s)}, \quad (3.139)$$

where $1/Z_i(s)$ is the transfer function of order $n + 2$, where n is the order of $H_r(s)$, and where zero-initial conditions are assumed.

By expressing the identified transfer function in a partial fraction expansion:

$$\frac{1}{Z_i(s)} = \sum_{k=1}^{n+2} \frac{R_k}{s - p_k}, \quad (3.140)$$

where $R_k, p_k \in \mathbb{C}$ are the residuals and poles of $1/Z_i(s)$, an analogue to Prony's approximation, in (3.136), can be obtained, where the impulse response of the radiation is a superposition of complex exponentials. Given that the signals involved, force and velocity, are real, the poles can only be real or complex-conjugate pairs, thus yielding, respectively, exponential or harmonic modes [72].

What is convenient about a representation of the type in (3.140) or in (3.136) is that the poles give information about the transient motion of the system. This transient motion will consist of harmonic or exponential modes specified by the poles, p_k , whose relative importance is given by the corresponding residuals R_k . The real part of the poles (which has to be negative for the system to be stable) will give the decay of the natural modes and the imaginary part the frequency of the natural oscillations. In the case of the mechanical oscillator analysed in Section 3.2, the transient motion, given in (3.94), is given by one decaying harmonic oscillation, defined by the two complex-conjugate poles of the transfer function, of order 2.

In the case of the heaving cylinder, whose frequency response was given in Fig. 3.8(a), a transfer

function of the type in (3.140) is calculated from a 4th order approximation of the radiation, which gives a very good fit, as shown in Fig. 3.9 (the toolbox developed in [71] was utilised). The 6 poles and residuals result in 3 complex-conjugate pairs:

$$\begin{aligned} p_{1,2} &= -0.3573 \pm j0.7091 & R_{1,2} &= (-0.0024 \pm j0.0007) \times 10^{-6} \\ p_{3,4} &= -0.0030 \pm j0.6500 & R_{3,4} &= (+0.2693 \mp j0.0001) \times 10^{-6} \\ p_{5,6} &= -0.2830 \pm j0.3358 & R_{5,6} &= (-0.0006 \mp j0.0005i) \times 10^{-6}, \end{aligned} \quad (3.141)$$

that yield a transient response composed of three decaying harmonic natural modes. In particular, the complete time-domain response of the floating system to an harmonic forcing $f_{ex}(t) = F_0 \cos(\omega t)$ is given by:

$$v(t) = \sum_{k=1,3,5} A_k e^{b_k t} \cos(\omega_k t + \alpha_k) + \frac{F_0}{|Z_i(\omega)|} \cos[\omega t - \angle Z_i(\omega)], \quad (3.142)$$

which is composed of three transient oscillations at frequencies $\omega_k = \Im\{p_k\}$, damped by a factor $b_k = \Re\{p_k\}$, whose amplitudes, A_k , and phases, α_k , are related to the initial conditions, and by a steady-state oscillation at the frequency of the excitation, with amplitude and phase related to the frequency response $1/Z_i(s = j\omega)$.

The system has an arbitrary number of natural frequencies, that equal the desired order of the approximation. However, note how the natural mode at approximately 0.65 rad/s has a much bigger residual (and a much slower decay) than the other two. Such a component will dominate the transient response of the system and, as one may expect, its frequency is approximately the natural frequency of the floating system, defined in (3.131), with the value of 0.6487 rad/s.

Emerging from this small example, and as discussed in more detail in [66], some of the components of the radiation model may not have a big impact on the force-to-velocity model of the floating system and can be neglected. In particular, after the identification of a model of the radiation, one may proceed to perform an order reduction of the model $1/Z_i(s)$, where only the dominant components are kept. In the example of (3.141), it was pointed out that one complex-conjugate pair of poles significantly dominates over the other two, by at least two order of magnitudes, so that intuitively the complete system can be reduced to the second order, and can be described as a simple 2nd order mechanical oscillator. A reduced-order system is also useful for the control design stage, as will be clearer in Chapter 8.

3.4 Wave power absorption

The motion of oscillating bodies in water is translated in useful mechanical and/or electrical energy through some mechanisms that are usually referred to as Power take-off (PTO) systems [1]. The free oscillating bodies analysed in Section 3.3, and shown in Fig. 3.5, in fact dissipate all the wave power into radiation and viscous losses, as from (3.134).

A PTO mechanism will, in general, be present in order to obtain useful energy from the relative oscillation between the oscillating body and a reference (that can also be another moving body), as

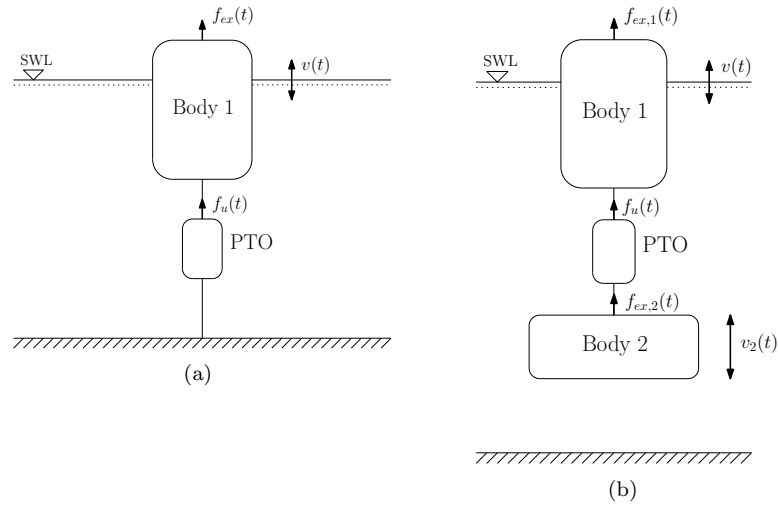


Figure 3.10: Typical oscillating bodies for wave energy conversion: (a) Bottom-referenced floating body; (b) Self-reacting bodies.

shown in Fig. 3.10. The PTO introduces an additional force into the dynamic equation of motion of the floating system, that we will refer to as the PTO force.

Due to the wide range of solutions for wave energy conversion with oscillating systems, a variety of possibilities for the specific realisation of the PTO unit has been proposed. In Section 3.4.1, a brief overview of some of the main solutions is outlined. It is, however, not meant to be an exhaustive overview of the topic as not fully within the scope of this thesis. The interested reader is referred to more comprehensive sources [73, 1, 74, 75].

Throughout the remainder of the thesis, the PTO mechanism will be left unspecified and treated as a generic force that can be manipulated, as required, by an automatic controller, eventually within certain constraints. Section 3.4.2 extends the dynamic model of the oscillating system for wave energy conversion when a PTO force is included.

3.4.1 Mechanisms for power take-off

Given the wide variety of principles of systems for wave energy conversion, the range of possibilities for the choice of the PTO mechanism is also quite diverse. Even when the focus is put, more specifically, on WECs consisting of oscillating bodies, a standard solution for the secondary energy conversion, from mechanical oscillation to electricity or to different forms of mechanical energy, does not exist.

The main type of machinery currently considered for the secondary conversion step, in the case of oscillating bodies in water, are [1, 75]:

- Directly-coupled electrical generators, or
- Hydraulic systems consisting of piston pumps, accumulators and hydraulic motors.

In the latter case, the hydraulic generator is usually coupled with an electrical machine for the final conversion step into electricity, but not necessarily, as for example in the case of several WECs

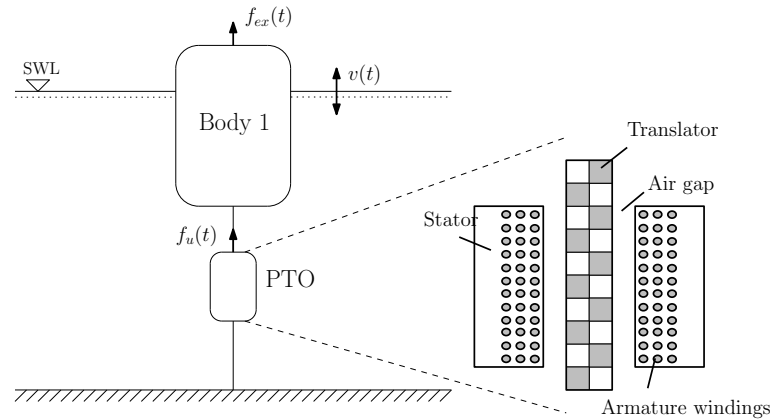


Figure 3.11: Direct-drive linear generator [1].

pumping fluid in the same circuit and sharing the electrical-conversion step [76].

Direct-drive electrical generators

In applications which involve reciprocal motion it may be convenient to couple the mechanical system directly with an electrical generator. The idea of direct drive is appealing, since it produces simple systems with few intermediate conversion steps and reduced mechanical complexity, but demands on the generator increase [1]. Typical designs with direct-drive generators were proposed for the particular case of WECs consisting of sea-bottom-referenced rigid bodies oscillating in heave, like the Archimedes Wave Swing (AWS) [77, 78, 79] and the simple heaving cylinder WEC developed within the Swedish Centre for Renewable Electric Energy Conversion [80, 81, 82].

The basic principle of a linear generator, shown in Fig. 3.11, is the motion of a translator, on which magnets are mounted with alternating polarity, with respect to a stator, containing windings of conductors. Due to the changes in the magnetic field caused by the relative motion between translator and stator, a voltage is induced in the armature windings, in accordance with Faraday's law [1]. Between the translator and the stator is a physical gap, most commonly an air gap.

In order to be connected to the grid, the current from a directly-driven linear generator is by necessity conditioned [83, 1]. Most commonly the stator windings would be connected to a DC link via a rectifier and from the DC link to the grid via a DC/AC converter [83]. The rectification can be passive, using a diode rectifying bridge in the simplest configuration [1], in which case the PTO can be represented by a purely resistive load, although the rectifier can only be modelled through non-linear theory. As an alternative, it was shown [83, 84] how more complex power electronics, through an active rectifier and a bank of capacitors for phase compensation, allow for higher power transfer at the generator. Reactive power requirements increase demands on the sizing of the generator (higher cost) but provides also more flexibility in the control of the WEC, as the PTO can be seen as a complex load, with both a resistive and a reactive part [1].

Different topologies for the actual design of the linear generator exist, but in general designs that show high efficiency at slow speeds and high forces should be preferred, due to the nature of the problem. Consider that the vertical speed of the sea surface is in the order of 1-2 m/s, that is about 15-50 times lower than conventional rotating machines. In order to obtain comparable

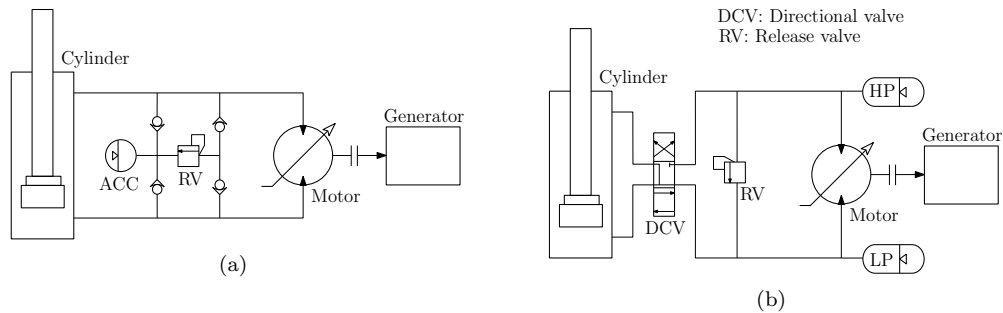


Figure 3.12: Typical topologies for hydraulic PTOs [87]: (a) variable pressure and bi-directional flow; (b) constant pressure and uni-directional flow.

power outputs, 15-50 times higher forces are required. A direct-drive linear generator would have to be necessarily larger and heavier than a traditional machine. Advances in the research of high-energy-density permanent magnets, however, led to the development of novel topologies that can meet the low-speed/high-torque requirement with smaller and lighter (cheaper) designs [85, 83]. Given the quite high shear forces that can be experienced in the sea, particular attention should also be given to topologies and materials that can allow increased shear stress capabilities with minimum cost and size [86].

Hydraulic systems

Small and light-weight hydraulic machines can handle enormous forces and hydraulics have no rival when trying to capture power from large objects that are being pushed around relatively slowly by large wave forces [73, 1]. Hydraulic PTO systems for wave energy conversion usually fall into two broad categories [87]: variable pressure and constant pressure systems.

The basic design of a variable pressure hydraulic PTO is shown in Fig. 3.12(a). A single cylinder is coupled to a variable-displacement motor and the pressure difference between the two hydraulic lines controls the reaction force provided by the PTO. The motor drive has to be able to provide four-quadrant operation, since either of the two lines can be at a higher pressure level. A combination of check valves with a relief valve and an accumulator are included in the hydraulic circuit to prevent over pressure and cavitation.

A constant-pressure system is shown in Fig. 3.12(b). The main difference to the variable-pressure design is the presence of an high- and a low-pressure accumulator that determines a unidirectional flow of the fluid through the circuit. The hydraulic motor is therefore not required to operate in four quadrants, but additional valves are required in order to control the reversing flows generated by the piston. In the proposed design, a three-position directional valve is included, such that the reaction force provided by the PTO can be approximately zero or assume a maximum, negative or positive, value (that is related to the pressure difference between the two lines).

In both cases, the hydraulic motor is coupled with an electrical, rotating generator, which can be of constant- or variable-speed type. Note that the constant-pressure design is intrinsically able to provide energy storage through the accumulators, while the basic variable-pressure design is not able to provide such a characteristic. Hybrid systems that combine elements of both categories are also possible [87].

The finite life of seals and the consequent need for period service, in addition to the inclusion of oil which is a potential pollutant to the sea are among the features that can undermine the applicability of hydraulic PTOs in systems for wave energy conversion. The possibility to work as a generator or motor (although at different efficiencies) and the ability to easily include energy storage represent quite positive characteristics for dealing with the oscillatory and irregular nature of wave energy. Furthermore, the compactness of designs that deal with high forces, at relatively low velocity, make hydraulic PTO a valid alternative to direct-drive electrical systems.

3.4.2 Dynamics of an oscillating body PTO system

The dynamics of the floating body, when a PTO system is included, is expressed as in (3.124), where the input is the excitation force, $f_{ex}(t)$, plus the PTO force, $f_u(t)$, namely:

$$m\ddot{x}(t) + m_\infty\ddot{x}(t) + \int_0^{+\infty} h_r(\tau)\dot{x}(t-\tau)d\tau + K_v\dot{x}(t) + K_b x(t) = f_{ex}(t) + f_u(t). \quad (3.143)$$

In the frequency domain, and in analogy with (3.127), the dynamic equation (3.143) can be written as:

$$\frac{X(\omega)}{F_{ex}(\omega) + F_u(\omega)} = \frac{1}{K_b - \omega^2 [m + m_\infty + m_a(\omega)] + j\omega [B(\omega) + K_v]}, \quad (3.144)$$

and, for the velocity response,

$$\frac{V(\omega)}{F_{ex}(\omega) + F_u(\omega)} = \frac{1}{Z_i(\omega)}, \quad (3.145)$$

where the intrinsic impedance, $Z_i(\omega)$, was defined in (3.129).

The PTO mechanism will be left unspecified through the following Chapters, but it can be generally assumed that $f_u(t)$ is a function of the position and its derivatives. The PTO force, therefore, can conveniently be expressed, in the frequency domain, as:

$$F_u(\omega) = -Z_u(\omega)V(\omega), \quad (3.146)$$

where $Z_u(\omega)$ is named load impedance or PTO impedance, that can, in general, be composed of a real part, or load resistance, $R_u(\omega)$, and an imaginary part, or load reactance, $X_u(\omega)$:

$$Z_u(\omega) = R_u(\omega) + jX_u(\omega). \quad (3.147)$$

From (3.146), the velocity response of the floating system, given in (3.145), can be finally written as:

$$\frac{V(\omega)}{F_{ex}(\omega)} = \frac{1}{Z_i(\omega) + Z_u(\omega)}, \quad (3.148)$$

where the excitation force, $F_{ex}(\omega)$, is the only external input and the dynamics of PTO adds to the intrinsic impedance of the system.

The average power transferred from the waves to the system, in this case, is partly absorbed by the PTO, the rest being lost in viscous friction and radiation:

$$P_{ex}(\omega) = P_r(\omega) + P_v(\omega) + P_u(\omega) = \frac{1}{2} \Re \{ F_{ex}(\omega) V(\omega)^* \} = \frac{1}{2} \frac{B(\omega) + K_v + R_u(\omega)}{|Z_u(\omega) + Z_i(\omega)|^2} |F_{ex}(\omega)|^2, \quad (3.149)$$

where

$$P_v(\omega) = -\frac{1}{2} \Re \{ F_v(\omega) V(\omega)^* \} = \frac{1}{2} \frac{K_v}{|Z_u(\omega) + Z_i(\omega)|^2} |F_{ex}(\omega)|^2 \quad (3.150)$$

$$P_r(\omega) = -\frac{1}{2} \Re \{ F_r(\omega) V(\omega)^* \} = \frac{1}{2} \frac{B(\omega)}{|Z_u(\omega) + Z_i(\omega)|^2} |F_{ex}(\omega)|^2 \quad (3.151)$$

$$P_u(\omega) = -\frac{1}{2} \Re \{ F_u(\omega) V(\omega)^* \} = \frac{1}{2} \frac{R_u(\omega)}{|Z_u(\omega) + Z_i(\omega)|^2} |F_{ex}(\omega)|^2, \quad (3.152)$$

and $P_u(\omega)$ is the average power absorbed by the PTO (flowing out of the system).

Using the relation for the excitation force, given in (3.113), equations (3.149) through to (3.152) can be alternatively expressed as a function of the wave spectrum, $|\Xi(\omega)|^2$. In the case of the absorbed power:

$$P_u(\omega) = \frac{1}{2} \frac{R_u(\omega)}{|Z_u(\omega) + Z_i(\omega)|^2} |H_{ex}(\omega)|^2 |\Xi(\omega)|^2. \quad (3.153)$$

Tuning of the PTO allows the possibility of manipulating the shape of the curve of the absorbed power, $P_u(\omega)$, such that it properly matches the wave spectrum for increasing the efficiency of the WEC. In broad terms, based on the analysis of oscillating systems in Section 3.2, the reactance of the PTO, $X_u(\omega)$, can be utilised to move the resonance of the system to a desired frequency. Acting on the load resistance, $R_u(\omega)$, on the other hand, influences the bandwidth and peakedness of the curve: higher PTO resistance increases the damping and therefore widens the curve, while lowering its peak.

It is important to note that the inclusion of a load reactance implies the possibility of reversing the energy flow between the device and the PTO system. One problem for devices with highly reactive characteristics, is that the energy needed to deflect the spring may be many times higher than the useful energy going into the PTO damper, which requires over-rating of the generator (at increased size and cost). Besides, if the reactive energy flow is not efficient, an unacceptable fraction may be lost [73], thus cancelling the expected benefits. Therefore, although reactive loading may allow the matching of a smaller structure (usually high resonance frequency) with a desired wave spectrum, it would be better applied to improve a good device, already resonant at nearly the correct part of the spectrum rather than to rescue a bad design [73]. More about the issues involved with the inclusion of a reactive load will be discussed in Section 4.1, where it will be analytically shown that optimal tuning of the PTO is such that the inertia and stiffness of the system are cancelled.

Given that, in general, the wave spectrum changes quite a lot at certain locations in the sea, the reaction force provided by the PTO, and its impedance, needs to be tuned in real-time such that the power curve of the WEC is adaptively tuned to the on-coming wave and high energy-efficiency

(as well as safety) can be achieved over a variety of conditions. Real-time control of the PTO force will therefore be the focus of the following Chapters.

Chapter 4

Real-time control of wave energy converters: A literature review

Abstract

Oscillating bodies for wave energy conversion, models for which were presented in Chapter 3, typically have pronounced resonances, which enable efficient power absorption only over a restricted range of frequencies. In order to cope with the variations of wave spectra, a control system, acting through the PTO system, can be designed such that efficient energy conversion occurs over a wide range of wave conditions.

A frequency-domain analysis gives the conditions on the velocity and forces, so that maximum wave energy is transferred from the waves to the PTO (see Section 4.1.1). The translation of such relations into a real-time controller that can optimally tune the motion of the WEC for achieving maximum efficiency is, however, not trivial. Frequency-domain optimal conditions, in fact, have a limited ability to take into account physical constraints and, at the same time, do not respect, in general, the law of causality, meaning that they require ideal knowledge of the future to be implemented. A wide variety of solutions has been proposed for the real-time control of WECs, in order to improve their efficiency, and their key differences all lie in how they deal with the difficulties of non-causality and physical constraints.

This Chapter has the objective of giving a comprehensive overview of the current state of the art in the field of the control of systems for wave energy conversion. The frequency domain analysis and the ideal conditions for maximum wave energy absorption are presented in Section 4.1. The main contributions from the literature to the problem of real-time control of WECs are then organised in Section 4.2. Some final remarks are finally given in Section 4.3.

4.1 Conditions for maximum wave energy absorption

Using frequency-domain analysis, analytical conditions for the achievement of a maximum wave energy transfer from the ocean waves to the oscillating system, were developed [6, 11]. Section 4.1.1 discusses such optimality conditions, which do not take into account any constraints about the system. The analytical analysis of wave energy extraction under certain physical limitations was also proposed, particularly in [7, 88, 11], and the associated literature is reviewed in Section 4.1.2. From the point of view of real-time control, the main issue arising when converting the optimal, frequency-domain conditions into the time domain, is their non-causality, that was widely discussed in [57, 6]. Section 4.1.3 deals with the non-causality.

4.1.1 Unconstrained optimum: complex-conjugate control

Consider a generic WEC, consisting of one body constrained to move in a single degree of freedom. A frequency-domain model, relating the velocity, $V(\omega)$, to the wave excitation force, $F_{ex}(\omega)$, was derived in Section 3.3.2 and expressed as:

$$V(\omega) = \frac{1}{Z_i(\omega) + Z_u(\omega)} F_{ex}(\omega), \quad (4.1)$$

where $Z_i(\omega)$ is the intrinsic impedance of the floating body, defined in (3.129), and $Z_u(\omega)$ is the impedance provided by the PTO system, that is left unspecified, and that introduces an additional force, $F_u(\omega)$, defined in (3.146) and repeated here for clarity:

$$F_u(\omega) = -Z_u(\omega)V(\omega). \quad (4.2)$$

Assume that the excitation is purely sinusoidal, with zero-phase at time $t = 0$. In complex amplitude notation:

$$\hat{f}_{ex} = F_{ex} \quad \iff \quad f_{ex}(t) = \Re \left\{ \hat{f}_{ex} e^{j\omega t} \right\} = F_{ex} \cos(\omega t). \quad (4.3)$$

Given the linearity of the system in (4.1), all the other signals will be harmonic and at the same frequency. The velocity, in particular, can be written as:

$$\hat{v} = V e^{j\varphi}, \quad (4.4)$$

where the amplitude, V , and the phase, φ , are given, with respect to the excitation force, by the magnitude and phase of the transfer function $1/(Z_i(\omega) + Z_u(\omega))$.

The average power transmitted by the waves to the system, termed excitation power and defined in (3.149), is given by:

$$P_{ex} = \frac{1}{2} \Re \left\{ \hat{f}_{ex} \hat{v}^* \right\} = \frac{1}{2} F_{ex} V \cos \varphi, \quad (4.5)$$

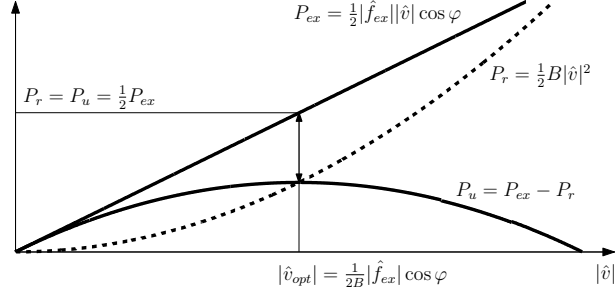


Figure 4.1: Power absorption versus excitation power and power lost in radiation [6].

while the average power lost in radiation, defined in (3.151), is:

$$P_r = \frac{1}{2} \Re \{ B \hat{v} \hat{v}^* \} = \frac{1}{2} B V^2, \quad (4.6)$$

where B is the radiation resistance calculated at the frequency of the excitation. As a result, the useful power absorbed by the PTO is, on average:

$$P_u = \frac{1}{2} F_{ex} V \cos \varphi - \frac{1}{2} B V^2, \quad (4.7)$$

if there are no losses other than radiation, that is $K_v = 0$ in (3.129).

Given a fixed value of the phase difference, φ , between velocity and excitation force, Fig. 4.1 shows the behavior of P_{ex} , P_r and P_u for different magnitudes of the velocity, $V = |\hat{v}|$. From (4.5) and (4.6), the excitation power increases linearly with the velocity, while the power lost in radiation is proportional to its squared magnitude. Therefore, the graph of P_u versus V is a parabola that increases from $V = 0$ up to a certain maximum, beyond which it starts decreasing. A maximum is obtained for the following magnitude of the velocity [6]:

$$\frac{\partial}{\partial V} \left[\frac{1}{2} F_{ex} V \cos \varphi - \frac{1}{2} B V^2 \right] = \frac{1}{2} F_{ex} \cos \varphi - B V = 0 \quad \Longleftrightarrow \quad V = \frac{F_{ex}}{2B} \cos \varphi \triangleq V_{opt}. \quad (4.8)$$

The resulting useful power equals the radiation power and corresponds to half the excitation power [6]:

$$P_{u,opt} = \frac{F_{ex}^2}{8B} \cos^2 \varphi = P_{r,opt} = \frac{1}{2} P_{ex,opt}. \quad (4.9)$$

If it were possible to control the magnitude of the oscillation velocity, one could tune its value to the one given in (4.8) for maximum wave energy extraction. If also the phase-lag between the velocity and the exciting force, φ , could be chosen, clearly the absorbed power, given in (4.9), would be maximised when $\varphi = 0$. As discussed in [11], it can be noted, from Fig. 4.1, that if smaller velocities than optimum were imposed, a bigger fraction of the excitation power would be absorbed while radiation losses would be reduced. In the limit, for very small velocities, $P_u \approx P_{ex}$, that is almost all the power transferred from the waves to the system is absorbed, although this would be quite a small fraction of the total wave power available. On the other hand, if bigger velocities than optimal would be imposed, the WEC would be highly inefficient and most of the power transferred

from the waves to the oscillating system could be returned to the sea, via radiation.

Complex-conjugate control

The discussion carried out so far, in terms of complex-amplitudes for a single frequency, intuitively leads to the conclusion that, for optimal power absorption, the velocity should be in phase with the excitation force and should assume a certain optimal magnitude. The problem of maximum wave energy absorption can, however, be dealt with in a more general formulation, where, in theory, all the frequencies may appear at the same time.

The average absorbed power, in general, is given by:

$$P_u(\omega) = \frac{1}{2} \Re \{ F_u(\omega) V^*(\omega) \}, \quad (4.10)$$

as from (3.152). By using properties of the Fourier transform of real signals (i.e. an even real part and odd imaginary part), (4.10) can be conveniently written as:

$$P_u(\omega) = \frac{1}{4} F_u(\omega) V^*(\omega) + \frac{1}{4} F_u^*(\omega) V(\omega) = \frac{1}{4} Z_u(\omega) V(\omega) V^*(\omega) + \frac{1}{4} Z_u^*(\omega) V(\omega) V^*(\omega) = \frac{1}{4} \frac{Z_u(\omega) + Z_u^*(\omega)}{[Z_i(\omega) + Z_u(\omega)][Z_i(\omega) + Z_u(\omega)]^*} |F_{ex}(\omega)|^2, \quad (4.11)$$

where (4.1) and (4.2) were also used. Maximisation of (4.11), with respect to $Z_u(\omega)$, yields the optimal PTO impedance that allows maximum power transfer from the waves to the load [6]:

$$P_u(\omega) = P_{u,OPT}(\omega) \triangleq \max \quad \iff \quad Z_u(\omega) = Z_{u,OPT}(\omega) \triangleq Z_i^*(\omega). \quad (4.12)$$

By setting the PTO impedance to the complex-conjugate of the intrinsic impedance of the system, maximum wave energy absorption can be achieved, and this is independent of the spectral distribution of the excitation force (and of the wave). For obvious reasons, condition (4.12) is termed *complex-conjugate* control (or *reactive* control, as discussed later in this Section) in the wave energy literature [6]. Analogous results can be found for the power transfer from a source to a load in an electrical circuit [89] or in a flexible structure [90].

The ideal maximum power obtained with complex-conjugate control, from (4.11) and (4.12), is:

$$P_{u,OPT}(\omega) = \frac{1}{8B(\omega)} |F_{ex}(\omega)|^2 = P_{r,OPT}(\omega) = P_{ex,OPT}(\omega), \quad (4.13)$$

which equals the radiated power and therefore half the excitation power. Note that (4.13) is the same result obtained in (4.9), when $\varphi = 0$. With complex-conjugate control, in fact, the velocity and the excitation force are always in phase:

$$V_{OPT}(\omega) = \frac{1}{2B(\omega)} F_{ex}(\omega), \quad (4.14)$$

and the system is always at resonance. Fig. 4.2 shows the absorbed power over a range of frequencies when complex-conjugate control is applied, in comparison with the case where the

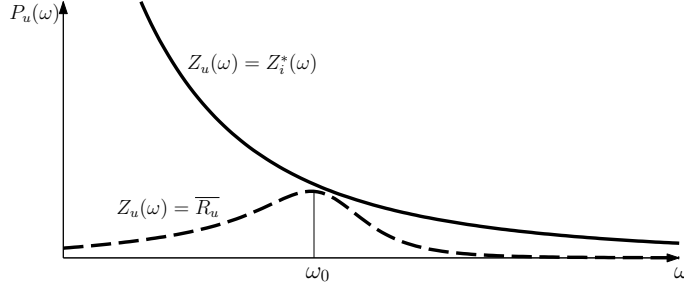


Figure 4.2: Power absorption when PTO impedance is the complex-conjugate of the intrinsic impedance, compared to the case of a constant PTO resistance, $\overline{R_u}$.

load impedance, $Z_u(\omega)$, is set to a constant, real, value. In the latter situation, as discussed in Sections 3.3.2 and 3.4.2, maximum power is absorbed at the natural frequency of the system, given in (3.131), with the peakedness and width of the curve given by the value of the relative damping, R_u . When $Z_u(\omega) = Z_i^*(\omega)$, the system always works at resonance and the theoretical maximum is achieved at all frequencies.

It is interesting to analyse the expression for the force required to be supplied by the PTO when the optimal condition (4.12) is imposed, namely:

$$F_{u,OPT} = -Z_i^*(\omega)V(\omega). \quad (4.15)$$

Given the fact that an imaginary part is present in the impedance, complex-conjugate control implies that reactive power is supplied by the load. From the discussion in Section 3.4.1, the presence of reactive power means that energy flows from the PTO into the system for part of the cycle, which in general implies higher ratings and complexity in the design of the machinery for the conversion of mechanical energy into electricity [83]. In addition to increased design complexity, inefficiencies in the bi-directional energy flow also need to be taken into account and could seriously undermine the effectiveness of complex-conjugate control [73, 11].

Note that due to the requirement for reactive power, complex-conjugate control is sometimes referred to as reactive control, in the wave energy literature [6]. Throughout the present thesis, the term complex-conjugate control will be utilised since it is specific, while reactive control will be referred to any type of controller that requires reactive power, including but not limited to complex-conjugate control.

Optimum control in the case of passive PTO

In the case of a passive PTO ¹, the load impedance is constrained to be purely resistive, as discussed in Section 3.4.1. Analytical conditions for maximising the wave power absorption of the system, when the load machinery cannot provide reactive power, can also be derived from (4.11), by imposing $Z_u(\omega) = R_u(\omega)$. It is straightforward to derive that the PTO resistance should be set

¹In the wave energy literature, a PTO mechanism is *passive* when it is not able to implement a bi-directional energy flow. According to the model utilised throughout this thesis, introduced in Section 3.4.2, a passive PTO implements a purely resistive impedance, with no imaginary part (no reactive power). Throughout the thesis, this meaning for passive PTO or passive PTO system is adopted, not to be confused with the definition of passive system in systems theory.

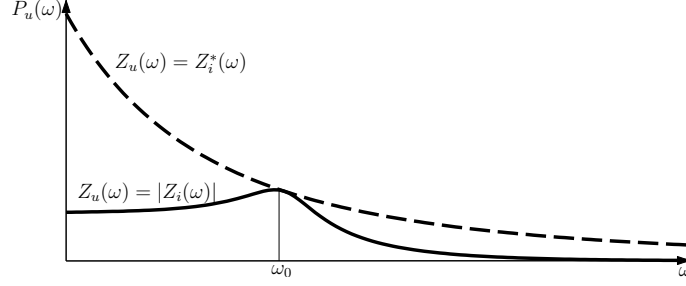


Figure 4.3: Power absorption when PTO is purely resistive and it is tuned to optimal value.

to the *magnitude* of the intrinsic impedance of the system, as found in [6]:

$$R_{u,opt}(\omega) = |Z_i(\omega)|. \quad (4.16)$$

Figure 4.3 shows the average absorbed power when an optimal resistive load (4.16) is utilised, compared to the ideal optimum achieved with the complex-conjugate condition (4.12). The curve exhibits a resonant behavior, as expected, since a purely resistive load cannot move the natural frequency of the system, but can only modify the width and peakedness of the curve, as discussed in Section 3.4.2. Note that maximum power absorption is obtained at the natural frequency of the system and that only at such a frequency is the ideal optimum achieved.

4.1.2 Maximum wave energy absorption subject to physical constraints

The amplitude of the optimal velocity, in (4.14), and of the optimal PTO force, in (4.15), in general, may be excessively high for practical implementations. When deriving the condition of complex-conjugate control, given in (4.12), limitations upon the motions and forces were not considered.

Based on an empirical relation between the volume of the WEC and its maximum displacement, Budal [6, 11] proposed an upper bound to the power absorption that limits the ideal curve of Fig. 4.2, at lower frequencies (longer waves). A more formal analysis about the optimal power absorption when constraints on the oscillation velocity are included, was proposed in [7].

Budal's upper bound

For WECs consisting of single bodies oscillating in the heave direction, it is reasonable to assume (at least for a body of cylindrical shape) that the design amplitude for heave excursion does not exceed $\nabla/2S_w$ [6], where ∇ is the volume of the body and S_w is its water-plane area. At a given frequency, ω , the heaving velocity is therefore bounded as:

$$|\dot{v}| < \omega \frac{\nabla}{2S_w}. \quad (4.17)$$

For waves at very low frequencies that, from the dispersion relationship (3.18), have large wavelengths, one can use the small-body approximation (dimension of the body small compared

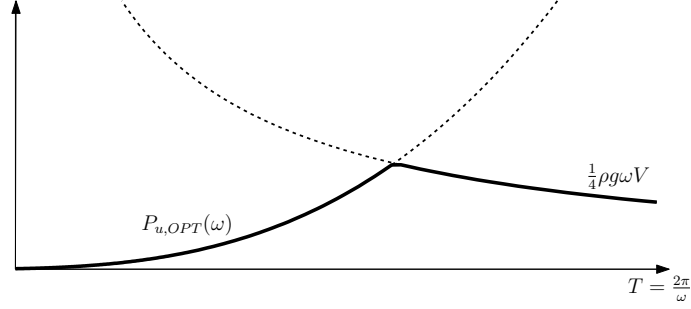


Figure 4.4: Budal diagram giving upper bound of power absorption based on maximum physical displacement of single body in heave [6]. Incident wave amplitude is $|\hat{\eta}| = 1$ m.

to the wavelength) to determine an upper bound for the excitation force [6]:

$$\frac{|\hat{f}_{ex}|}{|\hat{\eta}|} < \rho g S_w, \quad (4.18)$$

where $\hat{\eta}$ is an harmonic incident wave, ρ is the water density and g is the acceleration due to gravity. Note that the upper bound in (4.18) equals the hydrostatic force resulting from the equilibrium between buoyancy and gravity, given in (3.121), which makes sense in the limit as $\omega \rightarrow 0$, where the incident wave is reduced to a static displacement with infinite wavelength.

From (4.17) and (4.18), an upper bound of the maximum power absorption, given in (4.7), can be deduced:

$$P_u < \frac{1}{2} |\hat{f}_{ex}| |\hat{v}| \cos \varphi < \frac{1}{2} |\hat{f}_{ex}| |\hat{v}| < \frac{\rho g \omega \nabla}{4} |\hat{\eta}|, \quad (4.19)$$

which is termed *Budal's upper bound* [11].

Fig. 4.4 shows the maximum wave-power absorption when complex-conjugate control, i.e. condition (4.12), is achieved, together with Budal's upper bound (4.19), given by physical limitations involving the maximum heaving excursion. The graph is related to a cylinder oscillating in heave relatively to the sea bottom. For very short waves, characterised by small periods, the maximum power absorption given by complex-conjugate control is well below Budal's upper bound, due to the fact that such waves have a limited influence (force) on the system's motion. When the wavelength (and period) increases, that is at low frequencies, the force due to the incident waves is quite significant and the physical bound becomes more stringent than the theoretical maximum attainable with complex-conjugate control.

Note that Budal's upper bound is only derived, analytically, for quite specific assumptions, that are cylindrical shape, heaving motion and a single body. A similar behavior, however, is to be expected for more generic systems that, due to economic constraints, impose a limit on the power-to-size ratio [6, 11]. Analytical expressions cannot be derived in such situations and more complex numerical techniques need to be adopted.

Upper bound under motion constraints

Evans derived expressions for the maximum power absorption of a body when its velocity, and hence its amplitude, is constrained [7].

In the case of harmonic excitation, the excitation force and the velocity of the system can be expressed in terms of their complex amplitudes, as in (4.3) and (4.4) respectively. The absolute maximum for the power transfer from the waves to the PTO was derived in (4.8), when the force and velocity are in phase:

$$\hat{v}_{OPT} = \frac{1}{2B} \hat{f}_{ex}, \quad (4.20)$$

where $B \triangleq B(\omega)$ represents the radiation resistance, calculated at the frequency of the excitation.

The power absorption can be written in terms of the optimal velocity [7, 88]:

$$P_u(\hat{v}) = \frac{1}{8B} \hat{f}_{ex} \hat{f}_{ex}^* - \frac{1}{2} B (\hat{v} - \hat{v}_{OPT}) (\hat{v} - \hat{v}_{OPT})^*, \quad (4.21)$$

that is clearly a maximum if $\hat{v} = \hat{v}_{OPT}$. In (4.21), the notation $(\cdot)^*$ indicates the complex-conjugate operation. Assume that the magnitude of the velocity is constrained to:

$$\hat{v} \hat{v}^* \leq \beta^2. \quad (4.22)$$

Then, an optimal solution for the velocity, within the constrained region, is most easily determined by introducing a Lagrange multiplier, μ , into (4.21), as proposed in [7, 88]:

$$G(\hat{v}) = P_u(\hat{v}) - \frac{1}{2} \mu (\hat{v} \hat{v}^* - \beta^2), \quad (4.23)$$

where the coefficient 1/2 is introduced for convenience of notation. It can be shown that values of the velocity that maximise the power, $P_u(\hat{v})$, given the constraint in (4.22), have to satisfy the following necessary conditions [91]:

$$\frac{\partial}{\partial \hat{v}} G(\hat{v}) = 0 \quad (4.24)$$

$$\hat{v} \hat{v}^* \leq \beta^2 \quad (4.25)$$

$$\mu \geq 0 \quad (4.26)$$

$$\mu (\hat{v} \hat{v}^* - \beta^2) = 0. \quad (4.27)$$

Condition (4.24) means that the gradient of the lagrangian function, $G(\hat{v})$, with respect to the velocity, is zero. Equation (4.25) simply expresses the constraint (4.22), while (4.26) and (4.27) give important conditions on the Lagrange multiplier, μ . In particular, (4.27) is the *complementarity condition*, meaning that $\mu = 0$ if the constraint is inactive, in which case $G(\hat{v}) = P_u(\hat{v})$ and the optimal solution is the unconstrained \hat{v}_{OPT} , given in (4.20). When μ is strictly positive, on the other hand, the optimal solution lies on the border of the constrained region, that is $\hat{v} \hat{v}^* = \beta^2$.

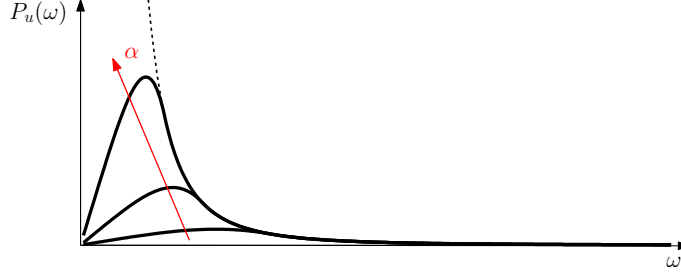


Figure 4.5: Power absorption under motion constraints [7]. The dotted line represents the unconstrained maximum.

By expanding the gradient of $G(\hat{v})$, the following is obtained:

$$\frac{\partial}{\partial \hat{v}} G(\hat{v}) = -B(\hat{v} - \hat{v}_{OPT}) - \mu \hat{v} = 0 \iff \hat{v} = \frac{B}{B + \mu} \hat{v}_{OPT} = \frac{1}{2(B + \mu)} \hat{f}_{ex}, \quad (4.28)$$

where μ can be found from the complementary condition (4.27). In particular, μ is such that $\hat{v}\hat{v}^* = \beta^2$, when $\hat{v}_{OPT}\hat{v}_{OPT}^* > \beta^2$, that is when the absolute unconstrained optimum is not a feasible solution.

In simple terms, therefore, at any given frequency of the excitation, maximum power absorption is achieved if the velocity is in phase with the excitation force and if its magnitude is optimally related to the excitation force through half the inverse of the radiation damping. In the case where the optimal velocity magnitude exceeds the given constraint, then a maximum power is given by a velocity that is still in phase with the excitation force, and that has the maximum magnitude allowed by the constraint. Such conditions were also intuitively deduced from the analysis carried out in Section 4.1.1, as well as from Fig. 4.1.

Given harmonic motions at a frequency ω , the velocity constraint can be expressed as a position constraint [7]:

$$\hat{v}\hat{v}^* \leq \beta^2 = \omega^2 \alpha^2, \quad (4.29)$$

where the magnitude of the position, $\hat{x} = (1/j\omega)\hat{v}$, is constrained to be lower than α . Fig 4.5 shows how the maximum power-absorption curve, in the frequency domain, is affected by changing the constraint on the amplitude of the motion, as opposed to the ideal maximum from complex-conjugate control, given in (4.12).

4.1.3 Non-causality of optimal conditions in the time domain

Sections 4.1.1 and 4.1.2 give the analytical solutions for the maximisation of the primary energy transfer from the waves to the WEC, including the case where constraints restrict the allowed motion. Optimal conditions relating the velocity of the system, or the PTO force, and the wave excitation force were derived in the frequency domain.

A control system could therefore make use of such relations for tuning the system operation, from knowledge of the incident wave or wave excitation force. A practical implementation of the controller in real-time, however, requires that the frequency-domain relations are translated into the time-domain.

For sinusoidal waves, the optimal, frequency-domain conditions can directly be applied in the time domain. In general, however, real waves are modelled as a stochastic process with a spectral distribution that covers a wide or narrow range of frequencies, as discussed in the detail of Section 3.1.2. The optimal conditions, therefore, should ideally be imposed at different frequencies at the same time.

It turns out that a direct translation of the frequency-domain conditions results in non-causal relations, that cannot be implemented in real-time. In the case of complex-conjugate control, (4.12), two alternative conditions were found, in Section 4.1.1, for maximising the wave-power absorption under no constraints:

$$\begin{cases} F_u(\omega) = -Z_i^*(\omega)V(\omega) \\ V(\omega) = \frac{1}{2B(\omega)}F_{ex}(\omega). \end{cases} \quad (4.30)$$

From real-time measurements or estimations of the velocity or excitation force, one may consider implementing the conditions, given in (4.30), in the time domain to calculate the optimal load force or velocity for the system such that maximum energy is extracted from the waves:

$$f_u(t) = - \int_{-\infty}^t h_f(\tau)v(t-\tau)d\tau \quad (4.31)$$

$$v(t) = \int_{-\infty}^t h_v(\tau)f_{ex}(t-\tau)d\tau, \quad (4.32)$$

where

$$h_f(t) = \mathcal{F}^{-1} \{Z_i^*(\omega)\} \quad (4.33)$$

$$h_v(t) = \mathcal{F}^{-1} \left\{ \frac{1}{2B(\omega)} \right\}. \quad (4.34)$$

As widely discussed in [57, 6], however, both the convolutions in (4.31) and (4.32) are non-causal. The impulse response $h_v(t)$, in fact, is the inverse Fourier transform of the real even function $1/2B(\omega)$ and, from the properties of the Fourier transform, it is itself even and therefore non-causal (non-zero for negative values of t). With regard to $h_f(t)$, it may be written, on the basis of some properties of the Fourier transform, that:

$$h_f(t) = \mathcal{F}^{-1} \{Z_i^*(\omega)\} (t) = \mathcal{F}^{-1} \{Z_i(\omega)\} (-t) \triangleq z_i(-t). \quad (4.35)$$

The inverse Fourier transform of the intrinsic impedance, namely $z_i(t)$, is causal because radiation is a causal process [6]. As a consequence, based on (4.35), $h_f(t)$ is anti-causal, being zero for any $t > 0$.

Note that the optimal condition that relates the velocity to the excitation force in the case of motion constraints, (4.28), is also non-causal, as it still represents a real and even function in the frequency domain.

The issue of non-causality is central to the design of a controller for wave energy conversion systems. As it will become clear in the following Sections, all of the proposed solutions in the literature deal with the non-causality problem mainly in three ways:

- By assuming regular waves, so that there is no need for prediction,
- By trying to derive a causal approximation of the optimal conditions, or
- By using predictions of the velocity, excitation force or wave elevation.

4.2 Real-time control

The conditions of complex-conjugate control, given in (4.12), can be translated in the time-domain and be utilised in order to calculate the oscillation velocity or PTO force such that ideal, maximum power transfer from the waves to the WEC is achieved. Section 4.2.1 discusses the different approaches to a real-time implementation of complex-conjugate control, that mainly differ on how they deal with the issue of non-causality, highlighted in Section 4.1.3.

Complex-conjugate control requires reactive power and bi-directional energy flow between the oscillating system and the PTO, that is not always possible, as from the discussion in Section 3.4.1. Ad-hoc solutions were developed in order to maximise the efficiency of wave energy conversion systems, by making use of a purely passive load. Such solutions usually try to keep the oscillating system in phase with the excitation force by keeping the WEC fixed during parts of the cycle (*latching*) or by coupling and decoupling the PTO machinery at intervals (*clutching* and *de-clutching*). Latching and (de)clutching, here classified as discrete (on-off) controllers, are discussed in Section 4.2.2.

Another main issue associated with complex-conjugate control is that physical constraints are not explicitly taken into account. In particular, constraints involving motion and forces are critical for practical implementation of control systems for wave energy conversion. Approaches based on the solution, in real-time, of a constrained optimisation problem, usually over a receding horizon, were proposed. Section 4.2.3 deals with model-based and predictive types of controllers suggested for wave energy conversion.

Another category of control solutions, proposed in the wave energy field, consists of the real-time tuning of the PTO impedance, that is its damping, or resistance, and its reactance (if an active system is available). An intuitive analysis on the effects that variations in the damping and reactance of the PTO can have on the response of the WEC, and on its power transfer from the waves, was proposed in Section 3.4.2. A variety of approaches for the tuning, in real-time

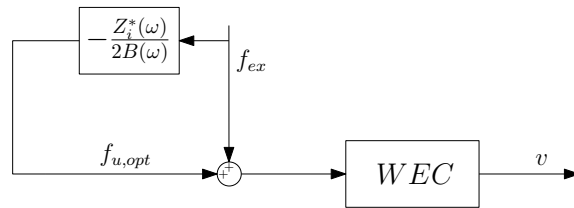


Figure 4.6: Feedforward realisation of complex-conjugate control. The optimal PTO force is calculated from estimates and/or predictions of the excitation force.

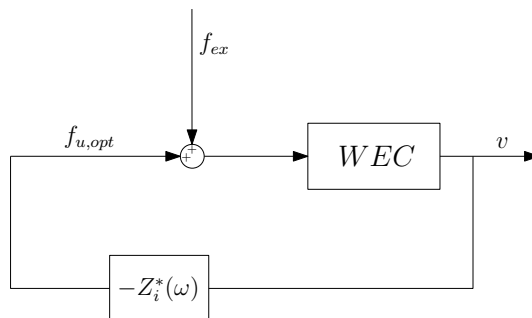


Figure 4.7: Feedback implementation of complex-conjugate control. The optimal PTO force calculated from measurements and/or predictions of the excitation force.

(on different time scales), of the impedance provided by the PTO, based on the incident wave spectrum, is reviewed in Section 4.2.4.

Section 4.2.5, finally, gives an overview of the possible solutions from other engineering problems that are analogous to or the dual of wave energy conversion. Active control of noise and vibrations, in particular, offers a common framework where the tuning of an oscillation to a stochastic external excitation of a harmonic nature is sought. The problem is typically turned into a standard H_2 or H_∞ control problem, which gives access to a wide and well developed knowledge in the field of control engineering.

4.2.1 Real-time complex-conjugate control

The optimal conditions that go under the label of complex-conjugate control, described in detail in Section 4.1.1, were derived in the frequency domain. Real waves, however, are hardly regular and are usually treated as a stochastic signal with a certain power spectral density, that is a superposition of regular waves, as proposed in Section 3.1.2.

Practically, it is necessary to consider the problem of real-time control of WECs, in irregular waves, in the time domain, because the optimal conditions depend on the wave frequency and real waves contain many components at different frequencies [92]. As justified in Section 4.1.3, transposition of the conditions for maximum wave energy absorption into the time domain yields non-causal laws that cannot be directly implemented in practice.

A variety of solutions has been proposed in the literature to implement complex-conjugate control in real time and to overcome non-causality. Falnes [6] gives an overview of the possible structures of the controller, by identifying three main categories:

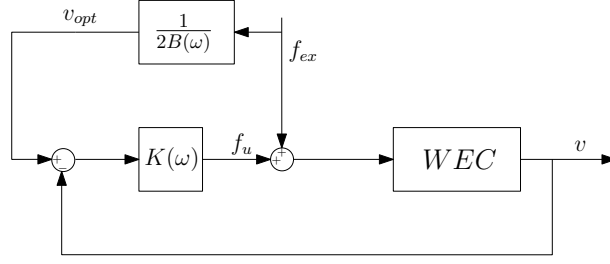


Figure 4.8: Velocity-tracking architecture for the realisation of complex-conjugate control. Optimal velocity calculated from estimates of excitation force and from optimal condition of complex-conjugate control. A low-level controller, $K(\omega)$, imposes the desired velocity on the WEC by acting on the PTO force.

- The optimal PTO force is calculated in real-time from estimates and/or predictions of the excitation force. The calculated optimal force is then applied to the system, ideally producing the desired motion. As from Fig. 4.6, the control action is purely of a feedforward type.
- The optimal PTO force is calculated in real-time from measurements and/or predictions of the of the oscillation velocity. The calculated optimal force is then applied to the system, ideally producing the desired motion. The approach is shown in Fig. 4.7, and a feedback link is clearly realised.
- An optimal velocity is calculated by making use of estimates and/or predictions of the excitation force. A velocity-tracking, feedback loop is then utilised in order to impose the calculated velocity on the system, by acting on the PTO control force. The structure of this control scheme is shown in Fig. 4.8.

The three categories are obviously related to the three alternative optimal conditions that result from the unconstrained maximisation of the power in the frequency domain, derived in Section 4.1.1:

$$F_u(\omega) = -Z_i^*(\omega)V(\omega) = -\frac{Z_i^*(\omega)}{2B(\omega)}F_{ex}(\omega) \quad (4.36)$$

$$V(\omega) = \frac{1}{2B(\omega)}F_{ex}(\omega), \quad (4.37)$$

that can alternatively be expressed in the time domain, as given in (4.31) and (4.32). Note that two alternative expressions, in (4.36), give the optimal PTO force in terms of either the wave force (feedforward solution) or the velocity (feedback).

All the proposed approaches for the realisations of complex-conjugate control in real-time fall into these three categories and are now discussed.

Feedforward control

In [92], one of the first attempts to implement complex-conjugate control in the time domain was presented. A feedforward control action is calculated from the non-causal law:

$$f_u(t) = - \int_{-\infty}^{+\infty} h_c(\tau) f_{ex}(t - \tau) d\tau, \quad h_c(t) = \mathcal{F}^{-1} \left\{ \frac{Z_i^*(\omega)}{2B(\omega)} \right\}, \quad (4.38)$$

which corresponds to the block diagram depicted in Fig. 4.6.

The non-causality is resolved by estimating the future excitation force from wave measurements, $\eta(-l, t)$, collected at some point l metres distant from the device, in the direction of the approaching wave. In particular, the excitation force, at time $t + LT$, is given by:

$$f_{ex}(t + LT) = \int_{-\infty}^{+\infty} h_l(\tau) \eta(-l, t + LT - \tau) d\tau, \quad (4.39)$$

where the kernel function, $h_l(t)$, related to the propagation properties of the wave elevation and to the geometry of the system, is also non-causal. The relation in (4.39), however, becomes approximately causal if the distance, l , is large enough, and such that $|h_l(t)| \approx 0, \forall t < LT$ [92, 57]. As a result:

$$f_{ex}(t + LT) \approx \int_{+LT}^{+\infty} h_l(\tau) \eta(-l, t + LT - \tau) d\tau, \quad (4.40)$$

which only depends on values of the wave elevation up to time t .

Performance close to ideal is reported [92], but only based on simulation results. A unidirectional progressive wave was simulated, based on a Pierson-Moskovitz spectral distribution, in deep water conditions so that the approximated dispersion relation, given in (3.22), could be safely utilised for the spatial prediction for the wave elevation. Note that the purely feedforward structure makes the solution potentially quite sensitive to any type of errors, due to modelling uncertainties and/or predictions, that will inevitably arise in real applications. A practical implementation of such algorithm was never reported.

Feedback control

An alternative approach was proposed by Korde [9, 93, 94, 95]. The solution is based on the calculation of the optimal reaction force from measurements and predictions of the velocity of the system:

$$f_u(t) = - \int_{-\infty}^0 z_i(-\tau) v(t - \tau) d\tau, \quad z_i(t) = \mathcal{F}^{-1} \{ Z_i(\omega) \}, \quad (4.41)$$

that is derived directly from (4.31) and (4.35) and that realises the feedback loop in Fig. 4.7.

A convenient decomposition of the optimal control force, based on the definition of intrinsic

impedance given in (3.129), is proposed [93]:

$$f_u(t) = (m + m_\infty)\dot{v}(t) + K_b \int_{-\infty}^t v(\tau)d\tau - K_v v(t) - \int_{-\infty}^{+\infty} h_1(\tau)v(t-\tau) + \int_{-\infty}^{+\infty} h_2(\tau)v(t-\tau), \quad (4.42)$$

where $h_1(t)$, is the inverse Fourier transform of the radiation resistance:

$$h_1(t) = \mathcal{F}^{-1} \{B(\omega)\}, \quad (4.43)$$

and $h_2(t)$ is defined as:

$$h_2(t) = \mathcal{F}^{-1} \{j\omega m_a(\omega)\}. \quad (4.44)$$

Note that, since $B(\omega)$ and $m_a(\omega)$ are real and even, the resulting impulse responses $h_1(t)$ and $h_2(t)$ are, respectively, even and odd real functions, and therefore non-causal.

By noting that $|h_1(t)|, |h_2(t)| \approx 0$ for $-\psi \leq t \leq +\psi$, the control law is approximated as:

$$f_u(t) \approx F_{PID}(t) - F_\beta(t) + F_\alpha(t), \quad (4.45)$$

where

$$F_{PID}(t) = -K_v v(t) + K_b \int_{-\infty}^t v(\tau)d\tau + (m + m_\infty)\dot{v}(t) \quad (4.46)$$

$$F_\beta(t) = \int_{-\psi}^{+\psi} h_1(\tau)v(t-\tau) \quad (4.47)$$

$$F_\alpha(t) = \int_{-\psi}^{+\psi} h_2(\tau)v(t-\tau). \quad (4.48)$$

Interestingly, the $F_{PID}(t)$ component, defined in (4.46), has a Proportional integral derivative (PID) type of relation with the velocity. The presence of a derivative term makes the PID non-proper (more zeros than poles) and therefore not directly implementable in practice. It is, however, a standard component in real-time control systems and the non-realizability is typically overcome by inclusion of a high-frequency pole. Note that the proportional term is only related to the viscous losses, modelled through the constant of proportion K_v .

The components $F_\beta(t)$ and $F_\alpha(t)$ are non-causal and require knowledge of future values of the velocity up to ψ seconds into the future. It is interesting to note that $F_\beta(t)$, being only related to the radiation resistance, produces a force component that only requires passive loading, that is a damping component. On the other hand, the force $F_\alpha(t)$, together with the integral and derivative actions of the PID component, only produce a reactive load, which matches the inertia and spring of the system, so that the reactive part of the system is cancelled. In other terms, $F_\alpha(t)$ and $F_{PID}(t)$ (when omitting the proportional term), require a bidirectional energy flow between the PTO machinery and the oscillating system.

In [93], it is shown how inclusion of the sole causal component, $F_{PID}(t)$, significantly increases the energy absorption, compared to the case with no control, particularly at frequencies lower than

the natural frequency of the proposed system. Additional improvement in the performance with the non-causal components, F_α and $F_\beta(t)$, is reported but not significant. The non-causality is resolved with a recursive AR multi-step-ahead predictor applied to the measured velocity. Only values of up to $\psi = 2$ seconds into the future are utilised and the authors claim that better predictions over longer horizon could significantly increase the performance of the proposed controller. However, no quantitative analysis was presented for such cases, and the proposed choice for the future horizon was not supported. The authors have also reported that quite high velocities are imposed by the resulting control force acting the oscillating system, so that a saturation on the velocity is included [95].

Note that the feedback structure of the controller may undermine the stability of the system, particularly in the presence uncertainties in the model and/or in the predictions. No stability analysis or sensitivity of the controller to uncertainties was, however, presented by the authors.

In [96] a controller of the type given in (4.45) is proposed for the maximisation of the efficiency of the AWS converter. The system is approximated with a second-order model, following the approach outlined in Section 3.3.3, so that only the $F_{PID}(t)$ component is present and it is implemented with the addition of a high-frequency pole.

An equivalent approach is also discussed in [8], where some guidelines on how to choose the parameter, in order to ensure stability, are given. Robustness and sensitivity to model uncertainties, however, are not analysed.

Velocity-tracking control

For the design of an optimal wave-absorber piston in one degree of freedom (surge), Maisondieu and Clement [97] proposed a causal estimation of the optimal oscillation velocity of the piston, based on the optimal law in (4.14), that becomes, in the time domain,:

$$v(t) = \int_{-\infty}^{+\infty} h_v(\tau) f_{ex}(t - \tau) d\tau, \quad h_v(t) = \mathcal{F}^{-1} \left\{ \frac{1}{2B(\omega)} \right\}, \quad (4.49)$$

as already discussed in Section 4.1.3.

The excitation force, $f_{ex}(t)$, is estimated from the measurements of the total hydrodynamic force and velocity feedback. The authors pointed out that the real and even impulse response relating the optimal velocity to the excitation force, $h_v(t)$, is close to an impulse. A Dirac delta approximation (that means a pure proportional relationship) is therefore proposed. A significant efficiency in the wave absorption is achieved if the gain of the causal approximation is adjusted to the frequency-domain curve $B(\omega)$, based on real-time estimates of the central frequency of the incident wave train.

Note that a control system is required to impose the optimal velocity on the oscillating system, that is the velocity-tracking loop of Fig. 4.8. The authors, however, assumed an ideal loop and neglected its design.

A similar approach, specific to the control of the AWS wave converter, was proposed in [96, 98]. A second-order model of the system was identified in the frequency domain [96] (standard frequency

domain identification techniques, as proposed in Section 3.3.3, were adopted):

$$M\dot{v}(t) + Rv(t) + K \int_{-\infty}^t v(\tau)d\tau = f_{ex}(t) + f_u(t). \quad (4.50)$$

The optimal relation (4.49), therefore, is reduced to a simple proportion:

$$v(t) = \frac{1}{2R} f_{ex}(t), \quad (4.51)$$

which can be directly implemented in real-time for the generation of a reference velocity of oscillation for the system. Physical constraints of the system are also taken into account and a modification of (4.51) is proposed such that the velocity never exceeds the limit value of 2.2 m/s [96, 98]:

$$v(t) = \frac{2.2}{\max_t |f_{ex}|} f_{ex}(t). \quad (4.52)$$

In (4.52), $\max_t |f_{ex}|$ is kept constant over a sea state and future knowledge of the excitation force is assumed.

Note that the reference-generation logic in (4.52) presents two major drawbacks: (a) it is over-conservative most of the time, since the amplitude of the incident wave elevation, and of the resulting force, can vary quite a lot in the short-term, due to wave grouping [6], and (b) from the discussion in Section 4.1.1 and from Fig. 4.1, the relation in (4.52) does not consider the fact that, when the excitation force is sufficiently small, a smaller velocity than the maximum allowed by physical constraints would be optimal. In essence, the reference-generation logic in (4.52) is rather suboptimal. Overall, an efficiency between 179 % and over 500 % higher than the no-control case was reported [98]. However, a comparison with ideal values, given by complex-conjugate control, might give a better impression of the quality of the control system.

Several solutions for the low-level control loop, to impose the reference-velocity on the system, were also proposed [68, 99, 98]. Given that the behavior of the AWS is strongly non-linear [77], since it is a submerged type of WEC and its dynamics are significantly affected by the tidal level, non-linear types of controllers were proposed: internal model control, based on a neural-network model of the system [98, 100], and feedback linearisation, based on a first-principles non-linear model of the system [99]. The sensitivity of the control system to different sea states and to variations in tidal levels was also analysed [101].

In his review paper, Hals [8] proposes a control structure where the reference velocity is calculated from (4.51), based on a second-order model of a WEC consisting of a single, heaving body. The low-level controller implements a Proportional (P) or Proportional integral (PI) controller, whose performance is reported to be quite poor.

Finally, an alternative solution, where a non-causal relation analogous to (4.49) is utilised for the calculation of a reference to be imposed on the system, was also proposed in [102], for the maximisation of the efficiency of an OWC type of WEC. Based on a similarity between the model of an OWC and that of an oscillating body in waves, the same optimal relation as in (4.49) can be derived [6], with a pressure in place of the velocity and an excitation air-mass flow instead of the excitation force. A causal transfer function, $H_p(j\omega)$, is identified such that it is as close

as possible to $1/2B(\omega)$. The causality condition is translated into conditions for the coefficients of the denominator of the transfer function $H_p(j\omega)$. The approximation tries to minimise the error in the band of frequencies where the excitation force, and therefore the wave spectrum, is contained. As pointed out in [6], however, when the sea-state changes, a new $H_p(j\omega)$ would have to be identified, which makes the approach not very attractive. Results, neither in simulation nor in an experimental setup, were published.

4.2.2 Discrete control: Latching and Declutching

As an alternative to optimal complex-conjugate control, Budal *et al* [103] proposed a control method, based primarily on practical intuition, for the enhancement of the efficiency of a simple heaving buoy. The strategy consists of clamping the buoy when it is as close as possible to its extreme positions (points of zero velocity) and then releasing it at a proper time relative to the trough or crest of the wave. With proper timing of the two operations of latching and unlatching, the motion of the buoy is in phase with the wave excitation force. For obvious reasons, the proposed approach goes under the name of *latching* control.

In essence, latching control tries to realise the phase condition implied by complex-conjugate control, that is the zero phase-lag between velocity and excitation force, as from (4.12). The optimal amplitude ratio between excitation force and velocity is not pursued. An advantage compared to complex-conjugate control is that latching is a purely passive strategy, since there is only braking action involved and the energy flow does not need to be reversed during part of the cycle.

As shown in the block diagram of Fig. 4.9(a), the control force, $f_u(t)$, is modelled as a variable damping multiplied by the velocity, $v(t)$ [12]:

$$f_u(t) = -[R_u + u(t)G_0]v(t). \quad (4.53)$$

From (4.53), the total damping, $R_u + u(t)G_0$, is the sum of a constant due to the PTO, R_u , which determines the power absorption while the system is unlatched, and of a component due to the latching mechanism that, in general, is different from the natural PTO characteristics. When the system is latched, $u(t) = 1$ and a very large damping, G_0 , is added to the system; otherwise, when $u(t) = 0$, only the PTO damping, R_u , is present.

Given that the total force is controlled through a discrete variable, $u(t) \in \{0, 1\}$, latching control is here classified as a discrete control method. The objective of the controller is to determine the optimal latching/unlatching sequence, $u(t)$, such that the wave energy absorption is maximised.

If the incident wave were sinusoidal, as in Fig. 4.9(b), it would be relatively easy to determine the optimal unlatching instant, such that the next velocity extremum would happen at the same instant as the next wave force extremum. In fact, considering that the latching time is always determined by the zero-crossing instant of the velocity (body's excursion at an extremum), the unlatching time is derived from the difference between half the wave period and the time that the system, left free to move, takes to go from zero to a maximum velocity. Note that clamping the motion at zero velocity is also beneficial since it introduces a minimum stress on the latching mechanism.

In the unlatched phase, the buoy follows the dynamics of a free body oscillating in the waves,

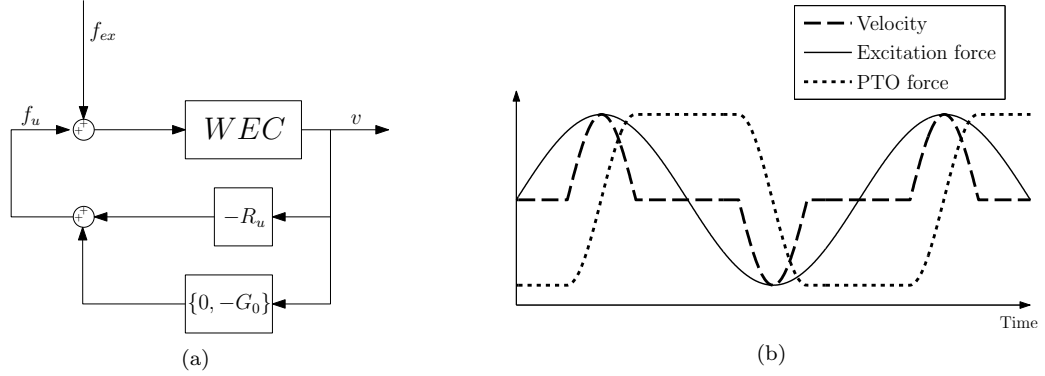


Figure 4.9: Latching control: (a) Block diagram; (b) Typical behavior of velocity and PTO force compared against excitation force [8].

with an additional damping due to the PTO. As analysed in Section 3.2.5, if the PTO damping is relatively small, the floating body oscillates at approximately its natural frequency, where the transient dies out after a number of oscillations. Such a behavior was shown with a numerical example in Section 3.3.3. The same conclusion is drawn in [104], based on analytical considerations applied to a second-order oscillator. As an intuitive consequence, latching can only be applied to slow down the dynamics of the system and, therefore, to set the motion of the buoy in phase with waves at a frequency lower than its natural frequency.

In [104], an analytical procedure was developed in order to optimise the latching time in regular waves. The approach consists of choosing, among the all possible evolutions of the system from the initial latching time, the unlatching instant that maximises the amplitude of the motion (and that results in maximum energy absorption). A finite-order approximation of the system, based on the Prony's method [64], is utilised for simulating the evolution of the system. The horizon over which the maximisation is performed, that determines the period of the motion, is an integer, odd multiple of the period of the excitation force. Choosing a period that is 3 times the period of the incident waves permits an increase in the efficiency of latching also at waves with frequency higher than the natural period of the system [104].

In realistic seas, waves are of stochastic nature (refer to Section 3.1.2) and the buoy can be unlatched at the proper time only based upon a prediction of the wave excitation force [103]. While in regular waves the obvious criterion is to select the right release time such that the next velocity and excitation force extremum are in phase, in fact, in irregular waves such an approach may become meaningless [104]. While latching always happens at zero velocity, the optimal unlatching time is chosen based on off-line simulations and such that the average absorbed energy is maximised.

Optimal command theory [12, 105] was proposed for the real-time optimisation of the unlatching time, for the control of a heaving buoy and of a four degree-of-freedom, self-reactive floating system called SEAREV. Given a non-linear state-space representation of the WEC:

$$\dot{x}(t) = f[x(t), u(t), f_{ex}(t), t], \quad (4.54)$$

where the inputs are the external excitation force, $f_{ex}(t)$, and the discrete control variable $u(t) \in \{0, +1\}$, that determine the total external force (4.53). Given a future time-horizon L , the optimal

sequence, $u(t)$, is calculated such that the absorbed energy is maximised:

$$\max_{u(t)} E[u(t)] = \int_t^{t+L} R_u v(t)^2 dt, \quad (4.55)$$

where $v(t) = \dot{x}(t)$, given in (4.54).

Optimal command theory, based on Pontryagin's maximum principle [106], was utilised for the solution of the problem (4.55), leading to quite promising results that do not assume a monochromatic sea and can comply with the stochastic nature of the wave excitation force [12, 105, 107]. Future knowledge of the excitation force over the time horizon L is assumed, though, and the need for prediction is estimated to be about 100 seconds [12], which is not trivial. At the same time, the sensitivity of the algorithm to eventual inaccuracies in the prediction was not verified. The performance of the approach is also quite sensitive to the damping, R_u , that is applied by the PTO during the unlatched period, which directly affects the power absorption, as from (4.55).

A more practical solution to the real-time implementation of latching control was proposed in [108] and in [109]. The solution was applied to an oscillating body in one degree-of-freedom, coupled with an hydraulic PTO, of the type described in Section 3.4.1 and shown in Fig. 3.12(a). The oscillating buoy is latched when the velocity is zero and unlatched when the wave excitation force exceeds a certain level that can be tuned through a parameter connected to the hydraulic circuit. Optimisation of the parameter determining the unlatching time and the damping during the unlatched phase, over several irregular sea states, can be performed and imposed on the system on a look-up-table basis. A comparison with the performance obtained from optimal command theory and to ideal performance of complex-conjugate control were not reported.

Some notes of criticism were pointed out in relation to latching control strategy as a feasible approach in practical systems for wave energy conversion [110]:

- Ineffectiveness in waves at a higher frequency than the natural frequency of the system. Such a limitation would be of significant importance for very large systems, with slow dynamics. More economical designs (smaller size and mass), on the other hand, will make the systems resonant at relatively high frequencies, which allows an effective application of latching with most high-energetic waves, that usually appear at very low frequencies,.
- The calculation of the optimal unlatching time is problematic in real-time and may require prediction of the excitation force over a long future horizon.
- Strong requirements are placed on the latching mechanism, that must be able to withstand large impulsive loads required to stop the device, in the case of wrong estimations of the exact zero-crossing instant of the velocity.
- Inclusion of motion constraints is not accounted for during the unlatching period, and the system may be subject to excessive excursions in large waves. An additional control during the unlatching time would, therefore, be fundamental in order to regulate the damping realised by the PTO, thereby controlling the excursion.
- The quality of the power output is not considered, and the impulsive nature of the motion intuitively indicates that the absorbed power will be of rather discontinuous nature, with very large peaks alternating with periods of zero power.

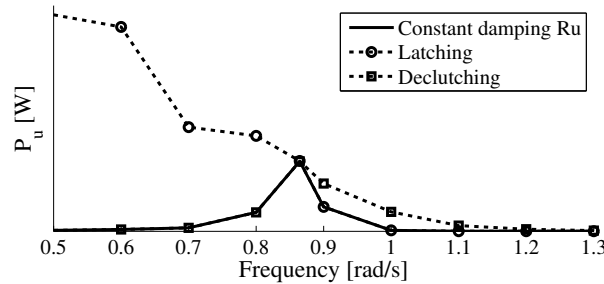


Figure 4.10: Performance of latching and declutching control strategies applied to a heaving WEC, in regular waves, compared against constant linear damping [112].

It is important to mention an other control strategy of discrete nature, that may be considered as the dual with respect to latching, for the (unlikely) case that the wave period is smaller than the natural period of the oscillating system [73]. The method, called *declutching* or *unlatching*, consists of allowing the primary moving element to move freely (null PTO force) for part of the cycle and then engaging the power take-off mechanism at the desired velocity for part of the cycle. The problem of sudden engagement of a friction clutch are just as unpleasant as those of the brake required by latching, but hydraulics may provide a satisfactory answer [73].

Optimal calculation of declutching time was proposed in [111], again by making use of optimal command theory and Pontryagin's maximum principle. When ideal prediction of the excitation force is assumed, superior performance, by a factor of about 200 % is demonstrated against simple linear damping.

The effectiveness of latching and declutching as control strategies for WECs was also confirmed by studies based on numerical optimisation techniques. Over a period of oscillation, effectively, the combined damping provided by the PTO and other external mechanisms goes between very large values (latching) and very small values (declutching). Based on such a general behavior, Genetic algorithms (GAs) were utilised for the optimisation of the damping profile under different sea conditions [112, 10, 113]. Simulation results for regular waves, shown in Fig. 4.10, confirm that latching profiles are optimal for waves with longer period than the natural period of the system, while declutching types of strategies are more optimal for shorter-period waves. Positive outcome of the numerical optimisation include the values of the optimal damping during the unlatching time (when latching is applied) and during the clutching time (when declutching is utilised).

4.2.3 Optimisation-based control

The problem of tuning the oscillation of a WEC for maximum wave energy extraction, as outlined in Section 4.1, is a maximisation problem, possibly subject to constraints on the allowed motions and forces or on the energy flow (passive or active PTO). It would be natural, therefore, to think about solving a real-time constrained optimisation problem for the calculation of the optimal velocity and/or PTO forces that maximise a certain function, typically the energy absorption.

A family of control methods that is particularly well suited for handling constraints as a part of the control problem includes the various concepts known as MPC [114, 13]. Traditionally, MPC has

been applied with success in chemical engineering, plant control, and process control applications. In other words, relatively slow processes in which actuator dynamics are relevant and constrained. This describes the ocean wave energy application well [115], although the dynamics involved are faster than typical process control. Computational complexity, in particular, needs to be kept in mind in wave energy applications, where sampling periods would not be larger than 0.5 or 1 second (typically 1.28 or 2.56 Hz).

MPC, for a wave energy device, was originally proposed in [116], for the control of the AWS wave energy converter. Further elaborations were applied to a heaving point absorber [117, 118] and to the optimal control of a wave-powered desalination unit [119]. A comprehensive treatment and formulation of the MPC applied to an oscillating system for wave energy conversion was then proposed in [13], where a heaving, semi-submerged sphere is utilised as a case study for the reported numerical results.

In essence, MPC optimises the operation of the system, that is the PTO force, $f_u(t)$, and/or the velocity, $v(t)$, such that the average power, or the energy, transmitted to the PTO over a *finite* future horizon, is a maximum. In particular, at each time instant, t , the following functional is maximised, over a given time horizon, L :

$$\max J(t) = - \int_t^{t+L} f_u(\tau)v(\tau)d\tau, \quad (4.56)$$

possibly also subject to constraints on the system's variables.

The problem is conveniently posed in discrete time and a finite-order, linear approximation of the model of the oscillating system is derived, by means of Prony's method [64] or using frequency domain techniques [71], as described in Section 3.3.3. The discrete-time model is put into a state-space form of the type:

$$\begin{cases} z[k+1] = Az[k] + B_1f_u[k] + B_2f_{ex}[k] \\ v[k] = Cz[k] \end{cases}, \quad (4.57)$$

where, as usual, $f_{ex}[k]$ is the wave excitation force, $v[k]$ is the system's velocity and $z[k]$ is a state variable whose dimension represents the order of approximation of the complete state-space system. The squared bracket notation indicates discrete-time signals, i.e. $x[k] \triangleq x(kT_s)$, where T_s is the sampling period.

For robustness of the numerical optimisation, the function to be maximised is re-written [13] as:

$$\max_{\tilde{v}[k]} J[k] = \sum_{j=0}^L f_{ex}[k+j]v[k+j] - f_r[k+j]v[k+j] = \tilde{f}_{ex}[k]\tilde{v}[k] - \tilde{f}_r[k]\tilde{v}[k], \quad (4.58)$$

which is the discrete-time equivalent of (4.56), where the absorbed power is expressed as the difference between the excitation power, $f_{ex}[k]v[k]$, and the power lost due to radiation, $f_r[k]v[k]$. Maximisation is performed with respect to the velocity trajectory over the receding horizon L , defined by the vector $\tilde{v}[k] \triangleq [v[k+1], \dots, v[k+L]]^T$. Following the same notation for the velocity, the future trajectories of the excitation and radiation force, in (4.58), are expressed as $\tilde{f}_{ex}[k] \triangleq [f_{ex}[k+1], \dots, f_{ex}[k+L]]^T$ and $\tilde{f}_r[k] \triangleq [f_r[k+1], \dots, f_r[k+L]]^T$.

Maximisation of $J[k]$ with respect to the force was found to give rise to numerical issues in the optimisation and to yield less accurate solutions. The optimal PTO force was, therefore, derived from the equations of motions and from the optimal velocity, resulting from (4.58) [13]. Note that, at each time step k , the velocity $v[k+1]$ is imposed on the system and a new optimisation is run so that the future values of the trajectory are updated.

Constraints concerning the position, velocity and PTO force can be all written as linear inequalities involving the vector $\tilde{v}[k]$:

$$F[k]\tilde{v}[k] \leq b[k], \quad (4.59)$$

where the matrix $F[k]$ and the vector $b[k]$ depend on the position, velocity and force constraints, on dynamic properties of the system and on the initial state at the current instant, that is $z[k]$ (refer to [13] for the details).

Another constraint could be included in order to enforce passivity of the PTO, that is unidirectionality of the energy flowing into the PTO (absorbed power with the same sign over the optimisation horizon L). Such a constraint, involving the product between velocity and control force, is however non-linear and makes the optimisation problem non-convex and more difficult to be accurately solved in real-time. The passivity constraint, within an MPC framework, has not been investigated, to the best of the author's knowledge.

Very efficient quadratic-programming, gradient-based, optimisation algorithms can be utilised for the solution, in real-time, of the problem in (4.58), subject to the constraints in (4.59) and (4.57), if future knowledge of the excitation force, over the time-horizon L is available. Interestingly, the motion resulting from application of MPC, when velocity and position constraints are applied, has a behavior similar to latching, as was shown in Fig. 4.9(b).

Important results, approaching the analytical upper bounds outlined in Section 4.1, are reported in the case of ideal predictions of the wave excitation force. A significant performance drop, between 20 % and 50 % depending on the sea state is, however, verified when using imperfect predictions [13]. A simple sinusoidal extrapolation using the Kalman filter [103] (refer to Section 6.4.3 for a detailed description) was utilised for the prediction of the wave excitation force. Improvements may be expected with other approaches, including AR models, as proposed in [119], [118] and [115].

A different type of MPC formulation for the wave energy control problem was recently proposed in [115]. The function to be optimised, in particular, is expressed as the classical MPC problem of optimal tracking with weighting of the control effort and within given constraints of the system's variables:

$$\max_{\tilde{v}} J[k] = \{\tilde{v}[k] - \tilde{y}[k]\}^T Q_y \{\tilde{v}[k] - \tilde{y}[k]\} + \Delta \tilde{f}_u[k]^T Q_u \Delta \tilde{f}_u[k], \quad (4.60)$$

where the control input weighting operates on the variation with respect to the previous input value, $\Delta \tilde{f}_u[k] \triangleq \tilde{f}_u[k] - \tilde{f}_u[k-1]$. The matrices Q_y and Q_u are standard weight matrices, typical of quadratic optimal control, which express the compromise between tracking performance and

control effort. The trajectory of the reference velocity, $\tilde{y}[k]$, is generated as:

$$\tilde{y}[k] = \frac{1}{2R} \tilde{f}_{ex}[k], \quad (4.61)$$

similar to that proposed as a causal approximation of complex-conjugate control, in (4.51), where R is some approximation of the radiation resistance of the floating system, which is typically frequency dependent [115]. Note that in this case, though, prediction of the excitation force is still required over the time horizon L .

The alternative formulation in (4.60) will offer a performance that is only as good as the reference trajectory for the velocity. In particular, it seems to be a rather sub-optimal approach in comparison to (4.58), where the velocity trajectory the result of the optimisation that maximises the energy absorption. A justification of the different approach, (4.60), with respect to (4.58), was not given [115].

Another interesting model-based predictive controller was proposed in [120]. The constrained optimisation problem is converted into a (suboptimal) non-linear program through the discretisation of the PTO force and of the motion. Force and motion are expressed as linear combinations of orthogonal basis functions, whose choice determines the properties of the cost function and the constraints. Appropriate choice of the approximating basis functions, although resulting in a suboptimal solution, permits a guaranteed convergence and a small computational effort, which suits the real-time implementation. Promising numerical results are shown for the optimisation of a self-reactive two-body WEC with amplitude constraints. In the same paper [120], the authors also propose the design of a Linear quadratic (LQ) controller for the low-level loop that imposes the desired trajectories, resulting from the optimisation, onto the system.

4.2.4 Control of the PTO impedance

In Section 3.4.2 it was shown how, typically, the action of the PTO machinery on an oscillating system for wave energy conversion is modelled as a mechanical impedance, termed Z_u . A resistive part, or damping, R_u , contributes to the average active power that is absorbed by the PTO, while a reactive part, or stiffness, X_u , produces a bi-directional energy flow between the load and the oscillating system. A distinction between passive PTOs, that can only provide the resistive part, and active PTOs is therefore made.

The modification to the dynamics of the system, when an additional mechanical impedance is introduced, was also qualitatively analysed based on the behavior of mechanical oscillators, described in Sections 3.2 and 3.3. In particular, it was seen that the resonant behavior of the system can be conveniently altered in order to match the spectral distribution of the excitation force, directly related to the wave spectrum, in the case of WECs. Increasing R_u makes the resonance curve of the system wider, that is more efficient in a wider range of seas, and less peaky, reducing the efficiency at resonance. By introducing a stiffness term, X_u , it is possible to move the resonance frequency of the system, so that a high efficiency could, in theory, be achieved over sea states centred around different frequencies. Additional damping and/or inertia can also be provided by means of alternative types of mechanisms than the PTO. In [121], for example, an experimental heaving floating body is connected to a hydro-pneumatic PTO, consisting of a hydraulic circuit

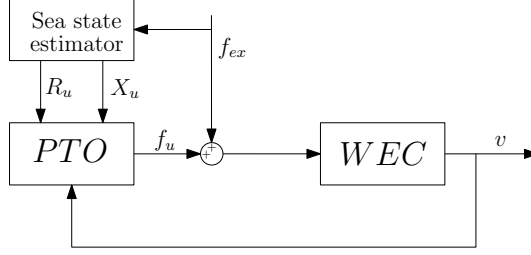


Figure 4.11: Typical block diagram for control strategies that set the damping and stiffness coefficients realised by the PTO to adapt the response of a WEC to the prevailing sea state.

and a hyperbaric accumulator. A sliding mass is fixed on a beam arm that connects the floater to the hydraulic circuit of the PTO, mounted on-shore. By changing the position of the mass, the inertia of the floating mass, and therefore its resonance frequency, can be changed.

A common branch of control strategies for maximising the efficiency of WECs consists of tuning the damping and stiffness implemented by the PTOs to the sea state, as described in [73]. A typical, quite generic, block scheme for such types of controllers is shown in Fig. 4.11. Based on measurements of the excitation force (or on remote sensing of the wave conditions), an estimate of the sea state is produced, that involves estimation of the wave spectrum and/or summary statistics, i.e. significant wave height, energy/peak period (described in Section 3.1.2). The resistance and reactance, R_u and X_u , of the PTO are then chosen according to some logic, that could involve an optimisation loop or a look-up table, based on simulations or experimental testing. The PTO will, then, provide a certain force on the system that depends on the chosen impedance and the velocity of the system, as from (3.146):

$$f_u(t) = R_u(t)v(t) + X_u(t)\dot{v}(t). \quad (4.62)$$

A lower-level control system may be required in order to implement the desired damping in the PTO.

Reactive control optimal conditions, given in (4.12), can be utilised to set the load impedance such that maximum energy is transferred from the waves to the system [6]. In particular, the PTO impedance should be set as the complex-conjugate of the intrinsic impedance of the system, at the frequency of the incident wave. Similar conditions, in the frequency domain, were also derived for WECs consisting of two self-reacting bodies [56, 122]. Alternatively, genetic algorithms were also proposed for the optimisation of a non-linear damping profile [113, 10, 112], to be applied over each period of an incident regular wave. Extension of such approaches to irregular waves is, however, not straightforward and would most likely require extensive numerical calculations off-line, that would produce a sort of look-up table to be utilised during the operation of the system, on the basis of some real-time estimate of the sea state.

In [123, 124], the optimal damping and stiffness are regulated by a linear generator in order to optimise the energy efficiency of a heaving body in regular waves. As also proposed in [125], vectorial $d - q$ control of the current at the generator can provide accurate control of the desired load impedance. However, inefficiency of the bi-directional flow is not taken into account and the real-time tuning to the sea state is not discussed.

In the case of passive PTOs, several numerical studies has been proposed where the damping coefficient of an oscillating system for wave energy conversion is optimised over different sea states [126, 127, 128], taking into account limitations on the motion of the device. In [129, 130, 81], the damping coefficient of a linear generator connected to a single-body heaving buoy is optimised after experimental data is collected in the open sea. How the linear damping coefficient would be implemented in practice and tuned in real-time is not, however, discussed. In [131], a practical solution for the tuning of the damping realised by a hydraulic type of PTO mechanism is proposed, as well as its influence on the performance over different sea states.

In [132], a method for tuning the damping and stiffness in real-time is proposed. Measurements of the wave elevation or estimations of the wave excitation force are low-pass filtered in real-time and then processed in order to derive an instantaneous wave period, as a combination of zero up-crossing, crest-to-crest, zero down-crossing and trough-to-trough periods. Based on the estimated period, the damping and stiffness are derived from a compromise between maximum performance and constraints on the minimum damping to be applied to the system, such that excessive motions are avoided.

A real-time tuning strategy based on fuzzy logic was also proposed [133, 134, 135]. The approach implements a predictive model that simulates the future behavior of the WEC over a certain future time-window, based on a linear state-space model and on AR predictions of the wave elevation. The future simulation of the system is input in a fuzzy inference system that, based on practical rules, determines the appropriate damping to be implemented by the PTO. A low-level control loop, based on H_2 robust control, is also implemented in order to impose the desired damping on the system, while reducing the sensitivity to modelling uncertainties and to errors in the wave predictions.

The present overview of methods for optimising the external damping and stiffness to be provided to a system for wave energy conversion, such that its performance is improved, is not exhaustive, and other solutions have been proposed. However, an effort has been made to cover a range of techniques that give an overview of each category.

Advances in other categories of real-time controllers, that were reviewed in Sections 4.2.1 through to 4.2.3, have made the solutions discussed in this Section, however, less attractive. There are a lot of disadvantages, in fact, in controlling a WEC through the impedance provided by the PTO mechanism. The main problem is that, in essence, damping (and stiffness) control may be regarded as a purely open-loop control. The motion and forces are outside the control loop, although they are affected by the controlled variable. Imperfect knowledge of the model, which is typically the case in wave energy (refer to Section 3.3.1), may result in unexpected motions of the system for a given value of the applied damping. A more robust approach would be to include the external force, or even better the motion of the system, into the control loop, which leaves the choice of the damping to a lower-level controller, that implicitly sets the appropriate damping in order to produce the desired force or motion.

Another problem is that, usually, the damping and stiffness coefficients provided by the PTO are assumed to be linear. Particularly for hydraulic systems, but also for electrical generators, linearity is an assumption that can be quite far from the reality of the system, as from the discussion in Section 3.4.1.

4.2.5 Solutions for the active control of sound and vibrations

For the sake of completeness, some solutions are now documented, here, which are typical in the field of the active control of sound and vibrations, which can be considered as a companion problem of wave energy conversion. Many different techniques, in fact, are available for designing controllers for the rejection of periodic noise [136], which can be seen as a narrow-band disturbance. Typical applications are the active suppression of vibrations in a structure [137, 136, 138, 139, 90, 140, 141, 142], or the active cancellation of noise [143, 144].

The main idea is that it is possible to remove an unwanted vibration from a structure by inducing a vibration that is 180 degrees out of phase with the original and of equal amplitude [139]. The same applies to noise cancellation. In wave energy, the idea is to move the oscillating system such as to produce a wave (via radiation) that is in counter-phase with the incident wave, according to the principle that a good wave-maker is also a good wave absorber [6].

Sievers and von Flotow [137] distinguish two possible architectures for the active isolation of vibration represented by narrow-banded disturbances:

Disturbance modelling . The disturbances are modelled as outputs of a linear, time-invariant system, forced with white noise. The state-space model of the system is augmented with disturbances states and then Linear quadratic Gaussian (LQG) theory is used to calculate the regulator and observer gains.

LQG control with frequency weighting within the cost function . The cost function of the LQG problem heavily weights the controlled output contribution in the frequency range of the input disturbance.

It is shown that both approaches produce a closed loop response representing a notch filter centred at the frequency of the disturbance [137, 136], minimising the sensitivity function in the spectral region of the vibration. In the particular case of SISO systems, the two approaches are shown to be equivalent [137].

Two main assumptions, however, are made: knowledge of a model of the system, and knowledge of the spectral distribution of the noise. While, for the case of flexible structures, the assumption of a known system model is not always realistic [136], in the case of wave energy that is not usually a problem, as the hydrodynamic models are reasonably well understood in the region of the active spectrum of the incident waves. On the other hand, the spectral distribution of the disturbance, that is the wave excitation force, is also well known in wave energy applications, but it is of changing nature over a relatively wide spectrum. Adaptive filters can be used in this case, in order to produce a feedforward control action based on real-time estimates of the model of the disturbance [145].

Ideal, analytical solutions for the optimal power absorption (and therefore cancellation) of narrow-banded vibrations were proposed in [138, 90, 140], for the control of vibrations in flexible structures. Consider the frequency-domain model:

$$y(\omega) = G(\omega)u(\omega) + d(\omega), \tag{4.63}$$

where d is a disturbance and $G(s)$ is the driving-point mobility, defined as a ratio between velocity, y , and excitation force, u . The problem is stated as finding an optimal control that, acting on the

force, u , is able to tune the velocity, v , such that minimum power flows between d and y . The solution is similar to complex-conjugate control, given in (4.12):

$$u_{opt}(\omega) = -\frac{1}{G^*(\omega)}y(\omega), \quad (4.64)$$

which is independent of the spectral distribution of the disturbance. The optimal compensator (4.64), however, suffers from the same problem as complex-conjugate control, that is non-causality. Based on prior information about the spectral distribution of typical vibrations, loop-shaping techniques based on H_2 and H_∞ control are therefore proposed [90, 140].

An application of solutions, typical of the control of sound and vibration, to a WEC was recently proposed by Scruggs and Lattanzio [146]. An optimal, causal controller for the maximisation of the wave energy extraction from an oscillating system in random sea, is found from the solution of a non-standard LQG problem. A state-space model of the excitation force, generated from a Pierson-Moskovitz spectrum, is identified and included in an extended model of the WEC, where the input disturbance is Gaussian white noise. A quadratic function, representing the absorbed power, is maximised and an optimal, causal and linear controller is found. The results show performances very close to what can ideally be achieved with complex-conjugate control. Spectral characteristics of the sea need to be known in advance, however, and it is concluded that the controller must necessarily sense and adapt to changes in the sea state, in order to remain close to its theoretical performance level.

4.3 Discussion and perspectives

This Chapter proposed a review of the main solutions to the problem of control of systems for wave energy conversion, with the objective of increasing the efficiency of the energy capture. The control action is in the form of an external force provided by the system for power conversion or PTO.

Most of the control solutions try to realise the ideal conditions, calculated analytically in the frequency domain, that go under the label of complex-conjugate control, as detailed in Section 4.1. The ideal conditions relate the optimal values of the velocity and PTO force to the external wave excitation force, but none of them can be directly implemented in real-time due to their non-causality, highlighted in Section 4.1.3. The approaches to the real-time implementation of complex-conjugate control, therefore, differ in which one of the optimal relations they are based on and on how they deal with the non-causality. Most of the proposed solutions either use the optimal conditions to directly calculate the PTO force to be imposed on the system (in a feedback or feedforward way), or they estimate the optimal velocity from the excitation force, leaving the task of choosing the PTO force to a reference-tracking, lower-level controller. As highlighted in Section 4.2.1, in particular, the latter approach would be preferable when non-linearities in the system are significant, since the low-level controller can be designed to be robust to model (and eventually prediction) uncertainties. In addition, the approach based on velocity tracking can also be extended to include constraints, since the reference-generation logic can easily incorporate

limitations on the motions, based on the analytical solution proposed in Section 4.1.2. The non-causality is solved with prediction or with causal approximations, based on a second-order model of the system or based on a spectral estimation of the incoming wave.

More practical solutions were proposed, where the control problem is formulated as the tuning of the impedance realised by the PTO system. As commented in Section 4.2.4, however, control of the damping and reactance is essentially an open-loop control and, due to modelling errors, a given PTO impedance may not produce the expected motions/forces. In addition, the assumption of linear damping is a strong one and most studies do not consider how the desired linear impedance may effectively be implemented by the PTO system.

Discrete types of control, where the external force is treated as a sequence of values belonging to a discrete set, have also been discussed in Section 4.2.2, mainly latching and declutching. In discrete control, the motion of the system is, essentially, only controlled for part of the cycle when it is either clamped (latching) or disconnected from the PTO (declutching). Apart from the physical difficulties, already highlighted in Section 4.2.2 and mostly involving the stresses in the latching/declutching mechanism, the uncontrolled operation is usually based on setting the damping/impedance of the PTO to a constant value, which suffers from the same difficulties as control of the PTO impedance (open-loop and realisability of a linear damper). Besides, the optimal control sequence requires optimal command theory to be determined in irregular waves, which needs predictions over a long future horizon in order to converge.

Given the nature of the wave energy control problem, among the most promising techniques proposed in the literature are model-based controllers that run a constrained optimisation in real-time. An optimal control input to be given to the system is determined, such that maximum wave power absorption is achieved within any given constraint. An overview of optimisation-based controllers was given in Section 4.2.3. The main difficulty is the necessity of having an accurate enough model of the system and, at the same time, ensuring that the optimisation algorithm converges to an optimum within the one sample period. Predictions of the excitation force are still required, in order to provide an accurate prediction of the behavior of the system over the optimisation time-horizon.

In Section 4.2.5, some alternative techniques typical of the active control of sound and vibrations were also proposed. The ideal control solution, in this case, shares some similarities with complex-conjugate control for wave energy, and its non-causality is typically dealt with an assumption about the spectral model of the disturbance. The latter is utilised in the design of a feedback loop, shaped on the basis of the optimisation of a H_2 or H_∞ functional. For non-stationary disturbances, which is the case in wave energy, adaptive filters based on estimation/prediction of the excitation are required.

As it emerged throughout the discussion in this Chapter, while usually acknowledged, the requirement of prediction of the incident wave or of the excitation force produced on the WEC was rarely addressed. Apart from some specific cases, it is not clear how long into the future predictions are required for and to what degree of accuracy. Information of this type could be very valuable at the design stage not only for the controller, but also for the overall WEC system. It may be possible and useful, in fact, to include a controllability criterion among the variables to be considered when the system geometry is chosen.

In addition, the problem of prediction itself was poorly addressed in conjunction with the

control problem. Future values of the wave or wave force are usually assumed to be ideally known or, if predictions are performed, the influence of the prediction quality on the performance of the controller is not clear. Based on an analysis of the prediction requirements, it would be interesting to compare and analyse different wave forecasting solutions and how they comply with the requirements.

The problem of prediction requirements and wave prediction will be analysed and investigated in more detail in the Chapters 5 and 6.

Chapter 5

Wave prediction requirements

Abstract

Real-time control of wave energy converters (WECs) can benefit from prediction of the incident wave or wave excitation force, as clearly emerged from the review in Chapter 4. However, a quantitative analysis of the prediction requirements of the different control strategies proposed in the literature has not, to date, been available.

The prediction requirements (how far ahead into the future do we need to predict?) are analysed and quantified, when unconstrained complex-conjugate control is implemented. The fundamental properties of the floating system that influence the length of the required forecasting horizon are characterised. The possibility of manipulating the control, based on prior knowledge of the wave spectral distribution, is also proposed for the reduction of the prediction requirements. The proposed methodology is validated on real wave data and heaving buoys with different geometries.

The main analysis and conclusions of this Chapter can also be found in [21, 20, 19, 15].

5.1 Introduction

Real-time control of WECs is based on the tuning of the system's motion for maximum wave energy absorption. An overview of the various solutions that exist in the literature was given in Chapter 4. The unconstrained optimal solution, namely complex-conjugate control, outlined in Section 4.1, specifies the conditions under which the system is always in resonance and maximum power transfer from the waves to the PTO is achieved. Alternative control solutions have also been proposed, where the limitation imposed by the physics of the system (e.g. amplitude of motion or velocity, applicable forces), neglected by complex-conjugate control, are also taken into account. In particular, some of the alternatives include latching [12], where the energy flow is constrained to be uni-directional, and model predictive control (MPC) [119, 117, 13], which handles the use of motion/forces constraints. Discrete control (latching/declutching) and MPC were already outlined in Sections 4.2.2 and 4.2.3.

In Section 4.3, as well as in the wave energy literature, it is acknowledged that the effectiveness of the different real-time control strategies depends, among other things, on the prediction of the

incident wave elevation or wave excitation force acting on the system [6, 12, 119, 135, 8].

The pre-requisites for the implementation of the afore-mentioned control solutions, in terms of prediction, have not been formally analysed and quantified. At the same time, it is of fundamental importance to understand how long into the future predictions are required for, and if there is any particular property of the WEC that may have an influence on the required future time horizon. Not only is such an analysis important to judge the adequateness of the forecasting solutions, but it can also be critical at the design stage of a WEC, when controllability may need to be considered.

A preliminary study, where the required and the achievable prediction horizon are qualitatively related to the bandwidth of the radiation of the system and to the bandwidth of the occurring sea state, is given in [147]. In the same study, the possibility of considering controllability at the design stage of a WEC is also considered, on the basis of relations between the floating system geometry and the prediction requirements. The conclusions, however, are only based on qualitative analysis, that are not supported by practical examples or quantitative calculations.

Throughout this Chapter, a quantitative analysis of the non-causality of the optimal conditions for maximum wave energy conversion, given by complex-conjugate control, is proposed. In particular, an attempt is made to build a link between some fundamental properties of a floating system for wave energy conversion and how long into the future predictions are necessary for an effective approximation of the non-causal optimal control. The possibility of manipulating the control, based on prior knowledge about the spectral distribution of the incident wave, such that the prediction requirements are reduced, is also analysed. The limiting case of a causal approximation is also discussed.

The focus is put on a WEC consisting of a single floating body constrained to move in one degree of freedom, as was modelled in Section 3.3.1. The adoption of a particular device geometry does not limit the generality of the results, it allows for a clearer understanding of the fundamental relations between the system and the prediction requirements.

The architecture of the complex-conjugate controller, and the analysis of its non-causality, are discussed in Section 5.2. The methodology proposed for the quantification of the prediction requirements is then presented in Section 5.3, along with the possibility of manipulating the controller to reduce the non-causality. Results obtained for some ideal systems over a variety of sea states are then discussed in Section 5.4. Finally, Section 5.5 points out the main conclusive remarks.

5.2 Analysis of non-causality

As discussed in Section 4.1, given the model of a floating body oscillating in one degree of freedom:

$$V(\omega) = \frac{F_{ex}(\omega) + F_u(\omega)}{Z_i(\omega)} = \frac{F_{ex}(\omega) + F_u(\omega)}{B(\omega) + K_v + j\omega \left[m + m_\infty + m_a(\omega) - \frac{K_s}{\omega^2} \right]}, \quad (5.1)$$

complex-conjugate control gives three optimal conditions such that an oscillating system extracts maximum energy from the incident wave:

$$F_u(\omega) = -Z_i^*(\omega)V(\omega) = -\frac{Z_i^*(\omega)}{2B(\omega) + 2K_v}F_{ex}(\omega) \quad (5.2)$$

$$V(\omega) = \frac{1}{2B(\omega) + 2K_v}F_{ex}(\omega). \quad (5.3)$$

Refer to Sections 3.3.1 and 3.3.2 for a full derivation of (5.1) and for details about the quantities involved. Section 4.1.3 highlighted the non-causality of the conditions (5.2) and (5.3), which, as a result, cannot be implemented in practice.

As reviewed in Section 4.2.1, one can use estimates/predictions of the excitation force to approximately calculate the optimal velocity in (5.3), or the PTO force, using (5.2). Alternatively, measurements and predictions of the velocity can be utilised in order to estimate the optimal PTO force, from (5.2). On the basis of such calculations, an approximation of complex-conjugate control can be implemented in real-time to tune a WEC for optimal operation.

Note that the use of the first equivalence in (5.2) requires prediction of the oscillation velocity of the system. The velocity, however, is also the controlled variable, as shown in the block scheme of Fig. 4.7, in Chapter 4. The ability to predict the velocity is therefore strictly related to the controller and cannot be treated separately. Since the objective of this Chapter is to give a clear quantification of the prediction requirements for the implementation of non-causal complex conjugate control, the focus is put on strategies where the variable to predict is the excitation force. The latter is independent of the dynamics of the system, by definition (refer to Section 3.3.1), and the identification of the requirements can be clearly separated from the problem of control.

The focus is therefore put on the second equivalence in (5.2), where the optimal force is calculated from the excitation force, and on (5.3). Equation (5.2) can be further expanded, based on the model in (5.1), as:

$$\begin{aligned} F_u(\omega) &= -\frac{Z_i(-j\omega)}{2B(\omega) + 2K_v}F_{ex}(\omega) = \\ &= \frac{-B(\omega) - K_v + j\omega \left[m + m_\infty + m_a(\omega) + \frac{K_s}{(j\omega)^2} \right]}{2B(\omega) + 2K_v}F_{ex}(\omega) = \\ &= -\frac{1}{2}F_{ex}(\omega) + \frac{m + m_\infty + m_a(\omega)}{2B(\omega) + 2K_v} [j\omega F_{ex}(\omega)] + \frac{K_s}{2B(\omega) + 2K_v} \left[\frac{1}{j\omega} F_{ex}(\omega) \right] \end{aligned} \quad (5.4)$$

By defining the non-causal transfer function:

$$H_{opt}(\omega) \triangleq \frac{1}{2B(\omega) + 2K_v}, \quad (5.5)$$

the optimal relationships in (5.3) and (5.2) can be written as:

$$V(\omega) = H_{opt}(\omega)F_{ex}(\omega) \quad (5.6)$$

$$F_u(\omega) = \frac{1}{2}F_{ex}(\omega) + [m + m_\infty + m_a(\omega)] H_{opt}(\omega) [j\omega F_{ex}(\omega)] + K_s H_{opt}(\omega) \left[\frac{1}{j\omega} F_{ex}(\omega) \right] \quad (5.7)$$

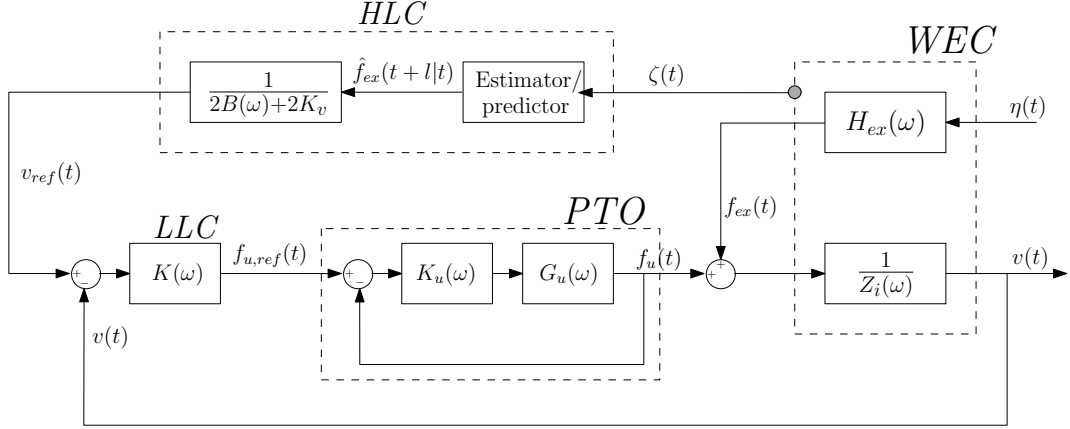


Figure 5.1: General structure for a non-causal controller of a WEC [15]. A high-level controller (HLC) generates the velocity reference, $v_{ref}(t)$, from predictions of the excitation force. The low-level controller (LLC) implements a velocity-tracking feedback loop.

The optimal velocity is related to the excitation force directly through $H_{opt}(\omega)$. On the other hand, the optimal load force, in (5.7), is related to the excitation force by means of a proportional component plus a derivative and integral term, filtered through the non-causal transfer function $H_{opt}(\omega)$.

The non-causality of the optimal conditions of interest is, therefore, totally captured by the transfer function $H_{opt}(\omega)$ and its correspondent kernel:

$$h_{opt}(t) = \mathcal{F}^{-1} \left\{ \frac{1}{2B(\omega) + 2K_v} \right\} = \frac{1}{2\pi} \int_{-\infty}^{+\infty} H_{opt}(\omega) e^{j\omega t} dt. \quad (5.8)$$

The analysis of the prediction requirements can, therefore, be centred on the non-causal transfer function relating the velocity to the excitation force, namely the function $H_{opt}(\omega)$ defined in (5.5). From (5.7), the non-causality of the relation between the excitation force and the optimal force would be of a similar nature.

A control structure like the one shown in Fig. 5.1 is therefore proposed for the quantification of the prediction requirements. The optimal velocity is calculated, based on (5.6), by using future values of the excitation force. A low-level velocity-tracking controller would therefore act on the PTO force, such that the reference velocity is imposed on the oscillating system for wave energy conversion.

One main problem with the analysis of (5.8) is that the radiation impedance, and its real part $B(\omega)$, are only available numerically for some frequencies, as an analytical solution is not, in general, feasible for the radiation problem (refer to the discussion of Section 3.3.3). This poses some problems for the calculation of the non-causal kernel $h_{opt}(t)$, which are dealt with in detail in Section 5.2.1.

5.2.1 Calculation of the non-causal kernel $h_{opt}(t)$

There are two possibilities for the derivation of the non-causal kernel in (5.8), $h_{opt}(t)$, considering that its frequency response is only known numerically for some frequencies. One approach is to approximate the numerical function in the frequency domain with a finite-order linear system in the Laplace domain, $H_{opt}(s)$, and then calculate the non-causal impulse response analytically. A second possibility would be to make use of the IDFT and calculate, numerically, a discrete-time signal approximating the impulse response function $h_{opt}(t)$.

Analytical calculation of the non-causal kernel through identification of the radiation

If a finite-order system approximating the radiation transfer function, $H_r(\omega) = B(\omega) + j\omega m_a(\omega)$, is available, an alternative representation of the dynamic equation of the heaving floating body, given in (5.1), can be written in the Laplace domain:

$$s(m + m_\infty)V(s) + \hat{H}_r(s)V(s) + \frac{K_s}{s}V(s) + K_v V(s) = Z_i(s)V(s) = F_{ex}(s) + F_u(s), \quad (5.9)$$

where zero initial conditions, about velocity and position, are supposed.

In (5.9), the transfer function $\hat{H}_r(s)$ is an approximation of the radiation of the system, defined in (3.116):

$$\hat{H}_r(s) \Big|_{s=j\omega_i} \approx H_r(\omega_i), \quad (5.10)$$

that can be identified from the data, $H_r(\omega_i)$, known only for some frequencies, ω_i , according to the different methods outlined in Section 3.3.3.

Based on (5.9) and (5.5), the non-causal transfer function of interest, $H_{opt}(\omega)$, can then be approximated in the Laplace domain:

$$H_{opt}(s) = \frac{1}{Z_i(s) + Z_i(-s)}, \quad (5.11)$$

where $Z_i(\omega)^* = Z_i(-s)$, for $s = j\omega$, with:

$$Z_i(s) = \hat{H}_r(s) + K_v + s \left(m + m_\infty + \frac{K_s}{s^2} \right). \quad (5.12)$$

The non-causal impulse response $h_{opt}(t)$, defined in (5.8), can be therefore calculated through Laplace inversion of (5.11):

$$h_{opt}(t) = \mathcal{L}^{-1} \left\{ \frac{1}{Z_i(s) + Z_i(-s)} \right\}, \quad (5.13)$$

where $X(s) = \mathcal{L} \{x(t)\}$ and $x(t) = \mathcal{L}^{-1} \{X(s)\}$ are Laplace transform pairs.

Note that $H_{opt}(\omega)$ is, from the definition in (5.5), a real and even function of ω (the radiation resistance $B(\omega)$ is real and even) so that it will have pairs of poles of opposite sign: real poles are symmetric with respect to the $j\omega$ axis; complex-conjugate poles are symmetric with respect to the origin. Because the impulse response is known to be non-causal, the region of convergence

considered for the Laplace inversion of $H_{opt}(s)$ must consist of the central stripe of the complex s -plane containing the $j\omega$ axis (we know that the frequency response exists) and bounded between the inner unstable and stable poles (which, as said, are symmetric with respect to the origin).

From some prior knowledge about the radiation transfer function, $H_r(s)$, it is possible to derive a general expression for $H_{opt}(s)$, which can give some important insights about the general shape of the impulse response $h_{opt}(t)$. In particular, as also discussed in Section 3.3.3, it can be shown that $H_r(s)$ has a zero at $s = 0$ and it is strictly proper, with the degree of the numerator being one less the degree of the denominator [71]:

$$\hat{H}_r(s) = \frac{b(s)}{a(s)} = \frac{b_{n-1}s^{n-1} + b_{n-2}s^{n-2} + \dots + b_1s}{s^n + a_{n-1}s^{n-1} + \dots + a_1s + a_0}. \quad (5.14)$$

Note that, in (5.14), the degree of the denominator, n , represents the order of the finite-order approximation of the radiation.

As a consequence, based on (5.12), the finite-order approximation of the intrinsic impedance is:

$$Z_i(s) = \frac{b(s)}{a(s)} + K_v + s(m + m_\infty) + \frac{K_s}{s} = \frac{s^2a(s)(m + m_\infty) + sK_v a(s) + K_s a(s) + sb(s)}{sa(s)} \triangleq \frac{d(s)}{sa(s)}, \quad (5.15)$$

which is not proper, since the degree of the denominator, $n + 1$, is lower than the degree of the numerator, $n + 2$.

A general expression for $H_{opt}(s)$ can directly be derived, from (5.15), as:

$$\begin{aligned} H_{opt}(s) &= \frac{1}{Z_i(s) + Z_i(-s)} = \\ &= \frac{-s^2a(s)a(-s)}{-sa(-s)d(s) + sa(s)d(-s)} = \\ &= \frac{s^2a(s)a(-s)}{s^2a(-s)b(s) + s^2a(s)b(-s) + 2K_v s^2a(s)a(-s)} = \\ &= \frac{a(s)a(-s)}{a(s)b(-s) + a(-s)b(s) + 2K_v a(s)a(-s)} \triangleq \frac{num(s)}{den(s)} \end{aligned} \quad (5.16)$$

From (5.16), the following general properties for the non-causal transfer function $H_{opt}(s)$ may be derived:

- $H_{opt}(s)$ is proper. The degree of the numerator, $O[num(s)]$, equals the degree of the denominator, $O[den(s)]$, and it is double the order of the radiation transfer function:

$$O[den(s)] = O[num(s)] = 2O[a(s)] = 2n. \quad (5.17)$$

- $H_{opt}(s)$ tends to a constant value at low and high frequencies:

$$\lim_{s \rightarrow +\infty} H_{opt}(s) = \lim_{s \rightarrow 0} H_{opt}(s) = \frac{1}{2K_v}. \quad (5.18)$$

In practice, the friction coefficient, K_v , can assume different values at different frequencies, so that the two limits in (5.18) are not necessarily equivalent.

- If there is no friction, that is $K_v = 0$, the transfer function $H_{opt}(s)$ is not proper and has a pole at $s = 0$:

$$K_v = 0 \quad \Leftrightarrow \quad \begin{cases} O[num(s)] = O[den(s)] + 1 = 2n \\ \lim_{s \rightarrow +\infty} H_{opt}(s) = +\infty \\ \lim_{s \rightarrow 0} H_{opt}(s) = +\infty \end{cases} \quad (5.19)$$

In practice, it may always be assumed that $K_v \neq 0$, so that a partial fraction expansion of (5.16), in the case of distinct poles, results in the following form:

$$H_{opt}(s) = \sum_{i=1}^n \left(\frac{R_i}{s - p_i} + \frac{-R_i}{s + p_i} \right) + \frac{1}{2K_f}, \quad (5.20)$$

where $p_i \in \mathbb{C}$ are the poles and $R_i \in \mathbb{C}$ are the correspondent residuals. Due to the real and even nature of the transfer function $H_{opt}(s)$, the poles appear in symmetric pairs about the origin and the correspondent residuals are of opposite sign. If the region of convergence is chosen to be the strip in the complex plane containing the $j\omega$ -axis, the correspondent non-causal impulse response will have the following general form:

$$h_{opt}(t) \approx \sum_{i=1}^n R_i e^{p_i t} u_1(t) + R_i e^{-p_i t} u_1(-t) + \frac{1}{2K_f} \delta(t), \quad (5.21)$$

where $u_1(t)$ is the unitary step function, null for $t < 0$ and unitary for $t \geq 0$, and $\delta(t)$ is the Dirac-delta function. Note how the impulse response, $h_{opt}(t)$, is an even function of time (and therefore non-causal), as expected from the inverse transform of an even and real function in the frequency domain. Note the presence of the approximation symbol in equation (5.21), which has been introduced to clarify that such analytical expression is only calculated from a finite-order approximation (in the Laplace domain) of the radiation dynamics.

Ultimately, following the approach based on the approximation of the system's radiation with a finite-order linear system, it is possible to derive an analytical expression for the non-causal impulse response of interest. The accuracy of the result depends on the accuracy of the identification (related to the order, n , and to the appropriateness of the model structure) and to any numerical error that may arise during the procedure, in particular in the inversion of the radiation to determine $H_{opt}(s)$, in (5.11), and in the calculation of the residuals for the partial fraction expansion, as from (5.20). Note that the radiation function of a floating structure, as discussed in Section 3.3, typically, has a resonant behavior, in the sense that it assumes very large values in a restricted range of frequencies, while it goes to zero outside this range. Such resonant characteristic may introduce significant errors in the inversion and partial fraction expansion, which represent poorly-posed numerical problems.

Non-causal kernel calculation from IDFT

The non-causal transfer function of interest, $H_{opt}(\omega)$, defined in (5.5), is only known, numerically, for some frequencies ω_i , at which the radiation impedance, $H_r(\omega)$, is estimated from some hydrodynamic software (refer to the discussion in Section 3.3):

$$H_{opt}(\omega_i) = \frac{1}{2\Re\{H_r(\omega_i)\} + 2K_f} \quad i = 1, \dots, N_r. \quad (5.22)$$

As an alternative to the identification of $H_r(\omega)$ and the Laplace inversion, the non-causal kernel function $h_{opt}(t)$ can be determined numerically using the IDFT.

One main issue, here, is that $H_{opt}(\omega)$ does not go to zero, in general, at infinite frequency, as also analytically shown in (5.18). An impulse response determined numerically, by means of discrete-time Fourier inversion, will therefore be affected by distortion due to aliasing. In particular, the resulting impulse response function would represent a system with transfer function which equals (5.22) up to $\omega = \omega_{N_r}$ and 0 for $\omega > \omega_{N_r}$ [62]. Inaccuracies at high frequencies would mostly affect the behavior of $h_{opt}(t)$ near the time $t = 0$, where the values of $h_{opt}(t)$ are likely to be most significant.

The distortion from aliasing, however, is easily overcome by noting, directly from (5.22), that:

$$\lim_{\omega \rightarrow \infty} H_{opt}(\omega) = \frac{1}{2K_v}, \quad (5.23)$$

since the radiation resistance, $B(\omega)$, goes to zero for infinite frequency [71].

A transfer function:

$$K_{opt}(\omega) = H_{opt}(\omega) - \frac{1}{2K_v}, \quad (5.24)$$

can be defined such that:

$$\lim_{\omega \rightarrow \infty} K_{opt}(\omega) = 0. \quad (5.25)$$

From the linearity of the Fourier transform, and from (5.8), the impulse response, $h_{opt}(t)$, is given by:

$$h_{opt}(t) = \mathcal{F}^{-1} \{K_{opt}(\omega)\} + \mathcal{F}^{-1} \left\{ \frac{1}{2K_v} \right\} = \mathcal{F}^{-1} \{K_{opt}(\omega)\} + \frac{1}{2K_v} \delta(t) \quad (5.26)$$

The IDFT can then be applied with no problems to $K_{opt}(\omega)$, yielding the following kernel function:

$$k_{opt}(t) = \mathcal{F}^{-1} \{K_{opt}(\omega)\}. \quad (5.27)$$

Note the similarity of (5.26) with (5.21), where the constant $1/2K_v$, giving rise to an impulse at $t = 0$, is separate from the rest of the impulse response function.

Note, also, that it is possible to obtain any desired time resolution, T_s , for the impulse response $k_{opt}(t = kT_s)$, by just zero-padding $K_{opt}(\omega_i)$ up to a frequency $\omega_N = \pi/T_s$. This would not

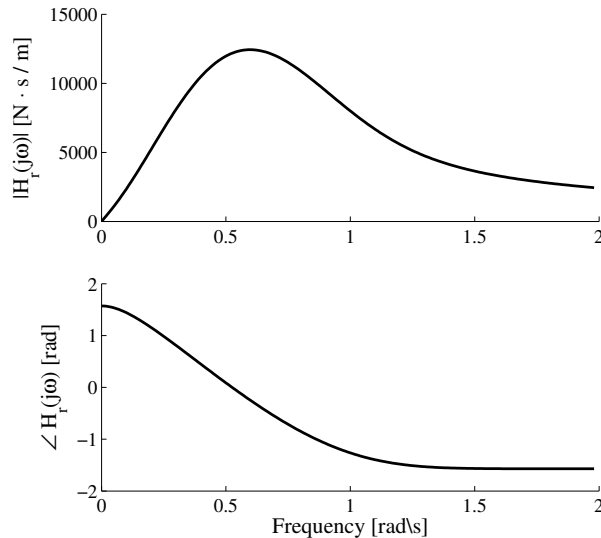


Figure 5.2: Radiation impedance, after the singularity at infinite frequency is removed, namely $H_r(j\omega) = Z_r(j\omega) - j\omega M_\infty$, of a heaving cylinder with radius $R = 5$ m, draught $h = 20$ m, height $H = 25$ m and mass $m = 1.62 \times 10^6$ Kg.

deteriorate the accuracy of the resulting impulse response function, as the frequency content of $K_{opt}(\omega)$ is practically zero at high frequencies (within a certain degree of accuracy).

Adopting the numerical approach based on the IDFT, as just described, has the advantage of reducing the complexity of the procedure and therefore the possible sources of approximation and error (identification and partial fraction expansion not required). The main drawback is that the result is not an explicit time-domain function, expressed as a combination of natural modes, which can be useful for analysis purposes.

A Numerical example

In order to exemplify and compare the two different possible approaches, that is identification and analytical Laplace inversion or numerical IDFT, the non-causal impulse response, $h_{opt}(t)$, is calculated for a specific floating system in one degree of freedom. The floating body consists of a heaving cylinder, whose geometry and radiation response, $H_r(\omega)$, are specified in Fig. 5.2. The radiation problem was solved through the hydrodynamic software WAMIT [59], as described in Section 3.3.1.

Following the methodology outlined in Section 3.3.3, three transfer functions, $H_r^{(n)}(s)$, of order $n = 4, 6, 8$ are identified in order to model the radiation [71]. Figure 5.3 compares the lowest-order approximation, $H_r^{(4)}(s = j\omega)$, with the data, $H_r(\omega)$, and the approximation is clearly very accurate in the region $[0.3 \ 1]$ rad/s, where the significant part of the radiation spectral content is contained. Higher order approximations are not shown as the difference in accuracy cannot be visually noticed.

A finite-order approximation of the non-causal transfer function $H_{opt}(\omega)$ can then be analytically calculated, by using (5.11) and (5.12), for each of the three approximations of the radiation, resulting in $H_{opt}^{(n)}(s)$, with $n = 4, 6, 8$. The analytical approximations and the numerical values are

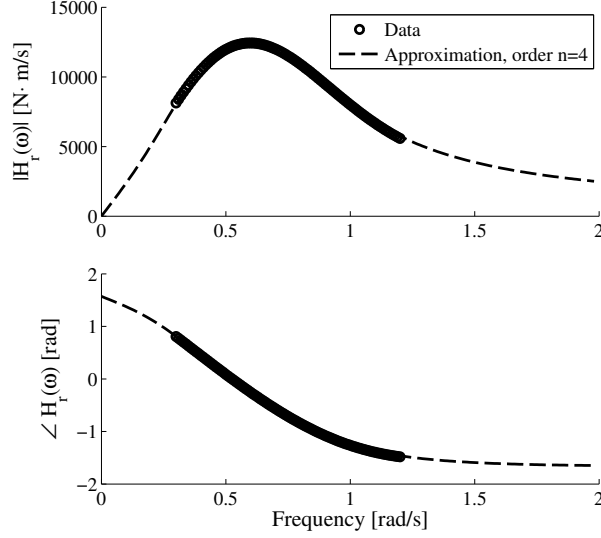


Figure 5.3: Finite-order approximation of the radiation of the floating cylinder, shown in Fig. 5.2. The order of the approximation is $n = 4$.

compared in Fig. 5.4, where also the relative error,

$$\epsilon^{(n)}(\omega) = \frac{|H_{opt}(\omega) - H_{opt}^{(n)}(s = j\omega)|}{|H_{opt}(\omega)|}, \quad (5.28)$$

is shown. The behavior of the error, $\epsilon^{(n)}(\omega)$, indicates how very small differences in the accuracy of the radiation identification may produce quite different accuracies in the approximation of the transfer function $H_{opt}(\omega)$, due to the inversion of the radiation. In particular, significant relative errors for the low-order approximations, $n = 4$ and $n = 6$, appear at lower and higher frequencies than for the region $[0.3 \quad 1]$ rad/s, where the identification was focused.

The optimal, non-causal function, $H_{opt}(\omega)$, can also be calculated numerically from the data, by using (5.22). After removing the singularity at infinite frequency, $1/2K_v$, based on (5.26), the IDFT can directly be utilised for the calculation of a numerical kernel, $k_{opt}(t)$, that only differs from the required $h_{opt}(t)$ for an impulse centred at $t = 0$. Fig. 5.5 shows the DFT, $K_{opt}(\omega)$, defined in the interval $[-100\pi, +100\pi]$, after zero-padding, that will produce a kernel $k_{opt}(t)$ with sampling period $T_s = 0.01$ s.

Let us now analyse the differences, when the kernel function of interest, $h_{opt}(t)$, is calculated analytically from the Laplace inversion of $H_{opt}^{(n)}(s)$, or numerically from the IDFT. From the fraction expansion of the transfer functions in the Laplace domain, $H_{opt}^{(n)}(s)$, the impulse responses $h_{opt}^{(n)}(t)$ are calculated, based on equation (5.13). Alternatively, the impulse response $h_{opt}(t)$ is also determined from the IDFT of $H_{opt}(\omega)$, shown in Fig. 5.5.

The impulse responses obtained using the two approaches are compared in Fig. 5.6, where the impulse at time $t = 0$, of amplitude $0.5/K_v$, is not shown. It is interesting to note that the higher the order of the identification, the closer the solution gets to the numerical kernel calculated from IDFT. The main inaccuracies that affect the approach with system identification are focused around $t = 0$, and are mostly due to the presence of fake natural modes that try to model the real

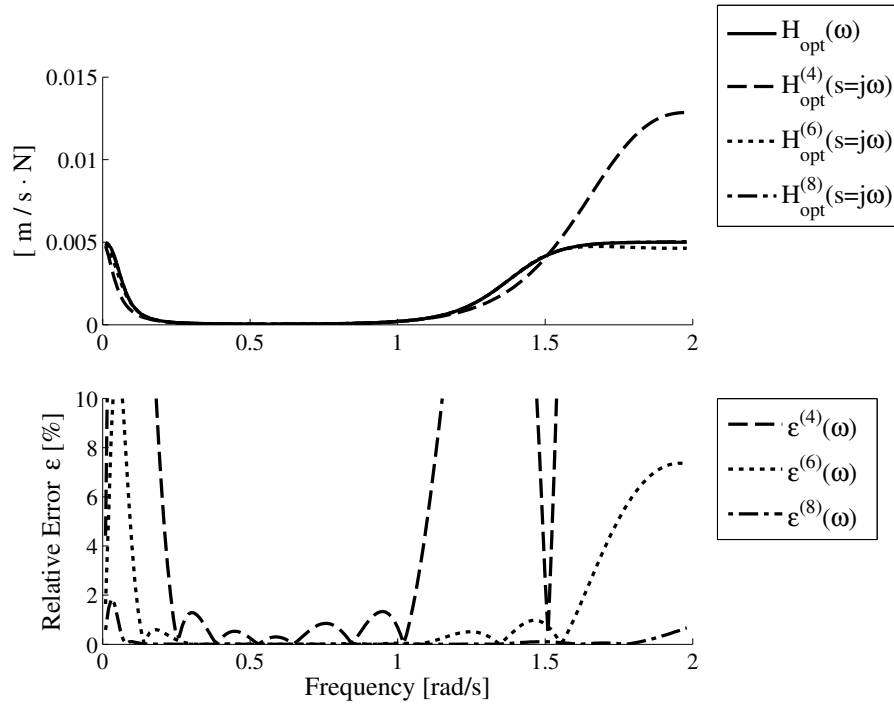


Figure 5.4: Error produced by finite-order approximation of the optimal, non-causal function $H_{opt}(\omega)$.

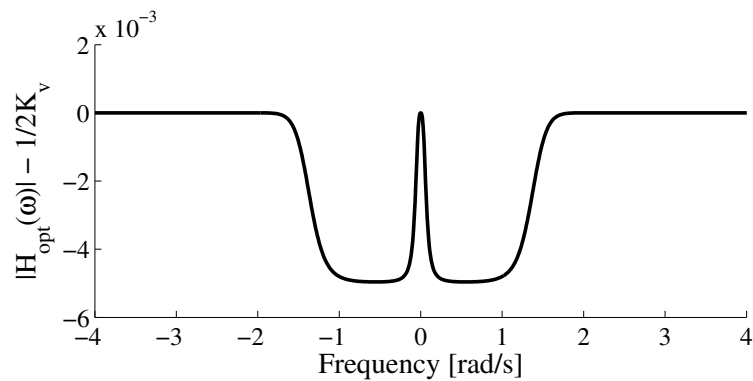


Figure 5.5: DFT of $K_{opt}(\omega) = H_{opt}(\omega) - 1/2K_v$, zero-padded up to 100π so to obtain a time resolution $T_s = 0.01$ s. For illustration purposes, only values up to 4 rad/s are shown here.

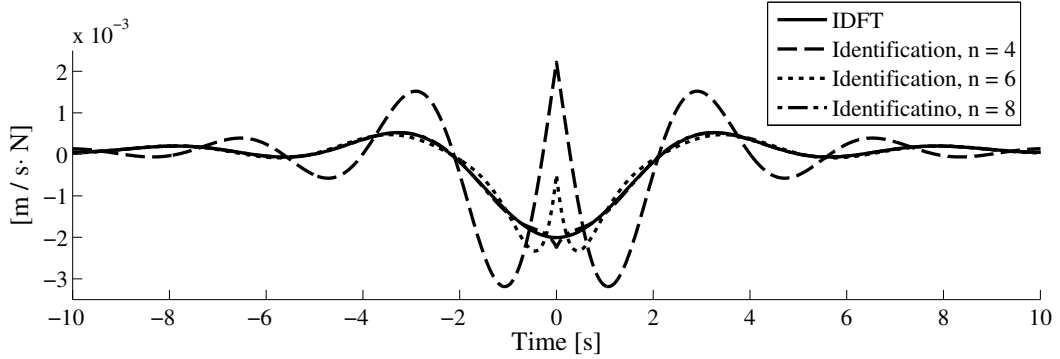


Figure 5.6: Approximations of the non-causal kernel function corresponding to $H_{opt}(\omega)$, using system identification and Laplace inversion, as opposed to numerical IDFT.

impulse at $t = 0$.

This example highlights the fact that the direct IDFT better suits our purpose of analysing the non-causality of $h_{opt}(t)$. The possibility to zero-pad the frequency response allows the achievement of any desired time resolution. On the other hand, while it would be very nice to have an analytical expression of the kernel, based on finite-order approximation and Laplace inversion, the inaccuracies due to inversion of a transfer function and partial fraction expansion may give misleading results. As a consequence, the quantification of the prediction requirements, in the remainder of this Chapter, is based only on the numerical knowledge of $h_{opt}(t)$.

5.3 Quantification of the prediction requirements

Once the non-causal kernel, $h_{opt}(t)$, is known, the optimal velocity of the system can be calculated, based on (5.3) and (5.8), as:

$$v_{opt}(t) = \int_{-\infty}^{+\infty} h_{opt}(\tau) f_{ex}(t - \tau) d\tau, \quad (5.29)$$

where the non-causality of the kernel function requires that the excitation force is known infinitely far into the future. Based on the block scheme of Fig. 5.1, the velocity calculated from (5.29) can be imposed on the WEC, through a feedback controller, resulting in maximum wave energy absorption.

The impulse response, $h_{opt}(t)$, as also numerically confirmed by Fig. 5.6, is, in general, an even function decreasing asymptotically towards zero, so that less and less weight is put on future (as well as past) values of the excitation force. In particular, it may be argued that the influence of future (and past) values of the excitation force on the optimal velocity, and ultimately on the wave power extraction, is negligible beyond a certain time horizon.

The required prediction horizon is determined from a range of approximations of the optimal

velocities, calculated from the integral in (5.29), truncated to an interval $[-L, +L]$:

$$v_{opt}^L(t) = \int_{-L}^L h_{opt}(\tau) f_{ex}(t - \tau) d\tau, \quad (5.30)$$

so that future values for the excitation force only up to $f_{ex}(t + L)$ are included. Note that the causal part of the integral is also truncated to maintain the evenness of the impulse response. In the extreme case of $L = 0$, the integral in (5.30) becomes causal and no future values of the excitation force are required. In order to keep the focus on the prediction requirements, ideal knowledge of the future excitation force is assumed, for the present.

The velocity $v_{opt}^L(t)$ is then ideally imposed onto the system. In particular, the low-level controller of Fig. 5.1 implements a direct feedforward action:

$$f_u^L(t) = (m + m_\infty) \dot{v}_{opt}^L(t) + \int_0^{+\infty} h_r(\tau) v_{opt}^L(t - \tau) d\tau + K_v v_{opt}^L(t) + K_b \int_{-\infty}^t v_{opt}^L(\tau) d\tau - f_{ex}(t), \quad (5.31)$$

directly calculated from the time-domain equations of motion, given in (3.143). As previously noted, the interest here is focussed on the analysis and quantification of the prediction requirements, rather than on the implementation of the controller. In practice, a pure feedforward action like that in (5.31) could give rise to unwanted behavior in the case of inaccuracies in the model and the excitation force predictions. The design of the velocity-tracking loop is dealt with in Chapter 8.

The performance of the WEC, in terms of power absorption, that is achieved from the use of (5.30), given the future horizon L , is measured by the RCW:

$$RCW(L) = \frac{P_u(L)}{P_w \cdot D}. \quad (5.32)$$

The RCW, defined in (5.32), represents the ratio of the average absorbed power, $P_u(L)$, to the total wave power incident over the width of the device, that is the average power per unit of wave front, P_w , defined in (3.45), multiplied by the width of the system, D (e.g. the diameter in the case of a cylinder). The average absorbed power, $P_u(L)$, depends on the considered future horizon, L , and is calculated as:

$$P_u(L) = \frac{1}{T} \int_0^T v_{opt}^L(t) f_u^L(t) dt, \quad (5.33)$$

where T is a finite simulation time.

Intuitively, it is expected that $RCW(L)$ increases when larger values of L are considered, but only up to a critical future horizon, beyond which the power gain from considering extra future information of the excitation force is negligible. Such quantification gives an idea of the *non-causality* of complex-conjugate control applied to the floating system, because we expect that the critical future horizon gets smaller if the non-causal impulse response $h_{opt}(t)$ goes more quickly to zero.

From well known relations between (stable) impulse response functions and corresponding transfer functions, the decay towards zero is dominated by an exponential related to the dominant time constant of the system, specifically the lowest frequency pole. Due to the presence of the radi-

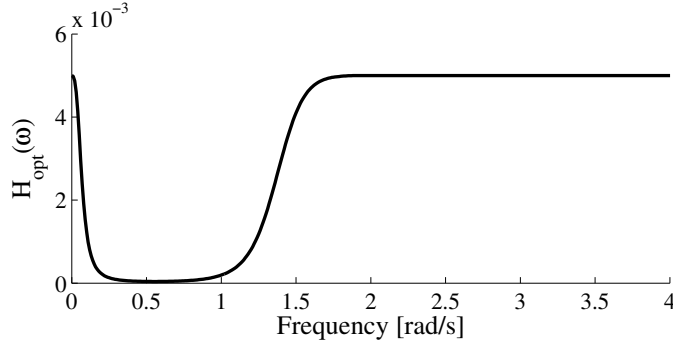


Figure 5.7: Non-causal transfer function, $H_{opt}(\omega)$, between excitation force and optimal velocity. It is a real and even function of the frequency.

ation resistance $B(\omega)$, $H_{opt}(\omega)$ is only known numerically for some frequencies, and an explicit finite-order representation is not immediately available. Besides, from the discussion in Section 5.2.1, numerical inaccuracies due to approximation and inversion would advise against the use of a finite-order approximation of $H_{opt}(\omega)$. From the behavior shown in Fig. 5.7, valid for systems with a single-peaked radiation function, it is straightforward to identify the lowest frequency pole. The function $H_{opt}(\omega)$ can, in fact, be seen as a low-pass filter cascaded with a high-pass filter, where the attenuation band corresponds to the resonance band of the system's radiation function. The lowest frequency pole, at ω_1 , can be estimated as the cut-off frequency (at -3 dB) of the low-pass filter.

The time constant $\tau_1 = 1/\omega_1$ is the dominant parameter that influences the decay to zero of $h_{opt}(t)$, and consequently the non-causality of the control action. As an example, Fig. 5.8 shows the relation between τ_1 and ω_1 for two different floating cylinders. Note that, in Fig. 5.8, the focus is put on the function $K_{opt}(\omega)$ and on the corresponding kernel, $k_{opt}(t)$, rather than on $H_{opt}(\omega)$ and $h_{opt}(t)$. Based on (5.26), however, the characteristics of non-causality of $h_{opt}(t)$ and $k_{opt}(t)$ are the same, since they only differ by an impulse at time $t = 0$, related to the singularity, for $\omega \rightarrow \infty$, of $H_{opt}(\omega)$.

5.3.1 Manipulation of control for reduction of requirements

The optimal conditions of complex-conjugate control, given in (5.2) and (5.3), do not rely on the spectral distribution of the excitation force. The optimal power transfer from the waves to the system, as discussed in Section 4.1, is found independently of the excitation. A critical evaluation of the non-causality of $H_{opt}(\omega)$, however, which also takes into account the typical frequency distribution of the excitation force, could offer the possibility of manipulating its shape such that the prediction requirements are reduced.

For a number of reasons, the wave excitation force is always contained within the stop band of $H_{opt}(\omega)$, in relation to Fig. 5.7:

- Waves do not appear at frequencies below $0.2 - 0.3\text{ rad/s}$ (wave periods above $30 - 40\text{ s}$).
- Waves at higher frequencies than the attenuation band of $H_{opt}(\omega)$ are filtered out by the

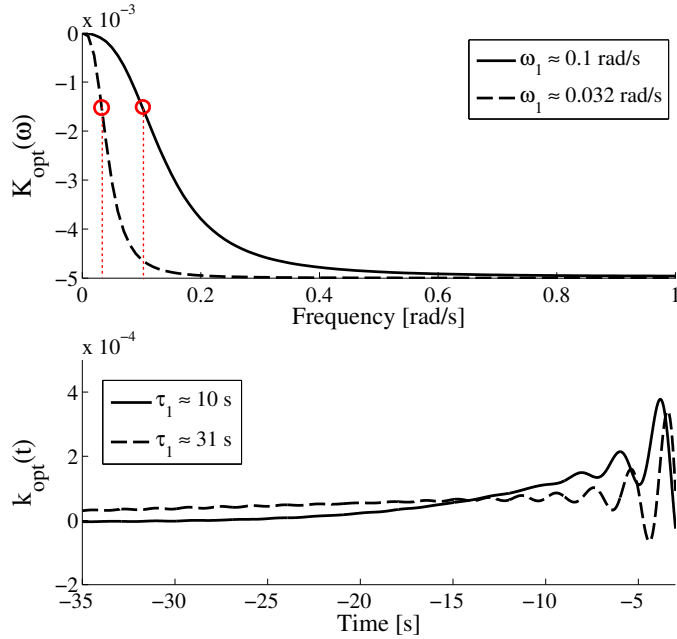


Figure 5.8: Relation between lowest frequency pole and non-causality of the impulse response. $K_{opt}(\omega)$ and $k_{opt}(t)$ are calculated for two heaving cylinders.

excitation transfer function, $H_{ex}(\omega)$, based on (3.114). There exists, in fact, a correspondence between the radiation and excitation bandwidth, based on the Haskind relation [21], [6].

- If the system is well-suited to the location of deployment, its radiation response shall roughly match most of the sea states, and this corresponds to the attenuation band of $H_{opt}(\omega)$, as discussed in Section 5.3.

Based on these considerations, it may be argued that the velocity generation, in (5.29), will mostly work at frequencies within the attenuation band of $H_{opt}(\omega)$ (0.4-1 rad/s in Fig. 5.7). As a consequence, there exists the possibility of manipulating the shape of $H_{opt}(\omega)$ in order to reduce its non-causality, while at the same time maintaining its effectiveness in most sea conditions.

In Section 5.3, the non-causality was related to the time constant τ_1 , which is the reciprocal of the lowest frequency pole of $H_{opt}(\omega)$. A possible intuitive manipulation may therefore consist of lowering the gain of $H_{opt}(\omega)$ outside the attenuation band, where its input (the excitation force) will not usually appear. This would move the first pole towards higher frequencies, thus reducing the time constant τ_1 . As an example, consider Fig. 5.9(a), where the original $H_{opt}(\omega)$ is modified to a new function termed $H_{red}(\omega)$. As a result, the impulse response $h_{red}(t)$, which is still real and even, decays much more quickly to zero than $h_{opt}(t)$, as shown in Fig. 5.9(b).

Note that the modification proposed here is not rigorous, in any sense, and it is only based on qualitative considerations. It is not within the scope of this Chapter to find the best re-shaping of $H_{opt}(\omega)$ which minimises the non-causality and at the same time maximises the approximation of the optimality condition, within a chosen frequency band. Some numerical examples, in Section 5.4.3, however, will serve as a demonstration of the potential benefits that simple modifications of $H_{opt}(\omega)$ may have on the reduction of the prediction requirements.

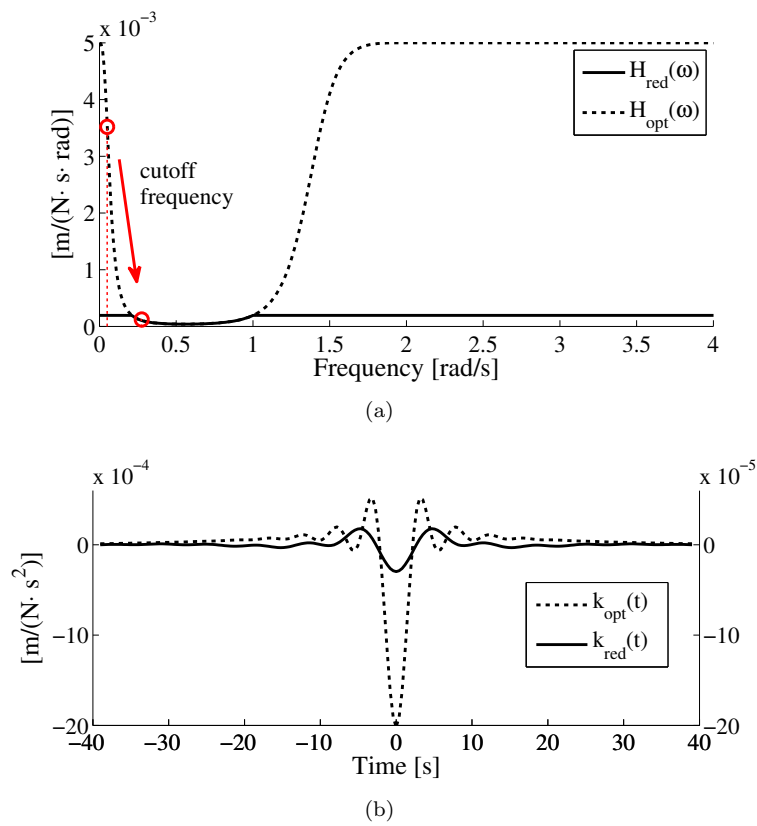


Figure 5.9: Manipulation of $H_{opt}(\omega)$, resulting in $H_{red}(\omega)$, such that the lowest frequency pole is moved rightward, thus decreasing the dominant time constant of the correspondent impulse response.

5.3.2 Causal approximation with a second-order model

A closer analysis of the non-causal function relating the excitation force to the optimal velocity, namely $H_{opt}(\omega)$, from Fig. 5.7, reveals that, within the range of frequencies of interest, discussed in Section 5.3.1, the function is quite flat. A constant approximation of $H_{opt}(\omega)$ could, therefore, be quite close to optimal in most sea states. At the same time, a constant approximation would completely remove the non-causality!

Note that a causal approximation, similar to what is discussed here, was also proposed in [97] and [96]. A formal discussion of the quality of the approximation and of its effectiveness, in terms of power capture, compared to the ideal solutions, for different systems and over different sea states was, however, not given.

In this Section, the constant approximation of the function $H_{opt}(\omega)$ is based on a reduction of the model of a WEC to second order, as also done in [96] for the AWS converter. The optimal condition relating excitation force to velocity, in (5.3), is reduced to a simple proportional relation, from which the constant approximation is derived.

Following identification of the floating system's radiation, adhering to the methodology described in Section 3.3.3, a transfer function approximating the dynamics of the WEC is available:

$$\frac{V(s)}{F_{ex}(s) + F_u(s)} = \frac{1}{Z_i(s)}, \quad (5.34)$$

as also proposed in (5.9), in Section 5.2.1, for the finite-order approximation of the non-causal function $H_{opt}(\omega)$.

The finite-order SISO system of (5.34) is equivalently described by state-space equations of the type:

$$\begin{cases} \dot{x}(t) = Ax(t) + B[f_{ex}(t) + f_r(t)] \\ v(t) = Cx(t) \end{cases}, \quad (5.35)$$

where $x(t)$ is a state vector of dimension equal to the order of the transfer function in (5.34) (2+ the order of the radiation, if the state-space realisation is minimal). Each component of the state vector, $x(t)$, can be associated with a positive real quantity, called the Hankel singular value, that quantifies its energy [72], as explained in more detail in appendix A. State components with a relatively low Hankel singular value can then be removed from the system with no or little effect on the overall dynamics.

Now, suppose that the order of the system, that is the dimension of A or the order of $1/Z_i(s)$, is n , and that the Hankel singular values are arranged in descending order, $\sigma_1 \geq \sigma_2 \geq \dots \geq \sigma_n \geq 0$, each of them associated with a particular component state of the system. If the floating system is expected to be dominated by a second-order dynamics, then the value of the first two singular values should be much larger than the value of the other singular values or, equivalently, $\sigma_2 \gg \sigma_3$. If that is the case, any state component other than the two associated with σ_1 and σ_2 may be neglected with little effect on the system's response. As an example, the model reduction procedure is applied to a range of four floating cylinders, whose geometries are specified in table 5.1. The cylinders all have the same mass distribution and radius, but different height. The ratio σ_2/σ_3 ,

cylinder	R [m]	h [m]	m [Kg]	σ_2/σ_3
1	5	6	2.6×10^5	230
2	5	8	3.9×10^5	464
3	5	15	1×10^6	1336
4	5	20	1.3×10^6	3204

Table 5.1: Reduction to second-order model, applied to some heaving cylinders. R is the radius, h is the draught and m is the submerged mass.

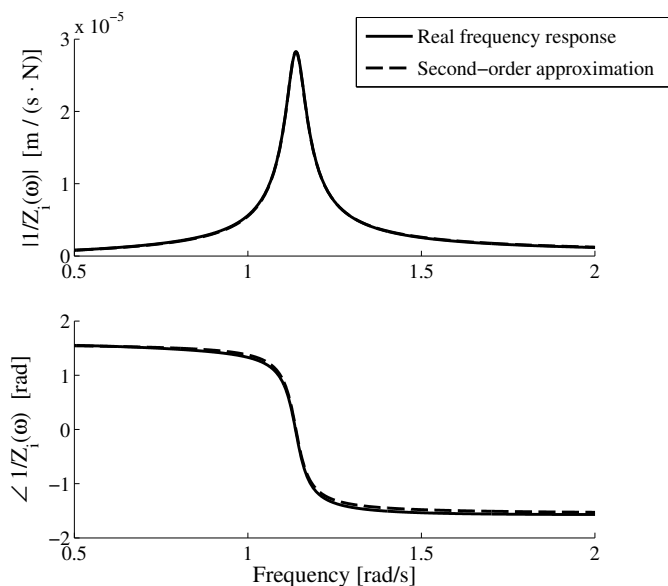


Figure 5.10: Comparison of real frequency response, $1/Z_i(\omega)$ against second-order approximation, for cylinder 1 of Table 5.1.

which determines how well the system is described with a second-order dynamics, is also shown in table 5.1. It is clear how the ratio increases with the increasing height of the cylinder, which means decreasing bandwidth, although in general it stays quite large (minimum is 230). In Fig. 5.10, the frequency response of the second-order model of cylinder 1, that is the one showing the lowest ratio $\sigma_2/\sigma_3 = 230$, is shown against the real frequency responses calculated from the hydrodynamic software.

Once a second-order model has been identified, the floating system in (5.1) is approximated by the following frequency domain model:

$$V(\omega) = \frac{b_1(j\omega)}{(j\omega)^2 + a_1(j\omega) + a_2} [F_{ex}(\omega) + F_u(\omega)], \quad (5.36)$$

which, in the time domain, using simple properties of the Fourier transform, corresponds to:

$$\hat{M}\dot{v}(t) + \hat{B}v(t) + \hat{K}_s \int_0^\infty v(\tau) d\tau = f_{ex}(t) + f_u(t), \quad (5.37)$$

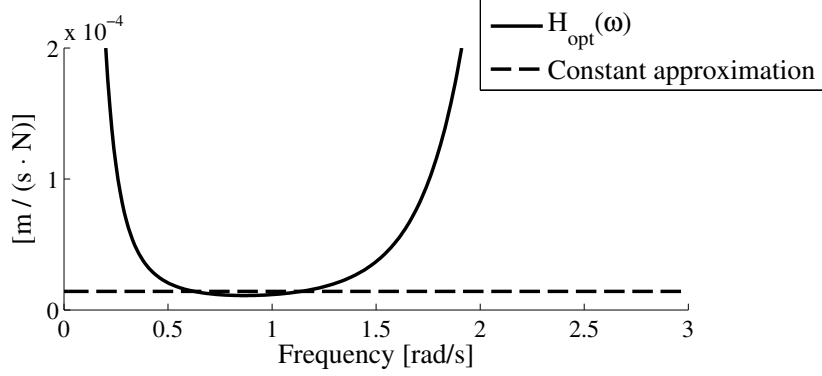


Figure 5.11: Velocity-generation law, $V(\omega)/F_{ex}(\omega)$, for reactive control calculated for the full system and a second-order approximation model (constant over frequency). The system is cylinder 2 of Table 5.1.

where:

$$\hat{M} = \frac{1}{b_1} \quad \hat{B} = \frac{a_1}{b_1} \quad \hat{K}_s = \frac{a_2}{b_1}. \quad (5.38)$$

The parameters a_1, a_2, b_2 are directly related to the state space matrices (A, B and C) in (5.35), following the reduction to a second-order model.

Note that the heaving cylinder in water approximately behaves as a mass-spring-damper mechanical oscillator with mass \hat{M} , damping \hat{B} and spring coefficient \hat{K}_s , as discussed in Section 3.2.4. The fluid memory effect, modelled by the frequency dependance of the radiation, has disappeared and the radiation impedance has been reduced to a constant. If reactive control is solved for such a second-order system, it is straightforward to show how the optimal conditions, given in (5.3) and (5.2), reduce to:

$$V(\omega) = \frac{1}{2\hat{B}} F_{ex}(\omega) \quad (5.39)$$

$$F_u(\omega) = - \left[\frac{1}{2} - j\omega \frac{\hat{M}}{2\hat{B}} - \frac{\hat{K}_s}{j\omega 2\hat{B}} \right] F_{ex}(\omega). \quad (5.40)$$

For a second-order oscillating system, maximum wave energy extraction is realised if the velocity, from (5.39), is simply proportional to the excitation force and if the optimal force, based on (5.40), is related to the excitation force through a classical PID relationship. As already mentioned in Section 5.2, the focus in this study is on the condition in (5.39), relating the velocity to the excitation force.

After reduction to second order, the implementation of reactive control is perfectly realisable, because the reference-generation logic needs simply to implement the following zero-order transfer function:

$$\hat{H}_{opt}(\omega) = \frac{1}{2\hat{B}}, \quad (5.41)$$

as opposed to the non-causal $H_{opt}(\omega)$ of (5.41). Such a causal realisation of reactive control is

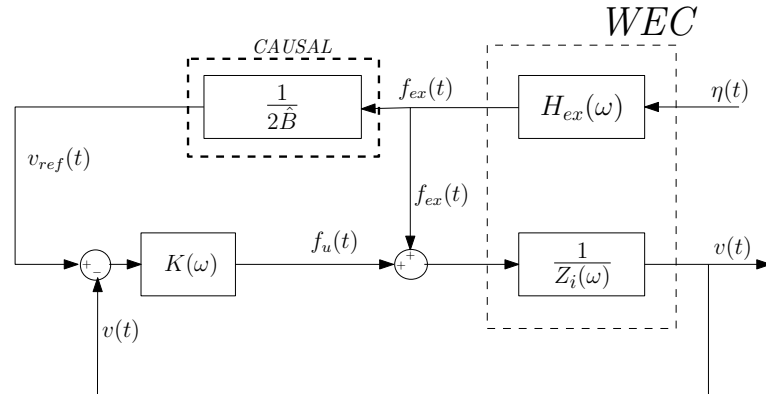


Figure 5.12: Real-time implementation of reactive control as a velocity-follower. For a second-order system, the reference generation is a purely proportional block, which is *causal* and realisable.

illustrated in the block diagram of Fig. 5.12.

More interestingly, the constant $1/2\hat{B}$, obtained from the model reduction, is an approximation of the flat part of $H_{opt}(\omega)$ around the resonance frequency of the device, as shown in Fig. 5.11. The approximation is close to the real transfer function in the frequency range $[0.6, 1.2]$ rad/s while is quite far from ideal outside such a range. The wave excitation force, however, is most likely to occur within the specified range, for the reasons outlined in Section 5.3.1.

5.4 Results

5.4.1 Wave data and systems geometry

The quantification of the prediction requirements, according to the methodology outlined in Section 5.3, is based on numerical simulations carried out with real wave measurements. The wave data was provided by the Irish Marine Institute and comes from real observations collected from a data buoy deployed off the West coast of Ireland, at the Atlantic Marine Energy Test Site (AMETS), west of Belmullet, county Mayo, at approximately $54^\circ 13' N$, $10^\circ 8' W$. The data consists of two consecutive 30 minutes sets for each hour, sampled at 1.28 Hz, covering the year 2010. Figure 5.13 shows the distribution of peak frequency (peak of the wave spectrum), ω_p , and significant wave height, H_s , calculated from (3.49) and (3.46), so to give an idea of the wave climate at the location.

For the current calculations, a number of data sets has been selected among all the ones available. In particular, all the sea states with a peak frequency approximately equal to values that range from 0.5 rad/s to 1 rad/s, with a frequency interval of 0.05 rad/s, were picked up. The distribution of peak frequency and significant wave height of such data sets is highlighted in Fig. 5.13 and the number of data sets available for each peak frequency is indicated in Table 5.2.

The wave energy conversion system consists of a bottom-referenced floating body constrained to move in the heave direction only, as modelled in Section 3.3.1. Both cylinders and spheres are

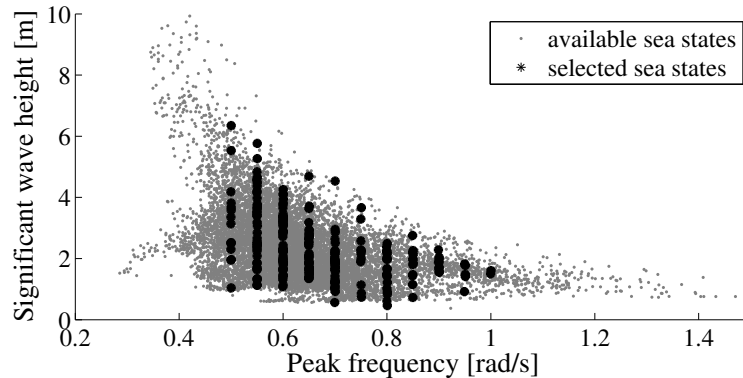


Figure 5.13: Distribution of peak (of energy) frequency, ω_p , and significant wave height, H_s , collected from a data buoy in Belmullet ($54^\circ 13' N$, $10^\circ 8' W$) over the year 2010. The data sets selected for the numerical simulations are highlighted.

ω_p [rad/s]	0.5	0.55	0.6	0.65	0.7	0.75	0.8	0.85	0.9	0.95	1.0
Num	15	40	52	37	31	11	19	12	9	5	2

Table 5.2: Number of data sets available per each peak frequency, as from Fig. 5.13.

considered, with varying values for the radius and the height (in the case of the cylinder). The geometry of the spheres and cylinders are specified in Table 5.3, where R : radius; h : draught at rest; m : mass; ω_0 : resonance frequency; $\Delta\omega$: bandwidth of the radiation resistance, $B(\omega)$; τ_1 : dominant time constant of the kernel function $h_{opt}(t)$, calculated as proposed in Section 5.3.

Note that, as the radius of the sphere increases, the bandwidth and the resonance frequency get smaller, while at the same time the dominant time constant of the non-causal impulse response, $h_{opt}(t)$, increases. From the analysis of the prediction requirements, it is therefore expected that bigger spheres (bigger τ_1) will require predictions of the excitation force longer into the future for an effective realisation of reactive control. For the cylinders, two parameters specify the geometry (the density is kept constant): the radius and the height/draught. From Table 5.3, it appears how the time constant τ_1 is mainly affected by the radius, with only slight changes for different heights. It would be expected, therefore, that heaving cylinders of different sizes, but with similar radii, would be equally (or similarly) demanding in terms of wave excitation force prediction.

5.4.2 Prediction requirements

The proposed WECs, whose geometry was specified in Section 5.4.1, were simulated over the selected set of real wave records, detailed in Fig. 5.13 and Table 5.2. Reactive control was implemented, as described in Section 5.3, based on the block scheme of Fig. 5.1. The system ideally follows the reference velocity calculated from the convolution of the non-causal kernel $h_{opt}(t)$ with the excitation force, as given in (5.30). The impulse response function $h_{opt}(t)$ was determined from $H_{opt}(\omega)$, by means of the IDFT, according to the methodology outlined in Section 5.2.1. The future values of the excitation force are assumed to be perfectly known. The performance, in terms of energy capture, was then assessed for each value, L , of the future horizon considered in

	R [m]	h [m]	m [kg $\times 10^5$]	ω_0 [rad/s]	$\Delta\omega$ [rad/s]	τ_1 [s]
S_1	4	4	1.38	1.63	1.60	10.87
S_2	5	5	2.70	1.43	1.45	14.16
S_3	6	6	4.66	1.32	1.37	18.62
C_1	3	4	0.93	1.40	1.03	10.00
C_2	3	8	1.86	1.08	0.79	9.97
C_3	3	12	2.80	0.92	0.66	9.94
C_4	3	16	3.73	0.82	0.59	9.91
C_5	3	20	4.66	0.74	0.53	9.89
C_6	5	4	2.59	1.23	0.98	19.80
C_7	5	8	5.18	1.02	0.75	19.80
C_8	5	12	7.77	0.89	0.63	19.76
C_9	5	16	10.40	0.79	0.56	19.7
C_{10}	5	20	12.90	0.72	0.51	19.76
C_{11}	7	4	5.07	1.14	0.95	31.06
C_{12}	7	8	10.10	0.98	7.2	30.96
C_{13}	7	12	15.20	0.85	0.62	30.96
C_{14}	7	16	25.40	0.70	0.54	30.96
C_{15}	7	20	31.71	0.64	0.50	30.9

Table 5.3: Geometry of heaving buoys. C : cylinder; S : sphere.

the calculation of the velocity, as described in Section 5.3. In particular, for each system and sea state, the relative capture width, $RCW(L)$, was calculated from (5.32).

As mentioned in Section 5.3, it is expected that $RCW(L)$ tends towards an ideal maximum value while L increases. The asymptotic behavior of $h_{opt}(t)$ was shown to be dominated by a decreasing exponential with a time constant, named τ_1 , inversely proportional to the first cut-off frequency of the function $H_{opt}(\omega)$. Table 5.3 indicates the value of τ_1 for the selected spheres and cylinders. Ultimately, it would be reasonable to expect that systems with a larger time constant τ_1 would require knowledge of the excitation force longer into the future for the calculation of a reference oscillation velocity that permits the achievement of a RCW close to the ideal maximum.

Figure 5.14 shows the detail of $RCW(L)$, calculated for the three different spheres of table 5.3 over three different wave conditions, that are identified by the peak frequencies of 0.5, 0.75 and 1 rad/s. In any case, as obviously expected, the power capture increases when more and more future information about the wave excitation force is included in the calculation of the reference velocity. More interestingly, the curves approach the optimal RCW at different time horizons and, in particular, the prediction requirements are more demanding for systems with a larger time constant τ_1 . In addition, note how this behavior is not dependent on the specific sea state, but only on the system's properties, while the sea state has an obvious influence on the absolute value of the RCW . Note that the optimal value of RCW changes with the size of the device, in accordance with the general theory of axis-symmetric heaving buoys [1].

In order to have a more general assessment of the relation between prediction requirements and properties of the WEC, the average value of the forecasting horizon required to obtain a $RCW > 0$ was determined, and this is shown in Fig. 5.15 against the corresponding time constant τ_1 of the sphere. It is clear how the prediction requirements increase nearly linearly with the dominant time constant of the function $H_{opt}(\omega)$. The standard deviation of the prediction requirement for each

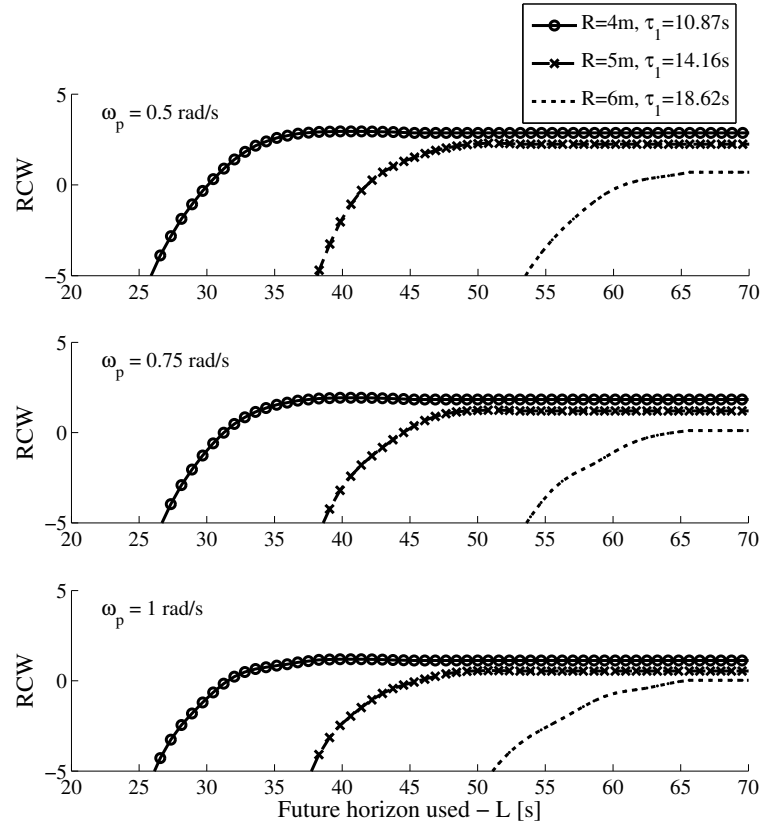


Figure 5.14: Performance of different spheres, achievable through complex-conjugate control when information of future excitation force, at different leading times, is included in the reference velocity calculation.

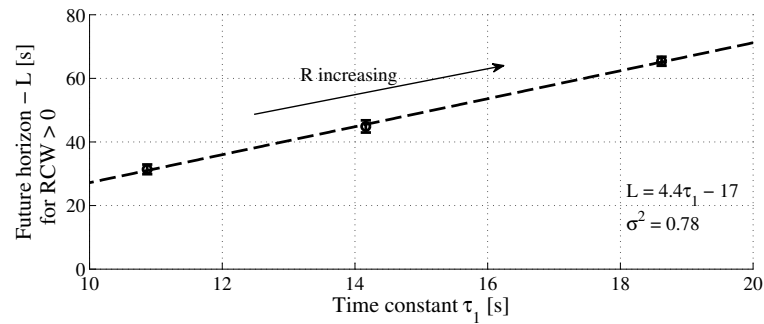


Figure 5.15: Average prediction horizon required by spheres with different values of τ_1 for the achievement of a positive RCW with complex-conjugate control.

device is also shown as the length of a bar centred about the mean value (the circle). Its value is generally small and this fact highlights the independence of the prediction requirements of the specific sea states (nearly 200 data sets were included in the calculations, as from table 5.2).

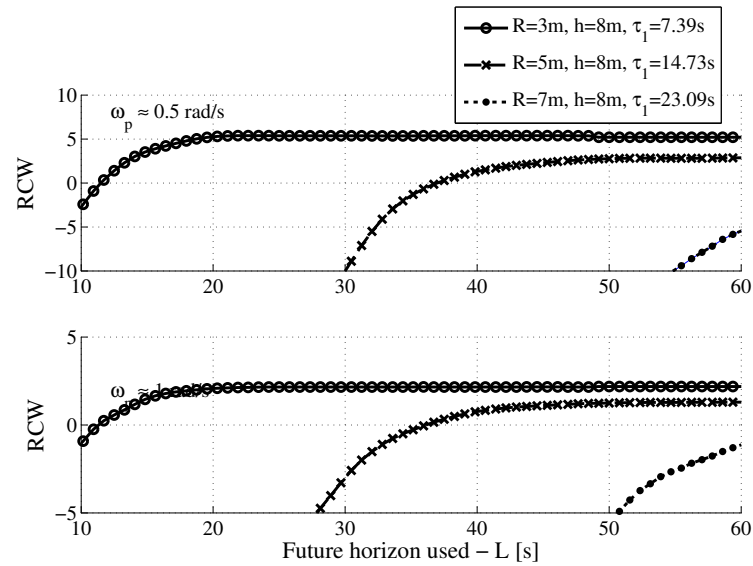
Regarding the other geometry considered in this study, the cylinder, Figures 5.16(a) and 5.16(b) show the details of $RCW(L)$, calculated over two particular sea states with peak frequency of 0.5 and 1 rad/s . Compared to the sphere, which is uniquely specified by the radius, the geometry of a cylinder is specified by two parameters. Figure 5.16(a) shows the results for three cylinders with same height and different radius are considered, while Fig. 5.16(b) shows the details of three specific cylinders with same radius but different heights. In Section 5.4.1, and particularly from table 5.3, it was noted how the time constant, τ_1 , of a cylinder is mainly affected by its radius. In fact, similarly to the results for the spheres, in Fig. 5.16(a), the performance of the control approaches the ideal value for future horizons whose length is directly proportional to τ_1 . Although the effect of the cylinder height on τ_1 is negligible, as shown in Table 5.3, Fig. 5.16(b) demonstrates that, however, the height has an actual effect on the prediction requirements. In particular, it seems that when the height increases the device is *less* demanding in terms of prediction.

A more general picture of the prediction requirements for cylinders is given in Fig. 5.17, where the distribution of the average and variance of the forecasting horizon, required for the achievement of a performance $RCW > 0$, is shown. The cylinders are parameterised on the base of their τ_1 , but the effects of changes in height are also highlighted.

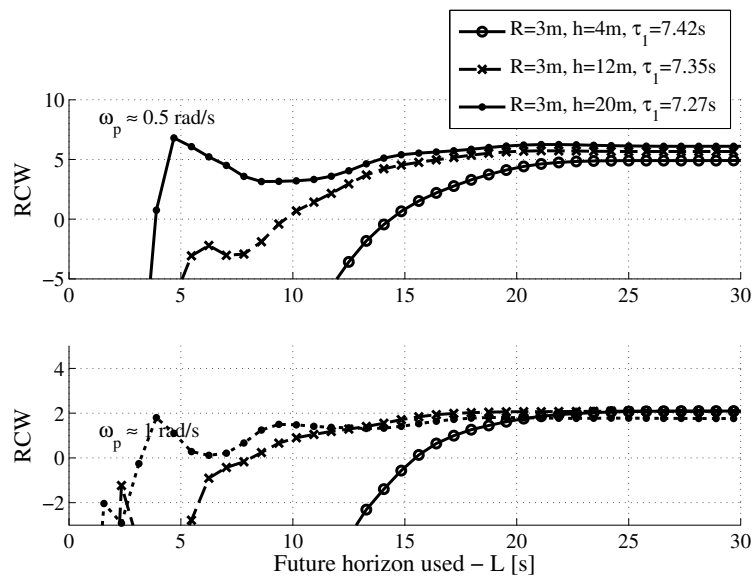
It would certainly be valuable if a more general property of the system, other than the cylinder height, may be linked to the prediction requirements, as in the case of the time constant τ_1 . If such a general property exists, it is likely to be a strong function of the radiation resistance. The radiation of a single-body floating system, such a sphere or cylinder in heave, has a general shape that resembles the response of a second-order harmonic mechanical oscillator, which is defined by a resonant frequency and a bandwidth. It is common to represent the bandwidth by means of the Q factor, closely related to the number of oscillations over which the amplitude of the oscillation falls off by a factor of e [55], as also discussed in Section 3.2. In other words, the Q factor is inversely proportional to the damping of the free oscillation of the oscillator. For the case of a heaving cylinder, Q can be readily calculated from a second-order model, as derived in Section 5.3.2, based on (3.68).

Similarly to Fig. 5.17, Fig. 5.18 gives a general picture of the prediction requirements where the cylinders are now parameterised with respect to the Q factor. Although its influence is not as strong as that of the time constant τ_1 , a pattern is clearly evident with the devices being more demanding when the Q factor decreases, for a given τ_1 .

The parameter τ_1 remains, though, the most critical in relation to the prediction requirements.



(a)



(b)

Figure 5.16: Performance of different cylinders, achievable through complex-conjugate control when information of future excitation force, at different leading times, is included in the reference velocity calculation: (a) constant height and changing radius; (b) constant radius and changing height.

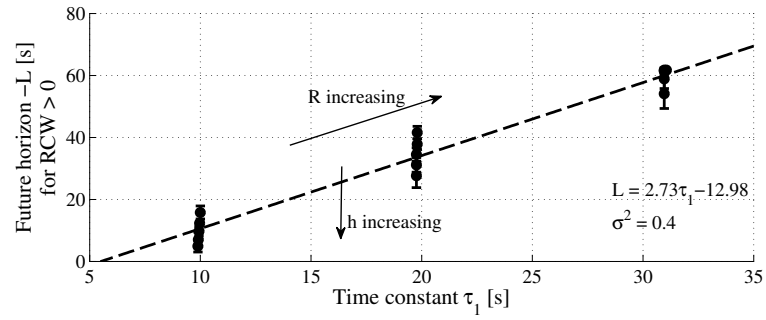


Figure 5.17: Average prediction horizon required by cylinders with different values of τ_1 for the achievement of a positive RCW with complex-conjugate control.

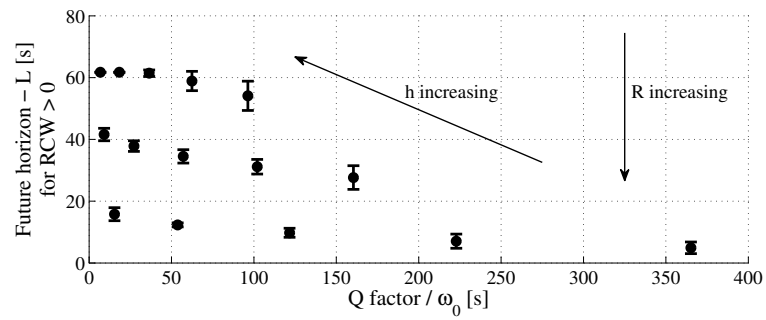


Figure 5.18: Average prediction horizon required by spheres with different values of the Q factor for the achievement of a positive RCW with reactive control.

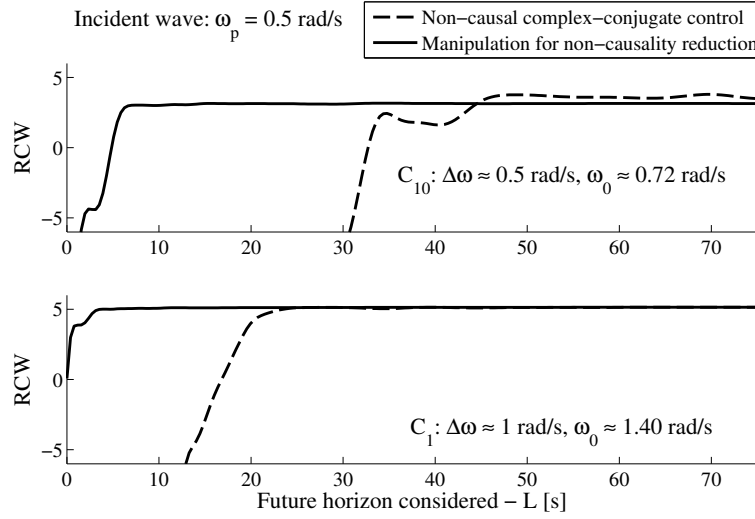


Figure 5.19: Modification of the velocity reference generation transfer function $H_{opt}(\omega)$ for reduced prediction requirements. Behavior of two systems in a sea state with peak frequency $\omega_p = 0.5$ rad/s.

5.4.3 Prediction requirement reduction

The possibility of manipulating the control, such that the non-causality is reduced, was proposed in Section 5.3.1. Intuitive modifications to the reference generator $H_{opt}(\omega)$ are applied, as shown in the example of Fig. 5.9(a). As a result of implementing reactive control based on the modified $H_{red}(\omega)$, Fig. 5.19 shows the behavior of $RCW(L)$ for two different systems, cylinders C_1 and C_{10} of Table 5.3. A stark reduction of the prediction horizon required for an effective implementation of reactive control is achieved. In addition, the performance drop is minor in both cases. The deviation from the optimal performance, in particular, will be affected by the bandwidth of the system (flatness of $H_{opt}(\omega)$) and by the excitation force spectral distribution, as noted in Section 5.3.1.

By applying the modification to the reference generation function, $H_{opt}(\omega)$, to all the cylinders, and calculating the prediction requirements in all the sea states, the results of Fig. 5.20 are obtained. The prediction requirements are significantly reduced to an horizon shorter than 10 seconds, that would obviously be much easier to be achieved with prediction algorithms. Also, it is interesting to note that the differences between the cylinders is minimal, so that no geometry seems to be particularly advantageous in terms of required forecasting horizon.

Figure 5.21 shows the distribution, with the bandwidth of the system, of the maximum RCW achievable, when $H_{red}(\omega)$ is adopted, as percentage of the RCW obtained from ideal complex-conjugate control. The average (dot) performance is usually well above 80%, and increases with the bandwidth of the system. The standard deviation (bar centred around dot) is quite large only for very narrow-banded systems. Note that $H_{red}(\omega)$ was only qualitatively derived from $H_{opt}(\omega)$ and lower performance losses could be achieved through an optimisation that takes into account the spectral distribution of the sea states, as also mentioned in 5.3.1.

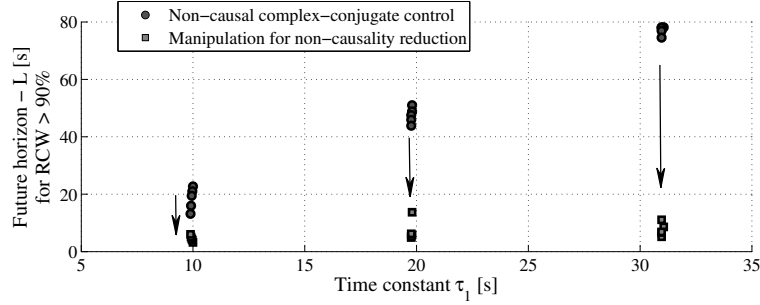


Figure 5.20: Modification of the velocity reference generation transfer function $H_{opt}(\omega)$ for reduced prediction requirements.

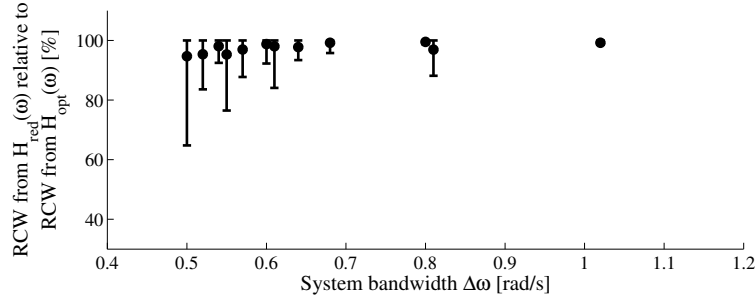


Figure 5.21: Maximum RCW that is achievable when using $H_{red}(\omega)$, as a percentage of the ideal RCW , obtained with $H_{opt}(\omega)$.

5.4.4 Causal approximation

The model-order reduction and the causal approximation of the optimal transfer function, $H_{opt}(\omega)$, as proposed in Section 5.3.2, is now performed for the floating cylinders of Table 5.3. The control scheme of Fig. 5.12 is then implemented, by imposing a reference-velocity, generated through a simple proportional relation with the excitation force, with a control force calculated from (5.31). The performance is measured with the RCW , as proposed in (5.32), and in this case it is not affected by the future horizon, since no predictions of the excitation force are required for the calculation of the reference velocity.

The achieved RCW is compared with the ideal maximum obtained with non-causal complex-conjugate control, where the function $H_{opt}(\omega)$ is implemented for the calculation of the reference velocity, as from the block scheme in Fig. 5.1 and as proposed in Section 5.3. The analysis is carried out over all the real wave-data proposed in Section 5.4.1, and shown in Fig. 5.13.

As an example, consider Fig. 5.22, showing the performance of three sample cylinders, C_1 , C_{10} and C_{15} of table 5.3, with the causal and non-causal control strategies, in a specific sea state, with peak frequency $\omega_p = 0.5$ rad/s. As seen from the results in Section 5.4.2, the performance of the ideal complex-conjugate control improves if more information (into the future) about the wave excitation force is taken into account. The prediction horizon required for approaching the ideal optimum is related to the properties of the radiation, through the time-constant τ_1 . Significantly, the performance of the causal approximation, which obviously does not improve with an increase in the future horizon considered, is very close to the maximum obtained with the non-causal control

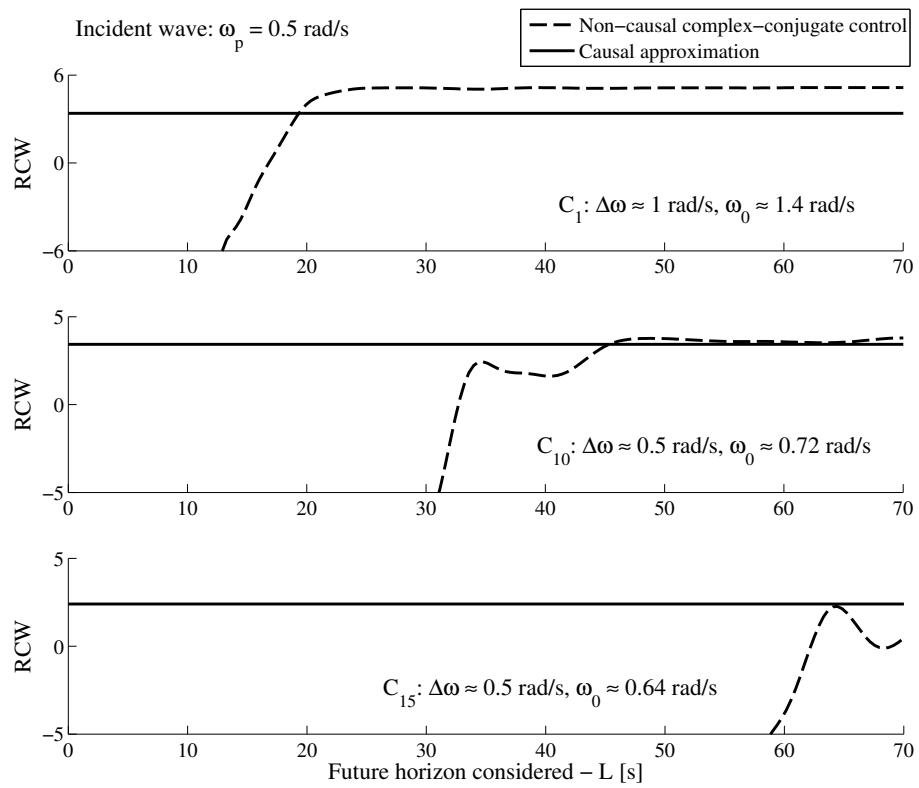


Figure 5.22: Causal approximation of complex-conjugate control against performance of ideal, non-causal controller.

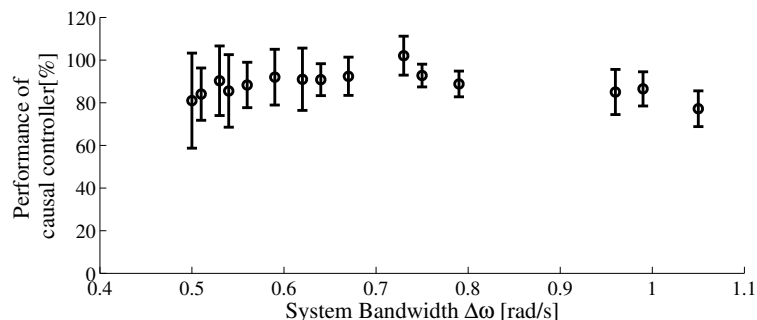


Figure 5.23: Average RCW obtained with causal approximation, as a percentage of ideal maximum achievable with non-causal complex-conjugate control.

in most cases.

As mentioned in Section 5.3.2, it may be expected that the accuracy of the approximation improves for systems with wider bandwidth, for which the optimal function, $H_{opt}(\omega)$, is flatter and closer to a constant. It is to be expected, however, that the achievable performance with the causal controller, compared to the ideal maximum, is also affected by the spectral distribution of the sea states. In particular, the further the incident waves are from the natural frequency of the system (where the constant approximation is more accurate) the higher the loss in performance will be, as it is clear from Fig. 5.11. The examples in Fig. 5.22 confirm such considerations, since the system with the widest bandwidth, C_1 , where the causal approximation is more accurate across a wider range of frequencies, as from table 5.1, shows the worst performance, relatively to the ideal maximum, of the causal controller in a sea state centred at a frequency very far from its natural frequency.

A more general picture is given by Fig. 5.23, where the average performance of the causal controller, as a percentage of the ideal optimum, over all the selected sea states, is plotted against the bandwidth of the system. As usual, the standard deviation is also shown as a bar centred around the mean, represented by a dot. The best performance is obtained with systems that have a relatively wide bandwidth, but at the same time a natural frequency that is not far from the waves, which in this case are between 0.5 and 1 rad/s. At the same time, quite a high variance in the performance and, on average, a lower effectiveness is experienced with narrow-banded systems, as expected. Overall, however, it is interesting to notice that the simple causal controller allows the achievement of performances that are usually above 70-80 % of the ideal maximum, which require predictions.

Ultimately, it has been shown how a simple proportional approximation of complex-conjugate control can provide a very effective method for calculating the reference velocity to impose on a wave energy conversion system. With very little loss in terms of performance, such an approach completely eliminates the needs to predict the excitation force. This also means that the control approach is very likely to be more robust, as it does not have to cope with the inevitable forecasting errors that will affect the reference velocity. Finally, we note that the prediction horizons required by the ideal reactive control can be quite large, more than 60 seconds, depending on the system, as shown in Section 5.4.2. The complexity of the control design, as well as of the instrumentation, and therefore the costs required for an implementation of the non-causal reactive control, may not

justify the marginal power gain.

5.5 Conclusion

This Chapter aims to provide a detailed study and quantification of the prediction requirements for an effective realisation of complex-conjugate control applied to systems for wave energy conversion. The term *prediction requirements* is taken to mean the forecasting horizon required, i.e. how long into the future prediction is required for.

Knowledge of the prediction requirements is fundamental for the appropriate definition of the wave forecasting problem, which will be dealt with in detail in Chapter 6. At the same time, from the analysis and discussion of the non-causal conditions that an oscillating system needs to satisfy for maximum efficiency, as articulated in Section 5.2, the possibility of relating the prediction requirements to fundamental properties of the floating system's radiation emerged. The present study, therefore, becomes fundamental not only for the definition of the forecasting problem, but also to provide the basis for a control-informed design of the system, where possible.

In Section 5.4, results were calculated for several WECs consisting of single-body heaving systems, of cylindrical and spherical shape, under a variety of real wave measurements (about 200 sea states). One parameter of the system, the time constant τ_1 , was found to be mainly responsible for the forecasting horizon required for the effective approximation of complex-conjugate control. Such a parameter, strictly related to the radius for the specific case of cylinders and spheres, was also related to the general shape of the reciprocal of the radiation resistance, so that the results could also be extended to different shapes. Another parameter having an influence on the prediction requirements, although with a less significance than τ_1 , was related to the damping of the free oscillation of the floating body's radiation response, or equivalently to the corresponding Q factor. Ultimately it was found that systems with bigger time constants τ_1 (usually physically larger systems) require predictions longer into the future for reactive control to be effective, and the relation between required prediction horizon and τ_1 is close to linear. For systems with the same τ_1 , higher Q factors allow the reduction of the prediction requirements. Such results are independent of the specific sea state.

In absolute terms, with the required prediction horizons going from as low as 10 seconds to more than 1 minute, one cannot fail to notice that, in some cases, the realisation of complex-conjugate could be impractical, unless a quite sophisticated solution for the wave prediction problem is found. However, a manipulation of the control, based on prior knowledge of the excitation force spectral distribution, was also proposed for the reduction of the prediction requirements, in Section 5.3.1. The possibility of making the control law causal was also proposed, based on a reduction of the system to a second-order model, as described in Section 5.3.2. The performance loss after manipulation of the controller is related to the bandwidth of the system and to the spectral distribution of the incident waves with respect to the resonance frequency of the floating system. The results, shown in Sections 5.4.3 and 5.4.4, indicate that, at the cost of a very small drop in efficiency, reshaping the non-causal control law can possibly yield a significant decrease in the

prediction requirements (or removal of a prediction need when a causal approximation is performed) which may, in turn, allow for simpler and cheaper solutions to the prediction problem.

Note that the focus, in this Chapter, was put on the non-causality of unconstrained complex-conjugate control. Physical constraints on the system, however, could make it impossible for a WEC to reproduce the desired optimal behavior in highly energetic seas, since very large motions and forces are required. As it emerged through Chapter 4, several control strategies, which take into account the constraints, were proposed in the wave energy literature and most of them, such as latching or MPC (refer to Sections 4.2.2 and 4.1.2), are based on the solution of an optimisation problem, which requires knowledge of the future wave excitation force. However, due to the numerical nature of the approach, it is not usually possible to produce an analytical and formal analysis of the non-causality and the prediction requirements can only be determined numerically and on a case by case basis. At the same time, restraining the analysis to complex-conjugate control allowed an understanding of the basic links that exist between the fundamental properties of a floating system (radiation and excitation) and its prediction requirements.

Having clearly identified the forecasting requirements, it is then possible to define and approach the problem of predicting the incident wave or the resulting wave excitation force, which will be done in Chapter 6. Once the problem of wave forecasting is successfully solved, the non-causal approximation of complex-conjugate control proposed in this Chapter, and particularly in the block scheme of Fig. 5.1, can be realised. In particular, a velocity reference can be produced from the predictions and a classical feedback controller can then be designed to track the desired velocity. Chapters 7 and 8 will study more in detail the control system design.

Chapter 6

Short-term forecasting of wave elevation and wave excitation force

Abstract

After analysis of the prediction requirements for the implementation of non-causal complex-conjugate control, in Chapter 5, the present Chapter presents a detailed analysis of the problem of wave and wave-force prediction. In particular, an approach where the wave elevation is treated as a time series, and is predicted only from its past history, is presented. A comparison of a range of forecasting methodologies on real wave observations from different locations shows how the relatively simple linear AR model, which *implicitly* models the cyclical behavior of waves, can offer very accurate predictions of swell waves for up to two wave periods into the future. The extension of the models to the prediction of the excitation force, required for the implementation of a non-causal controller of WECs is also investigated.

The main results of this Chapter are collected in a number of publications on wave forecasting [148, 23, 16, 22], and on the prediction of the wave excitation force [21, 19, 15].

6.1 Introduction

This Chapter focuses on the problem of forecasting the ocean wave elevation at a specific point of the sea surface based on past observations collected at the same point. The problem is strictly connected to the real-time control of a WEC which can, potentially, significantly increase its efficiency and energy capture ability, but that is well known to be described by non-causal relationships in the time domain [94],[6],[11], as widely discussed in Chapters 4 and 5.

The wave elevation, $\eta[k]$, observed at a particular point of the sea is treated as a pure univariate time series, so that the forecasting problem consists of determining the prediction, $\hat{\eta}[k+l|k]$, a number of steps ahead, l , based on all the information up to the current sampling instant, k . Most of the solutions proposed in the literature deal with the problem by trying to reconstruct the wave field at a certain point of the sea surface based on one or more distant measurements

[103],[149],[150],[151], as shown in Fig. 6.1(b). The spatial prediction, however, requires complex numerical models and a large enough array of measurements in order to properly deal with the wave radiation, refraction [152], multi-directionality [149] and with the non-linearities of the wave propagation.

Alternatively, the solution discussed here is based only on local measurements of the wave elevation (or of any other related quantity of interest, such as the wave excitation force), as illustrated in Fig. 6.1(a), which introduces certain important advantages:

- Multi-directionality and all the associated complications need not be considered.
- The wave propagation laws do not need to be modelled and no simplifying assumptions (e.g. linearity, dispersion relationship) are required.
- If the considered point corresponds to the position of the WEC, the radiated waves do not affect the measurements.
- No additional instrumentation around the device is required (possibly cheap solution).
- The well established theory about univariate time-series forecasting may be exploited.

Being purely stochastic, however, the univariate approach is not able to go further into the future than the correlation within the wave signal allows. Only the information contained in the present and recent-past evolution of the wave is available for the extrapolation of its future behavior. The purpose of this Chapter is therefore to understand how predictable the wave elevation or wave excitation force are and to compare the achievable forecasting horizon with the requirements of non-causal controllers, identified in Chapter 5.

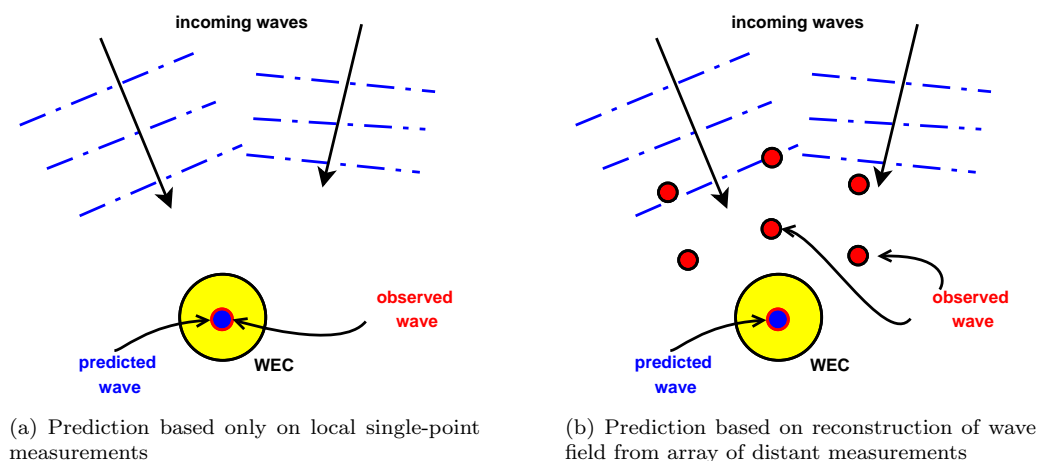


Figure 6.1: Two main approaches to wave forecasting

The Chapter is organised as follows. A survey of the solutions proposed for short-term wave prediction, with particular focus on wave energy applications, is given in Section 6.2. The available real data, and its detailed analysis through different tools, is presented in Section 6.3. Some possible solutions to produce the predictions are proposed in the methodology of Section 6.4, and evaluated on the real wave data in Section 6.5. Application of the proposed models to the wave excitation

force is investigated in Section 6.6 and the results are compared with the prediction requirements, analysed in Chapter 5. Conclusions are finally presented in Section 6.7.

6.2 State of the art of short-term wave prediction

The main approaches presented in the scientific literature, to cope with the forecasting requirements related to the real-time implementation of a non-causal controller for the achievement of maximum efficiency from a WEC, are presented in this Section. As emerged from Chapter 5, the excitation force is the quantity for which predictions are primarily required. However, almost all of the proposed solutions involve the prediction of the wave elevation, particularly based on a spatial propagation from measurements collected at a site distant from the location in the sea where the forecasts are required.

The first approach that may be found in literature, to the best of the author's knowledge, is the sinusoidal extrapolation based on the Kalman filter, which was provided by Budal *et al.* [103] and is described in Section 6.2.1. Then, methods making use of deterministic linear filters for the wave prediction, based on wave observations collected at several locations, are overviewed in Section 6.2.2, while Section 6.2.3 deals with similar digital filters to determine the future incident wave on a device from distant pressure measurements. An alternative approach to spatial prediction of waves through a linear harmonic model fitted to distant wave elevation observations is overviewed in Section 6.2.4.

Finally, Sections 6.2.5 and 6.2.6 present some solutions focused on the prediction of the velocity and of the wave excitation force, respectively, treated as a univariate time-series problems, where only past observations at the prediction site are utilised.

6.2.1 Wave pressure estimation by the Kalman filter

In [103], the Kalman filter [153] (appendix B gives an overview of the Kalman filter) is utilised to predict the parameters of the future evolution of the wave pressure acting on a heaving body, which is supposed to be proportional to the wave excitation force. The buoy is then latched and unlatched according to the predicted pressure in order to realise a phase control for improving the energy extraction (latching control was reviewed in section 4.2.2).

The pressure, $p(t)$, is modelled as a damped oscillation:

$$\ddot{p}(t) + d\dot{p}(t) + \omega^2 p(t) = 0, \tag{6.1}$$

where d represents the damping coefficient and the frequency, ω , is assumed to be slowly varying, that is $\dot{\omega} \approx 0$. It is supposed to be possible to measure the pressure at each sampling instant by knowing the observed incident wave. The model of the pressure is then put into a non-linear

state-space form:

$$\begin{aligned}\dot{p}_1(t) &= p_2(t) \\ \dot{p}_2(t) &= -dp_2(t) - \omega^2 p_1(t) \\ \dot{\omega}(t) &= 0,\end{aligned}\tag{6.2}$$

where $p_1(t) = p(t)$ and $p_2(t) = \dot{p}(t)$. In particular, the second state equation in (6.2) is non-linear in the frequency, ω .

Because of the presence of the damping coefficient, which ensures numerical stability when adopting a finite time resolution, a simple Euler integration can be applied in order to put the state-space form, in (6.2), into the discrete time domain:

$$\begin{aligned}p_1[k+1] &= p_1[k] + \Delta T p_2[k] \\ p_2[k+1] &= (1 - d\Delta T)p_2[k] - \Delta T \omega[k]^2 p_1[k] \\ \omega[k+1] &= \omega[k],\end{aligned}\tag{6.3}$$

where ΔT is the sampling time.

The relations in (6.3) are the state-space equations as presented in [103], but a disturbance term should be supposed to be acting on each of the three equations, for the application of the Kalman filter. As said, however, the equations in (6.3) are non-linear in ω , so that the state variables can not, theoretically, be estimated through the Kalman filter. It was found, however, that the Kalman gains for the reduced state-space form where ω is constant, which is linear, approach constant values, k_1 and k_2 respectively, for the states p_1 and p_2 . An analytical expression for the gain, k_ω , of the state variable representing the frequency, ω , is then provided, once k_1 and k_2 are fixed. The on-line estimates may finally be calculated, recursively, as:

$$\begin{aligned}\hat{p}_1[k+1|k+1] &= \hat{p}_1[k+1|k] + k_1 (p_m[k+1] - \hat{p}_1[k+1|k]) \\ \hat{p}_2[k+1|k+1] &= \hat{p}_2[k+1|k] + k_2 (p_m[k+1] - \hat{p}_1[k+1|k]) \\ \hat{\omega}[k+1|k+1] &= \hat{\omega}[k+1|k] + k_\omega (p_m[k+1] - \hat{p}_1[k+1|k]),\end{aligned}\tag{6.4}$$

where $\hat{x}[t+l|t]$ is the optimal estimate of $x[t+l]$, based on the information available up to time instant t (refer to appendix B for the details). The one-step-ahead predictions, in (6.4), are calculated from the non-linear model in (6.3):

$$\begin{aligned}\hat{p}_1[k+1|k] &= \hat{p}_1[k|k] + \Delta T \hat{p}_2[k|k] \\ \hat{p}_2[k+1|k] &= (1 - d\Delta T)\hat{p}_2[k|k] - \hat{\omega}[k|k]^2 \hat{p}_1[k|k] \Delta T \\ \hat{\omega}[k+1|k] &= \hat{\omega}[k|k]\end{aligned}\tag{6.5}$$

At each time step, k , the estimate of the state variables, $\hat{p}_1[k|k]$, $\hat{p}_2[k|k]$ and $\hat{\omega}[k|k]$, are available and the following harmonic model may be utilised to predict the wave pressure acting on the body,

at any leading time, l sampling instants into the future:

$$\begin{aligned}\hat{p}_1[k+l|t] &= \hat{p}_1[k|k] \cos(\hat{\omega}[k|k]l\Delta T) + \frac{\hat{p}_2[k|k]}{\hat{\omega}[k|k]} \sin(\hat{\omega}[k|k]l\Delta T) \\ \hat{p}_2[k+l|t] &= \hat{p}_2[k|k] \cos(\hat{\omega}[k|k]l\Delta T) - \hat{p}_1[k|k]\hat{\omega}[k|k] \sin(\hat{\omega}[k|k]l\Delta T).\end{aligned}\tag{6.6}$$

The power loss of the device due to inaccuracies in the predictions and therefore in the control (latching is applied) is estimated to be 5–15%, which seems to be a reasonably good achievement. However, some of the stated assumptions would be too restrictive for applications in a real sea, whilst this approach was tested in an artificial wave channel on a 1 : 10 scale and with 2-dimensional waves. Deriving the pressure acting on the device, in the real sea, from distant measurements of the wave elevation may be a problem, due to multi-directionality and to non-linearities appearing in the propagation of the wave. The wave elevation should preferably be collected, in the real sea, as near to the device as possible, but a correction for the radiated wave would then be necessary, in this case.

The present approach, however, is quite a valuable first attempt with an integration of the control and prediction algorithms (in this case of the wave pressure). Of particular interest is the possibility of adopting a very robust, effective, and above all linear, prediction algorithm such as the Kalman filter (although applied to a non-linear system), to predict not only the amplitude and phase of the oscillating quantity (here the wave pressure) but also its frequency, which in the harmonic model appears non-linearly.

6.2.2 Deterministic sea wave prediction and quiescent period predictive control (QPPC)

In [149], a complete overview of a Deterministic sea-wave prediction (DSWP) technique is given. This approach is concerned with the short-term prediction of the future sea surface elevation at the point of interest. It involves first measuring the elevation of the sea surface at some distance around the site where prediction is required and then using this data to build a model capable of estimating the wave elevation when it has propagated to the prediction site. Typical prediction time scales are a few tens of seconds ahead.

The main application of the DSWP model is in the estimation of the coupled heave and pitch near the bow or stern of moderate to large vessels. This is significantly influenced only by moderate-to large-wavelength swells, so that the higher-frequency wind waves can be filtered out prior to prediction. Otherwise, including the highly non-linear wind waves in a DSWP model would certainly be too computationally heavy in the few seconds available for forecasting while, in contrast, the non-linear aspects of the swells are significantly weaker [149].

The difficulties of the DSWP with high-frequency waves do not seem to represent a big issue in the wave energy area, however, since such waves normally present a very low energy content and, depending on the geometry of the WEC, may be filtered out by the system's dynamics and therefore be of no use.

Belmont *et al* [149] assert that a practical DSWP sea model will comprise a modest number, N , of long-crested seas with orientation angles, θ_i , created from N remote storms and that building a

DSWP prediction model basically involves the following two tasks:

1. Pre-prediction model parameter identification. The most important of these parameters are the number, N , of dominant component seas and the associates angles, θ_i .
2. Based on the identified parameters, the prediction model is built.

The full prediction scheme uses a linear combination of N linear filters parameterised by the directions, θ_i , and thus the core issue is the determination of the one-dimensional impulse responses associated with each of the separated long-crested seas. One of the possible forms of such a linear filter, in the case of deep water (that is when the seabed shape does not affect the waves, as defined in (3.22)), is as follows:

$$\eta(x, t) = \int_{-\infty}^{+\infty} \eta(0, \tau) \Gamma(x, t - \tau) d\tau, \quad (6.7)$$

where $\eta(x, t)$ is the wave elevation and $\Gamma(x, t)$ is an impulse response function derived from wave propagation laws based on linear theory, which in general is non-causal [57], as also noticed in Section 4.2.1. The filter in (6.7) allows the time-domain data, $\eta(0, t)$, measured over an interval $T_1 \leq t \leq T_2$ at the location $x = 0$, to be used to determine the surface elevation, $\eta(x, t)$, at a different point, x , along the direction of propagation. The particular form of the filter, in (6.7), is termed a *fixed-point* method of DSWP, because the wave elevation is measured at a fixed point of the sea (another formulation could be the *fixed-time* one, see [149]). The practical effect of the displacement between measurement and prediction site is, however, that for $t < 0$ the amplitude of $\Gamma(x, t)$ becomes very small and may be neglected (further details about this can be found in [57]). This means that the *fixed-point* method can be directly implemented in the conventional manner as a discrete convolution:

$$\eta(x, k\Delta T) = \frac{1}{N} \sum_{l=k-n}^k \eta(0, l\Delta T) \Gamma[x, (k-l)\Delta T], \quad (6.8)$$

where ΔT is the sampling period.

The numeric results presented in [149] show a good accuracy in the case of waves composed of a single, long-crested swell. In the same paper, the authors also mention the possibility of extending the DSWP in order to deal with the multi-directionality. However, the complexity of the problem significantly increases due to the requirement of measurements from several locations around the device, to the necessity of a preliminary and periodic procedure to identify and separate the different wave fronts, and to the higher number of filters producing a higher computational complexity during the on-line prediction of the future wave elevation.

An interesting application of DSWP to wave energy is proposed in [154] and [155], where the predictions are utilised in order to implement a Quiescent period predictive control (QPPC) system for wave energy devices. In very energetic sea states, in fact, large waves alternate with smaller waves (this is the phenomenon of wave grouping [6]). Therefore, it may be required that a WEC alternates its operation between energy production mode during the small waves and safety mode during the large waves.

6.2.3 Digital filters for wave forecasting

An attempt to forecast the waves incident upon an overtopping device, based on pressure measurements collected at some distance from it, is presented in [150] and it is utilised for adding extra information to the control logic of the Wave Dragon WEC. It is, in fact, part of a model to forecast the actual overtopping water on the device but, given the scope of the present Chapter, the focus here will be put on the wave forecasting algorithm.

The measurements are collected through a pressure transducer located about 52 m from the device and mounted 3.98 m above the sea bed. A digital filter, $H(\omega)$, is then designed in order to provide predictions of the incident wave elevation, at a pre-determined leading time, from the convolution of the filter with the observed pressure. The magnitude of the filter is based on the transfer function between pressure and wave elevation at the same point of the sea and the phase of the filter is based on the delay due to the waves travelling from the measurement point to the device (uni-directionality is assumed).

The approach is quite similar to the DSWP method, described in Section 6.2.2, but is less general and does not take into account multi-directionality. However, more focus is put on the transition from an analog impulse response to its digital implementation, whereas in the *DSPW* the discretisation procedure is assumed to be straightforward, in a rather simplistic way.

The relationship between the wave elevation and pressure, according to linear potential theory, is [6]:

$$p(x, y, z, \omega) = \rho g \frac{\cosh(kz + kh)}{\cosh(kh)} \eta(x, y, \omega), \quad (6.9)$$

where x and y define the sea surface, z is the direction normal to it (the depth), h is the water depth and k is the wave number, related to the wave frequency, ω , by means of the dispersion relationship, introduced in (3.18). The relationship in (6.9), between pressure and wave elevation, is a real function of the frequency and, therefore, gives the magnitude of the required filter, $|H(\omega)|$.

The phase delay of the filter, $H(\omega)$, is based on the required prediction horizon, on the travelling time of the wave and on the delay introduced by the digital filter:

$$\frac{\angle H(\omega)}{\omega} = \tau_C - \tau_{df} - \tau_{tr}(\omega). \quad (6.10)$$

In (6.10), $\angle H(\omega)$ denotes the phase of the filter, τ_C is the desired forecasting time horizon and τ_{df} is the delay introduced by the filter (related to the order). The travelling time of the wave, namely $\tau_{tr}(\omega)$, depends on the frequency (due to the dispersive nature of water waves, discussed in Section 3.1.1) and it is given by the distance, D , covered by the wave divided by the phase velocity, v_p :

$$\tau_{tr}(\omega) = \frac{D}{v_p} = D \frac{k}{\omega}. \quad (6.11)$$

Note that second equivalence in (6.11) is derived from the definition of phase velocity, given in (3.21), that is the frequency, ω , over the wave number, k .

Before calculating the impulse response from the designed transfer function, a cosine tapering function is applied in order to smoothly set to zero the start and end frequencies of the filter $H(\omega)$,

which ensures the reduction of ripples appearing in the resulting impulse response, due to the finiteness of the considered frequency band.

The digital filter's impulse response, $h[k]$, utilised for the implementation, in real-time, of (6.9), is then computed as the IDFT of a discretised version of $H(\omega)$, denoted by $H[n]$, known at N equally-spaced frequencies in the interval from 0 to the adopted sampling frequency, f_s , [62]:

$$\begin{aligned}
 H[n] &= \left[|H(\omega)| e^{\angle H(\omega)} \right]_{\omega=2\pi \frac{n}{N} f_s} \quad n = 0, \dots, N-1 \\
 h[k] &= \frac{1}{N} \sum_{n=0}^{N-1} H(n) e^{j \frac{2\pi n k}{N}} \quad k = 0, \dots, N-1.
 \end{aligned}
 \tag{6.12}$$

Note that N represents the order of the filter (the higher N the better the approximation but the longer the introduced delay, τ_{df}). A filter of order $N = 64$ was shown to be a good approximation of the theoretical filter, $H(\omega)$, at least in the central band of frequencies, [0.3, 0.5] Hz, where most of the wave energy is contained. The considered sampling frequency is 2.5 Hz.

Not very valuable results of this very interesting approach, however, were provided in [150]. Accurate predictions were calculated 11.2 s into the future, on real wave data, but from a much higher-order filter than $N = 64$, applied off-line, where the effective prediction horizon achieved is reduced to the large time-delay introduced by the filter (τ_{df} in (6.10) increases). Although interesting, the approach needs to be extended to multi-directional waves and need to take into account radiation and reflections from the WEC to be usable in practice. Such limitations were pointed out but not further investigated by the authors in [150].

6.2.4 Spatial wave forecasting through a linear harmonic model

In [151], an alternative approach to wave forecasting is presented, where the wave elevation is measured at one point of the sea surface and then predicted at different locations down-stream along the propagation direction. However, direction spreading of the wave and multi-directionality are not taken into account.

From the linear theory of random waves, as presented in Section 3.1.2, the wave field is assumed to be a superposition of m regular waves of frequency ω_i and initial phases φ_i , which propagate, along the x direction, according to:

$$\eta(x, t) = \sum_{i=1}^m A_i \cos(k_i x - \omega_i t + \varphi_i),
 \tag{6.13}$$

where the wave number, k_i , is related to the frequency, for the dispersive nature of the waves, as from (3.18).

From a set of observations, $\eta(0, t)$, collected for some time $t \in [0, T]$, at a location $x = 0$, phases and amplitudes of the wave components are estimated using Least squares (LS), after a reasonable number, m , of frequencies has been pre-determined, based on the wave spectrum. In particular, the observations are fitted to the following model, derived from (6.13), but linear in the

parameters:

$$\eta(0, t) = \sum_{i=1}^m a_i \cos(\omega_i t) + b_i \sin(\omega_i t), \quad (6.14)$$

with the coefficients, a_i and b_i , taking into account both the amplitude, A_i , and the initial phase, φ_i , of the regular waves.

The spatial forecasts of the wave elevation, d metres distant from the observation point, are then calculated as:

$$\eta(d, t) = \sum_{i=1}^m [a_i \cos(\omega_i t - k_i d) + b_i \sin(\omega_i t - k_i d)]. \quad (6.15)$$

The methodology offers very accurate predictions, so long as linear wave theory is valid, with both phase and amplitudes reported to be in good agreement with reality even at a distance of 3.75 times the longest wavelength in the generated wave train. When larger waves were simulated (ratio of significant wave height to water depth approximately 0.142) the phase of the regular waves is progressively lost when getting further from the measurement site, mostly due the non-linear interactions between waves of different frequency and to the loss of validity of the dispersion relationship (the authors assume deep water).

All the experiments where carried out with irregular waves, generated in a wave tank, constituted by few harmonics and not covering the full spectrum that can normally be observed in the open sea. Such a simplification, together with the conditions of uni-directionality, linearity and absence of a radiated wave, makes the extension of this method to the real case far from being straightforward, though some interesting concepts are proposed. In addition, the method proposed in [151] is not able to cope with the non-stationarity of the waves, which results in time-varying amplitudes and phases of the harmonic components.

6.2.5 Autoregressive models for wave forecasting

In contrast to the solutions reviewed through Sections 6.2.1 to 6.2.4, some authors have approached the problem of wave forecasting as a univariate time-series problem, where the wave elevation (or its effect on the system) is predicted on the basis of current and past measurements of the variable itself.

In [95], the implementation of non-causal complex-conjugate control is proposed based on the prediction of the oscillation velocity of a one-degree-of-freedom device for wave energy conversion. The velocity, $v[k]$, is modelled as a linear AR process:

$$v[k+1] = \sum_{j=1}^n a_j v[k+1-j] + \zeta[k], \quad (6.16)$$

that is a linear combination of n past values, weighted through the parameters, a_j , plus additive noise, $\zeta[k]$, assumed to be white and Gaussian. Based on (6.16), the l -step-ahead prediction of the

velocity, $\hat{v}[k+l|k]$, from the information available up to instant k , is calculated as:

$$\hat{v}[k+l|k] = \sum_{j=1}^n a_j \hat{v}[k+l-j|k]. \quad (6.17)$$

Note that, in (6.17), $\hat{v}[k+l-j|k] = v[k+l-j]$ when $k+l-j \leq k$, which means that the velocity measurements, up to instant k , are already acquired.

The estimation of the n parameters, a_j , was effected through the LS algorithm, but no details about the model order selection and about the prediction accuracy were given in [95]. Predictions of only 2 steps (0.8 seconds) into the future were utilised for the calculation of the control action. It may be argued, however, that an AR model could turn out to be unsuitable for predictions of the velocity, $v[k]$, longer into the future, since the velocity is a variable controlled in closed loop and the model does not reflect such a situation.

An application of AR models was also proposed for the prediction of the wave elevation as an input to a controller based on a fuzzy-logic inference engine [133] (refer to Section 4.2.4 for a review of the controller). The variable to be predicted, that is the incident wave elevation, is independent on the operation of the system, so that univariate time-series models with no exogenous component, for example AR and Autoregressive moving average (ARMA) models, could be successfully implemented for multi-step prediction.

An additional time-series model, from prior knowledge of the dynamic of the wave elevation, is proposed in [133], as a linear combination of second-order Kautz filters [156], that exhibit under-damped oscillatory behavior. In a step-by-step procedure, the frequencies of the elementary oscillations are determined from the wave spectrum, and LS is utilised for the estimation of the remaining parameters. The possibility to update the frequencies of the Kautz filters in real time, when variations in the wave spectral distribution occur, is not discussed.

The authors claim that best results are obtained with AR models. Comparison of AR, ARMA and hybrid AR-Kautz prediction models, however, is only reported for a very specific wave record, simulated from a Pierson-Moskovitz distribution. In addition, only the 1-step-ahead prediction error is compared, which could be misleading when the ultimate purpose is multi-step prediction.

6.2.6 Non-linear next wave estimation

Price [157] introduced an alternative approach to wave forecasting which is interesting to analyse in this thesis, although less general in the fact that it is specific to the application of latching control, which was described in detail in Section 4.2.2. In particular, the study is focused on forecasting only some specific events of interest for the controller, rather than the complete future evolution of the wave profile, which is quite different to the more general approaches so far reviewed in Sections 6.2.1 to 6.2.5. Similarly to the AR prediction model reviewed in Section 6.2.5, the solution proposed in [157] treats wave forecasting as a univariate time-series problem, where the only information utilised is constituted by past observations of the wave elevation at the same point of the sea surface where the prediction is required.

The main idea is to estimate the time until the next event of interest, which can be the time until the next peak or trough, that represents the key information for a latching controller in order

to properly decide when to latch or unlatch. In [157], it is also pointed out that the same approach may be utilised for the estimation of the time until the next few extremes of the excitation force, together with their magnitude, which would add further useful information for the optimisation of the control action.

The estimation of future wave excitation features is performed through models where the inputs are sets of features extracted from the observed time series, rather than the past time series itself. In particular, the input vector is composed of the following information:

- current excitation force and its first and second derivative,
- time since the last upward zero crossing,
- excitation force gradient at the last upward zero crossing,
- duration of previous crest and previous trough and respective maximum values,
- mean and variance of the duration of crests and trough for the last 14 waves,
- mean and variance of the magnitude of excitation force slope at zero crossings.

The output vector chosen for the study presented in [157] is the time until the next peak, but as it was already pointed out, the method may be easily extended to the prediction of different outputs.

Three models are compared:

1. **Quadrant approach:** the excitation force is assumed to be approximately sinusoidal, and each period is ideally split into four quadrants, two for the crest and two for the troughs according to the sign of the amplitude and of the first derivative of the excitation force (tables 6.1). Then, the time until the next peak, t_{nP} , is calculated as:

$$t_{nP} = t_{eQ} + n\frac{T}{4} \quad (6.18)$$

where t_{eQ} is the time until the end of the quadrant, calculated by means of the time since the last upward zero crossing and the estimated period, T (double the average of the last durations of crests and troughs in the input vector). The value of the integer n depends on the current quadrant, detected through the tables 6.1.

2. **Linear regression:** A linear Autoregressive with exogenous term (ARX) model between the input vector and each target (time until next peak) is identified.
3. **Neural networks:** a non-linear relationship between the described input vector and the time until the next peak, through a completely black-box approach with neural networks, is determined. In particular, several multi-layer perceptron architectures are trained and tested.

The three methodologies are compared with simulated data, generated from noisy sinusoids or from irregular wave-trains, based on a Pierson-Moskovitz spectrum (refer to Section 3.1.2). The simulated wave records were then applied to a hypothetical WEC geometry (a fully submerged vertical cylinder), in order to produce records for the wave excitation force.

(a)			(b)	
Quadrant	$sign(f_{ex})$	$sign(df_{ex}/dt)$	Quadrant	n
1	+	+	1	0
2	+	-	2	3
3	-	-	3	2
4	-	+	4	1

Table 6.1: (a) The current quadrant is individuated on the basis of the sign of the excitation force, f_{ex} , and of its first derivative with respect to time. (b) The n parameter, in (6.18), is chosen on the basis of the current quadrant.

Results show that the maximum accuracy is obtained with the neural networks, with the linear regression method being the weakest, above all in the case of data generated from a Pierson-Moskovitsz spectrum. This, of course, was expectable since it is very likely that the relationship between the proposed input vector and the output is highly non-linear.

This study represents a quite different and interesting point of view of the problem of wave forecasting, but it should be also kept in mind that it is not a very general solution. The approach, in fact, seems to be a very valuable one for the improvement and the optimisation of a discrete type of controller, such as latching control, although an experimental proof with real data was not provided. An extension to more general optimal control applications, however, may be too complex a solution than the reality of the problem actually requires, in this author's opinion.

6.3 Wave data analysis

Before delving into the derivation of models for the prediction of the wave elevation, a detailed insight into the properties of wave data is given. Real wave measurements, covering a variety of sea conditions at two different locations, are analysed with different tools in Sections 6.3.1 to 6.3.5.

The Irish Marine Institute provided real observations from a data buoy located in Galway Bay, on the West Coast of Ireland, at approximately $53^{\circ}13'$ N, $9^{\circ}18'$ W, (water depth nearly 20 metres). The observations used consist of 20-minute records sets for each hour, collected at a sampling frequency of 2.56 Hz, for parts of years 2007 and 2008. The location is sheltered from the Atlantic Ocean so that the wave height magnitude is generally small, which makes it unsuitable for full-size WECs, though a wave energy test site has been established there for 1/4-scale prototypes.

Wave elevation time series are also available from the Atlantic Ocean at Pico Island, in the Azores archipelago, at approximately $38^{\circ}33'$ N, $28^{\circ}34'$ W (water depth around 40 metres) [158, 159, 160]. They cover the year 2010, in the form of two contiguous 30-minute record sets for each hour, with a sampling frequency of 1.28 Hz (that is 2304 samples for each set).

6.3.1 Wave spectrum

The main tool for a preliminary analysis of waves is the wave spectrum, which shows how the energy is distributed across the different frequency components of the wave, assumed to be completely independent of each other. Although offering time-averaged information (a Wavelet transform would offer a more complete information in the time domain, refer to Section 6.3.2), the wave spectrum is very useful in providing some overall characteristics of the sea conditions in different situations and at different locations. The basic theory that describes the wave spectrum was introduced in Section 3.1.2.

Based on the wave spectrum, it is possible to derive certain summary statistics that capture the essential properties of the wave record. The main parameters, whose definition was proposed in Section 3.1.2, are the significant wave height, H_s , the energy frequency, ω_e , and the peak frequency, ω_p . The significant wave height, defined as four times the area under the spectrum, in (3.46), is a measure of the energy of the waves. The peak frequency identifies the harmonic component with the most energy within the wave train, while the energy frequency, defined in (3.47), is the frequency around which most of the the wave energy is concentrated. Fig. 6.2 shows the distribution of H_s and ω_p or ω_e , calculated over the available data sets at the two locations of Galway Bay and the Pico Island. Clearly, high-energy waves present a much narrower spread of ω_p and ω_e , centred at a low frequency (about 1 rad/s for the Galway Bay data, even lower for the waves from Pico), which means that the energy is more concentrated at the low frequencies and the spectral distribution has a well defined narrow peak (swell). The lower the energy, on the other hand, the greater the distance between the peak and the mean frequency. Such a property indicates a much flatter spectrum where the high frequency wind waves have a similar energy content to the low frequency swell.

The sample spectra of Fig. 6.3 are particularly illustrative in this respect. Three significant wave records are selected at each of the two locations, identified with the letter G , for Galway Bay, and with the letter P , for Pico Island. In particular, one wide-banded (sets G_1 and P_1) and one narrow-banded sea state (sets G_2 and P_2) from each of the two sites is considered. Then, a situation where wind waves predominate is selected from the Galway Bay data (set G_3) and a very high-energy waves, where the sea bottom may affect the wave distribution is chosen from the Pico Island data (set P_3).

As also highlighted from the discussion in Section 3.1.2, the major limitations of the wave spectrum are the assumptions of stationarity and linearity of the wave record. The wave spectrum is only a time-averaged representation of the wave energy and the different harmonic components appearing in the wave spectrum may not, in practice, occur at the same time. Also, there may be important non-linear interactions between waves at different frequencies, that the wave spectrum is not able to highlight, and that would be important to be considered, where significant, in a wave prediction model. The following Sections, 6.3.2 and 6.3.3, propose some tools for an analysis of the non-stationarity and of the potential non-linearity of the available wave records.

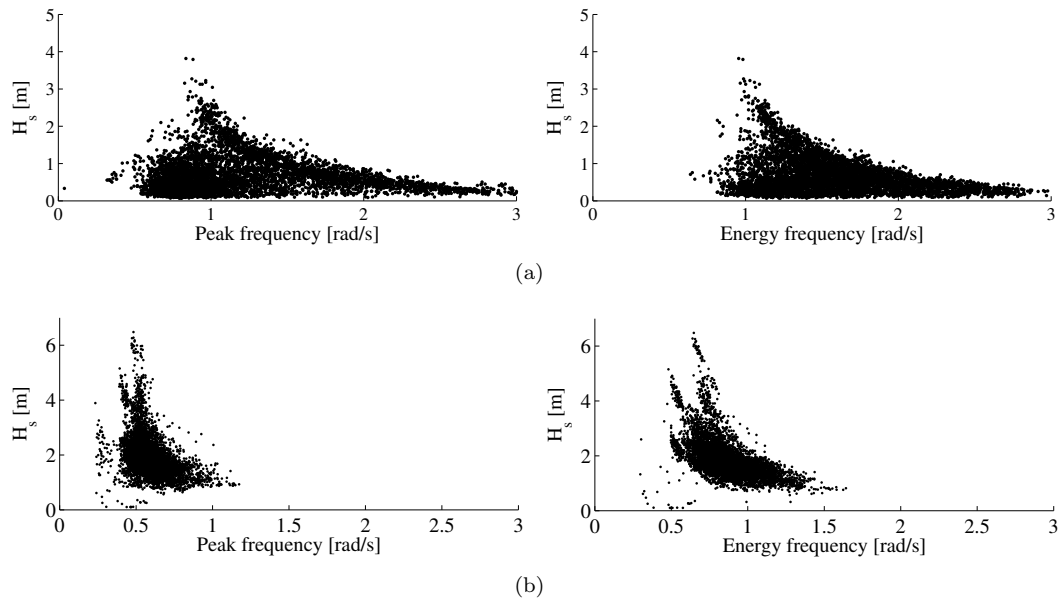


Figure 6.2: Correspondence between significant wave height H_s , peak frequency ω_p and energy frequency ω_e at the locations: (a) Galway; (b) Pico.

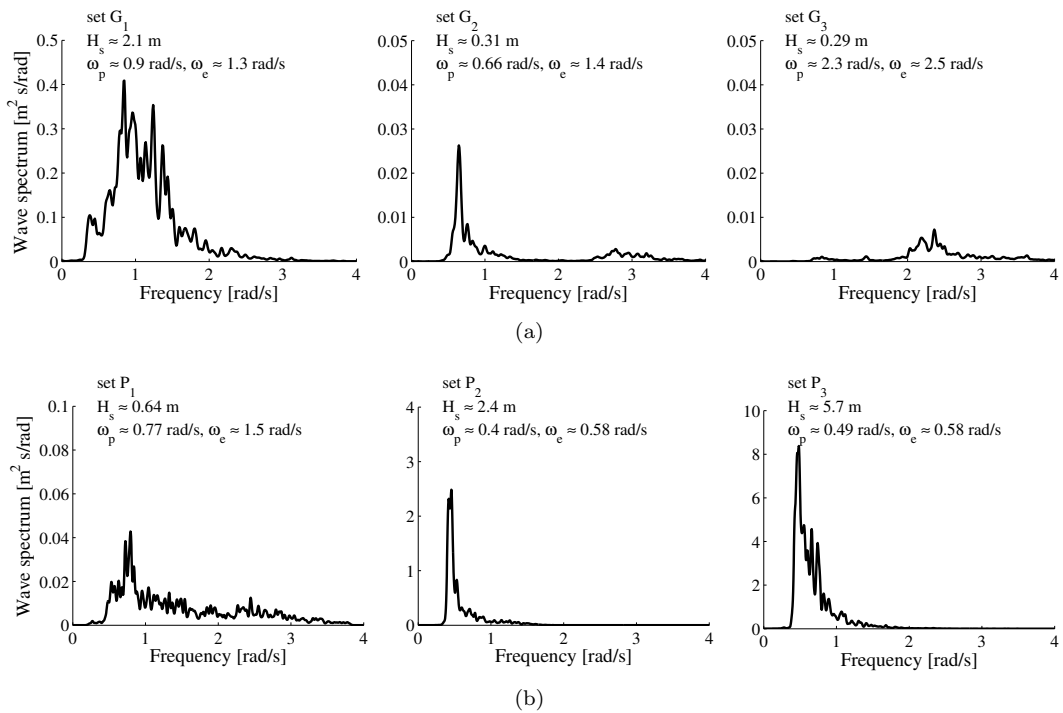


Figure 6.3: Typical wave spectra at the locations: (a) Galway Bay; (b) Pico Island.

6.3.2 Non-stationarity and the Wavelet transform

A better and more complete understanding of the energy distribution in the waves can be achieved through an analysis in both the frequency and time domain, that is something like a continuous evolution of the wave spectrum over time. An interesting tool that has been successfully applied to this proposal is the Wavelet transform [161, 162], since it allows the achievement of a good resolution both in time and frequency.

Wavelets have been successfully implemented in signal and image processing, ordinary and partial differential equation theory, numerical analysis and communication theory [162]. On the other hand, the application of the wavelet transform to ocean engineering and oceanography is not customary. This is mostly due to the fact that not all such oceanographic applications provide quantitative results, so that the wavelet transform has been regarded as an interesting tool to produce colorful pictures, yet purely qualitative results [162].

The Wavelet transform of a signal, $x(t)$, is defined from the following expression:

$$WT(t, b) = \int_{-\infty}^{+\infty} x(t)g^*(t; \tau, b)d\tau. \quad (6.19)$$

In (6.19), $g^*(t; \tau, b)$ is the complex conjugate of a continuously translated and dilated mother wavelet function $g(t)$:

$$g(t; \tau, b) = \frac{1}{\sqrt{b}}g\left(\frac{t - \tau}{b}\right), \quad (6.20)$$

where t is the translation parameter, corresponding to the position of the wavelet as it is shifted through the signal, and b is the scale dilation parameter determining the width of the wavelet. At low frequencies (high value of scale b), the frequency resolution is better but the time resolution is poor (more ambiguity regarding the exact time). On the other hand, at higher frequencies (low scale b), the frequency resolution is poorer and the time resolution is better. This main characteristic of the Wavelet transform, which is due to the fact that the signal is multiplied with a window whose width is changed as the transform is computed for each spectral component [162], is a significant improvement over the Short-term Fourier transform (STFT), where the window is constant and an appropriate compromise has to be made between time and frequency resolution [161]. In fact, a finer time resolution at higher frequencies is important because the signal is changing faster, while a poorer time resolution at low frequencies can be acceptable because the signal is changing more slowly.

A correspondence between the scale value, b , and the Fourier period, T , can be found, depending on the specific mother wavelet, $g(t)$, being used. In the case of the popular *Morlet wavelet*:

$$g(t) = e^{-\frac{1}{2}t^2} e^{jct}, \quad (6.21)$$

the following expression can be derived [162]:

$$b = \frac{c + \sqrt{c^2 + 2}}{4\pi} T \triangleq \alpha T \quad (6.22)$$

where c is a parameter defining the Morlet wavelet, having the nature of a frequency in some sense. Note that the physical dimension of b is time in seconds. Expression (6.22) can then be used to provide a physical meaning (the frequency) of the scale dimension of the transform $WT(t, b)$, which can then become a $WT(t, f)$ or $WT(t, \omega)$ in a very straightforward way.

Figures 6.4 and 6.5 show the Wavelet transform for some wave elevation data sets, respectively, from Galway Bay and from Pico. Although, as mentioned, it is not easy to derive any quantitative results from the Wavelet transform of the wave records, it is still possible to get some interesting information out of them. Note, in fact, how the different frequency components of the Fourier spectrum may appear in different time instants so that, in the short term, the bandwidth of the wave signal could actually be much narrower than the Fourier transform suggests.

6.3.3 Linearity analysis

Ocean waves are not typically linear, and it would be helpful and valuable to quantify how far from linearity they are so that, in the particular case of wave forecasting, a proper model can be chosen. Based on the theory of irregular waves, introduced in Section 3.1.2, linear waves can be expressed as a linear superposition of harmonic components (sines and cosines). More precisely, a linear wave signal satisfies the property of homogeneity (additivity) and scaling with respect to its harmonic components. Interactions (cross-products) between different harmonics represent non-linearities of the ocean wave signal.

The emergence of non-linearities in waves manifests itself, in the first instance, by a non-symmetric distribution of the wave elevation time series around its mean value (usually zero, the still water surface level), due to the presence of higher and narrower peaks than troughs, modelled by quadratic, cubic, ... and so on, terms of the linear harmonic components, according to Stokes theory [163]. The degree of asymmetry depends on the significance of the water depth, h , with respect to the wavelength, λ (the difference between the greatest elevation and the greatest depression is minimum for $h \gg \lambda$ and maximum otherwise). The non-linearity is expected, therefore, to be more consistent at the high-energy and low-frequency components of the waves when the water depth is not sufficiently large. Statistical analysis of the time history of wave records indicates that the wave profiles, in deep water, defined by condition (3.22), are distributed according to a Gaussian curve, apart some very small deviations on rare occasions [44]. A higher-order statistical analysis, through the indices of kurtosis and skewness, would therefore be useful to assess the extent of a non-Gaussianity of the wave records.

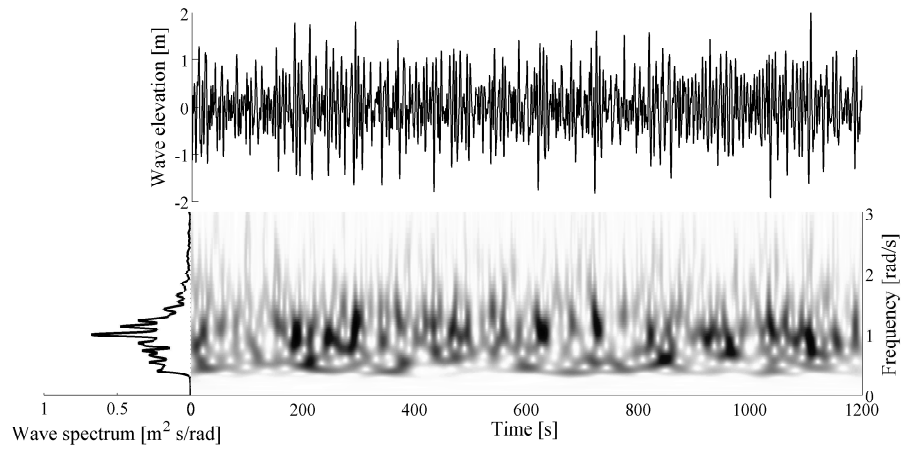
Given the n th-order central moments, μ_n , of a certain random variable x :

$$\mu_n = E\{(x - \mu)^n\}, \quad (6.23)$$

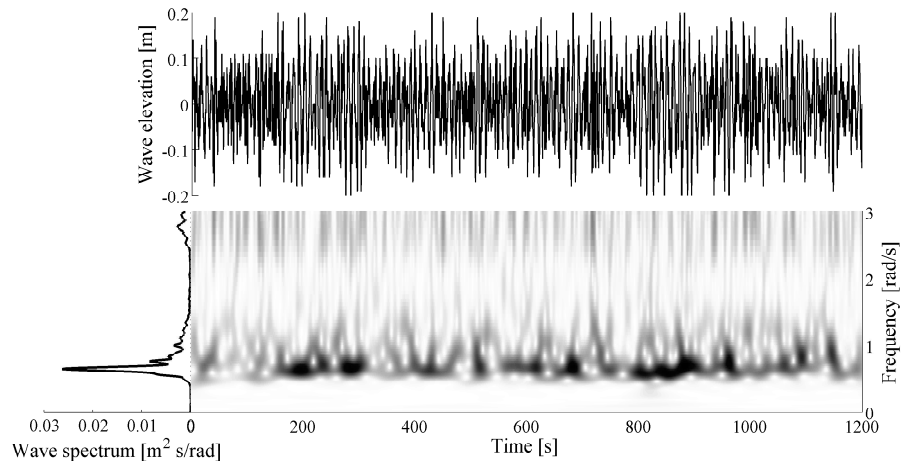
where $E\{\cdot\}$ is the expectation operator and μ is the mean, $E\{x\}$, of the random variable x , then the two indices of kurtosis, κ , and skewness, γ , are given by [164]:

$$\gamma = \frac{\mu_3}{\sigma^3} \quad (6.24)$$

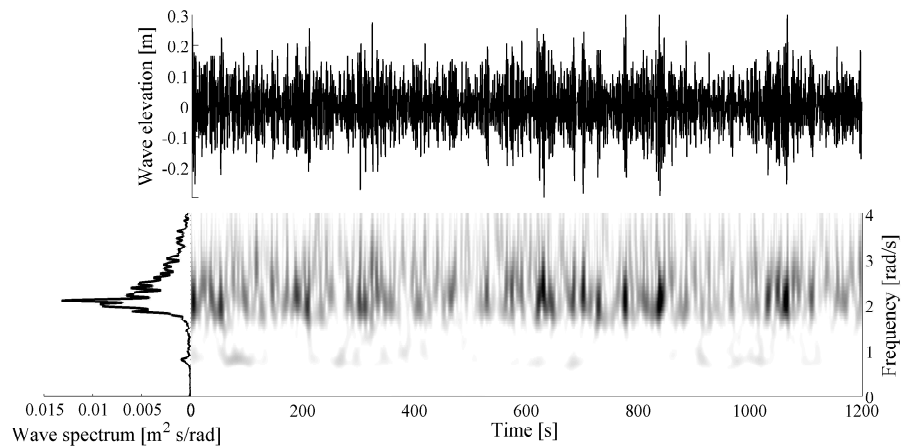
$$\kappa = \frac{\mu_4}{\sigma^4}, \quad (6.25)$$



(a) Set G_1

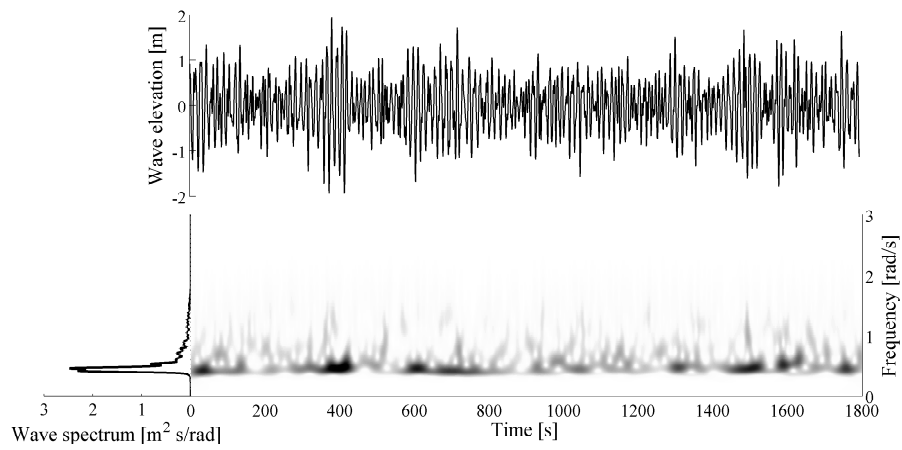


(b) Set G_2

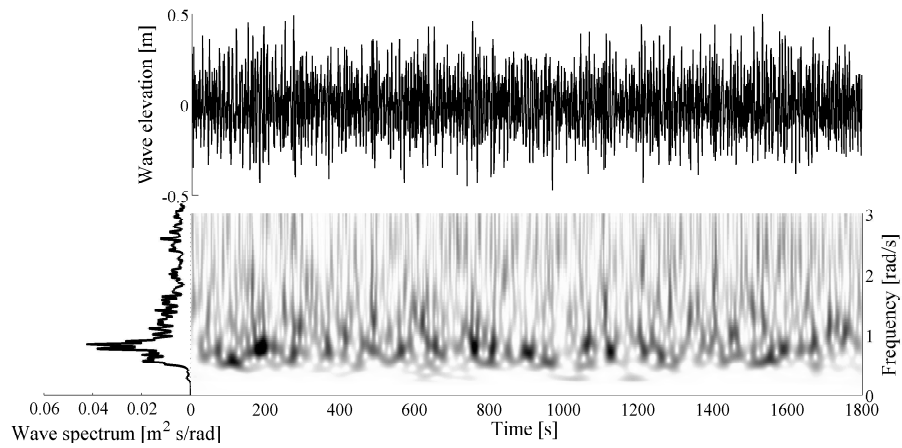


(c) Set G_3

Figure 6.4: Wavelet transform for three different data sets from Galway Bay.



(a) Set P_2



(b) Set P_2

Figure 6.5: Wavelet transform for two different data sets from the Pico Island.

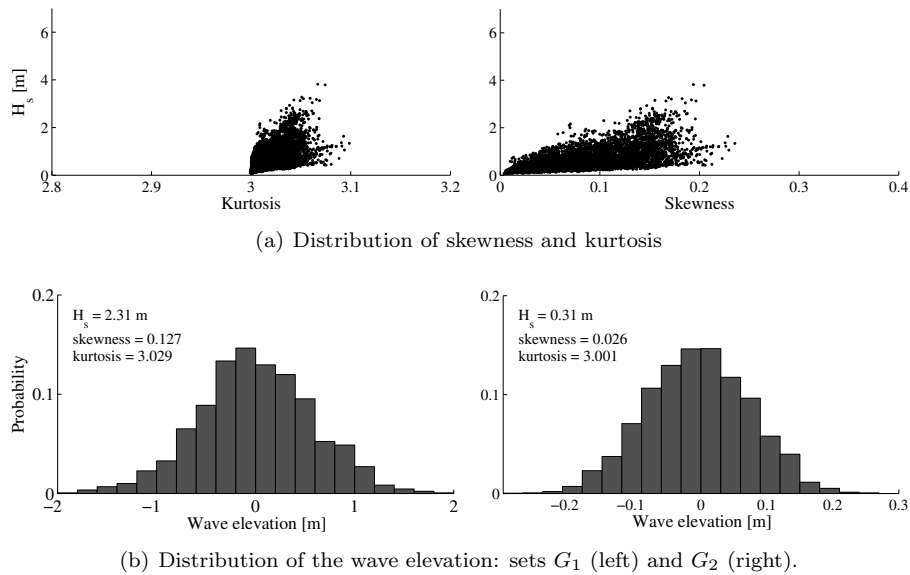


Figure 6.6: Gaussianity analysis at the Galway Bay.

where $\sigma^2 \equiv \mu_2$ is the central moment of order 2. The skewness measures the asymmetry of the distribution: $\gamma = 0$ denotes a symmetric distribution, otherwise, if $\gamma > 0$, the distribution is more concentrated around a value greater than the mean and viceversa if $\gamma < 0$. The kurtosis represents a degree of peakedness as compared to a Gaussian distribution, in which case $\kappa = 3$: if $\kappa > 3$ the distribution is termed *leptokurtic* (sharp peak), otherwise, if $\kappa < 3$, it is termed *platykurtic* (mild peak) [164].

Figures 6.6 and 6.7 show the distribution of κ and γ against the significant wave height (energy), for the available records from the two locations of Galway Bay and the Pico Island. As expected, higher-energy data sets show a slight deviation of the indices of skewness and kurtosis from the normality condition, particularly in the case of Galway Bay, where the water depth is smaller (nearly 20 m), while at Pico Island only very high-energy waves move away from normality, as shown in the wave distribution of Fig. 6.7(b).

From a wave energy point of view, although the interest is obviously focused on high-energy waves, the non-symmetry effect may not be an issue if deep water locations are considered. There is, however, another possible non-linearity, which is due to the interactions occurring between different harmonic components of the waves, which are neglected in the classical linear wave theory and in Fourier/Wavelet analysis. A higher-order analysis, via the bispectrum [44], proved to be effective in order to detect cross-frequency interactions; however, the bispectrum is hard to quantify and, in our analysis, we will not go beyond visual inspection. Non-linear cross-frequency interactions are known to be more present in wind waves, which represent high-frequency and low-energy waves and are less interesting from a wave energy point of view. A low-pass filtering of the wave elevation time series, in particular, may help to reduce their effect so that they are not taken into account by the forecasting model.

Figures 6.8 and 6.9 represent the bispectra calculated for some significant data sets from Galway Bay and Pico Island, respectively. The off-diagonal components appear if an interaction between two corresponding frequencies exists, and it is evident how they are usually strong for high fre-

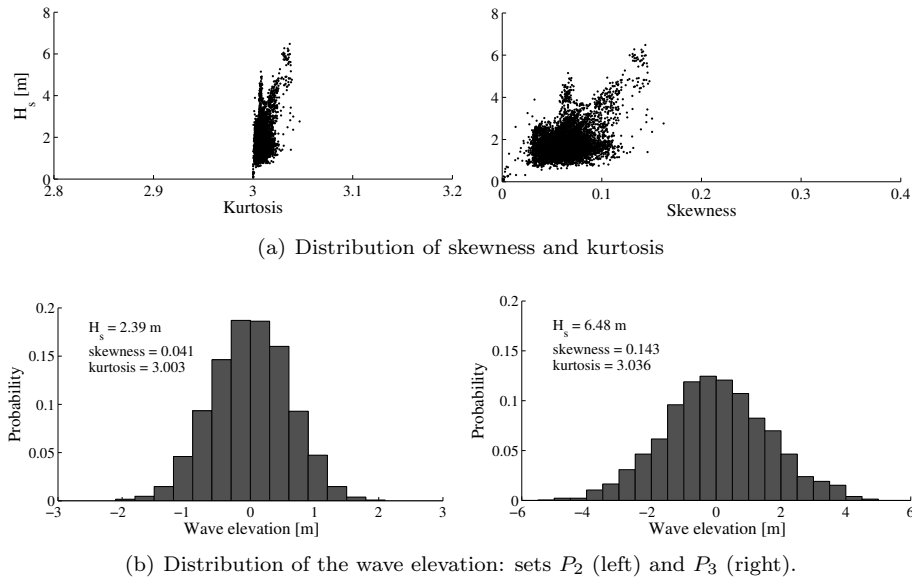


Figure 6.7: Gaussianity analysis at the Pico Island.

quency wind waves interacting with the swell (as in Fig. 6.8(c)) or for broad spectra resulting from the superposition of different sea states (Fig. 6.8(a) and Fig. 6.9(b)). The bispectrum is, on the other hand, much more concentrated around the diagonal for narrow-banded swell systems, as it can be noted from Fig. 6.8(b) and Fig. 6.9(a).

6.3.4 Predictability measure

Since the focus of this Chapter is on the multi-step prediction of the wave elevation (or of its effect on the WEC, such as the excitation force), one of the striking questions is this: Is there any chance to predict future values of a given wave time series? Usually, we design a predictor for a special signal or problem and then measure the resulting prediction quality. If there is no *a priori* knowledge on the optimal predictor, the achieved prediction accuracy will depend strongly on the particular prediction model used. Here, it is argued that, for prediction feasibility analysis, it is not necessary to design any particular predictors; we just have to know how much information about future signal values can be obtained from the past [165].

A measure of predictability, simpler than the very general approach proposed in the literature (based on the mutual information notion [165],[46],[166],[167]), will be adopted here, which supposes that a linear relationship exists that relates the future values of the wave elevation to the past. This is, of course, a limiting assumption, but it is still very valuable in providing at least a qualitative study over the predictability of the wave elevation. At the same time, from the analysis of Section 6.3.3, linearity of the wave elevation may be assumed in most situations, at least at the low frequencies of interest for wave energy.

In particular, a predictability index, $R^2[l]$, of a signal, $x[k]$, is defined as the ratio of the variance of the optimal l -step-ahead prediction, $\hat{x}[k+l|k]$, to the variance of the signal itself [45]. In the

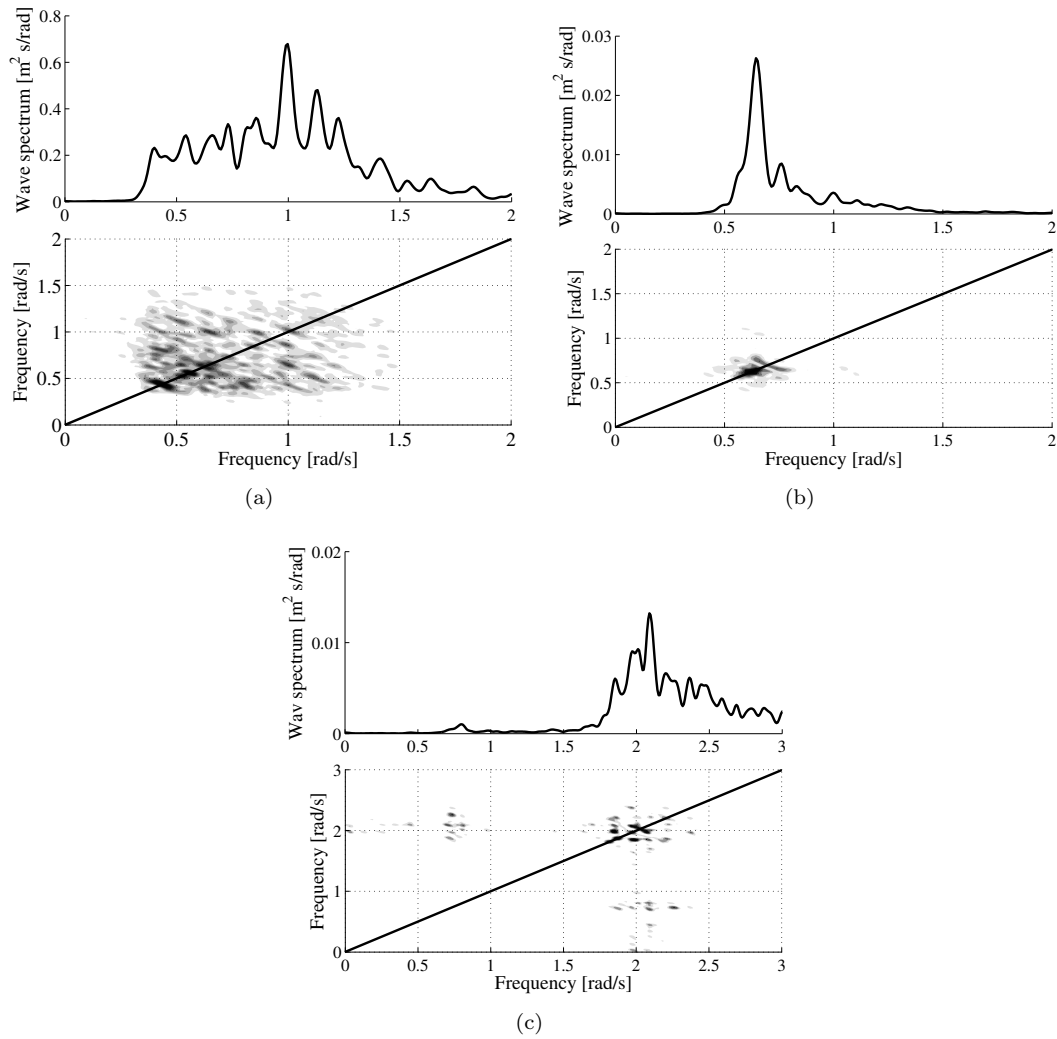


Figure 6.8: Bispectrum of some data sets from Galway Bay: (a) G_1 ; (b) G_2 ; (c) G_3 .

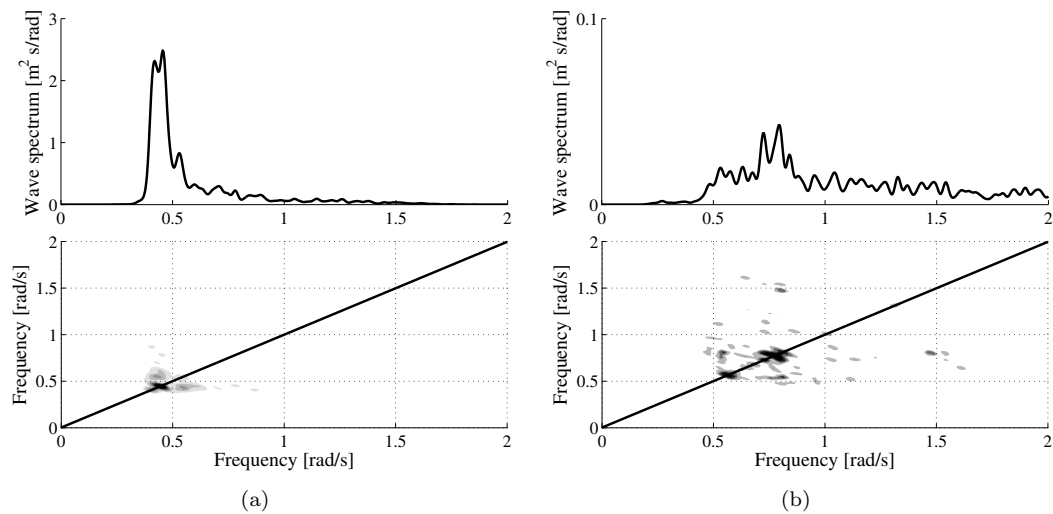


Figure 6.9: Bispectrum of some data sets from the Pico Island: (a) P_2 ; (b) P_1 .

case of the wave elevation, named $\eta[k]$ as usual:

$$R^2[l] \triangleq \frac{E\{\hat{\eta}[k+l|k]^2\}}{E\{\eta[k]^2\}} = 1 - \frac{\hat{\sigma}_l^2}{E\{\eta[k]^2\}}. \quad (6.26)$$

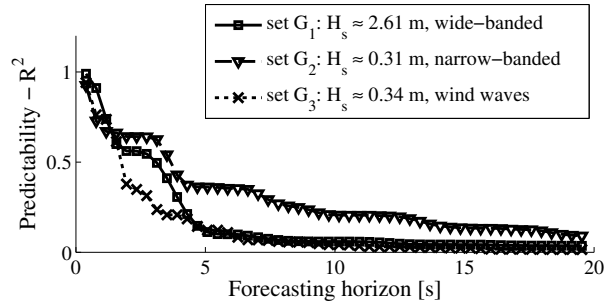
In the second equivalence of (6.26), it is assumed that the prediction error, $\hat{\epsilon}[k+l|k] \triangleq \eta[k] - \hat{\eta}[k+l|k]$, is zero-mean and uncorrelated with the optimal prediction. The variance of the optimal prediction error, $\hat{\sigma}_l^2$, is defined as $\hat{\sigma}_l^2 \triangleq E\{\hat{\epsilon}[k+l|k]^2\}$.

A very efficient algorithm for the estimation of $R^2[l]$, under the assumption of a linear univariate time series, was proposed in [45] and it is adopted here for the analysis of the available wave data. More in particular, the time series is modelled as a Moving average (MA) process with very large lag, whose coefficient are calculated from a AR model of very large order. The MA model is then utilised for the calculation of the variance of the multi-step prediction error, $\hat{\sigma}_l^2$. Figure 6.10 shows the estimated predictability index, $R^2[l]$, over a forecasting horizon of 50 samples, for different wave records at the two locations of Galway Bay and Pico Island. As expected, predictability is a non-increasing function of the prediction horizon. All the sea states considered for the Galway Bay location, as seen in Fig. 6.10(a), show a relatively poor predictability, which dies out very quickly after 2 – 4 seconds (5 – 10 samples), with a slightly better behavior of the narrow-banded waves and of the high-energy one. A much better predictability (index R^2 is relatively high for more than 5 seconds) results for the high-energy and narrow-banded waves at Pico Island, in Fig. 6.10(b), mostly due to the smaller influence of the non-linearities analysed in Section 6.3.3, consisting of either asymmetry in the wave distribution or non-linear interactions between different frequency components.

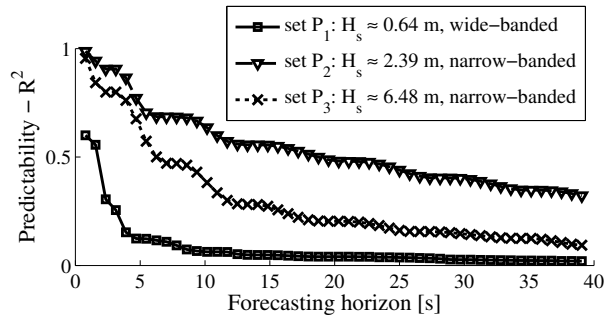
In a wave energy context, however, one might be interested in forecasting only the high-energy components, so that a low-pass filter can be applied to the time series and a focus would be put exclusively on the low-frequency components. Besides, wave components at high frequency may be filtered out by the WEC, depending on its geometry, and there would be no value in their prediction. More details about the low-pass filtering characteristics of the device will be given when the focus is moved from the prediction of the wave elevation to the prediction of the wave excitation force, in Section 6.6.

In Fig. 6.11, the estimated predictability index, $R^2[l]$, is shown for the pre-filtered waves at Galway Bay and when different cut-off frequencies, ω_c , are applied. Ideal zero-phase low-pass filters are approximated with off-line forward and backward filtering through type-I Chebyshev filters (order 15, maximum error in the pass-band 10^{-3}) discretised with the bilinear transform (no pre-warping was required since distortion does not affect the frequencies in the pass band). The cut-off frequencies have been chosen according to the specific shape of the wave spectra (shown in Fig. 6.3).

It is clear, by comparison with Fig. 6.10, how the overall predictability significantly improves compared to the non-filtered waves. Moreover, the smaller the cut-off frequency, i.e. the lower the frequencies we limit the analysis to, the better the predictability of the filtered time series, when a swell at the low frequencies is present, and more accurate predictions, further in the future, can be expected. The highly non-linear wind-waves system, set G_3 in Fig. 6.11, shows only a minor improvement with filtering, though. This should not, however, be a big issue in a wave-energy context, where such waves are of little interest due to the very low-energy content, distributed at



(a) Galway Bay data



(b) Pico Island data

Figure 6.10: Predictability index, $R^2[l]$, estimated for the selected wave records.

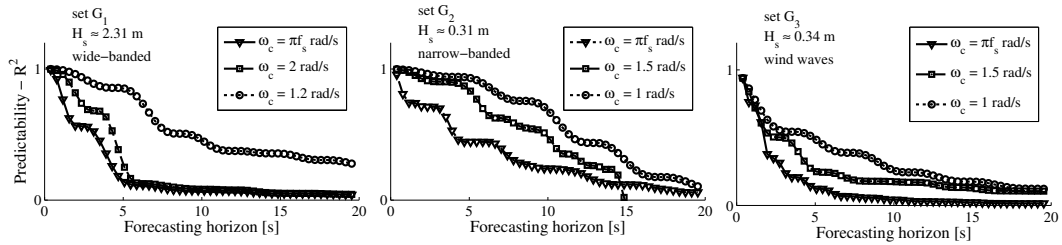


Figure 6.11: Predictability of some wave elevation data sets from the Galway Bay, when low-pass filtering with different cut-off frequencies, ω_c , is applied.

relatively high frequency, as compared to the dynamics of WECs.

Figure 6.12 depicts the situation for the Pico Island data. In this case, the narrow-banded swells, that are sets P_2 and P_3 , derive the best improvement from considering only the low frequency components. The same improvement is not achieved for the wide-banded sea state, set P_1 , that is more strongly affected by the non-linearities analysed in Section 6.3.3.

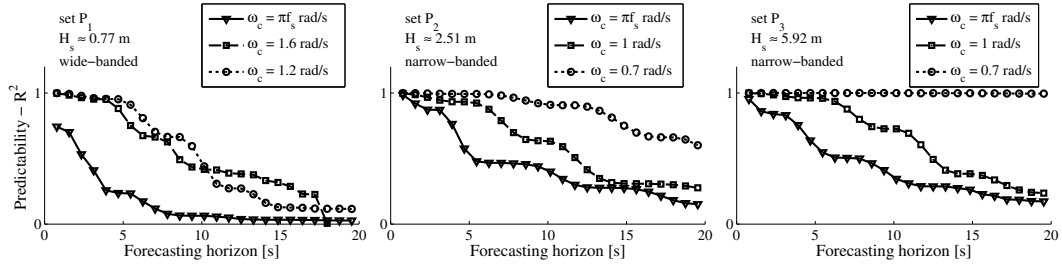


Figure 6.12: Predictability of some wave elevation data sets from the Pico Island, when low-pass filtering with different cut-off frequencies, ω_c , is applied.

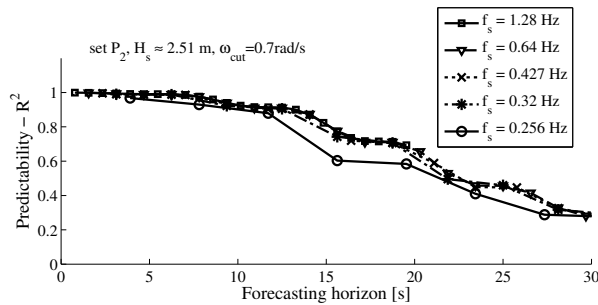


Figure 6.13: Estimated predictability for a wave elevation time series from the Pico Island, when different sampling frequencies are adopted.

6.3.5 Effect of the sampling frequency on the predictability

In general, if a signal has a limited support in the frequency domain, $[0 \ \omega_m]$ rad/s, then all the information is maintained if the signal is discretised with any sampling frequency $f_s \geq \omega_m/\pi$ Hz. Lower sampling frequencies give rise to the *aliasing* phenomenon, thus causing the sampled time series not to be uniquely representative of the original signal.

If a wave elevation time series is low-pass filtered before the prediction, this means that it can be sampled, without any loss of information, with $\omega_s \geq \omega_c/2$, where ω_c is the cut-off frequency of the filter (assuming an ideal filter with ideal transition). A given time span of the wave elevation signal is represented by fewer samples if the sampling frequency is lower. It may be, therefore, that the choice of the sampling frequency could affect the performance of a prediction algorithm, in particular its forecasting horizon in terms of seconds.

In theory, the information that the past of a signal has about its future, will not be affected by the sampling frequency, if aliasing is avoided. Therefore, a proper forecasting model that manages to extract all the information to produce the prediction, should not perform differently by changing the sampling frequency. Figure 6.13 shows, in fact, how the predictability of a certain wave-elevation data set is not affected by a change in the sampling frequency, when this is greater than the Nyquist frequency.

In practice, however, when performing the prediction, some differences might arise, so it is interesting to assess the effect of the sampling frequency on the prediction accuracy of the forecasting models that will be presented in Section 6.4. This analysis will be carried out in Section 6.5.5.

6.4 Forecasting models

6.4.1 Cyclical models

From linear wave theory [6], introduced in Section 3.1.2, a real ocean wave may be modelled as a linear superposition of regular waves with different frequencies, propagating in different directions:

$$\eta(x, y, t) = \int_0^{+\infty} d\omega \int_{-\pi}^{+\pi} A(\omega, \beta) \cos(\omega t - kx \cos \beta - ky \sin \beta + \varphi(\omega, \beta)) d\beta, \quad (6.27)$$

where k is the wave number, β represents the direction of propagation in the x - y plane, and $A(\omega, \beta)$ and $\varphi(\omega, \beta)$ are the amplitude and initial phase of each harmonic component, respectively. If a specific location, (x_0, y_0) , is considered, the following simplified expression can be obtained:

$$\eta(x_0, y_0, t) = \int_0^{+\infty} d\omega \int_{-\pi}^{+\pi} A(\omega, \beta) \cos(\omega t + \phi(\omega, \beta)), \quad (6.28)$$

where the directionality information is obviously lost and the constant terms, $kx_0 \cos \beta$ and $ky_0 \sin \beta$, are included in the phase $\phi(\omega, \beta)$.

Based on such knowledge about the real process, it is quite straightforward to choose, as a forecasting model for the wave elevation, a simple cyclical model, where the frequency domain is discretised over a number, m , of frequencies [148, 23, 16]:

$$\eta(t) = \sum_{i=1}^m a_i \cos(\omega_i t) + b_i \sin(\omega_i t) + \zeta(t) \quad (6.29)$$

An error term, $\zeta(t)$, has been introduced and the phase and amplitude information for each harmonic component is now contained in the parameters a_i and b_i .

The model (6.29) is completely characterised by the amplitudes, a_i and b_i , and by the frequencies, ω_i . It could then be fitted to the data through some non-linear estimation procedure (the model is non-linear in the frequencies) and utilised to predict the future behavior of the wave time series. It needs, however, to be adapted to the time variations of the wave spectrum (amplitudes and phases of the frequency components are non-constant), but a first approach can be considered, where the frequencies are chosen at the model-design phase and then kept constant during its utilisation and estimation. In this way, the model becomes perfectly linear in the parameters a_i , b_i and can be easily estimated and on-line adapted to the spectral variations of the sea.

The problem of choosing the frequencies can be divided in two sub-problems:

1. **Choice of the range:** This is quite an easy matter, as statistical information about the location can be utilised to properly define an upper and lower bound for the range. At this point, one may decide to include the range of higher frequencies where the low energy wind waves are, or to simply consider a narrower range including only the swell.
2. **Distribution of the frequencies in the range:** A robust choice would be a constant spacing between the frequencies over all the range, but a more efficient non-homogeneous distribution was also proposed in [23]. The latter, however, suffers from the problem of specificity, so that

if the wave spectrum changes the frequencies might not be appropriate any more. If the frequencies are kept constant, then it would not be a proper choice.

Once the frequencies are determined, a model for the amplitudes has to be chosen. In [23, 16] it was pointed out that they have to be adaptive to the wave, since constant amplitudes gave very poor results. Two adaptive models are proposed here, in particular:

Structural model: based on Harvey's structural model [168], the model in (6.29) is expressed in the following discrete-time form:

$$\eta[k] = \sum_{i=1}^m \psi_i[k] + \zeta[k] \quad (6.30)$$

$$\begin{bmatrix} \psi_i[k+1] \\ \psi_i^*[k+1] \end{bmatrix} = \begin{bmatrix} \cos(\omega_i T_s) & \sin(\omega_i T_s) \\ -\sin(\omega_i T_s) & \cos(\omega_i T_s) \end{bmatrix} \begin{bmatrix} \psi_i[k] \\ \psi_i^*[k] \end{bmatrix} + \begin{bmatrix} w_i[k] \\ w_i^*[k] \end{bmatrix}, \quad i = 1, \dots, m \quad (6.31)$$

where it can be verified that $\psi_i(0) = a_i$ and $\psi_i^*(0) = b_i$. From (6.31), then, the following state-space form is easily derived:

$$\begin{aligned} x[k+1] &= Ax[k] + w[k] \\ \eta[k] &= Cx[k] + \zeta[k], \end{aligned} \quad (6.32)$$

where

$$x[k] \triangleq [\psi_1[k] \quad \psi_1^*[k] \quad \dots \quad \psi_m[k] \quad \psi_m^*[k]]^T \in \mathbb{R}^{2m \times 1} \quad (6.33)$$

$$w[k] \triangleq [w_1[k] \quad w_1^*[k] \quad \dots \quad w_m[k] \quad w_m^*[k]]^T \in \mathbb{R}^{2m \times 1} \quad (6.34)$$

$$A \triangleq \text{diag} \left\{ \begin{bmatrix} \cos(\omega_i T_s) & \sin(\omega_i T_s) \\ -\sin(\omega_i T_s) & \cos(\omega_i T_s) \end{bmatrix} \right\} \in \mathbb{R}^{2m \times 2m} \quad (6.35)$$

$$C \triangleq [1 \quad 0 \quad 1 \quad 0 \quad \dots \quad 1 \quad 0] \in \mathbb{R}^{1 \times 2m}. \quad (6.36)$$

Dynamic harmonic regression (DHR): Introduced by Young [169], it expresses a cyclical model of the type in (6.29), where a_i and b_i evolve according to a Generalised random walk (GRW):

$$\begin{bmatrix} x_i[k+1] \\ x_i^*[k+1] \end{bmatrix} = \begin{bmatrix} \alpha & \beta \\ 0 & \gamma \end{bmatrix} \begin{bmatrix} x_i[k] \\ x_i^*[k] \end{bmatrix} + \begin{bmatrix} \delta & 0 \\ 0 & 1 \end{bmatrix} \begin{bmatrix} \epsilon_i[k] \\ \epsilon_i^*[k] \end{bmatrix}, \quad (6.37)$$

where

$$x_i[0] = a_i \quad \text{for } i = 1, \dots, m \quad (6.38)$$

$$x_{i-m}[0] = b_i \quad \text{for } i = m+1, \dots, 2m \quad (6.39)$$

and x_i^* models a slope for the evolution of each parameter x_i . The disturbance terms, ϵ_i and ϵ_i^* , are assumed to be Gaussian noises and introduce the variability in the model. A particular form of (6.37) was implemented in this study, where the dynamic matrices are

chosen in order to represent Harvey's local linear trend [168]:

$$\begin{bmatrix} x_i[k+1] \\ x_i^*[k+1] \end{bmatrix} = \begin{bmatrix} 1 & 1 \\ 0 & 1 \end{bmatrix} \begin{bmatrix} x_i[k] \\ x_i^*[k] \end{bmatrix} + \begin{bmatrix} 1 & 0 \\ 0 & 1 \end{bmatrix} \begin{bmatrix} \epsilon_i[k] \\ \epsilon_i^*[k] \end{bmatrix}, \quad i = 1, 2, \dots, 2m. \quad (6.40)$$

A state-space form can easily be derived, from (6.29) and (6.40):

$$\begin{aligned} x[k+1] &= Ax[k] + \epsilon[k] \\ \eta[k] &= C[k]x[k] + \zeta[k] \end{aligned} \quad (6.41)$$

where

$$x[k] \triangleq [x_1[k] \quad x_1^*[k] \quad \dots \quad x_{2m}[k] \quad x_{2m}^*[k]]^T \in \mathbb{R}^{4m \times 1} \quad (6.42)$$

$$\epsilon[k] \triangleq [\epsilon_1[k] \quad \epsilon_1^*[k] \quad \dots \quad \epsilon_{2m}[k] \quad \epsilon_{2m}^*[k]]^T \in \mathbb{R}^{4m \times 1} \quad (6.43)$$

$$A \triangleq \text{diag} \left\{ \begin{bmatrix} 1 & 1 \\ 1 & 0 \end{bmatrix} \right\} \in \mathbb{R}^{4m \times 4m} \quad (6.44)$$

$$C[k] \triangleq [\cos(\omega_1 T_s) \quad 0 \quad \dots \quad \cos(\omega_m T_s) \quad 0 \quad \dots \quad \sin(\omega_1 T_s) \quad 0 \quad \dots \quad \sin(\omega_m T_s) \quad 0] \in \mathbb{R}^{1 \times 4m}. \quad (6.45)$$

Both Harvey's structural model and the DHR have the advantage of a state space representation, which is particularly suited to the application of the Kalman filter for a recursive on-line adaptation (refer to appendix B). The initialisation is provided through means of regular LS on a number of past observations and then the Kalman filter is recursively applied on-line, once an appropriate covariance matrix for the state and output disturbances is provided. When the estimate of the state, $\hat{x}[k|k]$, is available at any instant, k , the l -step-ahead prediction of the wave elevation, $\hat{\eta}[k+l|k]$, based on the information up to the instant k , is obtained through the free evolution of the model:

$$\hat{\eta}[k+l|k] = C[k+l]A^l \hat{x}[k|k]. \quad (6.46)$$

There is one significant limitation to this approach with cyclical models, that will be highlighted also in the results, in Section 6.5. The use of constant frequencies requires, for the sake of robustness, a dense and complete set of frequencies, which adds considerable complexity to the model. In the next Section 6.4.2, it will be shown how AR models implicitly overcome such a difficulty in a very effective, and simple, way.

6.4.2 Auto Regressive (AR) models

Since a pure time-series problem is under study, there is the advantage of the existence of a well established theory, which it is possible to utilise. In a comparison with the cyclical models, where the *a priori* knowledge that we have about the real system is explicitly taken into account, it is particularly interesting to analyse the properties of classical AR models. Applications of AR models to wave forecasting (or to prediction of resulting motion of a WEC) may already be found in the wave-energy literature [95, 133], as discussed in Section 6.2.5, but they were only reported as preliminary work with limited and simplistic analysis.

The wave elevation, $\eta[k]$, is assumed to be linearly dependent on a number, n , of its past values:

$$\eta[k] = \sum_{i=1}^n a_i[k] \eta[k-i] + \zeta[k], \quad (6.47)$$

with an additional disturbance term, $\zeta[k]$. If the parameters, a_i , are estimated and the noise is supposed to be Gaussian and white, the best prediction of the future wave elevation, $\hat{\eta}[k+l|k]$, at instant k , is then given by:

$$\hat{\eta}[k+l|k] = \sum_{i=1}^n \hat{a}_i[k] \hat{\eta}[k+l-i|k], \quad (6.48)$$

where, obviously, $\hat{\eta}[k+l-i|k] \equiv \eta[k]$ if $k+l-i \leq k$ (i.e. the information is already acquired and there is no need for prediction).

The properties of such a very simple forecasting model become clearer if an explicit solution of the difference equation (6.48) is provided [170]:

$$\hat{\eta}[k+l|k] = \sum_{i=1}^n b_i[k] f_i[l]. \quad (6.49)$$

In (6.49), the coefficients, $b_i[k]$, depend only on the forecasting origin (so they stay constant at each instant, over the prediction horizon) and are a function of the initial conditions (the past n observations), whereas $f_i[l]$ are functions of the lead time, l , and, in general, they include damped exponential and damped sinusoidal terms completely determined by the roots, p_i , of the transfer function, $\varphi(z)$, describing equation (6.47) in the Z -domain:

$$\eta(z) = \frac{\zeta(z)}{\varphi(z)} \triangleq \frac{\zeta(z)}{\prod_{i=1}^n (z - p_i)}. \quad (6.50)$$

Based on (6.49), the general shape of the prediction function is completely determined by the poles, p_i , while the particular realisation of the general structure is determined, at each sampling instant, by the past values of the time series. It is particularly interesting to analyse the shape of the forecasting function, in (6.49), in the case of $n/2$ (when n is even) couples of complex-conjugate

poles, p_i and p_i^* :

$$\hat{\eta}[k+l|k] = \sum_{i=1}^{n/2} c_i[k] |p_i|^l \sin(\angle p_i k + \varphi_i[k]). \quad (6.51)$$

Thus, an AR model with only complex-conjugate poles is *implicitly* a cyclical model, where the frequencies are related to the phase, $\angle p_i$, of each pole and the amplitudes and phases of the harmonic components are related to the last n observations of each time instant k , so that they adapt to the observations.

Since the purpose of the model is multi-step prediction, the AR coefficients, a_i , are estimated from a number, N , of batch observations through the minimisation of a multi-step-ahead cost functional, referred to as Long-range predictive identification (LRPI) [171]:

$$J_{LRPI} = \sum_{k=1}^N \sum_{j=1}^{N_l} [\eta[k] - \hat{\eta}[k|k-j]]^2, \quad (6.52)$$

where N_l is the forecasting horizon over which the AR model is to be optimised. The function J_{LRPI} is minimised with a standard algorithm for non-linear least squares problems, the Gauss-Newton algorithm, initialised with the estimates from regular LS [171].

Note that an adaptivity mechanism is already present even if the parameters of the AR model are only estimated once on a batch data set. Only the frequencies, in this case, are fixed, while amplitudes and phases are automatically updated on the basis of the recent past information. A further degree of adaptivity can be introduced with an on-line estimation of the AR model parameters, a_i , which would introduce an on-line adaptivity of the frequencies as well. If we express the model (6.47) in vectorial form:

$$\eta[k] = \psi[k]^T \vartheta[k] + \zeta[k], \quad (6.53)$$

where

$$\psi[k] \triangleq [\eta[k-1] \quad \eta[k-2] \quad \dots \quad \eta[k-n]]^T \in \mathbb{R}^{n \times 1} \quad (6.54)$$

$$\vartheta[k] \triangleq [a_1[k] \quad a_2[k] \quad \dots \quad a_n[k]]^T \in \mathbb{R}^{n \times 1}, \quad (6.55)$$

then a general recursive estimation of the time-varying parameter vector, $\vartheta[k]$, is given as:

$$\hat{\vartheta}[k+1] = \hat{\vartheta}[k] + K[k] \left(\eta[k+1] - \psi[k]^T \hat{\vartheta}[k] \right), \quad (6.56)$$

as a sum of free evolution (prediction) and innovation (correction based on new information). How the gain vector, $K[k] \in \mathbb{R}^{n \times 1}$, is chosen depends on which specific estimation algorithm is utilised. The most common approaches are the Recursive least squares (RLS) with forgetting factor and the Kalman Filter, which are outlined hereafter.

Recursive least squares (RLS): With this approach the following functional is minimised:

$$J(\vartheta[k]) = \sum_{j=1}^k \lambda^{k-j} (\eta[j] - \psi[j]\vartheta[k])^2, \quad (6.57)$$

where more weight, via the forgetting factor, $\lambda < 1$, is given to recent observations, according to an exponential law. The recursive algorithm for the optimal value of $\vartheta(k)$, that minimises the functional $J(\vartheta[k])$, respects the general form in (6.56), with the gain, $K(k)$, given as:

$$K[k] = P[k]\psi[k] \quad (6.58)$$

$$P[k] = \frac{P[k-1]}{\lambda + \psi^T[k]P[k-1]\psi[k]}. \quad (6.59)$$

The forgetting factor, λ , is typically chosen in the range [0.97, 0.995] [172].

The matrix $P[k] \in \mathbb{R}^{n \times n}$ is the covariance matrix of the estimate $\hat{\vartheta}[k]$:

$$P[k] \triangleq E\{\hat{\vartheta}[k]\hat{\vartheta}^T[k]\}. \quad (6.60)$$

It is interesting to also introduce the information matrix, $R[k] \in \mathbb{R}^{n \times n}$, defined as:

$$\begin{aligned} R[k] \triangleq \psi[k]\psi[k]^T + \lambda\psi[k-1]\psi[k-1]^T + \dots + \lambda^{k-1}\psi[1]\psi[1]^T + R[0] = \dots \\ \dots = \lambda R[k-1] + \psi[k]\psi[k]^T, \end{aligned} \quad (6.61)$$

which can also be shown to correspond to [172]:

$$R[k] \equiv P[k]^{-1}. \quad (6.62)$$

One main problem of RLS with a forgetting factor occurs, when the measurements do not add new information to the system, that is when $\psi[k]$ is approximately zero for a certain time. In the latter situation, the information matrix decreases until it gets close to the null matrix (or some of its eigenvalues tend to zero). At the same time, some of the elements of the corresponding gain, $K[k]$, may significantly increase. When $\psi[k]$, then, increases again in magnitude, the estimate, $\hat{\vartheta}[k]$, can experience a very large growth, known as the phenomenon of blow-up. Some regularisation solutions have been proposed to cope with this problem [173]. One possibility is to monitor the covariance matrix, $P[k]$, and reset its values to acceptable ones when its eigenvalues assume too large values [172]. Another approach may be a variable forgetting factor, based on the state of the process (steady or transient) [172], or regularisation of the information matrix $R[k]$ [174].

Kalman filter: If the evolution of the state vector, $\vartheta[k]$, is assumed to be a Random walk (RW):

$$\vartheta[k] = \vartheta[k-1] + \varepsilon[k], \quad (6.63)$$

where $\varepsilon[k]$ is a Gaussian random process, then the Kalman Filter may be applied, resulting

in the recursive form of (6.56), where the gain, $K[k]$, is now given by [153]:

$$K[k] = Q[k]\psi[k], \quad (6.64)$$

with

$$Q[k] = \frac{P[k-1]}{R_2 + \psi^T[k]P[k-1]\psi[k]} \quad (6.65)$$

$$P[k] = P[k-1] + R_1 - \frac{P[k-1]\psi[k]\psi[k]^T P[k-1]}{R_2 + \psi^T[k]P[k-1]\psi[k]}, \quad (6.66)$$

where $R_1[k] = E\{\varepsilon[k]\varepsilon[k]^T\}$ and $R_2 = E\{\zeta[k]^2\}$. Here, $P[k]$ still represents the covariance matrix of the estimate, $\hat{\vartheta}[k]$. More detailed information about the Kalman filter may be found in appendix B.

Both RLS and the Kalman filter minimise the one-step-ahead prediction error, so that they may not be suitable for long range prediction, such as in our study of the wave forecasting problem. An adaptivity mechanism based on the LRPI function, in (6.52), can also be implemented, as proposed in [171]. However, as will also be shown in the results of Section 6.5.2, a static AR model maintains its accuracy for a long time after being estimated (more than 2 hours), in spite of spectral variations. Adaptive AR models, therefore, are not a priority and only some results based on the Kalman filter algorithm will be shown.

6.4.3 Sinusoidal extrapolation and the EKF

The main problem with the cyclical model is the choice of the frequencies, that must be kept constant in order for the model to be linear in the parameters. Efficient linear algorithms for the recursive estimation of the amplitudes (and phases) of the harmonic components can therefore be exploited. This means that the accuracy of the model is strictly connected to its capacity to cover as much as possible of the typical range of frequencies where the waves at the considered location are mostly concentrated. This approach lacks efficiency and requires a much more complex method than what would actually be required. In reality, few regular waves in the typical range will be active at each time instant, as it emerged from the non-stationary analysis, based on the Wavelet transform, in Section 6.3.3.

A more intelligent solution, then, would be to consider a few (or even one) cyclical component with an *adaptive frequency* which is updated on-line with the real observations. We propose, therefore, to model the wave elevation as a single cyclical component, as in the Harvey's structural model, in (6.31), but with a time-varying frequency, $\omega[k]$:

$$\begin{cases} \begin{bmatrix} \psi[k+1] \\ \psi^*[k+1] \end{bmatrix} = \begin{bmatrix} \cos(\omega[k]T_s) & \sin(\omega[k]T_s) \\ -\sin(\omega[k]T_s) & \cos(\omega[k]T_s) \end{bmatrix} \begin{bmatrix} \psi[k] \\ \psi^*[k] \end{bmatrix} + \begin{bmatrix} \varepsilon[k] \\ \varepsilon^*[k] \end{bmatrix}, \\ \eta[k] = \psi[k] + \zeta[k] \end{cases}, \quad (6.67)$$

where $\varepsilon[k]$, $\varepsilon^*[k]$ and $\zeta[k]$ are random disturbances and $\eta[k]$ is the wave elevation. Along with the components $\psi[k]$ and $\psi^*[k]$, the frequency, $\omega[k]$, also needs to be estimated. A state vector, $x[k]$,

composed of the quantities that need to be estimated, is then defined as:

$$x[k] \triangleq [\psi(k) \quad \psi^*(k) \quad \omega(k)]^T \in \mathbb{R}^{3 \times 1}. \quad (6.68)$$

The system in (6.67) can then be re-defined in terms of the state, $x[k]$, as:

$$\begin{cases} \begin{bmatrix} \psi[k+1] \\ \psi^*[k+1] \\ \omega[k+1] \end{bmatrix} = \begin{bmatrix} \cos(\omega[k]T_s) & \sin(\omega[k]T_s) & 0 \\ -\sin(\omega[k]T_s) & \cos(\omega[k]T_s) & 0 \\ 0 & 0 & 1 \end{bmatrix} \begin{bmatrix} \psi[k] \\ \psi^*[k] \\ \omega[k] \end{bmatrix} + \begin{bmatrix} \varepsilon[k] \\ \varepsilon^*[k] \\ \kappa[k] \end{bmatrix} \\ \eta[k] = \psi[k] + \zeta[k] \end{cases} \quad (6.69)$$

In (6.69), a model for the variability of the frequency, $\omega[k]$, has been introduced, where a RW is proposed, driven by the additional white noise, $\kappa[k]$. The model is non-linear in the frequency and an explicit state-space structure cannot be formulated, so the following form is adopted:

$$\begin{cases} x[k+1] = f(x[k], w[k]) \\ \eta[k] = [1 \quad 0 \quad 0] x[k] + \zeta[k] \end{cases}, \quad (6.70)$$

where $f(x[\cdot], w[\cdot]) \in \mathbb{R}^{3 \times 1}$ is a vectorial, non-linear function and $w[k] \triangleq [\varepsilon[k] \quad \varepsilon^*[k] \quad \kappa[k]]^T \in \mathbb{R}^{3 \times 1}$ is the vectorial form of the state disturbance.

The optimal estimate (in the sense of minimising the variance) of $x(k)$, based on the observations, $Z_{k-1} = \{\eta(0), \dots, \eta(k-1)\}$, is known to be given by the conditional mean value [53]:

$$\hat{x}[k|k-1] = E\{x[k]|Z_{k-1}\}. \quad (6.71)$$

An explicit expression which is usable in practice is difficult to obtain, though, because of the non-linearity of the system. The application of a very efficient algorithm for linear (and Gaussian) systems, that is the Kalman filter (refer to appendix B), is, however, possible in the form of its (sub-optimal) extension to non-linear problems, known as the EKF. The EKF assumes that the discrete time steps (sampling time T_s) are sufficiently small to permit the prediction equations to be approximated by a linearised form, based on the truncation of the Taylor expansion of the model (6.70), at the first order [175]:

$$x[k+1] \approx f(\bar{x}[k], w) + \left[\frac{d}{dx} f(x[k], w[k]) \right]_{x[k]=\bar{x}[k]} (x[k] - \bar{x}[k]), \quad (6.72)$$

where $\bar{x}[k]$ represents an opportune working point for the state of the system, whose variation is supposed to be small within the time step, T_s , considered. Based on the linear approximation, the following state-space form can be derived to describe the model in (6.70):

$$\begin{cases} x[k+1] \approx A[k]x[k] + F[k] + w[k] \\ \eta[k] = Cx[k] + \zeta[k] \end{cases}, \quad (6.73)$$

where

$$A[k] \triangleq \left[\frac{d}{dx} f(x[k], w[k]) \right]_{x[k]=\bar{x}[k]} \in \mathbb{R}^{3 \times 3} \quad (6.74)$$

$$F[k] \triangleq f(\bar{x}[k], w[k]) - A[k]\bar{x}[k] \mathbb{R}^{3 \times 1} \quad (6.75)$$

$$C \triangleq [1 \ 0 \ 0] \mathbb{R}^{1 \times 3}. \quad (6.76)$$

The iterative equations for computing the gain, $K[k]$, of the Kalman filter [153] can directly be derived from this linear state-space form (6.73), where the operating point at each step is set as the optimal one-step-ahead estimate of the state, $\bar{x}[k] = \hat{x}[k+1|k]$, which is updated based on the non-linear model:

$$\begin{aligned} \hat{x}[k+1|k] &= f(\hat{x}[k|k], [0 \ 0 \ 0]^T) \\ \hat{x}[k+1|k+1] &= \hat{x}[k+1|k] + K[k](\eta[k+1] - C\hat{x}[k+1|k]). \end{aligned} \quad (6.77)$$

The direct extension to an n -variable-frequencies model may be given by the following:

$$\begin{aligned} \mathbf{x}(k) &= \begin{bmatrix} \mathbf{x}_1(k+1) \\ \dots \\ \mathbf{x}_n(k+1) \end{bmatrix} = \begin{bmatrix} \mathbf{f}_1(\mathbf{x}_1(k), \mathbf{w}_1(k)) \\ \dots \\ \mathbf{f}_n(\mathbf{x}_n(k), \mathbf{w}_n(k)) \end{bmatrix}. \\ \eta(k) &= [1 \ 0 \ 0 \ \dots \ 1 \ 0 \ 0] \mathbf{x}(k) + \zeta(k) \end{aligned} \quad (6.78)$$

As will be shown in the results of Section 6.5.3, however, the multiple-frequencies model has the problem that the Kalman filter would update all the frequencies in the same way, which makes it not really effective in practice.

6.4.4 Neural networks

It was shown, in Section 6.3.3, how the non-linearities appearing in the large, low-frequency waves, due to the relatively small water depth, are not really relevant. However, it is interesting, in the authors opinion, to look at a comparison of the models suggested so far with a most widespread tool for time series modelling and forecasting such as Neural networks (NNs).

In spite of the modelling capability and the ease of building up a suitable structure, NNs have the great disadvantage of offering a model completely enclosed in a black box where any analysis and evaluation of the properties is prevented. So, while in the cyclical and AR models an analysis of the estimated parameters and frequencies and their variations in an adaptive structure can provide indications about the real process behavior and its main characteristics, this would not be possible with NNs.

For the problem under study, a non-linear relationship of the following type is created through a multi-layer perceptron [176]:

$$\eta[k] = \mathbf{NN}(\eta[k-1], \eta[k-2], \dots, \eta[k-n]), \quad (6.79)$$

so that the non-linear dependance between the current wave elevation and n past values is realised.

Only structures with one linear output neuron and two hidden layers, consisting of non-linear neurons, varying between three and seven neurons each, were considered. Several orders of regression, n , were also considered. The model is trained using the Levenberg-Marquard algorithm [177] on a set of batch data and is then utilised for multi-step-ahead prediction.

In addition to the proposed structure, many other structures could be considered. For example, *a priori* knowledge about the harmonic nature of the process may be included and a non-linear relationship of the following type may be considered instead:

$$\eta(k) = \text{NN}(\cos(\omega_1 T_s k + \varphi_1), \dots, \cos(\omega_n T_s k + \varphi_n)), \quad (6.80)$$

though such an input structure would retain some of the limitations of cyclical models with fixed frequencies, as discussed in Section 6.4.1.

6.4.5 Further possibilities

Since the field of time-series prediction is quite broad, other popular techniques are considered in this Section, though actual results are not produced. As will be discussed hereafter, some of the methods seem to be unsuitable to the problem of wave forecasting, while others do not promise to bring about any improvement to the algorithms analysed in Sections 6.4.1 to 6.4.4.

ARMA models

An ARMA model is the close equivalent to an AR model, where the noise is not assumed to be sequentially uncorrelated (i.e. white noise), but is modelled by a regression [170]:

$$\eta[k] = \sum_{i=1}^{n_a} a_i \eta[k-i] + \sum_{i=1}^{n_c} c_i \zeta[k-i] + \zeta[k], \quad (6.81)$$

and, in the Z -domain:

$$\eta(z) = \frac{\vartheta(z)}{\varphi(z)} \zeta(z). \quad (6.82)$$

The shape of the forecasting function, $\hat{\eta}[k+l|k]$, is the same as for an AR model, found in (6.49), and it is determined only by the autoregressive part, i.e. the poles of the transfer function in (6.82). The MA terms change the way in which the forecast function is fitted to the past observations and to the forecasts. For a purely AR model, the forecast function is that unique curve, of the form required by $\varphi(z)$, which passes through the n_a pivotal points $\eta[k]$, $\eta[k-1]$, \dots , $\eta[k-n_a+1]$ [170]. In the presence of some MA terms, $n_c > 0$, the forecast function is determined by the points $\hat{\eta}[k+n_c|k]$, \dots , $\hat{\eta}[k+1|k]$, $\eta[k]$, \dots , $\eta[k+n_c-n_a+1]$, so that the way in which it is fitted to the observations is modified by the MA coefficients through the first n_c predictions.

An ARMA model would not, therefore, present modelling capabilities significantly different to pure AR models. In practice, however, to obtain a parsimonious parametrisation, it is sometimes necessary to include both autoregressive and moving average terms in the model [170]. In fact, a finite MA process can be written as an infinite-order AR process, and vice-versa, so that if a process

were really a MA of order 1, an AR model would necessarily be a non-parsimonious representation of it, and conversely for a AR process of order 1.

In conclusion, an ARMA model would not allow us to obtain better results over simple AR models, but the introduction of some moving average terms may be considered at a later stage in order to reduce the complexity of the forecasting model.

Gaussian Processes

Assuming that a certain function underlies the observed data sets, in our case a function relating the past and future values of the wave elevation time series, the idea behind a Gaussian process (GP) model is to place a prior directly on the space of functions [178], without assuming any function parametrisation. The only hypothesis made is that the prior is considered to be Gaussian and is completely specified by its mean and covariance function.

In particular, the prior distribution, $P(y)$, of the function y performing the input-output mapping is given as a zero-mean (a mean value different from zero would not affect any of the following considerations) Gaussian process with covariance matrix, Q :

$$P(y) \sim \mathfrak{N}(0, Q). \quad (6.83)$$

Denoting the input set by $\{x_n\}$, $n = 1, \dots, N$, and the corresponding target values by $\{t_n\}$, $n = 1, \dots, N$, and assuming that each target value, t_n , differs by additive Gaussian white noise, of variance σ_ϵ^2 , from the corresponding function value, $y(x_n)$, then the target values follow a Gaussian prior distribution as well:

$$P(t) \sim \mathfrak{N}(0, C) \quad (6.84)$$

$$C \triangleq Q + \sigma_\epsilon^2 I, \quad (6.85)$$

where I is an identity matrix of the same dimension as Q .

By means of the covariance matrix, C , it is then possible to infer a target, $y(x_{N+1})$, given a vector of observed targets, $T_N = [t_1, \dots, t_N]^T$, according to Bayes' rule:

$$P(t_{N+1}|T_N) = \frac{P(t_{N+1}, T_N)}{P(T_N)}, \quad (6.86)$$

where $P(t_{N+1}|T_N)$ is the probability of t_{N+1} conditioned on all the observations T_N and $P(t_{N+1}, T_N)$ is the joint probability density.

It can be shown [178] that:

$$P(t_{N+1}|T_N) = \frac{1}{Z} e^{-\frac{(t_{N+1} - \hat{t}_{N+1})^2}{2\sigma_{\hat{t}_{N+1}}^2}}, \quad (6.87)$$

with

$$\hat{t}_{N+1} = K^T C_N^{-1} T_N \quad (6.88)$$

$$\sigma_{\hat{t}_{N+1}}^2 = \kappa - K^T C_N^{-1} K, \quad (6.89)$$

where \hat{t}_{N+1} is the mean value of the prediction at the new point, x_{N+1} , and $\sigma_{\hat{t}_{N+1}}^2$ gives the error bars on this prediction. In (6.87), Z is a scalar coefficient, while the matrix $C_N \in \mathbb{R}^{N \times N}$, the vector $k \in \mathbb{R}^{N \times 1}$ and the scalar κ , in (6.88) and (6.89), come from the following form of the covariance matrix, $C_{N+1} \in \mathbb{R}((N+1) \times (N+1))$, of the vector $T_{N+1} = [t_1, \dots, t_{N+1}]^T$:

$$E \{T_{N+1} T_{N+1}^T\} \triangleq C_{N+1} = \begin{bmatrix} C_N & K \\ K^T & \kappa \end{bmatrix}. \quad (6.90)$$

The crucial aspect in building a GP model is, therefore, the choice of the covariance function shape, $C[y(x_i), y(x_j)]$, from which the covariance matrix, $C = \{C_{ij}\}$, can be calculated, according to the equations:

$$C_{ij} = C[y(x_i), y(x_j)] + \delta_{ij} N(x_i), \quad i, j = 1, \dots, N \quad (6.91)$$

where $N(x_i)$ is a noise model, with $\delta_{ij} = 1$ for $j = i$, otherwise $\delta_{ij} = 0$.

The covariance function usually has a particular parametric structure, and can result from the combination of elemental covariance functions expressing certain peculiar characteristics (trend component, a cyclical component, etc...), that can be derived from a-priori knowledge of the process [179]. The parameters in the covariance function, termed *hyper-parameters*, are optimised with respect to the available observations through a maximum likelihood procedure [178]. The covariance function can then be utilised to calculate the covariance matrix, C_{N+1} , according to (6.90), by which the mean and variance of the estimate can be found, based on (6.88) and (6.89).

The attractiveness of GPs lies in the fact that models can be determined using a relatively small number, N , of observations and the covariance functions can be easily synthesised from a-priori knowledge of the system. In addition, GPs perform in a safe manner when extrapolating outside the region of the training data, by giving confidence intervals (on the basis of the variance of the estimate) which help to indicate where the model is unreliable (e.g. for forecasts too far ahead in time). A further positive feature is that on-line data addition, that is the introduction of new observations into the model, can be performed in a really straightforward manner (see [178] for details), assuming that it does not imply a change in the hyper-parameters, thus permitting the model to adapt to the evolution of the real process.

The implementation of a GP model, however, presents some numerical problems in at least two ways. First of all, the optimisation of the hyper-parameters is not a convex problem and, secondly, the on-line prediction requires an $N \times N$ matrix inversion, which is an ill-conditioned problem. This latter problem puts, of course, an upper limit on the quantity, N , of training data which can be included in the model. Careful use of numerical tools may help to overcome both of the above issues.

However, the major drawback, in the specific case of wave forecasting is that, in order to model the cyclical characteristics of the sea, the harmonic components of the covariance function, and in particular their frequencies, have to be permanently assigned in the initial hyper-parameter estimation procedure, which is the same problem of cyclical models with fixed frequencies, as articulated in Section 6.4.1. A covariance function without explicit cyclical components could still be able to represent the harmonic behavior of the wave elevation, just like a simple AR model without explicit seasonal components, but then the extraction of the physical characteristics of

the real process from the estimated model becomes barely possible. This particular reason led the author to exclude GPs as a possible candidate for a wave forecasting model.

Particle filters

Bayesian methods, such as GPs and the Kalman filter, provide a rigorous general framework for dynamic state-estimation problems. The Bayesian approach is to construct the Probability density function (PDF) of the state based on all the available information. For the linear-Gaussian estimation problem, the required PDF remains Gaussian at every iteration of the filter, and the Kalman filter relations propagate and update the mean and covariance of the distribution. For non-linear or non-Gaussian problems there is no general analytic (closed form) expression for the required PDF [180]. Particle filters (PFs) were introduced as a new way of representing and recursively generating an approximation to the state PDF [180]. The central idea is to represent the required PDF as a set of random samples, rather than as a function over state-space. As the number of samples becomes very large, they effectively provide an exact, equivalent, representation of the required PDF. Estimates of moments (such as mean and covariance) of the state-vector PDF can be obtained directly from the samples [180].

Since their introduction, PFs have become a very popular class of numerical methods for the solution of optimal estimation problems in non-linear, non-Gaussian scenarios. In comparison with standard approximation methods, such as the popular EKF, the principal advantage of particle methods is that they do not rely on any local linearisation technique or any crude functional approximation [181].

Assume a discrete-time model, where the state vector, $x[k]$, evolves according to a non-linear function, $f(\cdot, \cdot)$, of the previous state and a white-noise disturbance, $w[k]$:

$$x[k+1] = f(x[k], w[k]), \quad (6.92)$$

and that the measurements, $y[k]$, are related to the state vector via the following observation equation:

$$y[k] = g(x[k], \zeta[k]), \quad (6.93)$$

where $g(\cdot, \cdot)$ is, in general, a non-linear function of the state and a white-noise disturbance, $\zeta[k]$. By assuming knowledge of the initial PDF of the state, and of the statistical properties of the disturbances, the problem is to construct the PDF of the current state, $x[k]$, based on all the available information, that is the set $Y_k \triangleq \{y[0], y[1], \dots, y[k]\}$.

The required PDF, namely $P(x[k]|Y_k)$, can be constructed recursively in two stages [180]: (a) a prediction based on the PDF at instant $k-1$, $P(x[k-1]|Y_{k-1})$, and the state dynamics, in (6.92), and (b) update based on the new measurement, $y[k]$, and the observation equation, in (6.93). More

formally [180]:

$$P(x[k]|Y_{k-1}) = \int P(x[k]|x[k-1]) P(x[k]|Y_{k-1}) dx[k-1] \quad (6.94)$$

$$P(x[k]|Y_k) = \frac{\int P(y[k]|x[k]) P(x[k]|Y_{k-1})}{P(y[k]|Y_{k-1})}, \quad (6.95)$$

where (6.94) is the prediction of the PDF and (6.95) is its update via Bayes' rule.

In the case of linear models and Gaussian disturbances, the Kalman filter (detailed in appendix B) gives an analytic solution to the Bayesian recursive estimation in (6.94) and (6.95). However, for most non-linear and/or non-Gaussian models, it is not possible to compute the PDFs distributions in closed-form and numerical methods need to be employed. Particle methods are a set of flexible and powerful simulation-based methods which provide samples approximately distributed according to the required PDFs. Such methods are a subset of the class of methods known as Sequential Monte Carlo (SMC) methods and an overview is given in [181].

In the specific application to wave forecasting, PFs could be a valid alternative for the implementation of a cyclical model with adaptive frequency that is not linear, such as the description in Section 6.4.3, for which the EKF was proposed. As previously mentioned, a particle filter would be more general since it would not require a linearisation of the system or employ any other simplifying assumption about the PDF of the state and disturbances. At the same time, however, the EKF is computationally quite efficient, since only a 3-states dynamic equation is involved, while models based on PFs are, in general, computationally expensive, which is the price that must be paid for their flexibility [181]. An extension of the model to multiple harmonics, with variable frequencies, as proposed in (6.78), could also be possible with PFs.

However, the nature of the wave records to be predicted is mostly Gaussian and only weakly non-linear, apart from some sea states of smaller importance (very low-energy conditions), based on the analysis of Section 6.3. In addition, adaptive AR models, as outlined in Section 6.4.2, implicitly implement cyclical models with variable frequencies that are capable of tracking the non-stationarity of ocean waves, in a linear framework. The increase in computational complexity required by PFs is not, therefore, justified since the additional modelling abilities are not required in the specific application to wave forecasting for real-time control of WECs.

6.4.6 Confidence intervals

The predictions alone, as computed by any of the models presented through Section 6.4.1 to 6.4.4, do not give complete enough information about the future of the signal, since they are inevitably affected by an estimation error. It would be fundamental to have an indication about the significance of this error and about the confidence that we can put in the forecasts computed by the prediction algorithm.

At every instant, k , the future values of the wave elevation are approximated through some prediction model:

$$\hat{\eta}[k+l|k] = \eta[k+l] + \hat{\epsilon}[k+l|k], \quad (6.96)$$

where $\hat{\eta}[k+l|k]$ is the l -step-ahead prediction and $\hat{e}[k+l|k]$ is the prediction error.

If a stochastic time-series model is utilised as a predictor, the one-step-ahead prediction is usually calculated as a combination, not necessarily linear (e.g. NNs), of past values of the wave elevation:

$$\hat{\eta}[k+1|k] = \Upsilon(\eta[k], \eta[k-1], \dots, \eta[k-n]), \quad (6.97)$$

where $\Upsilon(\cdot)$ is an unspecified function. The multi-step predictions are then determined, recursively, as:

$$\hat{\eta}[k+l|k] = \Upsilon(\hat{\eta}[k+l-1|k], \hat{\eta}[k+l-2|k], \dots, \hat{\eta}[k+l-n|k]). \quad (6.98)$$

The one-step-ahead prediction error, $\hat{e}[k+1|k]$, can be assumed to be a white and Gaussian noise with zero mean and variance σ^2 :

$$\hat{e}[k+1|k] \sim \mathfrak{N}(0, \sigma^2). \quad (6.99)$$

The assumption in (6.99) is reasonable if the prediction model accurately captures all the dynamics of the real system. The multi-step ahead prediction errors, however, given the recursive nature of the predictor, will be a combination of white noises and, therefore, colored, with a certain spectral distribution. Given a specific prediction model, if it is linear (e.g. cyclical or AR models), it is possible to derive an accurate spectral model of the multi-step prediction error. In the case of a non-linear predictor, such as NNs, the spectral model is not sufficient to describe the multi-step-ahead error, represented by a non-linear combination of white noises.

In order to produce a general methodology to be applied to the different forecasting methods proposed in this Chapter, the assumption is made that the l -step-ahead prediction error is Gaussian:

$$\hat{e}[k+l|k] = \hat{\eta}[k+l|k] - \eta[k+l] \approx \mathfrak{N}(0, \sigma_l^2), \quad (6.100)$$

although correlated (not white). Then, the variance σ_l^2 is all that is needed in order to define the probability distribution of the predictions. The prediction error, in particular, is contained within a *confidence interval*, with probability δ :

$$-z_{\frac{\delta}{2}} \leq \hat{e}[k+l|k] \leq +z_{\frac{\delta}{2}}. \quad (6.101)$$

In (6.101), $z_{\frac{\delta}{2}}$ is the value of the probability distribution, such that:

$$P \left\{ -z_{\frac{\delta}{2}} \leq \hat{e}[k+l|k] \leq +z_{\frac{\delta}{2}} \right\} \triangleq \int_{-z_{\frac{\delta}{2}}}^{+z_{\frac{\delta}{2}}} p(y) dy = \delta, \quad (6.102)$$

where the probability density function $p(\cdot)$, with the distribution of the forecasting error considered

to be zero-mean Gaussian, assumes the following structure:

$$p(\hat{\epsilon}[k+l|k]) = \frac{1}{\sqrt{2\pi}\sigma_l} e^{-\frac{\hat{\epsilon}[k+l|k]^2}{2\sigma_l^2}}. \quad (6.103)$$

The estimate of the variance, σ_l^2 , could be calculated from the specific parameters of the model and from the statistical properties of the multi-step prediction error, which depend on the model and are not always simple to identify (e.g. in the case of NNs). A more straightforward alternative is adopted, where the estimate of the variance of the forecasting error is based purely on the past history of the prediction errors:

$$\hat{\sigma}_l^2 = \frac{1}{N-1} \sum_{k=1}^N \hat{\epsilon}[k+l|k]^2, \quad (6.104)$$

where N is the number of past observations available. Note that, although the variance has a non-flat frequency distribution, since the multi-step prediction error is correlated, there is only the interest, here, in deriving an overall value, which is sufficient to produce the confidence interval.

The estimate of σ_l^2 can also be recursively updated as soon as new observations become available [182], via:

$$\hat{\sigma}_l^2[k] = \frac{k-2}{k-1} \hat{\sigma}_l[k-1] + \frac{1}{k} (\eta[k] - \hat{\eta}[k|k-l])^2, \quad k \geq 2. \quad (6.105)$$

6.5 Results

The possible forecasting models, proposed in Section 6.4, were tested on some representative data sets, appropriately chosen among all those available (described in Section 6.3), as typical of different sea conditions. The wave spectra of the selected wave records are shown in Fig. 6.14, and were already utilised for the analysis carried out in Section 6.3. One wide-banded and one narrow-banded sea state, from the two sites of Galway Bay and Pico Island, are considered. Then, a situation where wind waves predominate is selected from the Galway Bay data and a very high-energy sea state, where the sea bottom slightly affects the wave symmetry (this was analysed through higher order spectral analysis and skewness and kurtosis indices, in Section 6.3.3), is chosen from the Pico Island data.

Based on the predictability analysis, and on practical considerations concerning the wave-energy application, as discussed in Section 6.3.4, the focus is put on the low frequencies. Ideal zero-phase low-pass filters are approximated with off-line forward and backward filtering through type-I Chebyshev filters (order 15, maximum error in the pass-band 10^{-3}) discretised with the bilinear transform (no pre-warping is applied). For each of the selected wave records, a cut-off frequency, ω_c , has been chosen according to the specific shape of the wave spectra, and it is indicated in Fig. 6.14. More in particular, the cut-off frequency is chosen based on visual inspection, such that the main low-frequency wave components (high energetic ones) are considered.

For the identification and validation of the forecasting models, each of the data sets is split

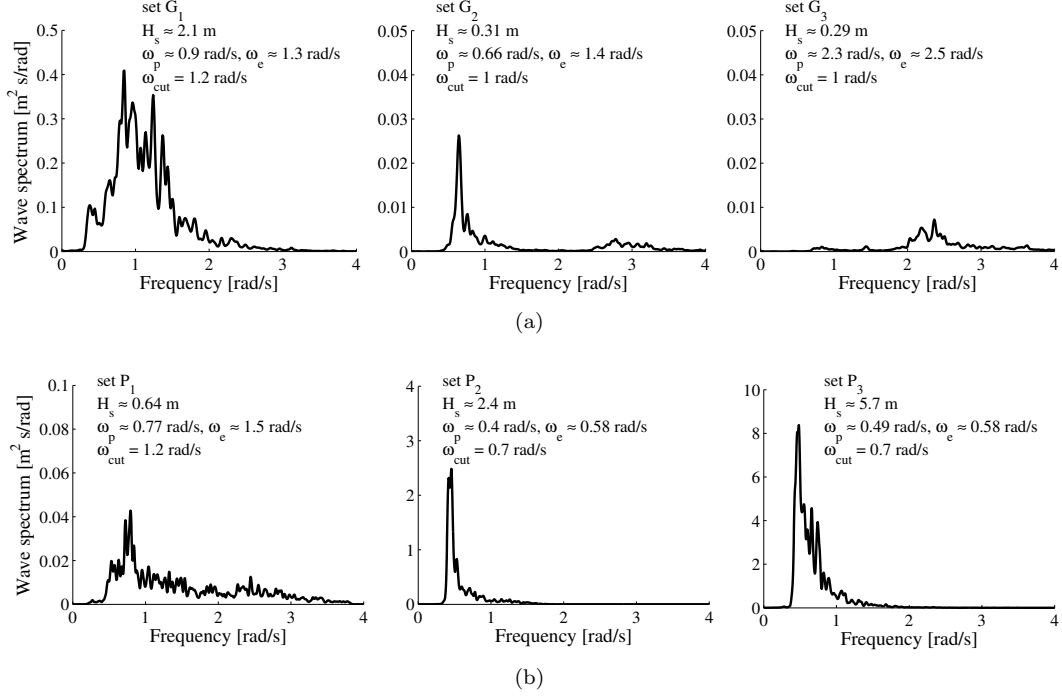


Figure 6.14: Data sets utilised to test the models of Section 6.4: (a) Galway Bay; (b) Pico Island.

up into a training and validation set. For the Galway Bay data, training and validation data sets consist of two consecutive sets of 3072 samples each (20 minutes at a sampling frequency of 2.56 Hz). In the case of the Pico Island data, because the consecutive data sets are actually contiguous in time, training and validation data consist of 4 consecutive sets each (9216 samples, that is 2 hours at a sampling frequency of 1.28 Hz), and the validation data follows the training data contiguously in time.

The prediction accuracy is measured with the following goodness-of-fit index, which depends on the forecasting horizon, l :

$$\mathcal{F}[l] = \left(1 - \frac{\sqrt{\sum_k [\eta[k+l] - \hat{\eta}[k+l|k]]^2}}{\sqrt{\sum_k \eta[k]^2}} \right) \quad (6.106)$$

In (6.106), $\eta[k+l]$ is the wave elevation and $\hat{\eta}[k+l|k]$ is its prediction based on the information up to instant k . A 100% value for $\mathcal{F}[l]$ means that the wave-elevation time series is perfectly predicted l steps into the future.

Note that $\mathcal{F}[l]$ has a direct correspondence with the variance of the prediction error, that, as discussed in Section 6.4.6, is utilised to characterise confidence intervals of the forecasts. In particular, if $\hat{\sigma}_l^2$ is an estimate of the variance of the l -step-ahead prediction error, as defined in (6.104), it can be shown that for large N :

$$\frac{\hat{\sigma}_l^2}{E\{\eta[k]^2\}} \approx (1 - \mathcal{F}[l])^2. \quad (6.107)$$

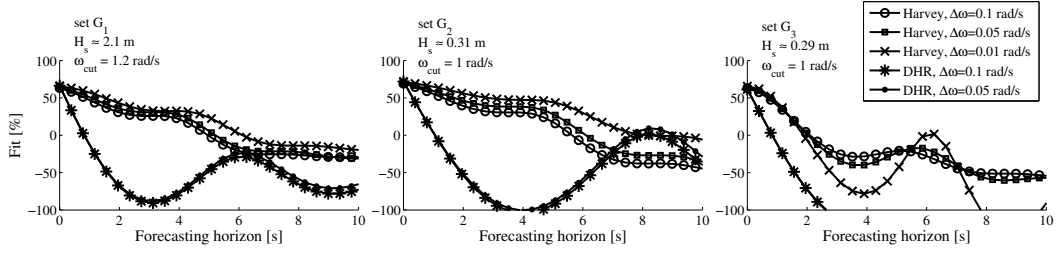


Figure 6.15: Prediction accuracy of cyclical models on wave data from the Galway Bay

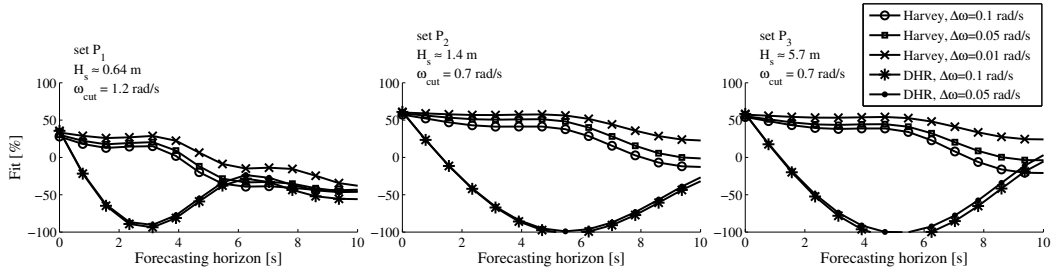


Figure 6.16: Prediction accuracy of cyclical models on wave data from the Pico Island

6.5.1 Cyclical models

The two structures for the cyclical models outlined in Section 6.4.1, Harvey’s structural model and the DHR, were tested against the data sets of Fig. 6.14. The frequencies of the models were chosen to be constantly spaced in a range between 0.3 rad/s (practically no waves appear below this frequency at the considered locations) and the applied cut-off frequency, ω_c , with different spacings, $\Delta\omega$. Another critical choice for the models are the initial mean value and covariance matrix of the state for the Kalman Filter algorithm, and the variance of the output-equation disturbance, specifically $\zeta[k]$ in (6.31) and (6.41). The initial expected value and covariance matrix of the state vector are determined from the regular LS applied, off-line, to the training data. The variance of the output disturbance, $\zeta[k]$, namely σ_ζ^2 , on the other hand, is determined by trial and error, with a reasonable value found to be $\sigma_\zeta^2 = 1$.

Figure 6.15 shows the performance of different cyclical models on the Galway Bay data sets. The accuracy is above 50% only for predictions up to 2 – 3 seconds into the future (around 5 – 8 samples) and drops down particularly quickly for the sea state constituted by mostly wind waves, G_3 . Slightly better results are obtained for the Pico Island data, in Fig. 6.16, when $\mathcal{F}(l)$ is above 50% up to 5 – 6 seconds ahead (around 6 – 8 samples), although this is not the case for the wide-banded sea state, P_1 . In all cases, the Harvey models give better results, which improve with decreasing frequency spacing, that is by considering a model with a more dense range of frequencies. The main problem of cyclical models, however, lies in their complexity: a spacing of $\Delta\omega = 0.01$ with a range $[0.3, 1.2]$ rad/s generates a state-space model of order 182 for Harvey’s cyclical model and order 364 for the DHR model. This sets a strict limit, in practical applications, on how small the spacing can be.

Some detailed time-series plots are shown in Fig. 6.17, comparing the wave predicted at a fixed leading time against the real (low-pass filtered) wave. Note that a 90% confidence interval is also

shown, and it is calculated under the assumption that the forecasting error is Gaussian. Based on the methodology proposed in Section 6.4.6, the variance is estimated in real time, from (6.105). Higher-order statistics are utilised for the validation of the Gaussianity assumption, following the approach outlined in Section 6.3.3, based on the indices of skewness, γ , and kurtosis, κ , defined in (6.24) and (6.25). Figure 6.18 shows that, effectively, in nearly 70% of the cases, the error distribution has a kurtosis $\kappa < 3.01$ and a skewness $\gamma < 0.05$, which means it is very close to Gaussian.

6.5.2 Auto-Regressive models

Before presenting the actual results achieved with static and adaptive AR models for the problem of wave forecasting, proposed in Sections 6.4.2, the selection of the model order is described in detail, because the nature of the problem makes it different from the usual applications. Slightly modified standard criteria, on the basis of a multi-step-ahead prediction error, are utilised, instead of the normally adopted one-step-ahead prediction error.

Choice of model order

An indication of the appropriate order, n , of an AR model to predict the wave elevation, can be obtained through minimisation of the classical criteria Akaike information criterion (AIC), proposed by Akaike [183], and Bayesian information criterion (BIC), proposed by Schwarz [184]:

$$AIC = \log(\hat{\sigma}_\zeta^2) + r \frac{2}{N} \quad (6.108)$$

$$BIC = \log(\hat{\sigma}_\zeta^2) + r \frac{\log(N)}{N}. \quad (6.109)$$

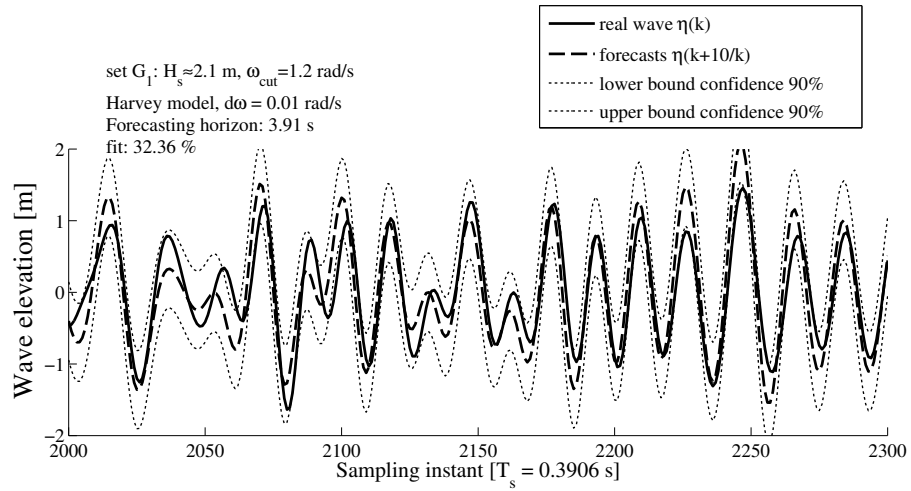
In (6.108) and (6.109), $\hat{\sigma}_\zeta^2$ is the estimate of the variance of the one-step-ahead prediction error $\zeta[k]$, appearing in (6.47), $r = n + 1$ is the number of parameters of the model (n coefficients plus the variance) and N is the number of observations utilised in the estimation procedure.

However, because we are interested in multi-step-ahead predictions, the two criteria are evaluated also with respect to the variance of the l -step-ahead prediction error, $\hat{\sigma}_l^2$:

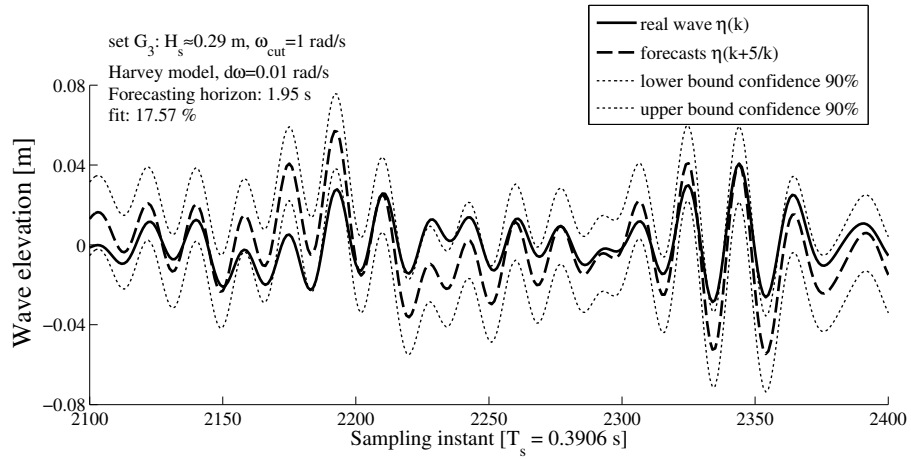
$$AIC_l = \log(\hat{\sigma}_l^2) + r \frac{2}{N} \quad (6.110)$$

$$BIC_l = \log(\hat{\sigma}_l^2) + r \frac{\log(N)}{N}. \quad (6.111)$$

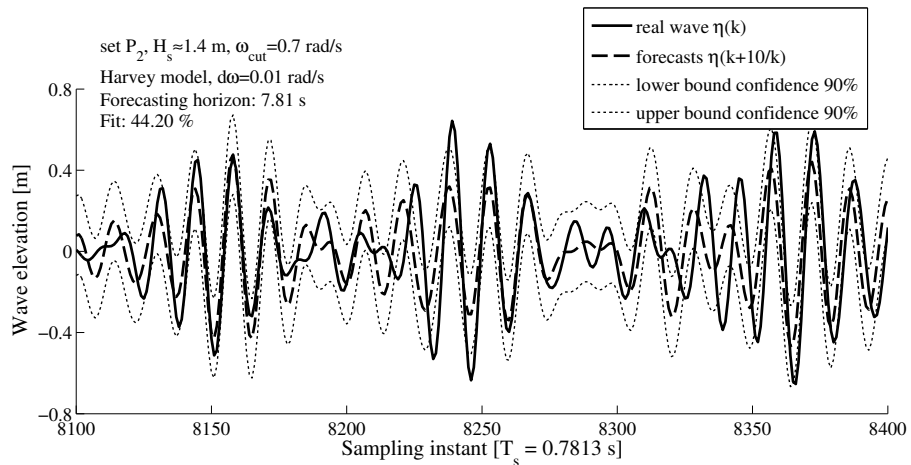
Figure 6.19 shows the resulting values of the two indices for a range of AR models (from $n = 1$ to $n = 50$) applied to the different data sets from Galway Bay and from Pico Island. As expected, the answers are different depending on the forecasting horizon considered. Accurate predictions very far into the future require relatively high-order models ($n > 30$), while good predictions for mid-range lead times, between 5 and 20 samples, can be obtained with reduced-order AR models ($12 < n < 20$). The model order depends also on the spectral range considered and on the specific sea state or location but, in general, an order slightly higher than 30 would be a good choice for any



(a)



(b)



(c)

Figure 6.17: Some time-series details of the multi-steps-ahead wave prediction, using cyclical models. The 90% confidence interval is also shown.

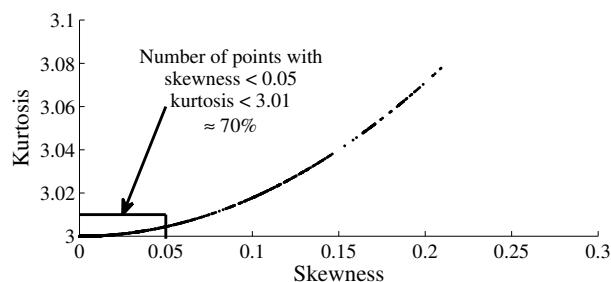


Figure 6.18: Distribution of skewness and kurtosis of the l -steps-ahead prediction error, for different l and for different cyclical models, over all the considered data sets from both the Pico Island and the Galway Bay.

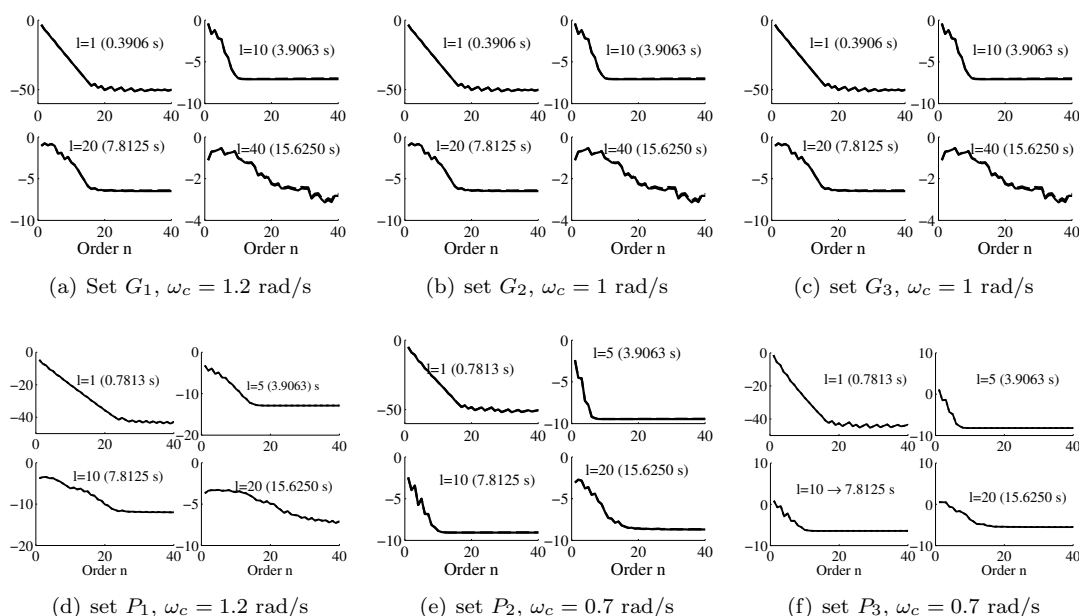


Figure 6.19: AIC_l (continuous line) and BIC_l (dashed line), for some l , evaluated for the Galway Bay and Pico Island data sets, low-pass filtered with cut-off frequency ω_c .

situation. In the following, therefore, a number of AR models are chosen based on these results, with the orders $n = 12, 16, 24, 32$.

Static AR models

The performance, in terms of $\mathcal{F}(l)$, of constant-parameter AR models, of different order, is shown in Fig. 6.20. The models are estimated according to the LRPI criterion, expressed in (6.52). In every case, the AR models significantly outperform any of the cyclical models analysed in Section 6.5.1. Predictions with an accuracy of more than 70% are obtained, in the case of the Galway Bay data, over a forecasting horizon of up to 15 seconds (almost 20 seconds in the case of the narrow-banded sea state G_2 , as shown in Fig. 6.20(b)). The sea state composed mostly of wind waves, G_3 , presents some difficulties in comparison with the others, as seen in Fig. 6.20(c), but the wave-energy significance of this sea state is quite poor, and the prediction accuracy is still

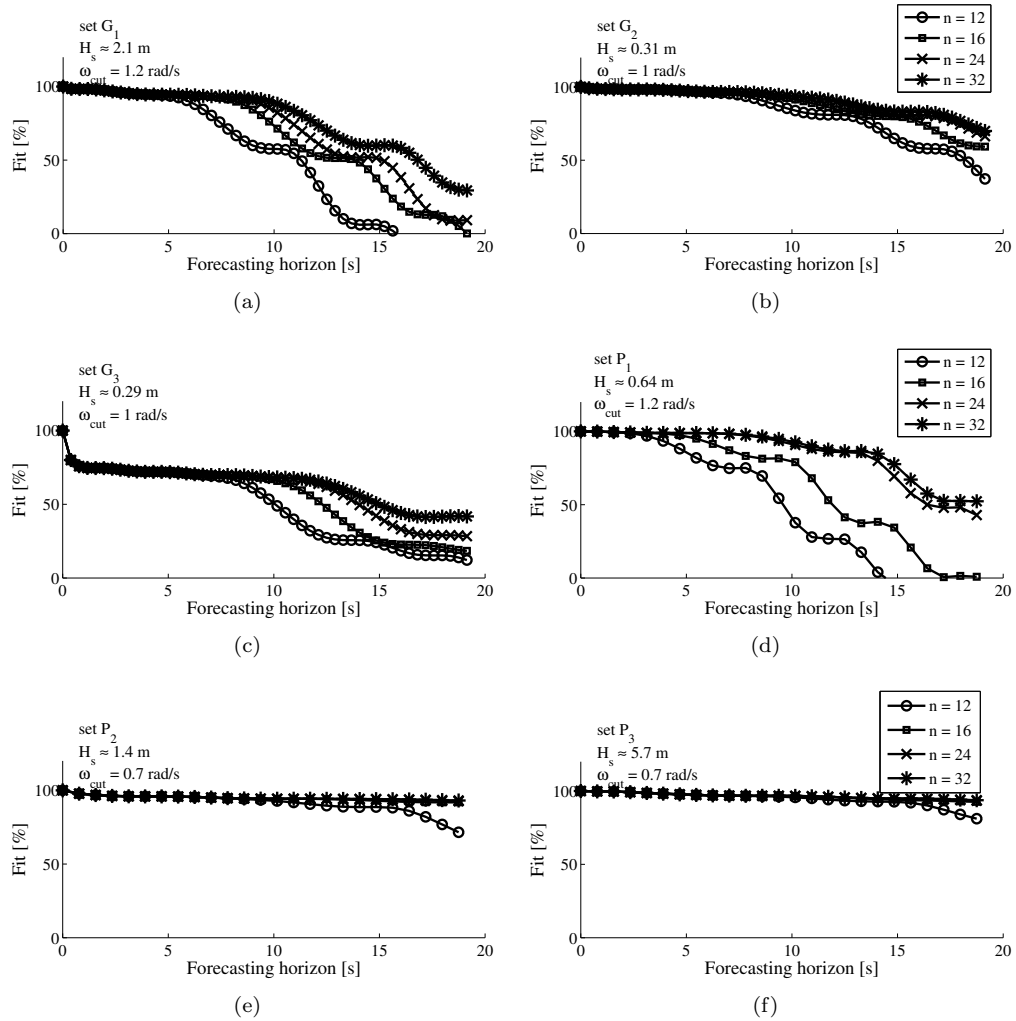
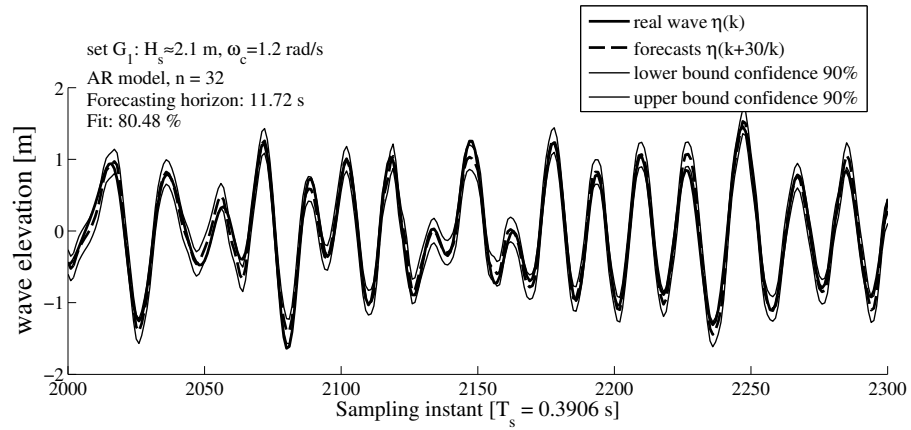


Figure 6.20: Prediction accuracy of AR models of different orders, n , over the wave data from the Galway Bay and the Pico Island.

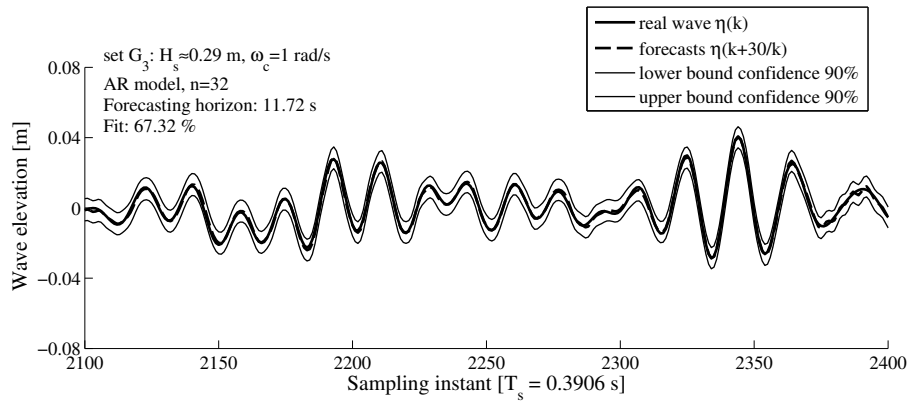
around 70% for almost 10 seconds into the future.

Better results are obtained for the narrow-banded and high-energy sea states of Pico Island, in Fig. 6.20(e) and in Fig. 6.20(f), where an accuracy of more than 90% is maintained for predictions up to 20 seconds in the future. In the latter situation, moreover, relatively low-order models, with $n = 16$ and $n = 24$, seem to be effective, as was expected based on the value of AIC_l and BIC_l , shown in Figs. 6.19(e) and 6.19(f).

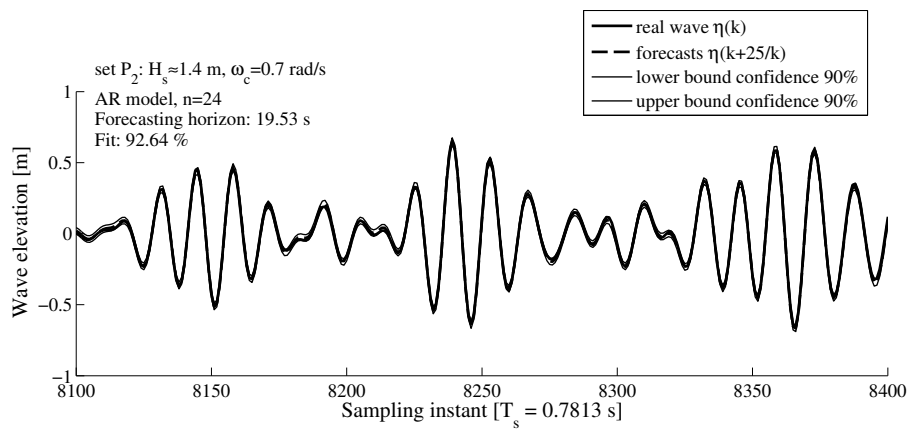
Detailed time-series plots, over the same data set and time interval as for the cyclical models, are shown in Fig. 6.21 for comparison, along with the confidence of the predictions. Note that the assumption of Gaussianity for the prediction error is stronger in this case, as can be seen from Fig. 6.22.



(a)



(b)



(c)

Figure 6.21: Some time-series details of the multi-steps-ahead wave prediction, and its 90 % confidence, using AR models.

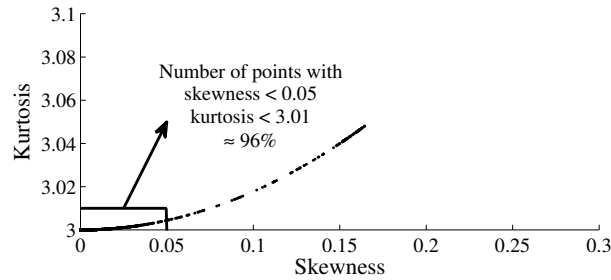


Figure 6.22: Distribution of skewness and kurtosis of the l -steps-ahead prediction error, for several l and for different AR models, over all the considered data sets from the Pico Island and from the Galway Bay.

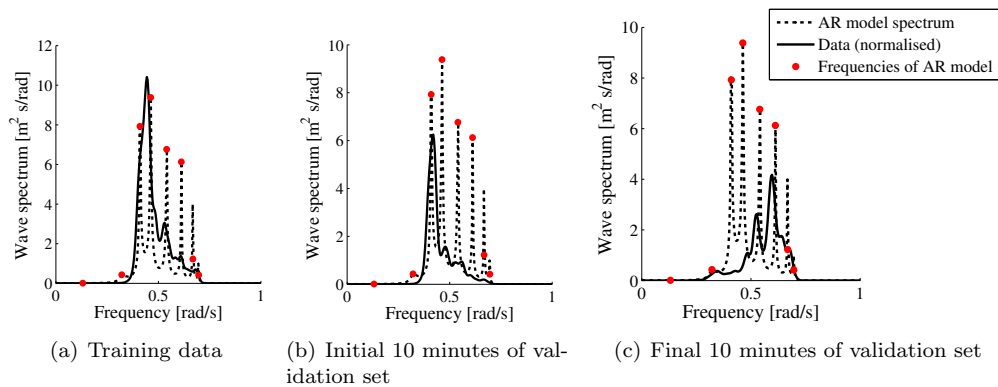


Figure 6.23: Spectrum of the AR model compared to wave spectra of training and validation data, which are amplified accordingly for clarity of exposition. The data correspond to set P_3 of Fig. 6.14(b).

Adaptive AR models

The results shown so far considered only static AR models, identified through a one-off batch estimation of the parameters, on a training data set. From the discussion in Section 6.4.2, AR models can be seen, given certain conditions on the pole locations, as cyclical models, where the frequencies are strictly related to the parameters. A model estimated on a certain training set, therefore, might not be suitable to describe all the different sea states that may occur at a certain location.

As an example, consider Fig. 6.23. The spectrum of the estimated AR model fits well the spectrum of the training wave data, in Fig. 6.23(a). The spectrum of the AR model is then also compared to the spectrum of the initial and final parts of the validation data set, respectively in Fig. 6.23(b) and Fig. 6.23(c). The wave record under analysis is P_3 , that is the large swell recorded at the Pico Island. It can be seen how the AR model spectrum can become unrepresentative of the current sea state, and it would be preferable to make the model adaptive to the variations of the sea conditions. However, the accuracy of the prediction, based on Fig. 6.20(f), seems to be quite robust to such significant changes in the spectral shape of the data. The models, though, have not been tested long enough to give a definitive answer.

One solution, to the issue of non-stationarity of the ocean waves, might be the implementation

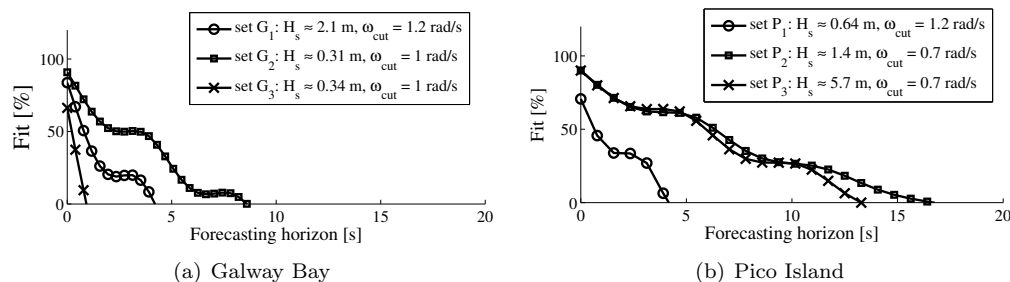


Figure 6.24: Prediction accuracy of single-component cyclical models with a variable frequency, estimated through the EKF.

of a recursive estimation algorithm to adapt the AR model, in real time, to each new observation. RLS with a forgetting factor or the Kalman filter, as explained in Section 6.4.2, may be adopted. Alternatively, a real-time algorithm for a recursive implementation of the multi-step LRPI criterion, in (6.52), is also available [171].

Static AR models, however, have shown quite a robust accuracy over 2 hours of simulation, after being trained on the previous 2 hours, even if the sea state undergoes some major changes, as shown in Fig. 6.23 for the set P_3 . Therefore, one practical possibility might be to run a batch estimation of the AR model, based on the minimisation of (6.52), at fixed intervals of time (e.g. every 2 hours) so to be sure that the model is always valid. The real-time adaptivity of the AR model does not seem, therefore, to be a crucial problem to solve at the moment and it is not further investigated here. Also, an adaptive implementation of the AR model would be quite straightforward to achieve and the real-time practical implementation would not pose any particular problem, from a computational point of view.

6.5.3 Sinusoidal extrapolation through EKF

In Section 6.4.3, the possibility of deploying a harmonic model with a single variable frequency, adapted to the observations in real time, by means of the EKF, was described. The advantages of the approach are its simplicity (the state variable is only of dimension 3, related to frequency, amplitude and phase) and there is a straightforward physical meaning of the model components. However, as shown in the results of Fig. 6.24, the model offers acceptable predictions only in the case of narrow-banded sea states, while it is completely inaccurate in other situations. This is obviously due to the fact that the model is capable of tracking only a single dominant frequency in the waves.

The approach is, though, a very interesting one and it would become an important solution if a suitable way to integrate multiple frequencies is found. In Section 6.4.3, in fact, it was stated that a pure superposition of single-frequency models, as in (6.78), is not an attractive solution, because the Kalman filter weights the innovation of all the single frequencies with the same Kalman gain, as it can be seen in Fig. 6.25. Therefore, no benefit from having more than one harmonic component in the model is gained.

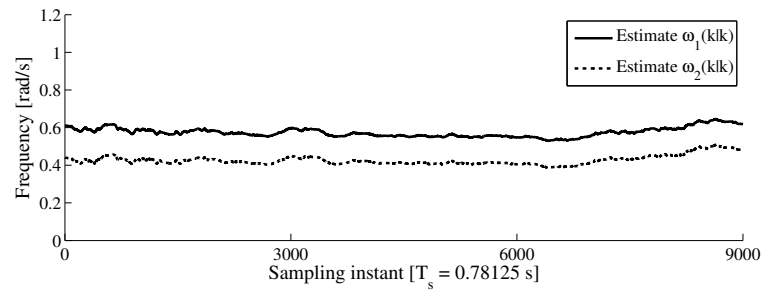


Figure 6.25: Frequencies of a two-components cyclical model, with variable frequencies, estimated through the EKF. The data set utilised is P_2 .

6.5.4 Neural networks

Several architectures for a feed-forward neural network were compared using the wave data of Fig. 6.14. Only structures with 1 linear output neuron and 2 hidden layers, made of a number of non-linear neurons (with hyperbolic tangent sigmoid transfer functions) with a count varying between 3 and 7 each, were considered. Several orders of regression, n (i.e. the number of inputs of the network), were also considered, ranging from 12 to 32, based on the results relative to the AR models. The models are trained using the Levenberg-Marquard algorithm [177] on a set of batch data and it is then utilised for multi-step-ahead prediction.

Figure 6.26 shows $\mathcal{F}(l)$ on some of the selected wave data. The first thing to notice is that, like all the other forecasting models considered, NNs perform much better for narrow-banded sea states. None of the considered structures, though, achieves the same level of accuracy as the AR models, for relatively long forecasting horizons (more than 6 – 7 seconds). However, in the case of the highly non-linear sea state of Galway Bay, G_3 , mostly consisting of wind waves, Fig. 6.26(e) and Fig. 6.26(f) show how NNs give a much better accuracy, $\mathcal{F}(l) \approx 100\%$ than the AR models, $70\% < \mathcal{F}(l) < 80\%$, for up to 6 seconds into the future. Such a type of sea state, however, has a very low importance from a wave energy perspective, so that a significantly better behavior in such situations cannot be really considered as a major decision variable in favor of NNs.

In Fig. 6.27, the details of the time-series prediction, on two data sets, are shown, along with the confidence intervals, calculated under the assumption of a Gaussian prediction error, according to the methodology outlined in Section 6.4.6. Note, however, that these confidence intervals are not really accurate and most of the times the true signal lies outside. This is due to the fact that the prediction error, in this case, unlike for AR models, is not close to having a Gaussian distribution, as it can be seen from the value of skewness and kurtosis of the prediction error, shown in Fig. 6.28.

The search of possible network configurations was not exhaustive, but was broad enough to conclude that NNs are not able to offer any significant improvement in the short-term prediction of the wave elevation, compared to simple AR models, especially considering the higher complexity and the lack of any physical meaning. Note that high-energy sea states with a well defined low-frequency swell, like P_2 , present relatively weak non-linearities (from analysis of the bispectrum, and of skewness and kurtosis indices, carried out in Section 6.3.3), unless shallow water conditions apply (which is not the case here).

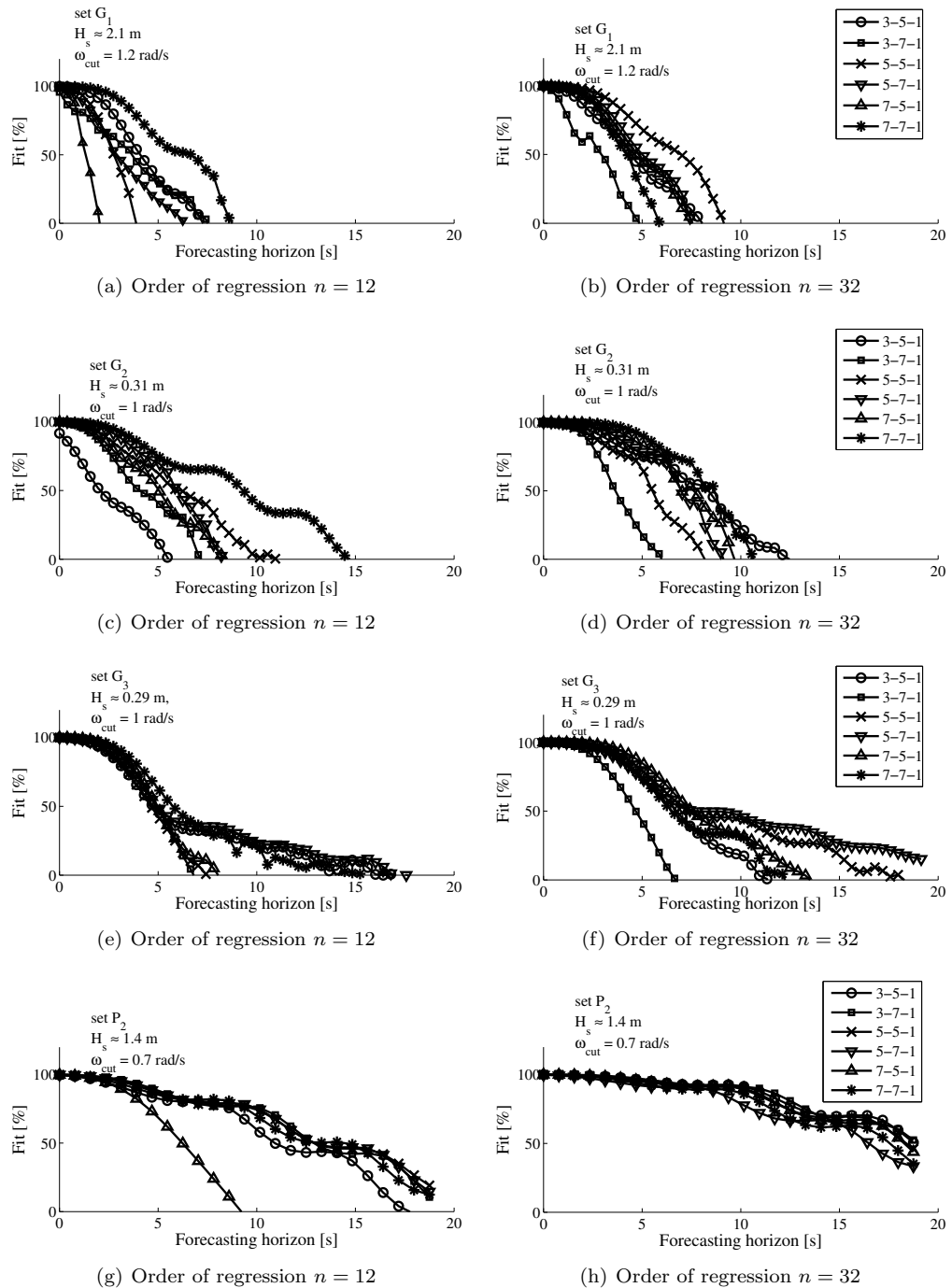
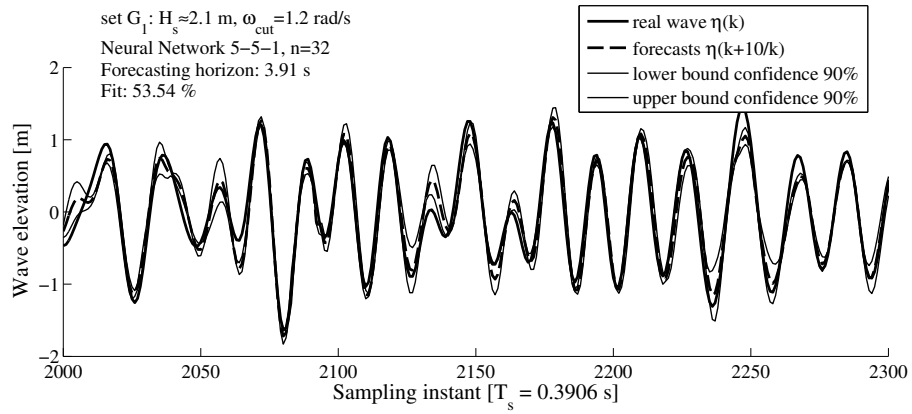
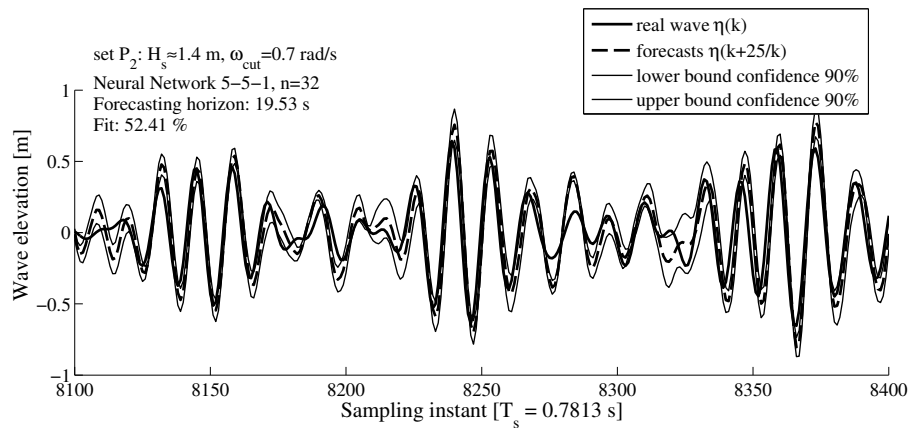


Figure 6.26: Prediction accuracy of neural networks.



(a)



(b)

Figure 6.27: Some screenshots of the multi-steps ahead wave prediction, and its 90% confidence, with neural networks.

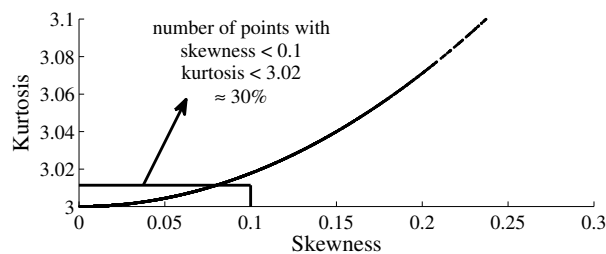


Figure 6.28: Distribution of skewness and kurtosis of the l -steps-ahead prediction error, for several l and for different neural networks over all the considered data sets from the Pico Island and from the Galway Bay.

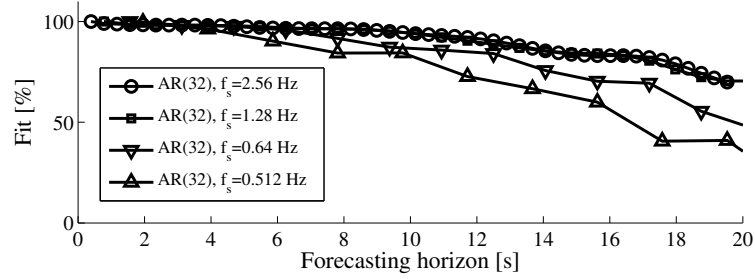
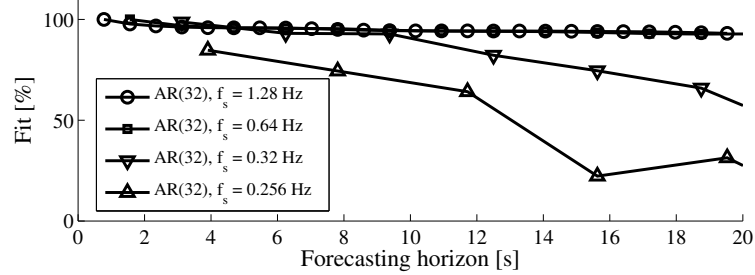
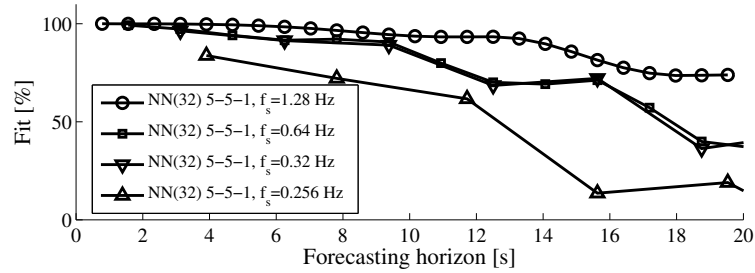
(a) Set G_2 , cut-off frequency $\omega_{cut} = 1$ rad/s (≈ 0.16 Hz)(b) Set P_2 , cut-off frequency $\omega_{cut} = 0.7$ rad/s (≈ 0.11 Hz)(c) Set P_2 , cut-off frequency $\omega_{cut} = 0.7$ rad/s (≈ 0.11 Hz)

Figure 6.29: Prediction accuracy of AR models and neural networks when the sampling frequency of the data is decreased.

6.5.5 Effects of sampling frequency on prediction

Following the discussion of Section 6.3.5, it is interesting to analyse how the sampling frequency of the wave-elevation time series can affect the results achieved with some of the models tested in this Section. In 6.3.5, it was pointed out how a model, capable of extracting all the information about the future evolution from past observations, shall not be affected by changing the sampling frequency, because, within the limits allowed by the Nyquist theorem, the amount of information in the signal does not change.

Figure 6.29 confirms this view, for AR models and NNs at least, with their ability to predict not affected by a change in the sampling frequency. A drop in performance is only experienced when the sampling frequency gets close to the Nyquist frequency, that is double the cut-off frequency, ω_c , adopted in the pre-processing procedure.

model		$G_1, \omega_c = 1.2 \text{ rad/s}$			$G_2, \omega_c = 1 \text{ rad/s}$			$G_3, \omega_c = 1 \text{ rad/s}$		
		$l = 10$	$l = 25$	$l = 50$	$l = 10$	$l = 25$	$l = 50$	$l = 10$	$l = 25$	$l = 50$
Harvey	$d\omega = 0.1$	25.6%	-	-	30.6%	-	-	-	-	-
	$d\omega = 0.05$	30.7%	-	-	38.3%	-	-	-	-	-
	$d\omega = 0.01$	32.4%	-	-	47.6%	-	-	-	-	-
EKF	-	5.4%	-	-	46.0%	-	-	25.3%	-	-
AR	$n = 12$	94.9%	58.2%	-	98.1%	87.1%	37.2%	72.2%	57.6%	12.2%
	$n = 24$	94.9%	88.3%	9.1%	98.1%	94.5%	66.3%	72.2%	68.8%	28.4%
	$n = 32$	94.9%	91.4%	29.3%	98.1%	94.6%	69.9%	72.2%	68.8%	41.8%
NN	7-7-1, $n = 12$	84.3%	-	-	89.4%	48.9%	-	86.1%	24.1%	-
	5-7-1, $n = 24$	84.4%	-	-	91.1%	59.6%	-	89.3%	39.8%	-
	3-5-1, $n = 32$	68.0%	-	-	85.3%	30.1%	-	93.8%	20.1%	-

Table 6.2: Goodness-of-fit $\mathcal{F}(l)$ of different forecasting models on the Galway bay data sets of Fig. 6.14(a)

. Sampling frequency is $f_s = 2.56$ Hz.

model		$P_1, \omega_c = 1 \text{ rad/s}$			$P_2, \omega_c = 0.7 \text{ rad/s}$			$P_3, \omega_c = 0.7 \text{ rad/s}$		
		$l = 5$	$l = 12$	$l = 25$	$l = 5$	$l = 12$	$l = 25$	$l = 5$	$l = 12$	$l = 25$
Harvey	$d\omega = 0.1$	15.0%	-	-	41.2%	-	-	38.0%	-	-
	$d\omega = 0.05$	20.4%	-	-	50.5%	5.6%	-	43.5%	0.3%	-
	$d\omega = 0.01$	28.8%	-	-	56.7%	28.5%	-	53.1%	27.5%	-
EKF	-	8.3%	-	-	55.2%	24.2%	-	56.3%	20.8%	-
AR	$n = 12$	96.9%	69.6%	-	95.9%	94.1%	71.6%	98.7%	96.4%	81.1%
	$n = 24$	99.0%	95.7%	42.9%	95.9%	94.5%	92.6%	98.7%	96.7%	93.4%
	$n = 32$	99.0%	96.5%	52.3%	95.9%	94.5%	93.1%	98.7%	96.7%	93.7%
NN	7-7-1, $n = 12$	87.4%	20.9%	-	93.1%	80.8%	12.4%	97.1%	86.0%	39.9%
	5-7-1, $n = 24$	73.8%	-	-	98.9%	90.4%	52.8%	99.7%	95.5%	71.8%
	3-5-1, $n = 32$	74.7%	-	-	98.7%	92.5%	50.6%	97.3%	91.5%	48.8%

Table 6.3: Goodness-of-fit $\mathcal{F}(l)$ of different forecasting models on the Pico island data sets of Fig. 6.14(b)

. Sampling frequency is $f_s = 1.28$ Hz.

6.5.6 Discussion

This study of this Section was focused on the problem of short-term wave prediction, which is a central topic in the wave energy field, in order to allow a greater effectiveness and economic viability of any WEC. A pure univariate time-series forecasting approach was followed and several possible solutions were proposed. Real data from Galway bay and Pico island were available for testing the proposed solutions, and some interesting analysis was provided in Section 6.3. In particular, a valuable tool for the predictability analysis, independent of any particular solution, was proposed in Section 6.3.4. A quantification of the predictability showed how lower-frequency waves are easier to predict and, from a wave-energy point of view, high-frequency components, which carry lower energy (as revealed by the Fourier analysis provided in Section 6.3.1), may be filtered out to improve the prediction.

Summary results, obtained using the models proposed in Section 6.5, over the 6 sea states considered in this study, shown in Fig. 6.14(a) and Fig. 6.14(b), are organised in Table 6.2, regarding the Galway Bay data, and in Table 6.3, for the data from Pico. Negative values of $\mathcal{F}(l)$ were omitted, as they mean that the prediction diverges.

The most straightforward models discussed were harmonic models where the wave elevation is explicitly represented as a sum of sines and cosines, on the basis of linear wave theory. It was underlined how many issues (particularly the high complexity of the resultant models) arise due to the problem of the choice of frequencies when they are kept constant, so that reasonable predictions are only achieved for a maximum of 5-6 seconds in the future (even less, only 2-3 seconds, for the Galway bay data), if only low frequencies are predicted. Cyclical models with adaptive frequencies could have been considered, but then they become non-linear in the parameters and the complexity will be even higher, so that other solutions should be explored first.

In Section 6.4.2, it was highlighted how AR models implicitly represent cyclical models, where the frequencies are easily estimated with linear LS (as they are related to the regression coefficients). The amplitudes and phases of each harmonic component are, moreover, implicitly adaptive to the recent observations due to the regression terms of the model, so that only a batch estimate of the model offered very good accuracy up to 15 seconds (in some cases even 20 seconds) predictions for the low-frequency components of the waves. It was also shown how the frequencies are automatically estimated in the significant range of the sample spectrum of the training data set. The possibility of adapting the model in order to track variations of the wave spectrum through variable frequencies in the model was also analysed, and it was concluded that no real benefit is obtained through real-time adaptive AR modelling. Since static AR models were shown to maintain their prediction ability for relatively long periods (no performance decrease over 2 hour simulations), their adaptivity is not seen as a main issue at the moment, and also a simple periodic batch estimate may be a feasible solution, or the use of a set of AR models, estimated from different sea conditions, and a switching logic deciding which one is the more appropriate in real time.

A cyclical model with a single variable frequency was also presented in Section 6.4.3, where the real-time frequency estimation is realised through the EKF. The methodology revealed such a model to be reasonably effective for narrow-banded sea states, with good predictions for 5-10 seconds, but it is completely ineffective for wider-banded waves. It is, however, a very light and computationally simple solution (only 3 states), so that if a suitable way to integrate multiple frequencies is found, some improvement in performance may be obtained. More work could be done in this direction, as simple aggregation of the single frequency models resulted in some problems and poor results.

Finally, a comparison with NNs, given in Section 6.5.4, showed how, although NNs offer an accuracy comparable with the *AR* models, it would not be very appealing to further extend this more computationally expensive option, as no significant improvement is expected. Moreover, NNs do not offer any possibility of intuitive analysis and extraction of the characteristics of the real process from the model, which instead is very straightforward with AR models.

As a conclusion, AR models (or more parsimonious ARMA models, from the discussion in Section 6.4.5) seem to be well suited to compute wave predictions for more than one wave period into the future, when the focus is put on lower-frequency waves. Concerning the use of the wave-prediction algorithms in real-time WEC control, the real-time filter implementation needs to be given further attention, since a zero-phase filter was assumed in the current analysis. In this case, the choice is justified, since the focus is on looking at the achievable prediction. In addition, as described in Chapter 5, the controller of a WEC requires the prediction of an *effect* of the wave elevation on the device, e.g. the wave excitation force, which is effectively a low-pass filtered version

of the wave elevation, with the filtering provided by the device itself.

Section 6.6 moves the focus on the prediction of the excitation force and puts the work in perspective with the prediction requirements, that were studied in Chapter 5.

6.6 Prediction of the excitation force

Most solutions for real-time control of WECs, consisting of oscillating bodies, as reviewed in Chapter 4, require future knowledge of the excitation force, rather than the wave elevation. As defined in Section 3.3.1, the excitation force is the force produced by the wave incident on a floating system, when the latter is assumed to be at rest (i.e. not accounting for the force due to radiation, caused by the motion of the floater).

The need for prediction is often recognised in the wave energy literature, but focus is usually put on the prediction of the wave elevation, rather than the excitation force. Focusing on the prediction of the wave elevation makes sense when solutions based on remote sensing of the waves and spatial propagation models are proposed, which is often the case, as emerged in the wave forecasting review in Section 6.2. Based on the mathematical model of the system, the future excitation force can then be calculated from knowledge of the future wave elevation, using (3.113).

This Chapter has focused on a different approach, where the incident wave elevation is predicted only from its past history, with no need of remote sensing, as explained in Section 6.1. However, it can be noted that there is no direct access to the undisturbed incident wave elevation, and that the latter should be reconstructed, through an observer, based on the wave or force measurements and on the system's motion. It does, therefore, make sense to focus directly on the wave excitation force, which is the quantity of primary interest and that is, intuitively, easier to estimate. Besides, as it will be highlighted in Section 6.6.1, the excitation force is a low-pass filtered version of the wave elevation, which solves the issue of introducing an artificial low-pass filtering procedure to allow for better predictions.

The present Section extends the application of the model proposed for the prediction of the wave elevation, in Section 6.4, to the prediction of the wave excitation force. After giving more details about the nature of the excitation force and its properties, in Section 6.6.1, the prediction model is specified in Section 6.6.2. Results over a range of wave conditions, for different WEC geometries, are summarised in Section 6.6.3, and compared with the prediction requirements, quantified in Chapter 5.

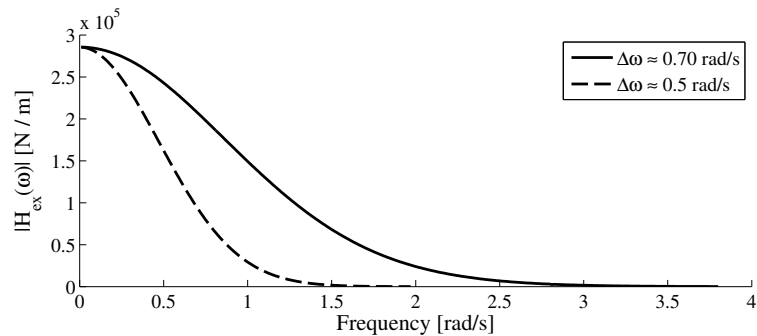


Figure 6.30: Magnitude of excitation filter, $H_{ex}(\omega)$, of two heaving cylinder with the same mass distribution and radius, $R = 3$ m, but different draught, $h = 4$ and $h = 20$ m, resulting in different bandwidth, $\Delta\omega \approx 0.7$ and $\Delta\omega \approx 0.5$ rad/s, respectively. The bandwidth is calculated as the frequency at which the magnitude is -3 dB, compared to the value at $\omega = 0$.

6.6.1 The wave excitation force

Based on linear potential theory, introduced in Chapter 3, the wave excitation force is defined as the effect of ocean wave incident on a floating body, when this is supposed to be at rest in its equilibrium position. A linear relation between the excitation force, $f_{ex}(t)$, and the incident wave elevation, $\eta(t)$, is expressed in the frequency domain, as from (3.114):

$$F_{ex}(\omega) = H_{ex}(\omega)\Xi(\omega), \quad (6.112)$$

where $F_{ex}(\omega)$ and $\Xi(\omega)$ are the Fourier transform of the excitation force and the incident wave, respectively, while $H_{ex}(\omega)$ is a transfer function, based on the system's geometry, that will be named the excitation filter.

Note that $H_{ex}(\omega)$ is a non-causal filter [6],[57], since the incident wave is not the direct cause of the force, but the fluid pressure on the wet surface is, as discussed in Section 3.3.1. What is of interest here, however, is that the magnitude of the excitation filter has low-pass characteristics. Depending on the system filtering properties, it may be expected that the wave excitation force is more or less easily predicted, for the same sea conditions. The predictability analysis, proposed in Section 6.3.4, and the results obtained with the different forecasting models proposed, in Section 6.5, have confirmed that low-frequency waves allow better predictions longer into the future, with simple regressive and linear models. As an example, Fig. 6.30 shows the excitation filter estimated for two heaving cylinders, with different bandwidth. The bandwidth is calculated as the frequency at which the magnitude is -3 dB, compared to the value at $\omega = 0$, where there is a maximum.

One issue with the wave excitation force is that it is not a directly measurable quantity, but rather a mathematical convenience for the solution of the hydrodynamics of the fluid domain. It is possible, however, to build an observer, based on measurements of the motion and on a model of the floating system, to derive an estimate of the excitation force, as proposed in [119]. Considering the linear model of a one-degree-of-freedom oscillating system in heave, given in (3.143), and assuming

that measurements of the velocity are available, the wave excitation force can be estimated as:

$$f_{ex}(t) = (m + m_\infty) \dot{v}(t) + \int_0^{+\infty} h_r(\tau) v(t - \tau) d\tau + K_v v(t) + K_b \int_0^t v(\tau) d\tau - f_u(t), \quad (6.113)$$

where m and m_∞ are the mass and added mass at infinite frequency, $h_r(t)$ is the radiation impulse response, defined in (3.118), K_v is a constant modelling a linear viscous force, K_b is the buoyancy coefficient, defined in (3.122), and $f_u(t)$ is the control force, produced by the PTO.

An alternative possibility for the estimation of the wave excitation force is to measure the wave elevation at some distance from the WEC and then implementing the definition in (6.112). As discussed in [57], the relationship in (6.112) becomes approximately causal by increasing the distance between the wave measurement point and the WEC. However, multi-directionality and wave radiation may require an array of measurements and a more complex model for the estimation of the excitation force.

In the following Sections of this Chapter, it will be assumed that the excitation force is known, with no need of estimation. The focus, here, is on determining the prediction horizon that is achievable for the excitation force with the proposed forecasting models. At the same time, since the excitation force is calculated in simulation, using the equations of the linear model, the observer in (6.113) would give a perfect estimate, so that its implementation is of no value, in such a context.

6.6.2 Prediction model

Among the models proposed for the prediction of the wave elevation, analysed in Sections 6.4 and 6.5, linear AR models have shown the best performance, at least when the focus is put on the low frequencies. The excitation force, from the discussion in Section 6.6.1, has the same dynamic as the wave elevation, but low-pass filtered by the dynamics of the system, specifically by the excitation filter, $H_{ex}(\omega)$.

Therefore, AR models are utilised here for the analysis of the achievable prediction of the wave excitation force. In particular, at instant k , the l -step-ahead prediction, $\hat{f}_{ex}[k + l|k]$, is calculated as:

$$\hat{f}_{ex}[k + l|k] = \sum_{i=1}^n \vartheta_i[k] \hat{f}_{ex}[k + l - i|k], \quad (6.114)$$

where ϑ_i , $i = 1, \dots, n$ are the coefficients of the AR model, of order n , and, obviously, $\hat{f}_{ex}[k + l - i|k] = f_{ex}[k + l - i]$ if $k + l - i \leq k$ (information acquired, no need of prediction).

As described in Section 6.5.2, the order of the model is chosen on the basis of a modified version of the classical AIC and BIC criteria, defined in (6.110) and (6.111), where the multi-step-ahead prediction error is taken into account. The coefficients, a_i are then identified from a set of training data, by minimisation of the LRPI, expressed in (6.52), whose details were given in Section 6.4.2. Once the parameters are estimated, the model is applied in real-time for the prediction of the excitation force. No adaptive mechanism that deals with the non-stationarity of the waves is implemented, since this is not considered an issue over the length of the considered data sets (20 minutes to 2 hours), following the discussion in Section 6.5.2.

ω_p [rad/s]	0.5	0.55	0.6	0.65	0.7	0.75	0.8	0.85	0.9	0.95	1.0
Num	15	40	52	37	31	11	19	12	9	5	2

Table 6.4: Number of data sets available per each peak frequency, as from Fig. 5.13.

The performance of the prediction algorithm is measured in terms of the index of goodness-of-fit, $\mathcal{F}[l]$, proposed in (6.106). From the discussion in Section 6.6.1, it is expected that the ability to predict the excitation force acting on a system is strictly connected to the filtering capability of the transfer function $H_{ex}(\omega)$. Systems having an excitation filter, $H_{ex}(\omega)$, with a narrower bandwidth will experience lower-frequency waves, which should allow for longer prediction horizons, in seconds.

6.6.3 Results for a range of floating systems

The performance of AR models for the prediction of the wave excitation force is evaluated on data sets based on real wave measurements. The wave data was provided by the Irish Marine Institute and comes from real observations collected from a data buoy deployed off the West coast of Ireland, in the Belmullet wave energy test site, at approximately $54^\circ 13'$ N, $10^\circ 8'$ W. The data consists of two consecutive 30 minutes sets for each hour, sampled at 1.28 Hz, covering the year 2010. Fig. 6.31 shows the distribution of peak frequency, ω_p , and significant wave height, H_s , so to give an idea of the wave climate at Belmullet.

Several reasons led the author to utilise data from a different location than Galway Bay and Pico Island, which were considered in the study of the wave forecasting algorithms, in Section 6.5. Firstly, the prediction requirements, in Chapter 5, were evaluated on wave data from Belmullet. Therefore, a clearer comparison between prediction requirements and achievable prediction is possible. At the same time, the Belmullet location has a wave climate that is similar to that of Pico Island, described in Section 6.3, that is exposed to north-easterly winds and therefore to large swells generated in the Atlantic Ocean. Galway Bay data were not considered since the proposed device geometries are closer to full scale systems, whereas Galway's wave climate is more suitable for quarter scale WECs.

For the calculations carried out in the following, the same sets utilised in Section 5.4, for the calculation of the prediction requirements, have been selected among all the ones available. In particular all the sea states with a peak frequency approximately equal to values that range from 0.5 rad/s to 1 rad/s, with step 0.05, were picked up. The distribution of peak frequency and significant wave height of such data sets is highlighted in Fig. 6.31 and the number of data sets available for each peak frequency is indicated in Table 6.4.

Given the wave-elevation records, the excitation force experienced by floating systems with different geometries was examined. In particular, the excitation force was calculated, off-line, from the non-causal relation given in (6.112). The resulting excitation-force time series is then utilised for training and validation of the AR prediction models, designed and identified based on the methodology given in Section 6.6.2.

The same geometries utilised in Section 5.4 were utilised here, for a fair comparison of the prediction requirements with the achievable prediction. In particular the WECs consist of bottom-

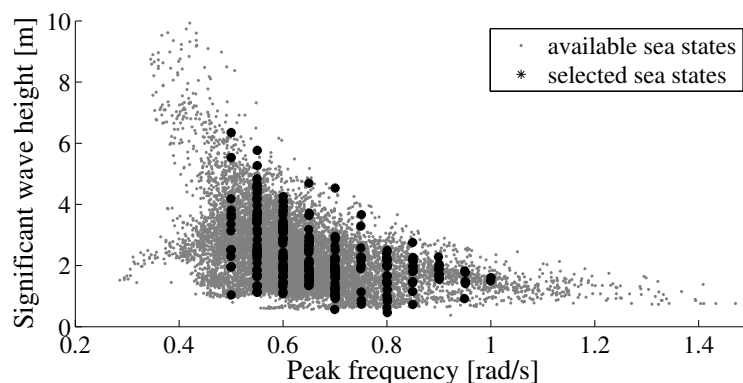


Figure 6.31: Distribution of peak frequency, ω_p , and significant wave height, H_s , collected from a data buoy in Belmullet ($54^\circ 13' N$, $10^\circ 8' W$) over the year 2010. The data sets selected for the numerical simulations are highlighted.

referenced floating cylinders constrained to move in the heave direction only, as modelled in Section 3.3.1. The geometry of the cylinders is specified in Table 6.5, where R : radius; h : draught at rest; m : submerged mass at rest; ω_0 : resonance frequency; $\Delta\omega$: bandwidth of the excitation filter, calculated as in Fig. 6.30; τ_1 : main time constant of the kernel function $h_{opt}(t)$, that indicates the forecasting horizon required by an effective controller, as from the results of Chapter 5.

Note that the bandwidth of the system, which is expected to have a strong influence on the ability to predict the excitation force, is mostly affected by the height/draught. At the same time, as already noticed in Section 5.4.1, it appears that the time constant τ_1 is mainly affected by the radius, while τ_1 only slightly changes for different heights. As demonstrated by the quantification of the prediction requirements, carried out in Section 5.4, heaving cylinders of different sizes, but with similar radius, would be equally (or similarly) demanding in terms of wave excitation-force prediction. One may, therefore, conclude that, for the implementation of non-causal reactive control, cylinders with small radius (small prediction requirements) and large height (improved predictability) would be more suitable.

In Fig. 6.32, the accuracy of the prediction, expressed through the quantity $\mathcal{F}(l)$, calculated from (6.106), is shown in detail for three different cylinders, C_1 , C_8 and C_{15} , in three different wave conditions, with a peak frequency of $\omega_p \approx 0.5$, 0.8 and 1 rad/s. Obviously, the accuracy of the prediction decreases with the prediction horizon, but for the same waves the accuracy at a given future horizon is different for different devices. As expected, in fact, cylinders with stronger filtering properties, that is narrower bandwidth, allow for better prediction. Note that the forecasting horizon is expressed in terms of the wave period (peak period), so that the difference in accuracy, for a specific system, in different sea states is minor (related to the bandwidth of the sea state or to eventual non-linearities).

A more general picture is offered in Fig. 6.33 where, for each device, the average forecasting horizon below which the prediction has an accuracy of $\mathcal{F}(l) \geq 60\%$ is shown. The forecasting horizon is expressed in terms of wave periods. As for the prediction requirements, analysed in Section 5.4, the variance of each value is also shown through the length of the bar which is symmetric about the mean value. The prediction accuracy increases almost linearly as the bandwidth of the systems decreases. In most of the cases, more than half a wave period can be predicted with an

	R [m]	h [m]	m [kg $\times 10^5$]	ω_0 [rad/s]	$\Delta\omega$ [rad/s]	τ_1 [s]
C_1	3	4	0.93	1.40	1.03	10.00
C_2	3	8	1.86	1.08	0.79	9.97
C_3	3	12	2.80	0.92	0.66	9.94
C_4	3	16	3.73	0.82	0.59	9.91
C_5	3	20	4.66	0.74	0.53	9.89
C_6	5	4	2.59	1.23	0.98	19.80
C_7	5	8	5.18	1.02	0.75	19.80
C_8	5	12	7.77	0.89	0.63	19.76
C_9	5	16	10.40	0.79	0.56	19.7
C_{10}	5	20	12.90	0.72	0.51	19.76
C_{11}	7	4	5.07	1.14	0.95	31.06
C_{12}	7	8	10.10	0.98	0.72	30.96
C_{13}	7	12	15.20	0.85	0.62	30.96
C_{14}	7	16	25.40	0.70	0.54	30.96
C_{15}	7	20	31.71	0.64	0.50	30.9

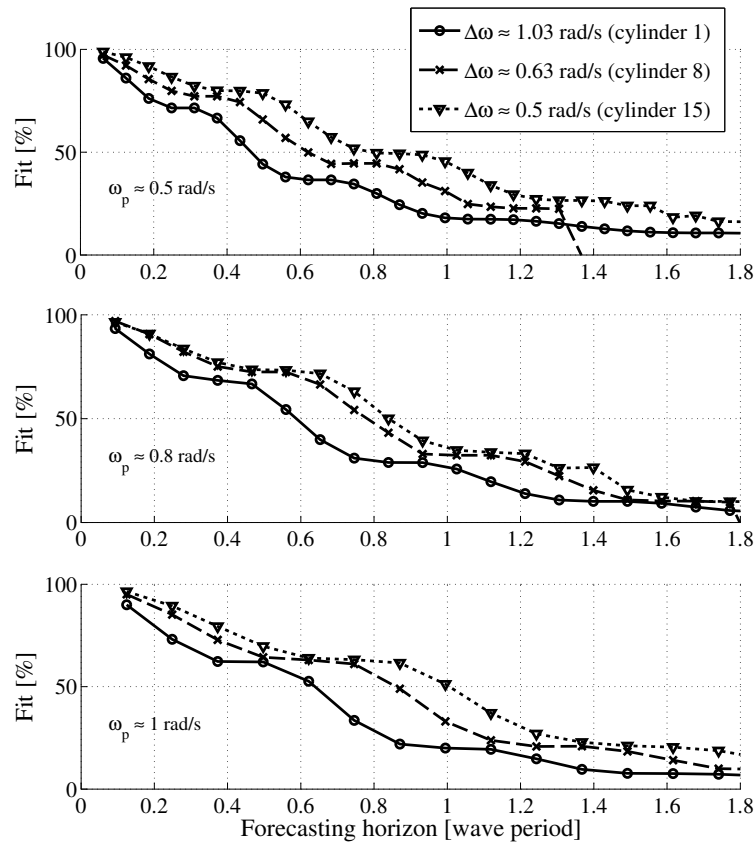
Table 6.5: Geometry of heaving buoys. C : cylinder

Figure 6.32: Accuracy of the the prediction of the wave excitation force acting on three cylinders, and produced by three different sea states. The prediction is calculated with AR models.

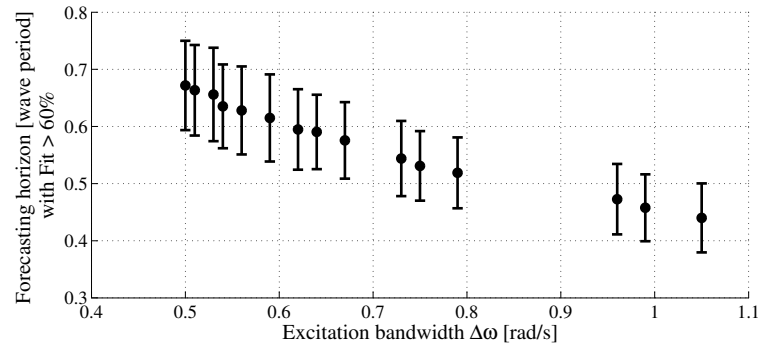


Figure 6.33: Average horizon for which the excitation force acting on a system can be predicted with more than 60% of accuracy.

accuracy above 60%. Note, however, that the variance of the prediction horizon, for each device, is quite significant since external parameters (wave properties) also have a strong influence on the prediction, as emerged from the results of Section 6.5.

In general, however, it emerges that more than 0.5 wave period in the future (about 4 to 12 seconds at the considered location) can be predicted with a $\mathcal{F} > 60\%$. By making a comparison with the required prediction horizon, quantified in Section 5.4 to well above 20 s in most situations, the performance of the predictor is quite inadequate.

The possibility of manipulating the control, such that the non-causality of the controller, and therefore the prediction requirements, are reduced, was proposed in Section 5.3.1. A stark reduction of the prediction horizon required for an effective implementation of reactive control was achieved, as shown in the results of Section 5.4.3, at the cost of a minor performance drop. In particular, the prediction requirements were significantly reduced to a horizon shorter than 10 s, which is well within the ability of the AR forecasting models proposed here, as shown in Fig. 6.33. Also, it is interesting to note that the differences between the cylinders are minimal, so that no geometry seems to be particularly advantageous in terms of the required forecasting horizon.

It may be concluded that, based on the comparison between prediction requirements and achievable prediction, the univariate approach to the problem of wave excitation-force prediction, proposed in this Chapter, is unsuitable to the approximation of non-causal complex-conjugate control. The correlation within the signal to be predicted does not allow its future behavior to be extrapolated long enough into the future, as required by complex-conjugate control, unless in some specific sea states (very narrow-banded and low-frequency swells) and for specific geometries not demanding in terms of prediction. However, the manipulation of complex-conjugate control, proposed in Chapter 5, reduced the prediction requirements well within the prediction horizon achievable with simple AR models, at the cost of a minor drop in performance (quantified in Section 5.4.3).

6.7 Conclusion

This study was focused on the problem of short-term wave and wave excitation-force prediction, which is a central topic in the wave-energy field, in order to improve the economic viability of a WEC. As opposed to the classic reconstruction of the wave field from distant measurements, an approach was proposed where the wave elevation is treated as a univariate time series and forecasted only on the basis of its past history.

Results on real wave elevation data from Galway bay and Pico Island showed how a relatively simple AR model, which implicitly models the cyclical behavior of the waves, can offer a very accurate prediction of the low frequency swell waves for up to 2 typical wave periods into the future. It was also shown that no real benefit can be expected in using non-linear forecasting models, such as neural networks, unless highly non-linear sea states are encountered. In deep water locations, however, non-linearities due to interactions between different wave components only occur for very low energy wind waves, which are of minor interest in a wave energy context (an analysis of non-linearities in waves is provided in Section 6.3.3).

Concerning the use of the wave prediction algorithms in the control of WECs, the real-time filter implementation needs to be given further attention, since a zero-phase filter was assumed in the current analysis. In this Chapter, we feel justified in the choice, since the focus is on looking at achievable prediction. In addition, as from the control review in Chapter 4 and from the discussion in Section 6.6.1, the controller of a WEC may require the prediction of the *effect* of the wave elevation on the device, e.g. the wave excitation force, which is effectively a low-pass filtered version of the wave elevation, with the filtering provided by the device itself.

The predictability of the excitation force was also examined in Section 6.6. AR models were utilised for the prediction of the excitation force experienced by a variety of floating cylinders. The same wave data and cylinder geometry as in Chapter 5 was utilised, for a comparison of the achievable prediction with the prediction requirements. Floating systems with a narrower bandwidth were found to allow better prediction of the excitation force, as expected from the results on the wave elevation records. However, accurate predictions were obtained for lead times between 0.5 and 1 wave period, which is well below the requirements for most systems (well above 20 seconds).

Simple manipulation of the control, based on prior knowledge of the excitation force spectral distribution, was also proposed for the reduction of the prediction requirements, in Chapter 5. Such reshaping of the non-causal control law allowed a significant decrease in the prediction requirements, so that they fall within the range of predictability achievable with simple AR models. Minor performance losses, in terms of energy capture, were verified in most sea states. The algorithm proposed in the present Chapter for the prediction of the excitation force, therefore, can be effectively utilised for the approximation of complex-conjugate control, in real time.

The integration between prediction and control will be more thoroughly discussed in the following Chapters 7 and 8.

Chapter 7

A real-time controller for wave energy converters

Abstract

A novel strategy for the control of oscillating wave energy converters (WECs) is proposed. The controller tunes the oscillation of the system such that it is always in phase with the wave excitation force and the amplitude of the oscillation is within given constraints. Based on a non-stationary, harmonic approximation of the wave excitation force the controller is easily tuned in real-time for performance and constraints handling, through one single parameter of direct physical meaning. The effectiveness of the proposed solution is assessed for a heaving system in one-degree of freedom, in a variety of irregular (simulated and real) wave conditions. A performance close to non-causal complex-conjugate control, in the unconstrained case, and to model predictive control, in the constrained case, is achieved. Additional benefits in terms of simplicity and robustness are obtained.

7.1 Introduction

As extensively discussed in Chapter 4, the efficiency of oscillating WECs can be significantly increased through an automatic control that tunes its oscillations to the incident wave elevation, in such a way as to improve the power transfer from the ocean to the system.

Suggested control strategies for wave energy conversion are often based on complex-conjugate control, that gives the optimal conditions, in the frequency domain, for maximum wave energy absorption [6, 11]. A real-time implementation of reactive control in the time domain, however, is not practical, due to its non-causality and to the fact that physical constraints are not taken into account.

The non-causality was dealt with in Chapters 5 and 6. In particular, it was concluded that simple AR models can give predictions long enough into the future, for the implementation of the non-causal relation between velocity and excitation force. In order to deal with the constraints, as reviewed in Chapter 4, alternative control solutions have also been proposed, where the limitation

imposed by the physics of the system (e.g. amplitude of motion or velocity and applicable forces), are explicitly accounted for. In particular, some of these alternatives include latching [12, 107] (refer to Section 4.2.2 for the details), where the oscillation in the system is delayed so to be in phase with the excitation from the waves, and MPC [119, 117, 13, 120], which is based on a constrained optimisation, as discussed in Section 4.2.3.

While, in theory, latching allows the achievement of high energy capture, its applicability has been questioned [110], due the excessive loads on the latching mechanism, the disappointing performance in the case of self-reacting point absorbers [185] and the long (some minutes) prediction horizon required for the real-time optimisation in irregular waves to converge [12]. Solutions based on MPC, on the other hand, have shown a lot of benefits, including the built-in ability to handle constraints [13, 120]. MPC, however, need to solve a constrained optimisation problem at each time-step, which can be time-consuming if a complex model of the WEC is utilised. Besides, the performance of the controller depends on a variety of variables (cost function, optimisation algorithm, future horizon, specification of the constraints, etc.) that are not always related to the physical domain of the problem and can only be tuned by extensive simulation. MPC-based controllers also require prediction of the excitation force which, although possible for 1-2 wave periods [16], as concluded in Chapter 6, introduces additional uncertainty into the solution.

This Chapter proposes an alternative real-time controller that, while being sub-optimal, is both simple and effective. In particular, the proposed controller has a hierarchical structure where a reference velocity is calculated as a scaled version of the wave excitation force, modelled as a sinusoid with variable frequency. The amplitude of the velocity is the main parameter of the controller, that can be tuned in real-time for performance and constraint handling. The reference velocity, generated by the high-level controller, is imposed on the system by a low-level control loop. Since the excitation force is assumed to be purely harmonic, the control solution turns out to be causal, and no prediction is required. The only requirement is an estimator that calculates the current phase, amplitude and frequency of the excitation force. Such a type of estimator was already analysed for the prediction of the wave elevation as a sinusoidal extrapolation using the EKF, in Section 6.4.3.

Since the controller keeps the velocity in phase with the external force, it is a reactive controller, that requires a PTO capable of implementing a bi-directional energy flow. Typical hydraulic PTOs and linear electrical generators that have been studied for applications in wave energy have the ability of inverting the energy flow [186, 87]. The non-ideal efficiency, however, needs to be taken into account for an appropriate evaluation of the performance of the device [187, 188]. This paper assumes ideal efficiency of the PTO, to maintain the focus on the controller concept. However, a quantitative discussion about the requirement of reactive power is proposed in Section 7.7, and it is shown how the nature of the controller allows the optimisation the performance in the presence of a non-ideal PTO efficiency, in a rather straightforward way.

The model of the considered WEC, and the specific geometry that will be utilised to exemplify the controller through the Chapter, is introduced in Section 7.2. The proposed controller is first discussed in Section 7.3, where no constraints are taken into account, and it is compared to the non-causal implementation of complex-conjugate control. The possibility of handling constraints in a simple and effective way is then proposed in Section 7.4, where the implementation of MPC is also proposed as a comparison. Section 7.5 details the harmonic model of the wave excitation force

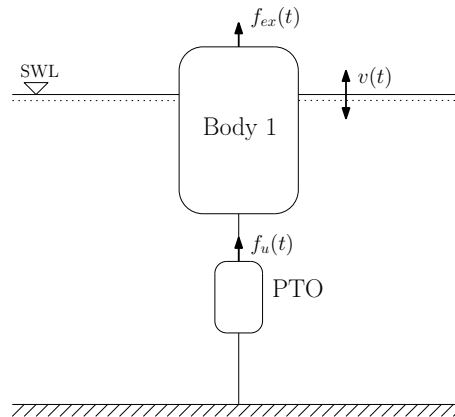


Figure 7.1: One-degree of freedom (heave) floating system for wave energy conversion.

and how it is fitted to the data. The low-level controller adopted in this Chapter is then reported in Section 7.6. Validation against complex-conjugate control (in the unconstrained case) and MPC (in the constrained case) is then reported in Section 7.7, under a variety of irregular, simulated waves. Performance with real wave data and the robustness to model parameter variations are also assessed. Conclusions and final remarks are outlined in Section 7.8.

7.2 The system

A single-body floating system, as in Fig. 7.1, is considered where energy is extracted from the relative motion with the sea bottom, through a generic PTO mechanism. The system is constrained to move in the heave direction only. The external forces acting on the WEC are the excitation from the waves and the control force produced by the PTO. Under the assumption of linearity, neglecting viscosity and other losses, based on the discussion in Section 3.4.2, the force-velocity model, in the frequency domain, is written [6] as:

$$j\omega V(\omega) + Z_r(\omega)V(\omega) + \frac{K_b}{j\omega}V(\omega) = F_{ex}(\omega) + F_u(\omega). \quad (7.1)$$

In (7.1), $V(\omega)$ is the heaving velocity, while $F_{ex}(\omega)$ and $F_u(\omega)$ are the wave excitation and PTO forces, respectively. The imbalance between gravity and the hydrostatic restoring force is modelled by the buoyancy coefficient K_b . The radiation force, due to waves radiated by the body's motion, is expressed through the radiation impedance $Z_r(\omega)$, defined in (3.116).

The model in (7.1) can be expressed in the compact form:

$$V(\omega) = \frac{1}{Z_i(\omega)} [F_{ex}(\omega) + F_u(\omega)], \quad (7.2)$$

where the intrinsic impedance, $Z_i(\omega)$, was already defined in (3.129)..

The excitation force, as already discussed in Sections 3.3.1 and 6.6, is the effect of the incident

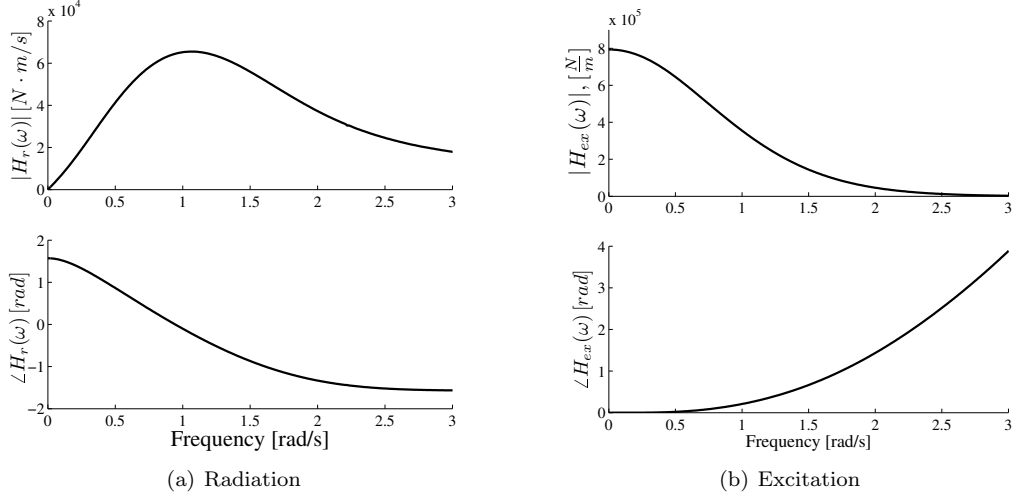


Figure 7.2: Radiation and excitation frequency responses for a floating cylinder with radius $R = 3$ m, height $H = 5$ m, draught $h = 4$ m, mass $M = 3.2 \times 10^5$ Kg, calculated using the hydrodynamic software Wamit [59].

wave on the floating system:

$$F_{ex}(\omega) = H_{ex}(\omega)\Xi(\omega), \quad (7.3)$$

where $\Xi(\omega)$ is the Fourier transform of the incident wave elevation, $\eta(t)$. The transfer function $H_{ex}(\omega)$ is a property of the WEC and has low-pass filter characteristics. Note, however, that $H_{ex}(\omega)$ is non-causal, since the incident wave is not the cause of the force (the pressure distribution is) [6] and cannot be implemented in real-time simulations.

The example WEC system considered in this study consists of a heaving cylinder with radius $R = 3$ m, height $H = 5$ m, draught $h = 4$ m, mass $M = 3.2 \times 10^5$ Kg. The radiation and excitation transfer functions, $H_r(\omega)$ and $H_{ex}(\omega)$, are identified numerically through the hydrodynamic software WAMIT [59] and are shown in Fig. 7.2.

Based on the procedure outlined in Section 3.3.3, a 4th-order approximation of the radiation, $\tilde{H}_r(s)\Big|_{s=j\omega} \approx H_r(\omega)$, as shown in Fig. 7.3(a), is identified in the frequency domain [69]. The floating system in (7.2) can then be approximately modelled as the following SISO system:

$$\frac{V(s)}{F_{ex}(s) + F_u(s)} = \frac{s}{s^2(m + M_\infty) + s\tilde{H}_r(s) + K_s} \triangleq \frac{1}{\tilde{Z}_i(s)}, \quad (7.4)$$

where s is the complex frequency in the Laplace domain. The input is the external force (from the waves or from the PTO), while the output is the system's velocity.

In particular, a 6th-order force-velocity system is obtained from (7.4), and it is specified by the following transfer function (coefficients rounded to one decimal place for brevity):

$$\frac{1}{\tilde{Z}_i(s)} = \frac{1.8 \times 10^{-6} \cdot s(s^2 + 1.1s + 0.4)(s^2 + 1.6s + 1.8)}{(s^2 + 1.2s + 0.4)(s^2 + 1.4s + 1.6)(s^2 + 0.1s + 1.5)}. \quad (7.5)$$

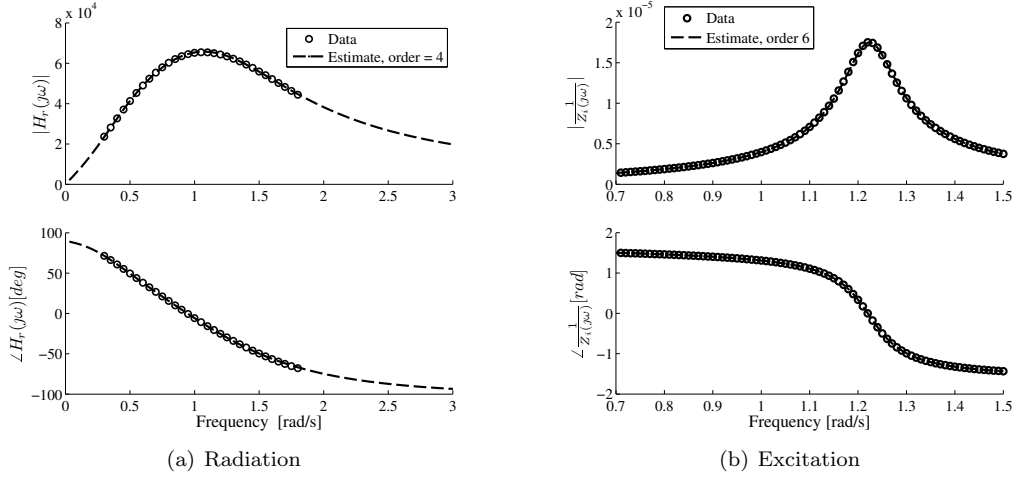


Figure 7.3: Finite-order approximation of the response of the WEC, calculated in the frequency domain, using the toolbox developed in [66].

In Fig. 7.3(b), the finite-order approximation $1/\tilde{Z}_i(s)$ is compared with the numerical (infinite-order) function $1/Z_i(\omega)$, as returned by the hydrodynamic software.

7.3 Unconstrained controller

The proposed controller is introduced here without taking into account of any motion or force constraint. As reviewed in Section 4.1.1, complex-conjugate control gives the conditions for maximum power transfer from the waves to the PTO, in the unconstrained case. Based on the study carried out in Chapters 5 and 6, a real-time implementation of the non-causal complex-conjugate control, through predictions of the excitation force, is proposed in Section 7.3.1. Section 7.3.2, then, outlines a causal approximation of complex-conjugate control. The main advantage of the causal solution is that it allows inclusion of the motion/forces constraints in a quite straightforward way, as it will be discussed in detail in Section 7.4.

7.3.1 Non-causal realisation through predictions

As extensively discussed in Section 4.1.1, maximum wave power absorption of a one-degree-of-freedom WEC, of the type modelled in Section 7.2, is achieved under the two following conditions:

$$V_{opt}(\omega) = \frac{1}{2B(\omega) + 2K_v} F_{ex}(\omega) \quad (7.6)$$

$$F_{u,opt}(\omega) = -Z_i^*(\omega)V(\omega) = -\frac{Z_i^*(\omega)}{2B(\omega) + 2K_v} F_{ex}(\omega), \quad (7.7)$$

that define the optimal velocity, $V_{opt}(\omega) = \mathcal{F}\{v_{opt}(t)\}$, and the optimal PTO force, $F_{u,opt}(\omega) = \mathcal{F}\{f_{u,opt}(t)\}$.

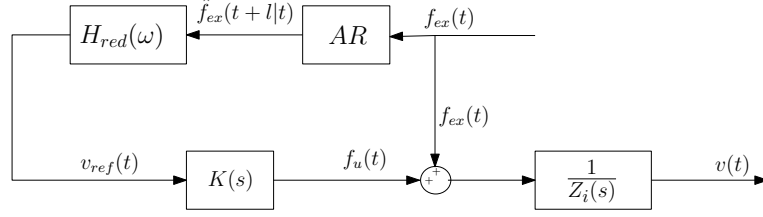


Figure 7.4: Non-causal approximation of complex-conjugate control.

As discussed in Chapter 5, it is convenient to implement the non-causal condition in (7.6) for the calculation of a velocity reference, based on predictions of the excitation force. A low-level controller would then impose such a velocity on the system by acting on the PTO force, as shown in Fig. 7.4.

At time t , the optimal velocity is given by:

$$v_{opt}(t) = \int_{-\infty}^{+\infty} h_{opt}(\tau) f_{ex}(t - \tau) d\tau, \quad (7.8)$$

where

$$h_{opt}(t) = \mathcal{F}^{-1} \left\{ \frac{1}{2B(\omega)} \right\} = \mathcal{F}^{-1} \{ H_{opt}(\omega) \}. \quad (7.9)$$

Note that the Fourier inversion of (7.9) is only valid in a generalised sense, as explained in Section 5.2.1. The function $H_{opt}(\omega)$, in fact, is not absolutely integrable, since it tends to a constant, $1/2K_v$, if friction losses are taken into account (K_v is the linear coefficient of viscous forces, introduced in (3.123)) or to infinity, if there are no losses, which is the case here, based on the model in (7.1).

Following the methodology proposed in Section 5.2.1, a manipulation of the function $H_{opt}(\omega)$ is applied for the reduction of the prediction requirements. As shown in Fig. 7.5, the resulting function, $H_{red}(\omega)$, has a significantly reduced non-causality, while still matching the optimal function, $H_{opt}(\omega)$, at the frequencies of interest, so that only a minor performance drop is expected. In quantitative terms, the dominant time constant, τ_1 , is reduced from $\tau_1 \approx 19.8$ s to $\tau_1 \approx 2.7$ s. As shown in Chapter 5, the time constant τ_1 is proportional (almost linearly) to the forecasting horizon required for an effective implementation of complex-conjugate control.

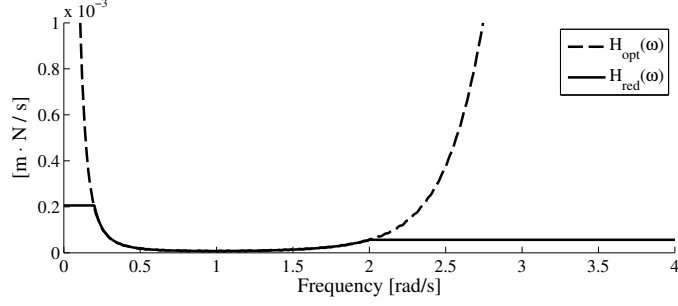
By defining the singularity of $H_{red}(\omega)$ at high frequencies, namely the constant $H_\infty = \lim_{\omega \rightarrow \infty} H_{red}(\omega)$, the kernel function $h_{red}(t)$ can be decomposed as:

$$h_{red}(t) = H_\infty \delta(t) + k_{red}(t), \quad (7.10)$$

where $\delta(t)$ is a Dirac delta function and

$$k_{red}(t) = \mathcal{F}^{-1} \{ H_{red}(\omega) - H_\infty \} = \mathcal{F}^{-1} \{ K_{red}(\omega) \}. \quad (7.11)$$

The Fourier transform in (7.11) is now well defined, since $K_{red}(\omega)$ has limited support and is absolutely integrable. The IDFT can therefore be applied to derive a discretised function representing $k_{red}(t)$.



(a) Frequency response.

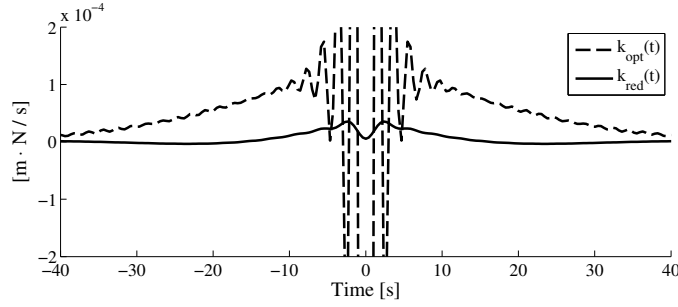

 (b) Impulse response (without singularity at time $t = 0$).

Figure 7.5: Non-causal reference generation, manipulated for the reduction of the prediction requirements.

By combining (7.8) and (7.10), the reference velocity is approximated as:

$$v_{ref}(t) = H_{\infty} f_{ex}(t) + \int_{-\infty}^t k_{red}(\tau) f_{ex}(t - \tau) d\tau. \quad (7.12)$$

In (7.12), the kernel function $k_{red}(t)$ is real and even, and it is approximately zero after some time $|t| > T$. Considering also that the actual implementation of the reference generator has to be in discrete time, the optimal reference velocity, based on reactive control, is ultimately calculated as:

$$v_{ref}[k] \approx H_{\infty} f_{ex}[k] + T_s \sum_{j=-L}^L k_{red}[j] f_{ex}[k - j], \quad (7.13)$$

where T_s is the sampling time and $L = T/T_s$ is the future (and past) horizon after which additional knowledge of the excitation force has no significant influence on the velocity calculation. Note that, as discussed in Section 5.2.1, when applying the IDFT to derive the kernel $k_{red}[k]$, it is possible to obtain any desired sampling time, T_s , by zero padding the function $K_{red}(\omega)$.

In the specific case of the function $H_{red}(\omega)$, shown in Fig. 7.5(a), a forecasting horizon of $L = 60$ steps is utilised, at a sampling frequency of $f_s = 2.56$ Hz, that is $T_s = 0.3906$ s. The amplitude of the Dirac delta in (7.10), H_{∞} , is 5.666×10^{-5} . Note that the choice of the function $H_{red}(\omega)$, as well as the future horizon considered in the calculation of the velocity, L , was not optimised. Extensive simulations on a variety of sea states and a numerical optimisation could be

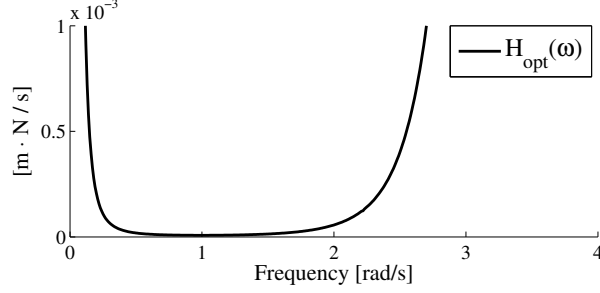


Figure 7.6: Optimal relation between excitation force and oscillation velocity. The phase is zero.

carried out, as proposed in Chapter 5. However, the focus of the present Chapter is on the causal solution of the controller, and an extensive search for an optimal non-causal law, as a compromise between performance and prediction requirements, goes beyond the designed scope.

7.3.2 Causal approximation

From the detailed discussion about complex-conjugate control, in Section 4.1.1, the oscillation velocity should always be kept in phase with the excitation force, for maximum wave energy absorption. Based on (7.6), the velocity should also have an amplitude that is modulated in the frequency-domain by the inverse of double the radiation resistance, $1/2B(\omega)$. In Section 7.3.1, the non-causal amplitude condition was implemented with a prediction of the excitation force, based on the results of Chapters 5 and 6. This Section, on the other hand, proposes a non-optimal simplification that does not require predictions, and that allows quite a straightforward way of dealing with constraints, as will become clear in Section 7.4.

Consider Fig. 7.6, which shows the behavior of the function $1/2B(\omega)$ for the heaving cylinder with a geometry as specified in Section 7.2. The function is a frequency-dependent gain to be applied to the excitation force, in order to obtain the velocity.

As explained in detail in Section 5.3.2, in practice, the excitation force is contained within a restricted band of frequencies, mostly within the flat part of $1/2B(\omega)$ (refer to Fig. 7.6), and a constant approximation, based on a second order model of the system, was proposed [20]. If a real-time estimate of the peak frequency of the excitation force is available, however, it is possible to adapt the constant from the curve in Fig. 7.6, in real-time.

Assuming that the excitation, $f_{ex}(t)$, is a narrow-banded harmonic process, defined by time-varying amplitude, $A(t)$, frequency, $\omega(t)$, and phase $\varphi(t)$:

$$f_{ex}(t) = A(t) \cos[\omega(t)t + \varphi(t)], \quad (7.14)$$

the reference velocity can be generated from the following adaptive law:

$$v_{ref}(t) = \frac{1}{H} f_{ex}(t), \quad \frac{1}{H} = \frac{1}{2B(\omega)} \quad (7.15)$$

where the value of the constant, H , is calculated from the curve $1/2B(\omega)$, based on a real-time

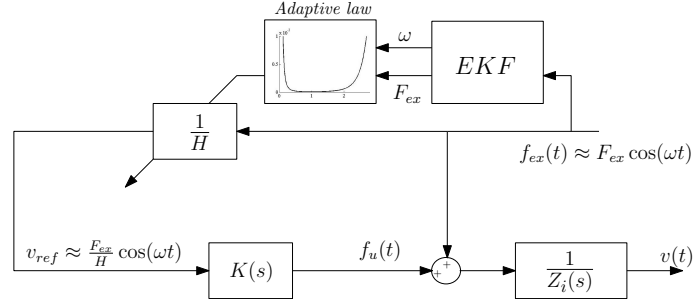


Figure 7.7: Causal approximation of complex-conjugate control.

estimate of the peak frequency of the wave excitation force.

An on-line estimate of the frequency, ω , can be obtained with the EKF [175], following the same approach proposed in Section 6.4.3 for modelling the wave elevation. More details about the estimation of the frequency, as well as about the estimation of the amplitude and phase of the excitation force, will be given in Section 7.5.

Figure 7.7 shows the block scheme of the proposed controller. The reference velocity is calculated as constant of proportionality multiplied by the excitation force, based on (7.15). The constant, $1/H$, is adapted on-line based on a real-time estimate of the frequency of the excitation, calculated with the EKF, and on the optimal amplitude relationship between velocity and excitation force given in (7.6). A feedforward controller, $K(s)$, imposes the desired velocity on the WEC by acting on the PTO force, as will be described in Section 7.6.

In Section 7.7.1, the proposed causal control is compared with the non-causal approximation of complex-conjugate control, and also with the theoretical maximum energy capture, given by the ideal complex-conjugate control. It is expected that the effectiveness of the controller is subjected to the nature of the excitation and its closeness to the narrow-banded process assumption. Mixed seas, characterised by multiple-peaked spectra, would also be expected to degrade the causal approximation of complex-conjugate control.

7.4 Handling constraints

In Section 7.3.2, a causal approximation of complex-conjugate control was proposed, based on a narrow-banded assumption about the wave excitation force. As highlighted in the review of Section 4.1.1, however, complex-conjugate control does not take into account physical constraints about the achievable motion/forces from the device.

In this Section it is shown how the narrow-banded assumption allows the treatment of the motion constraint in quite a straightforward way, that, although not optimal, is quite effective, as it will be demonstrated in the results of Section 7.7.2. In particular, Section 7.4.1 shows how the amplitude of the velocity can be modulated in order to keep the motion (position and velocity) and/or force within given constraints. A typical optimisation-based controller, MPC, is also proposed as a comparison, and is described in Section 7.4.2.

7.4.1 Handling motion constraints with the proposed controller

The control solution proposed in Section 7.3.2, where the velocity is simply calculated from the excitation force through a variable gain, allows the handling of physical constraints in a quite intuitive and effective way. Based on the narrow-band assumption in (7.14), the excitation force can be expressed, in complex notation, as:

$$\hat{f}_{ex} = F_{ex} \iff f_{ex}(t) = \Re \left\{ \hat{f}_{ex} e^{j\omega t} \right\} = F_{ex} \cos(\omega t), \quad (7.16)$$

where \hat{f}_{ex} is termed the complex amplitude of $f_{ex}(t)$, as already defined in (4.3). In (7.16), the phase at time $t = 0$ is assumed to be zero, without a loss of generality.

As a consequence of the proportional reference-generation law, in (7.15), the complex amplitude of the velocity, \hat{v} , and excursion, \hat{x} , can be expressed as:

$$\hat{v} = \frac{F_{ex}}{H} \quad (7.17)$$

$$\hat{x} = \frac{\hat{v}}{j\omega} = \frac{F_{ex}}{j\omega H}. \quad (7.18)$$

Suppose that the vertical excursion of the WEC is limited to $-X_{lim} < x < +X_{lim}$ metres. Based on (7.18), the position constraint can be written as an equivalent velocity constraint:

$$|\hat{x}| = \left| \frac{\hat{v}}{j\omega} \right| \leq X_{lim} \iff |\hat{v}| \leq \omega X_{lim}. \quad (7.19)$$

Therefore, from (7.17) and (7.19), it is possible to derive the following upper bound for the variable gain, $1/H$, such that the WEC does not exceed the maximum excursion, X_{lim} :

$$\frac{1}{H} \leq \frac{\omega X_{lim}}{F_{ex}}. \quad (7.20)$$

Based on (7.15) and (7.20), a reference-generation strategy can be implemented, as a compromise between performance maximisation and compliance with the motion constraint:

$$\frac{1}{H(t)} = \begin{cases} \frac{1}{2B(\omega)}, & \text{if } \frac{\omega X_{lim}}{F_{ex}} > \frac{1}{2B(\omega)} \\ \frac{\omega X_{lim}}{F_{ex}}, & \text{otherwise} \end{cases} \quad (7.21)$$

According to (7.21), when in the unconstrained region, the velocity is tuned to the optimal amplitude given by the ideal complex-conjugate control, as in (7.6). Otherwise, the maximum allowed velocity (lower than the optimal) is imposed, while keeping the velocity in phase with the excitation force. Note that a velocity calculated from (7.21) is optimal within the proposed parametrisation, which means that it gives the maximum energy extraction among all the velocities proportional to the excitation force and smaller than the constraint. The analytical study about the optimal wave-energy absorption under motion constraints was proposed in Section 4.1.2.

The control strategy in (7.21), utilised for the calculation of a reference velocity to be imposed on a WEC for maximum energy absorption, is represented in the block scheme of Fig. 7.8. A

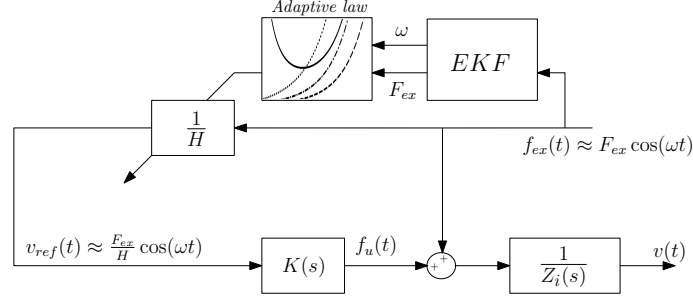


Figure 7.8: Causal controller with adaptive tuning of velocity amplitude for motion-constraints handling.

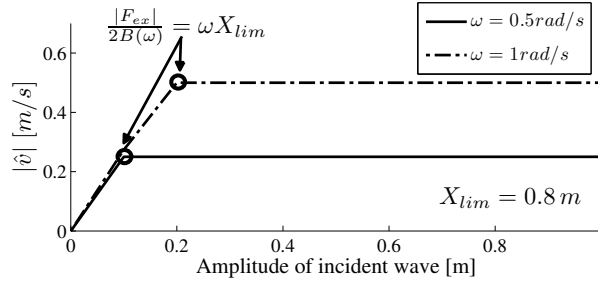


Figure 7.9: Magnitude of velocity reference, with respect to amplitude of incident wave elevation, based on (7.21). The magnitude of the excitation force, F_{ex} , is translated in amplitude of the incident wave elevation, $|\hat{\eta}| = |H_{ex}(\omega)F_{ex}|$, as from (7.3).

reference velocity for the WEC is generated as a scaled version of the wave excitation force acting on the device. A low-level controller imposes such a velocity on the system, by acting on the PTO force (refer to Section 7.6). Note that implementation of (7.21), does not require prediction of the wave force. The amplitude and frequency of the excitation force, required for tuning the controller, are estimated in real-time, as proposed in Section 7.5.

Given the geometry specified in Section 7.2, and a constraint $X_{lim} = 0.8 \text{ m}$, Fig. 7.9 shows the profile of the reference velocity, for two frequencies, as a function of the amplitude of the incident wave elevation, which is related to the amplitude of the excitation force, $|\hat{\xi}| = |H_{ex}(\omega)F_{ex}|$, as from (7.3). For small waves, the velocity is modulated based on the optimal condition in (7.6), given by the ideal complex-conjugate control. Above waves of a certain size, the amplitude of the velocity is kept at a constant maximum amplitude (smaller than optimal), given in (7.21), so that the constraints are satisfied. Note that the limit of the constrained region depends on the constraint, X_{lim} , on the frequency of the excitation, ω , and on the radiation resistance of the system, $B(\omega)$. Fig. 7.10 shows the frequency dependence of the constraint. In the case of 0.2 m waves, the controller would work at maximum allowed speed for $\omega < 1 \text{ rad/s}$, where $1/2B(\omega) = \omega X_{lim}/F_{ex}$, while, at higher frequencies, the system would be tuned at the optimal speed. When the WEC is excited by 0.5 m waves, the velocity is always tuned at the maximum allowed by the constraint (lower than the optimum), for the particular geometry considered here.

As mentioned in Section 7.1, and reviewed in Chapter 4, alternative control solutions, that were proposed in the literature, are based on the solution, at each time step, of a constrained optimisation problem. While such solutions can be considered optimal, they are obviously quite computationally

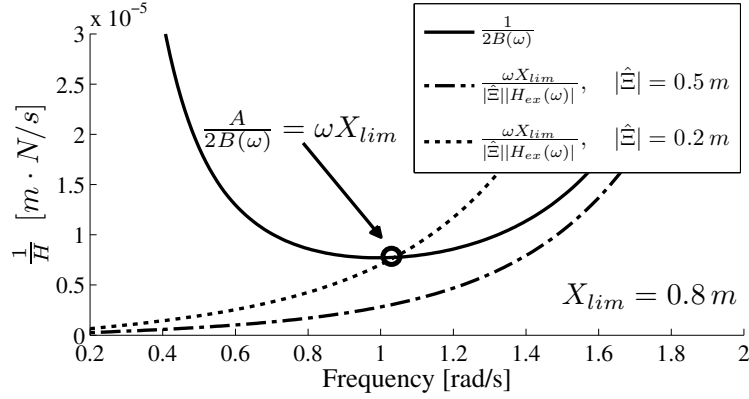


Figure 7.10: Ideal optimal value and upper limit, for a constraint $X_{lim} = 0.8$ m, of the adaptive constant $1/H$, as from (7.21). The magnitude of the excitation force, F_{ex} , is translated in amplitude of the incident wave elevation, $|\hat{\eta}| = |H_{ex}(\omega)F_{ex}|$, as from (7.3).

intensive and their optimality strictly depends on the accuracy of the model of the system, assuming that the optimisation reaches a global maximum/minimum. In addition, the performance of optimisation-based controllers depends on several parameters (e.g. time-horizon, optimisation algorithm, excitation force prediction, optimisation functional specification...) that most of the time can only be set from numerical simulation, rather than intuitive practical considerations.

In the case of the proposed controller, consider that:

- Ultimately, the controller is specified only through a single parameter, $1/H$, that is the constant of proportionality between excitation force and velocity. Such a parameter can be tuned for best performance, within given motion constraints, as in (7.21), but also based on other requirements. It could, for example, be tuned for the regulation of the power at a desired level (absorbed power is proportional to the velocity squared). Such a flexibility could be an important feature in the context of control of an array of WECs. A supervisory controller, in this case, could possibly adapt the behavior of the wave farm as a whole, by tuning the parameter $1/H$ of each individual device, which directly affects their power absorption and wave radiation.
- Unlikely optimisation-based solutions, the proposed controller relies on the model of the system only in the unconstrained region. In the constrained region, the low-level control loop depends on the model, while the reference-generation does not and performance robustness would inevitably benefit from this separation. Further discussion on improving the robustness will be mentioned when discussing the low-level controller, in outline in Section 7.6 and in more detail in Chapter 8.
- Predictions of the wave excitation force are not necessary. It is implicitly assumed that the future excitation force is sinusoidal.

In Section 7.7.2, the proposed controller is tested, in different sea conditions (narrow- and wide-banded waves, double peaked waves), against a popular constrained-optimisation-based controller, that is MPC, that was reviewed in Section 4.2.3.

7.4.2 Handling motion constraints with model predictive control

As outlined in Section 4.2.3, Model predictive control (MPC) optimises the operation of the WEC (velocity and/or force) such that the average power, or the energy, over a finite future horizon, is maximum. In particular, at each time step k , the following functional is maximised, over a given time horizon L :

$$J[k] = - \sum_{j=1}^L f_u[k+j]v[k+j], \quad (7.22)$$

possibly subject to constraints on the system's variables. In (7.22), $f_u[k]$ represents the PTO force and $v[k]$ the oscillation velocity of the device, so that the functional is proportional to the average energy over the time span L . Note that, given the convention adopted with the model definition in Section 7.2, the converted useful energy is negative, so that a minus sign is introduced in (7.22). Also note that the length of the receding horizon, L , has a different meaning than the quantity L used in (7.13), for the approximation of the reference velocity with non-causal complex-conjugate control. In both cases, however, L indicates the prediction horizon required in a practical implementation, and that's why the same symbol has been adopted.

The implementation of MPC, adopted in this Chapter, is based on the structure proposed in [13], and it is outlined here in detail, in order to clarify the comparison with the proposed controller. In particular, the absorbed power, in the objective function (7.22), is expressed as difference between excitation power, $f_{ex}[k]v[k]$ and power lost in radiation, $f_r[k]v[k]$:

$$J[k] = \sum_{j=1}^L f_{ex}[k+j]v[k+j] - f_r[k+j]v[k+j], \quad (7.23)$$

where $f_r[k]$ is the radiation force. Refer to Section 3.4.2 for the details about the energy balance equations in the case of a WEC equipped with a PTO system.

Suppose that the following discrete-time model of the radiation force has been obtained from the finite-order approximation, $\tilde{H}_r(s)$, obtained in Section 7.2:

$$\begin{cases} z_r[k+1] = A_r z_r[k] + B_r v[k] \\ f_r[k] = C_r z_r[k] \end{cases}, \quad (7.24)$$

where $z_r[k] \in \mathbb{R}^{n \times 1}$ is a state variable whose dimension, n , represents the order of the approximation. Note that the system in (7.24) does not exactly represent the radiation force but only its component after the singularity of the added mass at infinite frequency is removed, as highlighted in [13] and clarified in (3.119).

Based on (7.24), the objective function in (7.23) can be written in vectorial form [13]:

$$J[k] = \tilde{v}^T[k] \tilde{f}_{ex}[k] - \tilde{v}^T[k] \tilde{F}_r z_r[k] - \tilde{v}^T[k] \Upsilon \tilde{v}[k], \quad (7.25)$$

where all the signals have expressed as extended vectors over the future horizon L , with:

$$\begin{aligned}\tilde{v}[k] &= \left(v[k+1] \quad \dots \quad v[k+L] \right)^T \in \mathbb{R}^{L \times 1} \\ \tilde{z}_r[k] &= \left(z_r[k+1]^T \quad \dots \quad z_r[k+L]^T \right)^T \in \mathbb{R}^{L \times n} \\ \tilde{f}_{ex}[k] &= \left(f_{ex}[k+1] \quad \dots \quad f_{ex}[k+L] \right)^T \in \mathbb{R}^{L \times 1},\end{aligned}\tag{7.26}$$

and the matrices $\Upsilon \in \mathbb{R}^{n \times n}$ and $\tilde{F}_r \in \mathbb{R}^{L \times n}$ depends on the radiation properties:

$$\tilde{F}_r = \begin{pmatrix} C_r A_r \\ C_r A_r^2 \\ \dots \\ C_r A_r^L \end{pmatrix} \quad \Upsilon = \frac{1}{2} \left(\tilde{G}_r + \tilde{G}_r^T \right),\tag{7.27}$$

with

$$\tilde{G}_r = \begin{pmatrix} C_r B_r & 0 & \dots & 0 \\ C_r A_r B_r & C_r B_r & \dots & 0 \\ \vdots & & \ddots & \vdots \\ C_r A_r^{L-1} B_r & C_r A_r^{L-2} B_r & \dots & C_r B_r \end{pmatrix} \in \mathbb{R}^{n \times n}.\tag{7.28}$$

Without going too much into formal details (the interested reader can refer to [13]), the motion and forces constraints can be expressed linearly in the velocity:

$$\begin{aligned}R_x \tilde{v} &\leq b_x \\ R_v \tilde{v} &\leq b_v \quad , \\ R_f \tilde{v} &\leq b_f\end{aligned}\tag{7.29}$$

where the matrices $R_x, R_v, R_f \in \mathbb{R}^{2L \times 2L}$ are related to the WEC model and the matrices $b_x, b_v, b_f \in \mathbb{R}^{2L \times 1}$ are related to the constraints and the model. In the case of the proposed controller, discussed in Section 7.4.1, a constraint in the heaving excursion also causes a constraint on the velocity and on the PTO force, due to the nature of the controller. In the case of MPC, it is advised [13] to explicitly set all the constraints, in order to avoid peaks in some of the variables. For a fair comparison, the constraints in (7.29) are set such that, given the position constraint $\pm X_{lim} = 0.8$ m, the two controllers employ similar velocities and forces.

The function (7.25) is quadratic in the velocity, with the Hessian matrix, Υ , being positive semidefinite due to the properties of the radiation, as demonstrated in [13]. The maximisation (or minimisation of its opposition) of (7.25), subject to the constraints in (7.29), does not pose particular issues. It is solved through an active-set strategy, that first involves the calculation of a feasible point, based on the linearisation of the quadratic function, and then the generation of an iterative sequence of feasible points that converge to the solution [189]. The optimal force is then calculated directly using the model in (7.1). As discussed in [13], such an approach seems to be superior to a direct optimisation of the PTO force. While such an approach is followed for the determination of the PTO force, a solution based on a low-level velocity-tracking controller could

also be implemented, like the one discussed in Section 7.6 for the proposed controller.

7.5 Real-time estimate of amplitude, frequency and phase of the excitation force

The assumption, on which the proposed controller is based, is that the excitation force is approximately a narrow-banded process, as expressed in (7.14). As a consequence, complex-conjugate control can be approximated with a simple proportional condition between excitation force and reference velocity (no need of predictions), as discussed in Section 7.3.2, and motion constraints can be handled in quite a straightforward way, as proposed in Section 7.4.1.

The high-level controller, however, in order to properly tune the reference velocity, needs to avail of a real-time estimate of the frequency and amplitude of the wave excitation force, which can change with time. The problem is equivalent to the sinusoidal extrapolation method, outlined in Section 6.4.3, proposed for the prediction of the wave elevation, that is modelled as a harmonic process with varying amplitude, phase and frequency. In particular, the harmonic model of the wave excitation force:

$$f_{ex}[k] = F_{ex}[k] \cos(\omega[k]T_s k + \varphi[k]) + \zeta[k], \quad (7.30)$$

with a non-stationary amplitude, $F_{ex}[k]$, frequency, $\omega[k]$ and phase, $\varphi[k]$, can be alternatively written in a recursive form, as derived in Section 6.4.1,:

$$\begin{cases} \begin{bmatrix} \psi[k+1] \\ \psi^*[k+1] \end{bmatrix} = \begin{bmatrix} \cos(\omega[k]T_s) & \sin(\omega[k]T_s) \\ -\sin(\omega[k]T_s) & \cos(\omega[k]T_s) \end{bmatrix} \begin{bmatrix} \psi[k] \\ \psi^*[k] \end{bmatrix} + \begin{bmatrix} \varepsilon[k] \\ \varepsilon^*[k] \end{bmatrix}, \\ f_{ex}[k] = \psi[k] + \zeta[k] \end{cases}, \quad (7.31)$$

where $\varepsilon[k]$, $\varepsilon^*[k]$ and $\zeta[k]$ are random disturbances and $\psi[k]$, $\psi^*[k]$ are state components related to the amplitude and phase.

By defining a state vector, $x[k]$, composed of the three quantities to be estimated, i.e. components $\psi[k]$, $\psi^*[k]$ and the frequency, $\omega[k]$:

$$x[k] \triangleq [\psi(k) \quad \psi^*(k) \quad \omega(k)]^T \in \mathbb{R}^{3 \times 1}, \quad (7.32)$$

the model in (7.31) can be expressed in a non-linear state space form:

$$\begin{cases} \begin{bmatrix} \psi[k+1] \\ \psi^*[k+1] \\ \omega[k+1] \end{bmatrix} = \begin{bmatrix} \cos(\omega[k]T_s) & \sin(\omega[k]T_s) & 0 \\ -\sin(\omega[k]T_s) & \cos(\omega[k]T_s) & 0 \\ 0 & 0 & 1 \end{bmatrix} \begin{bmatrix} \psi[k] \\ \psi^*[k] \\ \omega[k] \end{bmatrix} + \begin{bmatrix} \varepsilon[k] \\ \varepsilon^*[k] \\ \kappa[k] \end{bmatrix}, \\ f_{ex}[k] = \psi[k] + \zeta[k] \end{cases}. \quad (7.33)$$

In (6.69), a model for the variability of the frequency, $\omega[k]$, has been introduced, where a RW is proposed, driven by the additional white noise, $\kappa[k]$.

The Extended Kalman filter (EKF) [175] can be applied to the non-linear model in (7.33) in order to calculate an on-line estimate of the state vector, $\hat{x}[k|k]$. The details of the algorithm were given in Section 6.4.3. In particular, the estimate, at instant k , is recursively calculated as a prediction term based on the estimate at instant $(k-1)$ and on the non-linear model (prediction), plus a correction based on the difference between the prediction and the new measurement, available at instant k , weighted through the Kalman gain, as given in (6.77). The Kalman gain is calculated with the usual Kalman filter algorithm (refer to appendix B.1 for the details), from a linearised version of the model in (7.33), where the frequency is assumed to be constant over a time step, T_s , and the operating point is the state estimate at the previous instant, $\hat{x}[k-1|k-1]$.

Once an estimate, $\hat{x}[k|k]$, is available, the amplitude and frequency of the wave excitation force are easily calculated as:

$$\begin{aligned}\hat{F}_{ex}[k|k] &= \sqrt{\hat{x}_1[k|k]^2 + \hat{x}_2[k|k]^2} \\ \hat{\omega}[k|k] &= \hat{x}_3[k|k],\end{aligned}\tag{7.34}$$

where, based on (7.32), $\hat{x}_1[k|k] = \hat{\psi}[k|k]$, $\hat{x}_2[k|k] = \hat{\psi}^*[k|k]$ and $\hat{x}_3[k|k] = \hat{\omega}[k|k]$.

Figure 7.11 shows an example of on-line estimation of the frequency and amplitude of the wave excitation force produced by irregular waves on the heaving cylinder, the geometry of which was given in Section 7.2. The irregular waves are simulated, with sampling frequency $1/T_s = 2.56$ Hz, from a one-peak Ochi spectral distribution, defined in (3.54), with significant wave height $H_s = 2$ m, peak frequency $\omega_p = 0.5$ rad/s and bandwidth defined by $\lambda = 3$. The power spectral distribution of the resulting wave excitation force is shown in Fig. 7.11(c) and it has a peak at approximately $\omega \approx 0.53$ rad/s. The frequency is slightly under-estimated, with $\hat{\omega}[k|k]$ oscillating around 5.295 rad/s, as from Fig. 7.11(b). The estimate of the amplitude, $\hat{F}_{ex}[k|k]$, accurately follows the dynamics of the real signal, as is shown in Fig. 7.11(a).

Note that a range of algorithms have been proposed for the estimation of the instantaneous frequency of a narrow-banded process, the EKF having been shown to suit the real-time estimation of a non-stationary process like the excitation force [190, 191].

7.6 Low-level controller: a basic approach

As described in Section 7.1, the control architecture proposed in this Chapter, shown in Fig. 7.8, is composed of a high-level controller, that produces a reference velocity, and a low-level controller that imposes the desired velocity on the system by acting on the PTO force, $f_u(t)$. The reference velocity can be generated by the unconstrained controller (causal or non-causal), discussed in Section 7.3, or by taking into account motion constraints, as proposed in Section 7.4. The velocity-tracking controller discussed in this Section applies in either case.

As in the block scheme of Fig. 7.12, the controller is composed of a feedforward part, $K(s)$, plus a direct compensation of the disturbance (the excitation force). The latter is not directly measurable in practice, but an observer can be designed for its estimation [119], as already discussed in Section 6.6.1.

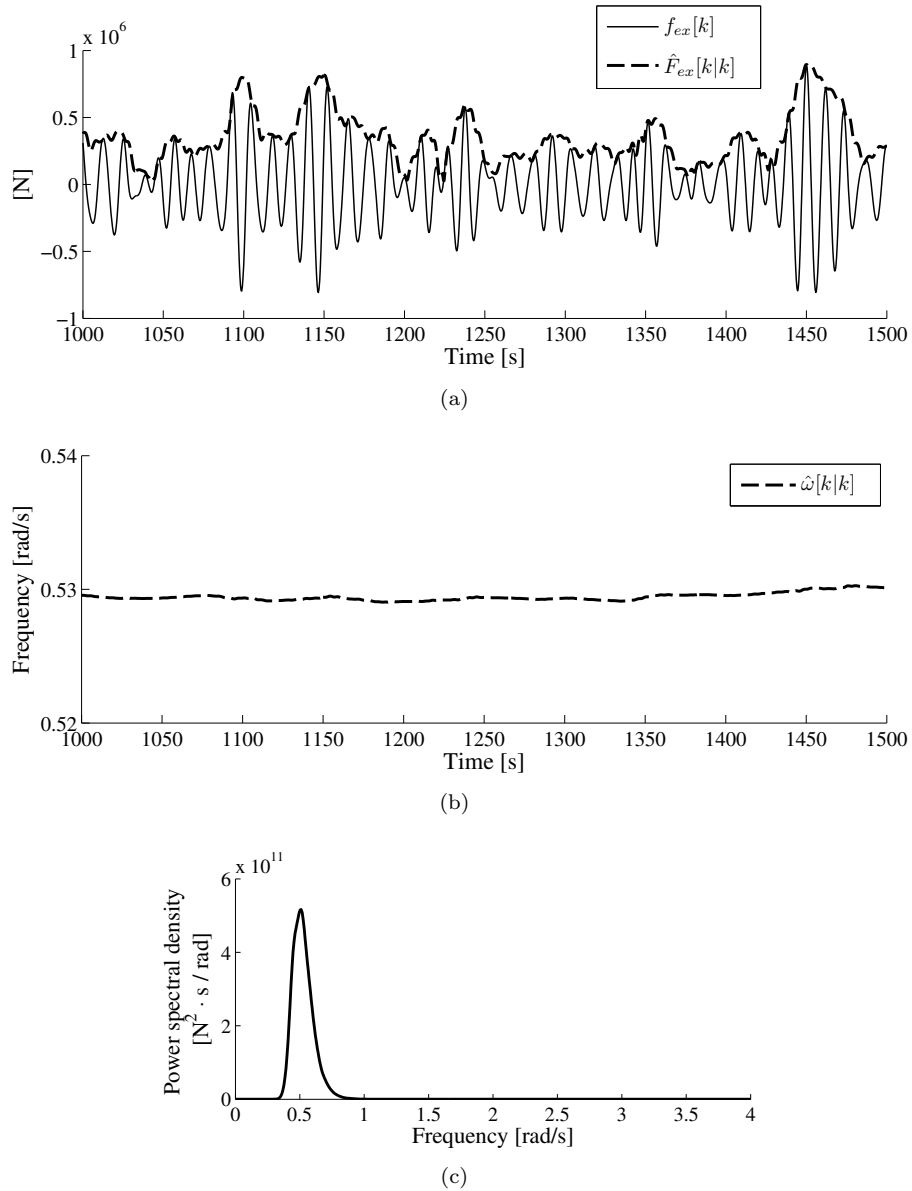


Figure 7.11: Real-time estimate of the amplitude and frequency of the wave excitation force with the EKF: (a) amplitude estimate; (b) frequency estimate; (c) Power spectral distribution of the wave excitation force utilised for the simulation (peak frequency is $\omega \approx 5.15$ rad/s).

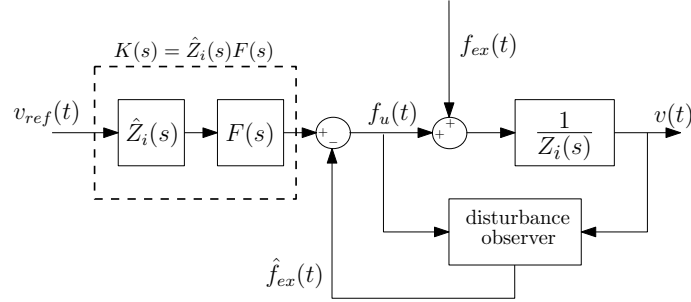


Figure 7.12: Low-level controller as a feed-forward with direct disturbance rejection.

The transfer function, $K(s)$, consists of an approximation of the system inverse, $\tilde{Z}_i(s)$, cascaded with a filter, $F(s)$, that ensures physical realisability and rejection of unwanted signals at certain frequencies. For perfect tracking, it would be desirable that $K(s)$ is such that:

$$K(s) \cdot \frac{1}{Z_i(s)} = \tilde{Z}_i(s)F(s) \cdot \frac{1}{Z_i(s)} \approx 1, \quad (7.35)$$

at least within a certain frequency-band of interest.

The inverse of the model is calculated from a fourth-order approximation of $1/\tilde{Z}_i(s)$, given in (7.5). The model-order reduction is based on a balanced state-space representation and rejection of the state modes with small singular values, as proposed in Section 5.3.2 and outlined in appendix A. Note that floating systems of the type being considered here are not minimum-phase systems, due to the present of a zero at $s = 0$. It is important that the filter $F(s)$ is designed such to have a zero at $s = 0$ in order to cancel the unstable pole arising from the model inversion. Note that cancellation of unstable dynamics is not an issue, here, because $F(s)$ and the model inverse, $1/\tilde{Z}_i(s)$, are not going to be implemented separately, while their product, $K(s)$, is.

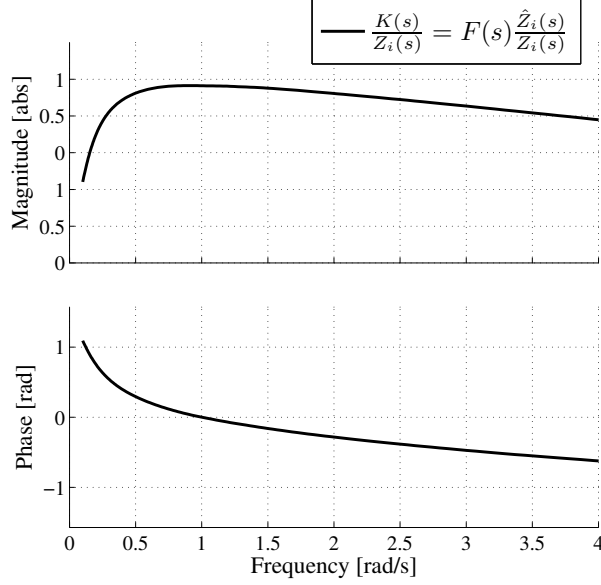
The filter $F(s)$ is tuned so that perfect-tracking (maximum sensitivity) is obtained in the desired range of frequencies, while robustness and low-sensitivity is realised outside this range. In our specific case, the filter $F(s)$ is shaped as a band-pass filter:

$$F(s) = \frac{s}{(s + 0.2)} \cdot \frac{5}{s + 5}, \quad (7.36)$$

where 0.2 and 5 rad/s are the cut-off frequencies of the high- and low-pass Sections, respectively. The zero at $s = 0$ ensures the stability of the controller, by cancelling the pole at $s = 0$ due to the model inversion.

The resulting open loop transfer function $K(s)/Z_i(s)$, shown in Fig. 7.13, approaches condition (7.35) in the region $[0.3, 2]$ rad/s, which corresponds to the active band of frequencies in the excitation force. Also based on the discussion carried out in Section 6.6.1, note that the excitation force resulting from any possible sea state is always contained in such a region for the given system, so that the controller $K(s)$ does not need to be adaptively tuned to the sea state, but its structure can be fixed at the design stage.

In the presence of model uncertainties (e.g. due to non-linearities) within the region of the frequencies of interest, feedback can be added to the controller for improved robustness, based

Figure 7.13: Open-loop transfer function $K(s)/Z_i(s)$.

on an IMC philosophy [192], and also proposed in [98] for the control of the Archimedes Wave Swing WEC. In order to maintain the focus on the performance of the high-level control strategy, the robustness design is not dealt with at this stage. However, a more advanced design will be discussed in Chapter 8, which focuses more specifically on the low-level controller.

7.7 Results

The proposed control method is validated on the heaving cylinder as specified in Section 7.2 under several wave conditions. Random waves are generated from single- and double-peaked standard wave spectral distributions. The 3- and 6-parameters Ochi spectral distributions [44] are utilised, which give the possibility of independently specifying the modal frequency, ω_p , the significant wave height, H_s , and the sharpness, λ :

$$S_{\eta\eta}(\omega) = \sum_{j=1,2} \frac{\left(\frac{4\lambda_j+1}{4}\omega_{p,j}^4\right)^{\lambda_j}}{\Gamma(\lambda_j)} \cdot \frac{H_{s,j}^2}{\omega^{4\lambda_j+1}} e^{-\left(\frac{4\lambda_j+1}{4}\right)\left(\frac{\omega_{p,j}}{\omega}\right)^4}, \quad (7.37)$$

where $j = 1, 2$ are the components of the spectrum (only one is included for the single-peak case) and $\Gamma(\cdot)$ is a Gamma function. More details about the Ochi spectral distribution were given when discussing the typical standard spectra, in Section 3.1.2.

Fig. 7.14 shows some examples of the spectral distributions. The double-peak spectra are parameterised with the ratio $H_{s,1}/H_{s,2}$, which is the relative energy of the two peaks, and with the spacing between the peaks, $\Delta\omega = \omega_{p,2} - \omega_{p,1}$. The variety of single-peak spectra has been chosen with ω_p ranging from 0.3 to 1.2 rad/s, λ from 0.5 to 5 (wide- to narrow-banded spectrum)

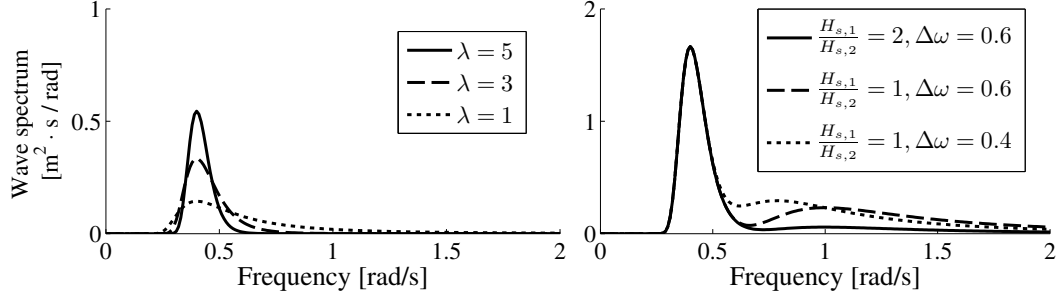


Figure 7.14: Some spectral shapes utilised for the simulation of the waves. Spectra centred around different peak frequencies are also utilised.

and $H_s = 1$ or $H_s = 3$ m. For the double-peaked spectra the low-frequency component has been kept fixed, with $H_{s,1} = 4$ m, $\omega_{p,1} = 0.3$ rad/s and $\lambda_1 = 3$, while the high-frequency sea state has a fixed $\lambda_2 = 0.5$, with varying $H_{s,2}$ and $\omega_{p,2}$, such that: the ratio $H_{s,1}/H_{s,2}$ ranges from 4 to 0.5; the frequency spacing $\Delta\omega = \omega_{p,2} - \omega_{p,1}$ ranges from 0.2 to 0.9 rad/s.

From each spectral distribution, a wave-elevation time series is generated, using (3.55), based on the approach proposed in [54] and described in Section 3.1.2. In particular 1-hour wave records, sampled at 2.56 Hz, are generated for each simulation, for a total of 9216 samples. The wave excitation force experienced by the heaving cylinder is calculated, off-line, using the non-causal law in (7.3). The system is then simulated in the time domain with the controller.

Initially, the unconstrained controllers described in Section 7.3, both non-causal and causal, are compared, in Section 7.7.1. Then the proposed controller is validated against MPC when motion constraints are in place, in Section 7.7.2. The performance of the controller with real wave data is also analysed and compared to the results calculated with simulated waves, in Section 7.7.3. Sensitivity to uncertainties in the model and in the estimation of the excitation force are finally discussed in Section 7.7.4.

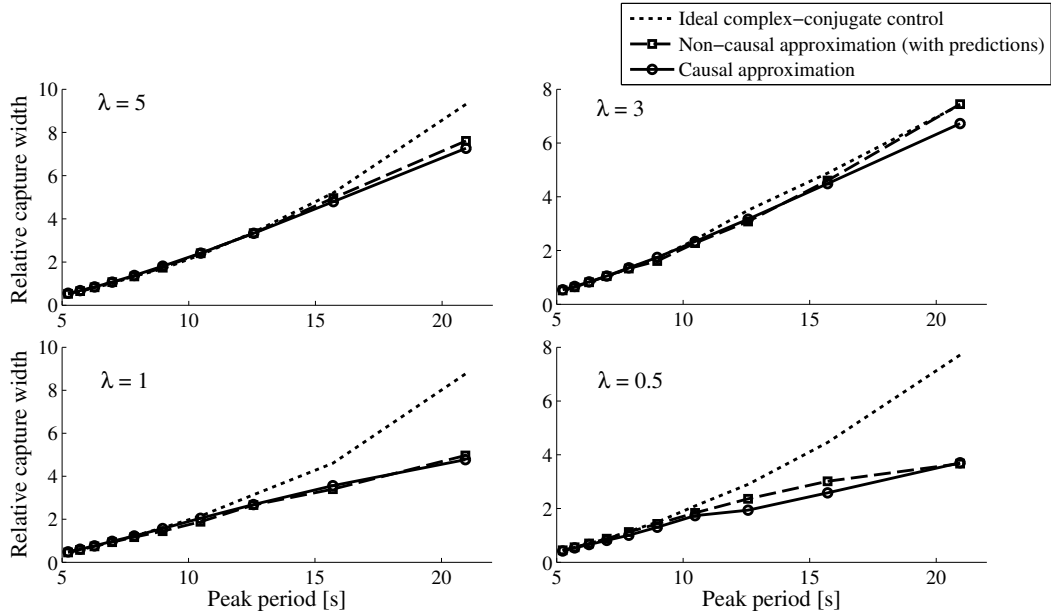
7.7.1 Unconstrained controller

The performance of the proposed controller is initially validated for the unconstrained case, using both the non-causal and the causal implementation, according to the methodology outlined in Section 7.3. The block scheme of the controllers was shown in Fig. 7.4, for the non-causal approach, and in Fig. 7.7, for the causal approximation. The two controllers have a similar structure, with a reference-velocity generator followed by a velocity-tracking loop, as designed in Section 7.6. The non-causal approach is approximated with predictions produced by an AR model, as proposed in Chapter 6. The causal approach is based on the real-time estimate of the instantaneous frequency of the excitation force, given by the EKF, as detailed in Section 7.5.

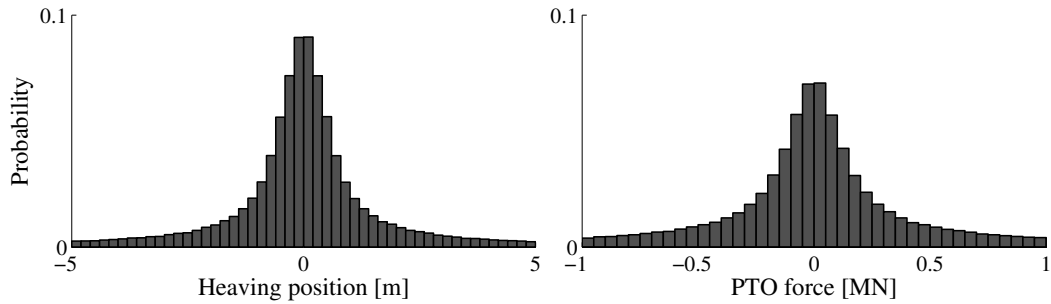
The performance is measured in terms of RCW:

$$RCW = \frac{\overline{P}_u}{2RP_w}, \quad (7.38)$$

which is the ratio between average absorbed power, \overline{P}_u , and average wave power, P_w , over a front



(a) RCW obtained with non-causal and causal controllers, compared with ideal complex-conjugate control.



(b) Distribution of heaving excursion and PTO force required by the causal controller (the distribution for the non-causal controller is similar).

Figure 7.15: Performance of unconstrained controllers.

as wide as the cylinder ($2R$). Note that deep water is assumed, so that the wave power, per metre of wave front, is calculated from the wave spectral distribution, $S_{\eta\eta}(\omega)$, based on the expression given in (3.45).

Figure 7.15(a) shows the RCW obtained with the causal and non-causal controllers, for wide-banded ($\lambda = 0.5$) and narrow-banded ($\lambda = 5$) wave spectra, centred around different periods, $2\pi/\omega_0$. The ideal maximum RCW, given by complex-conjugate control, is also shown as a comparison. The proposed controller performs very close to the optimal, particularly for narrow-banded waves. For wide-banded sea states, the performance is very close to the ideal maximum only for short to medium waves, while it significantly drops for very long waves. Note that only a minor improvement in performance is obtained with the non-causal approximation of complex-conjugate control, using predictions.

Note that RCW is quite large in most situations, and this is due to the fact that physical constraints are not taken into account, which is one of the limitations of ideal complex-conjugate

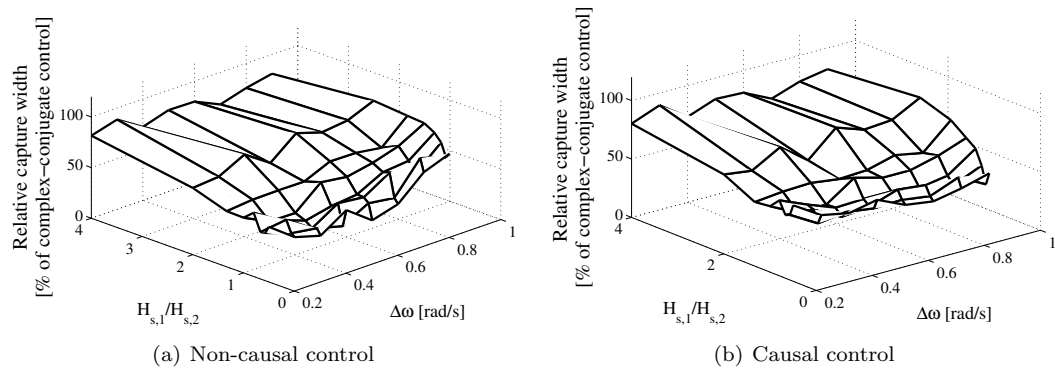


Figure 7.16: Performance of (a) non-causal and (b) causal control, as a percentage of ideal complex-conjugate control, with double-peaked spectra: $H_{s,1}/H_{s,2}$ is the relative energy between the two sea states; $\Delta\omega$ is the frequency spacing.

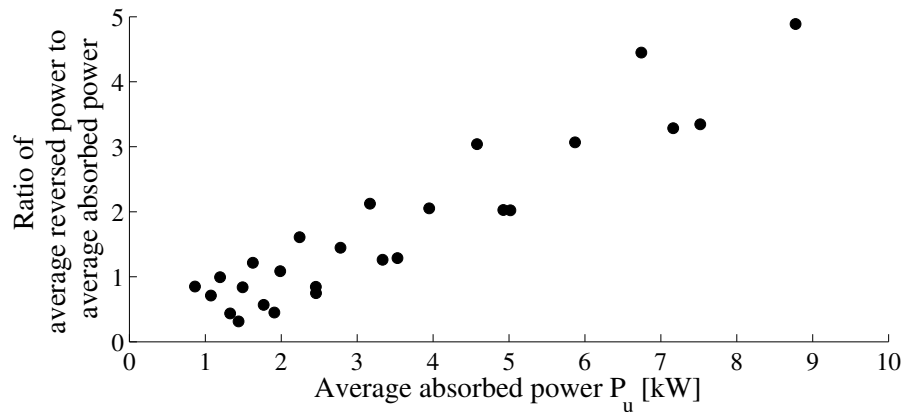


Figure 7.17: Ratio of average negative power to average absorbed power.

control. Fig. 7.15(b) shows the distribution of the heaving position and PTO force required to obtain the results of Fig. 7.15(a). The position typically ranges from -5 to 5 metres (with bigger excursions in some situations!), which is quite impractical for a floating cylinder 5 metres high and with a 4 metre draught. Also, PTO forces of more than 1×10^6 N are experienced in some occasions, which can require large and expensive PTO machinery.

The performance of the proposed controller in double-peaked seas is also assessed. Fig. 7.16 shows the behavior of the *RCW*, relative to ideal optimum from reactive control. Clearly, the performance is negatively affected (below 50% of optimum) when the two sea states have a similar energy content and when they are widely spaced.

A final analysis is carried out in order to determine the amount of energy that needs to be injected from the PTO back into the system, during part of the cycle, known to be an issue with complex-conjugate control [83]. Figure 7.17 shows the ratio of the average reverse power, that is the average absorbed power of negative sign, to the overall average absorbed power (that is always positive if the controller is effective). Most of the times a higher reverse energy flow is required than that absorbed (between 1 and 5 times!). The ratio seems to increase with the average power absorption of the system but, in general, it looks quite unreasonable, since it would require an

excessive over-specification of the PTO.

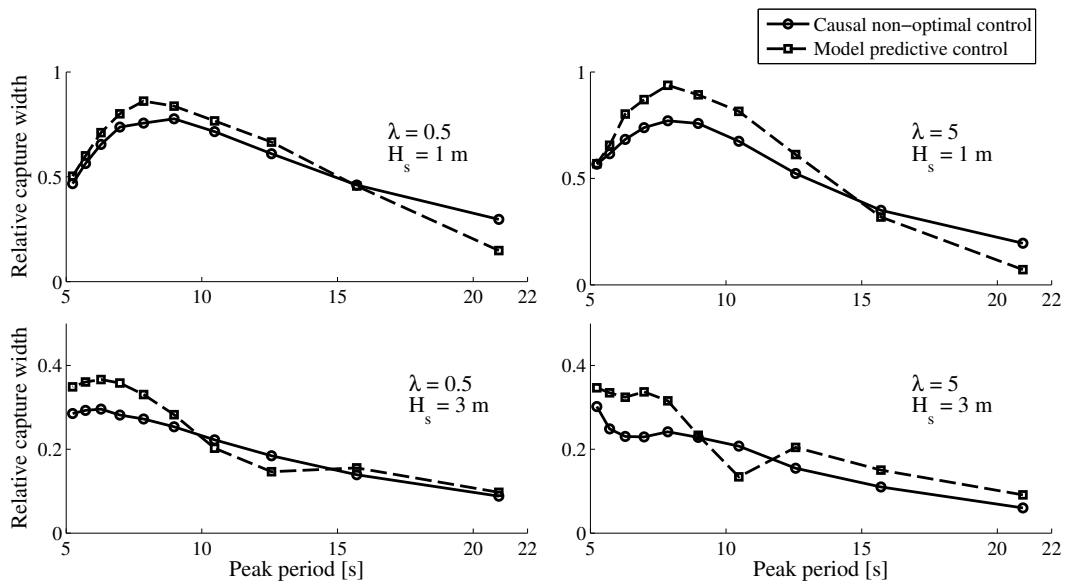
High levels of reverse power, together with the excessive motion required, make unconstrained complex-conjugate control impractical most of the times, apart from the case of very small waves (how small depends on the geometry and rating of the specific WEC).

7.7.2 Constrained controller

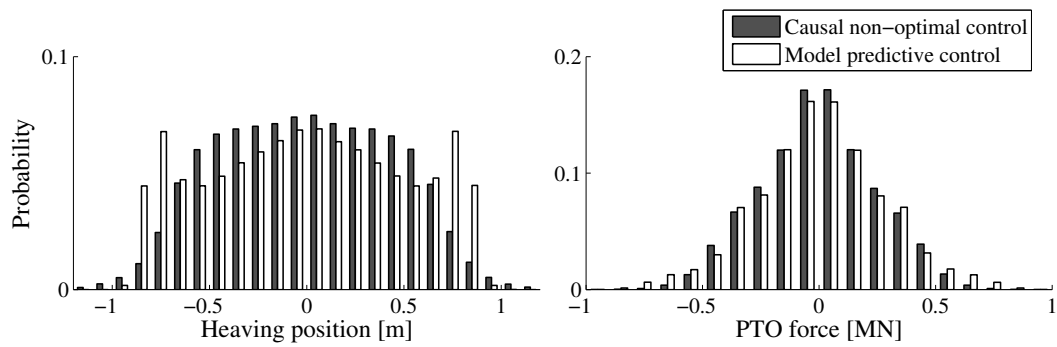
The proposed causal and non-optimal controller is also more appropriate when physical constraints are imposed, as described in Section 7.4. MPC, which solves a constrained optimisation problem at each time-step, is utilised as a comparison, following the approach proposed in [13] and described in Section 7.4.2. In particular, the future horizon for the optimisation is set to 30 steps (≈ 11.77 s), which is about double the resonance period of the floating cylinder (≈ 5.2 s). Predictions for the MPC controller are *not* assumed to be ideal and a forecasting algorithm, based on AR models, is implemented, as proposed in Chapter 6.

Fig. 7.18(a) shows the *RCW* obtained from the two controllers, in wide- ($\lambda = 0.5$) and narrow-banded ($\lambda = 5$) sea states for different peak periods, $2\pi/\omega_0$. Two different significant wave heights, $H_s = 1$ and $H_s = 3$ m, are also utilised. Due to the introduction of the constraints, the performance is similar to the one obtained in the unconstrained case only for short waves (small period), while it shows a peak for medium waves and it decreases again for longer waves, as theorised by Budal [6]. The sub-optimal controller performs quite closely to MPC for short and long waves. It is less efficient, however, around the peak. Note that, unlike the unconstrained case, the bandwidth does not seem to affect the performance for the constrained case, although it affects the relative efficiency compared with MPC, which offers better results for narrow-banded waves, $\lambda = 5$, most likely due to better predictions of the excitation force [17]. Note that for bigger waves, $H_s = 3$ m, the trend of the power capture with wave period is similar, but the peak moves towards the smaller-period waves.

An important point that emerges from Fig. 7.18(a) is that, for very long waves, the sub-optimal controller actually outperforms MPC (and quite significantly in some cases). Two main reasons may explain this unexpected behavior: (a) The sub-optimal nature of the proposed controller may cause a violation of the motion constraints, that is immediately reflected (in simulation) in a higher energy capture, and (b) The MPC controller depends on many parameters (optimisation algorithm, future horizon, specification of functional, ...) the choice of which is not always straightforward, and our choice is probably not *exact* enough for those waves. In particular, Fig. 7.18(b) shows the probability distribution of the vertical excursion of the WEC for the two controllers. The position goes slightly beyond the imposed constraint of 0.8 m in both cases and this unwanted behavior occurs slightly more frequently with the proposed causal controller. The violation of constraints, in the case of MPC, may be due to several reasons, among which the error in the prediction of the wave excitation force, or the inaccuracies in the model, which is based on a finite-order approximation of the radiation. Such behavior highlights one of the main benefits of the proposed controller, that although sub-optimal, requires tuning of a single parameter which has intuitive physical meaning ($1/H$), representing the modulation of the magnitude of the velocity with respect to the excitation force. Therefore, a safety margin can be easily included within the controller, through a more



(a) RCW compared with ideal reactive control.



(b) Distribution of heaving excursion and PTO force.

Figure 7.18: Performance of proposed non-optimal causal control, compared with optimal MPC.

conservative reference-generation strategy than in (7.21), in order to overcome possible constraint violations.

A further advantage of the proposed controller is the linearity achieved between excitation force, velocity, position and PTO force. This means that motion and force have the same harmonic behavior as the incident wave, with no abrupt variations that may adversely affect the longevity or survivability of the system components. The probability distribution of position, Fig. 7.18(b), shows how MPC keeps the system mostly close to the constraints, with higher velocities in moving from one extreme to the other. The proposed controller, on the other hand, imposes a smooth and harmonic oscillation in the system, so that the position is almost normally distributed around the zero. Such a behavior can also be observed, though to a much lesser extent, in the force. A sample time-series simulation, which makes clearer such considerations, is shown in Fig. 7.19, where the evolution of the position and the required control force are plotted for the two controllers.

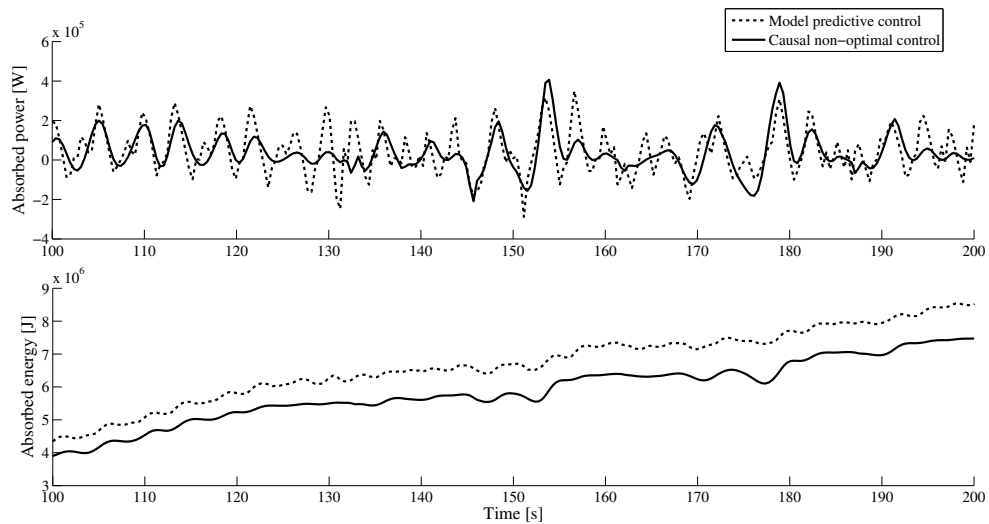
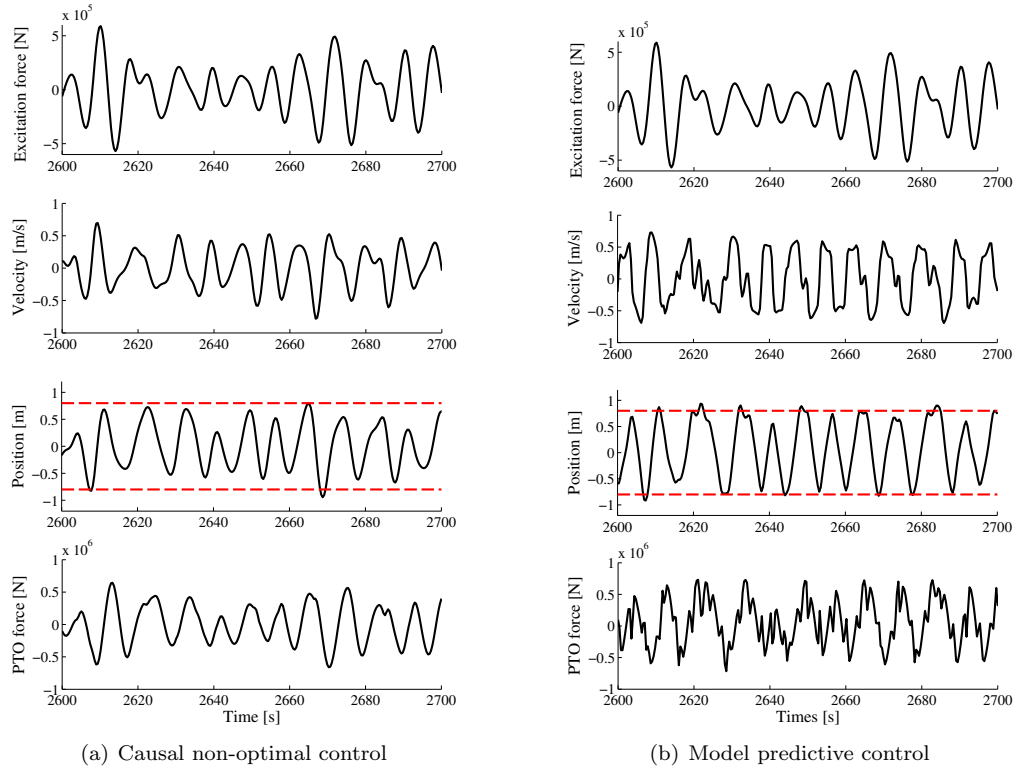
The performance of the sub-optimal controller, relative to MPC, with double-peaked waves, is shown in Fig. 7.20. Quite surprisingly, when the two peaks have a comparable size the sub-optimal controller outperforms MPC, particularly when $\Delta\omega$ is small. It seems, therefore, that MPC has a higher sensitivity to errors in the prediction of the excitation force, which can be quite poor for multi-peaked sea states [17].

The amount of reverse power required, in presence of constraints, is shown in Fig. 7.21, where the ratio of reverse power to absorbed power is compared between the proposed controller and MPC. Much less energy needs to be injected back from the PTO to the WEC, between 10% and 40% of the absorbed energy, than in the unconstrained case (100% to 500%). Hydraulic or electrical generators can be designed to accomplish such levels of reversible energy flow, and the proposed controller can easily be optimised by taking into account inefficiencies in the two modes of operations (by acting on the constant $1/H$). Such a possibility would be of interest for further studies.

7.7.3 Performance with real waves

The proposed controller is also validated with real wave data, provided by the Irish Marine Institute and coming from a data buoy in the Belmullet wave energy test site, off the West coast of Ireland. Three specific wave-elevation records of 30 minutes, sampled at 1.28 Hz, are selected, such that a variety of conditions are covered. Figure 7.22 shows the spectral distribution and the summary statistics, in terms of significant wave height and peak period, of the three data sets.

The performance of the proposed controller and of MPC is evaluated in the constrained case, in the same conditions utilised for the results with simulated waves, in Section 7.7.2. Table 7.2 summarises the results, by showing the average power absorption and the RCW with each of the records selected. The performance are well in line with what expected based on the general results of Fig. 7.18(a), obtained with simulated waves.



(c) Absorbed power and energy

Figure 7.19: Behavior of the proposed causal and non-optimal controller against MPC, for a given excitation force, produced by an irregular wave simulated from a single-peaked Ochi spectrum with $H_s = 2$ m, $\omega_p = 0.7$ rad/s and $\lambda = 1$. Overall performance over the sea state is $RCW \approx 0.37$ for the causal controller and $RCW \approx 0.44$ for the MPC.

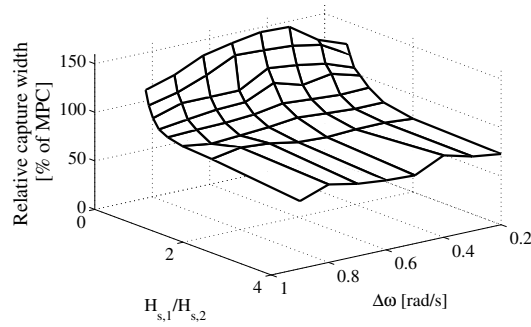


Figure 7.20: Performance of proposed controller, as a percentage of MPC, with double peak spectra: $H_{s,1}/H_{s,2}$ is the relative energy between the two sea states; $\Delta\omega$ is the frequency spacing.

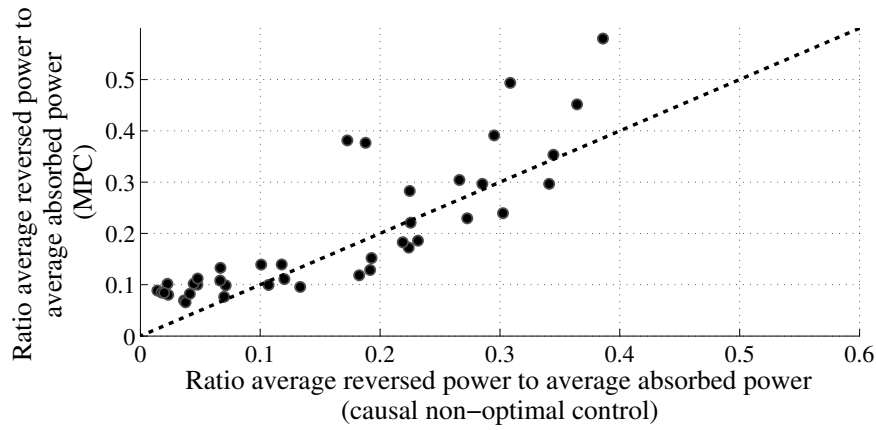


Figure 7.21: Ration of average negative power to average absorbed power.

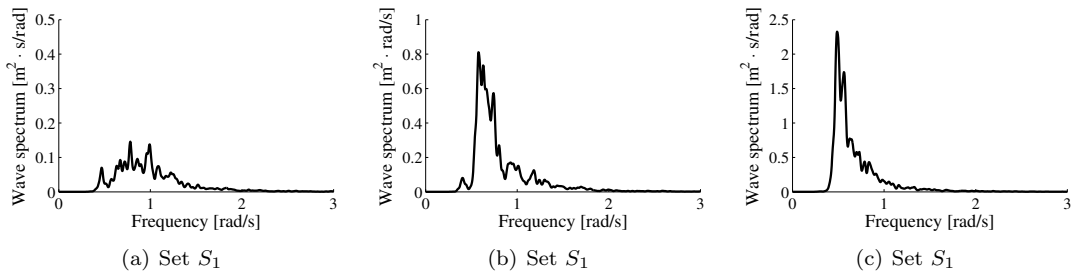


Figure 7.22: Wave spectrum of real wave data used to test the performance of the proposed controller. The data comes from the Belmullet wave energy test site ($54^{\circ} 13' N$, $10^{\circ} 8' W$) and it consists of 30-minutes wave-elevation records sampled at 1.28 Hz.

Set	Recorded	H_s [m]	ω_p [rad/s]	ω_e [rad/s]
S_1	1 st December 2010, 00.00-00.30 am	1.04	0.97	1.06
S_2	6 th December 2010, 00.00-00.30 am	1.80	0.61	1.84
S_1	10 th November 2010, 00.00-00.30 am	2.75	0.52	1.69

Table 7.1: Details of real wave records, whose spectrum is shown in Fig. 7.22, where H_s : significant wave height; ω_p : peak frequency; ω_e : energy frequency.

Set	P_w [kW/m]	Causal non-optimal control		MPC	
		\bar{P}_u [kW]	RCW	\bar{P}_u [kW]	RCW
S_1	3.75	27.2	0.73	31.3	0.81
S_2	15.3	53.6	0.35	63.6	0.41
S_3	38.2	74.8	0.20	40.3	0.11

Table 7.2: Performance of the proposed non-optimal and causal controller against MPC, with real wave data, whose spectrum is shown in Fig. 7.22.

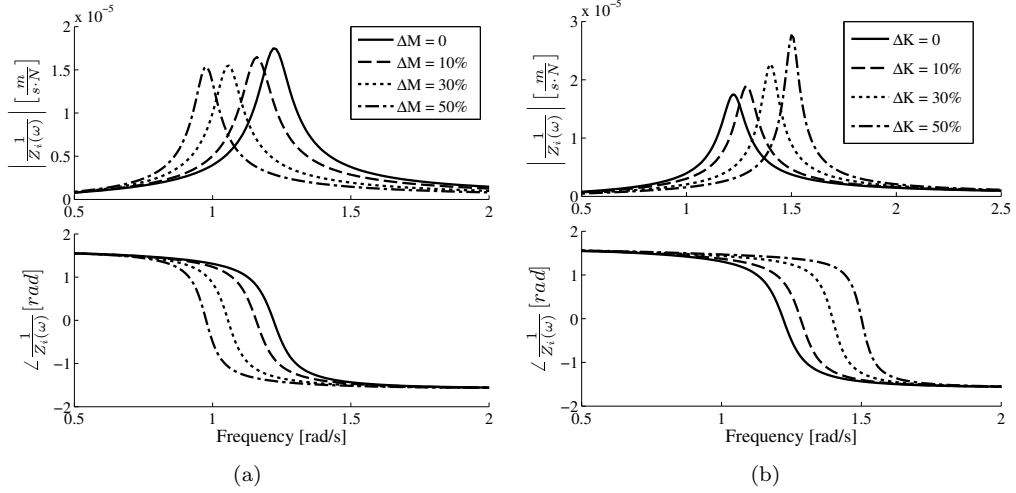


Figure 7.23: Variation of system's frequency response caused by variation in mass, ΔM , and stiffness, ΔK .

7.7.4 Robustness to parameter variations

It is interesting to evaluate the sensitivity of the controller with respect to uncertainties in the model. Particularly in wave energy, the normal operation of a device, involving relatively extreme motions, may be distant from the typical assumptions of linearity (small deviations around an equilibrium point), on which the model of Section 7.2 is based.

Since the model is similar to a damped mechanical oscillator, with relatively small damping, as discussed in Chapter 3 (Sections 3.2 and 3.3 in particular) it makes sense to apply variations to the main terms that define the system: the mass plus added mass, $M + M_a(\omega) + M_\infty$, and the buoyancy coefficient or stiffness, K_b . Such two terms contribute to specify the main parameter of the oscillating system, that is the natural frequency, based on (3.131).

Relative variations ranging from 10% to 50% of the two terms are applied, resulting in:

$$\frac{V(s)}{F_{ex}(s) + F_u(s)} = \frac{s}{s^2 [(m + m_\infty)(1 + \Delta M)] + sH_r(s) + K_b(1 + \Delta K)} \triangleq \frac{1}{\tilde{Z}_i(s)}, \quad (7.39)$$

which impose a change in the dynamics of the model, as shown in Fig. 7.23. For the analysis proposed in this Section, it is assumed that the transfer function $1/\tilde{Z}_i(s)$, defined in (7.5), is the model of the system, while $1/Z_i(s)$, as defined in (7.39), denotes the real plant.

Clearly the model is sensitive to variations in the critical parameters, mass and stiffness. A large variation in magnitude and phase is verified around the resonance frequency of the system,

in particular (in fact, mass and stiffness directly affect the position of the resonance frequency). It would therefore be expected that the performance of the controllers, in the presence of the proposed parameter variations, would depend on the frequency at which the excitation from the waves is concentrated.

The resonance frequency of the model of the system, $1/\tilde{Z}_i(s)$, is around 1.25 rad/s, as it can be seen from Fig. 7.23. An initial robustness analysis is therefore carried out with the WEC being excited by irregular waves centred at a frequency of 1.25 rad/s, assuming an Ochi spectral distribution with significant wave height $H_s = 1$ m and a sharpness factor of $\lambda = 0.5$. Fig. 7.24 shows how the RCW obtained with the proposed controller and with MPC is affected by parametric variations in such a wave condition. Both of the controllers are quite robust up to 10% variation of either mass and stiffness, while the performance drops significantly with larger variations. When $\Delta K = 20\%$ or $\Delta M = 20\%$, in fact, there is already a stark variation in the response of the system at the expected resonance frequency of 1.25 rad/s, since the real resonance frequency has moved to 1.4 and 1.1 rad/s, respectively.

It is important to stress that the way in which the two controllers are sensitive to parameter variations is different. MPC, as discussed in Section 7.4.2, relies on the model of the system in order to optimise its behavior over the receding horizon. The result of the optimisation is the optimal velocity and force that should be imposed such that the system can achieve the predicted and optimal performance. When the model is distant from the real system, the optimisation can return unexpected behavior. In the case of the causal and non-optimal controller, proposed in this Chapter, when operating in the constrained region, the velocity to be imposed on the system does not depend on the model, as from (7.21). The low-level controller, however, designed in order to impose such velocity on the WEC through the PTO force, is a feedforward action based on a model inversion, as detailed in Section 7.6. While the generation of the reference velocity (the high-level control) is not affected by system's variations, the resulting control action, or PTO force, calculated by the low-level controller, can be extremely sensitive to such variations, due to the inversion of the model.

As a consequence, there is scope, in the case of the proposed controller, for adding feedback to the low-level loop that is able to deal with model uncertainties. A compromise can be found between performance and robustness in a relatively straightforward manner, once the magnitude and nature of the uncertainty is quantified. Such a possibility will be investigated in Chapter 8.

Another important point emerges from an assessment of the robustness of the system when subjected to waves centred at a different frequency, further from resonance, where the model variation is not significant. Figure 7.25 shows the performance, in terms of RCW, of the proposed controller and of MPC, when the incident wave is centred around 0.7 rad/s, based on an Ochi spectral distribution, with $H_s = 2$ m and $\lambda = 1$. As expected, both the controllers seem to be quite robust, since only a light variation in performance is observed even in the case of 50% variations. However, while in the case of variation in stiffness there is a reduction in performance, a variation in the mass of the system, with respect to the modelled value, causes an *increase* in performance.

The improved performance should not be a complete surprise, since it is due to a violation of the motion constraints caused by the magnitude response of the system being under-estimated at the frequency of 0.7 rad/s. The violation of the constraints is highlighted in Fig. 7.26, where

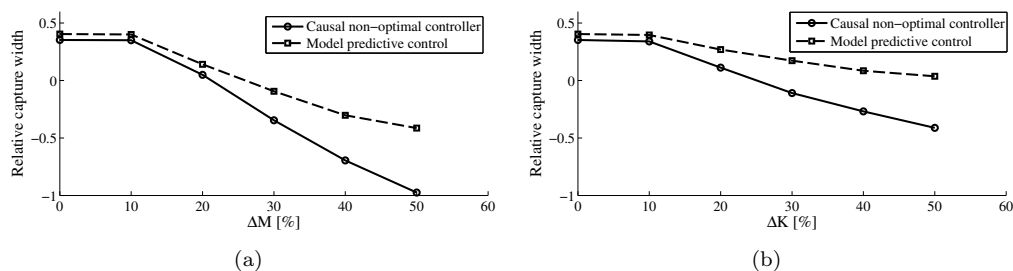


Figure 7.24: Performance of the proposed controller and of MPC with parametric variations in mass, ΔM , and stiffness, ΔK . The incident wave is simulated from an Ochi spectral distribution with significant wave height $H_s = 1$ m, peak frequency $\omega_p = 1.25$ rad/s (around the resonance frequency of the device) and spectral sharpness $\lambda = 0.5$.

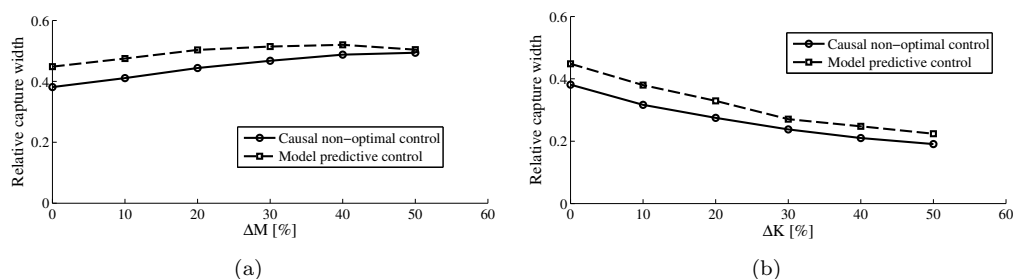


Figure 7.25: Performance of the proposed controller and of MPC with parametric variations in mass, ΔM , and stiffness, ΔK . The incident wave is simulated from an Ochi spectral distribution with significant wave height $H_s = 2$ m, peak frequency $\omega_p = 0.7$ rad/s and spectral sharpness $\lambda = 0.5$.

the probability for the heaving excursion going beyond the constraint of 0.8 m increases while the variation in mass (under-estimation of the magnitude response at 0.7 rad/s) increases.

7.8 Conclusion

A novel strategy for real-time control of bottom-referenced oscillating WECs is proposed. The controller has a hierarchical structure. The high-level controller sets the velocity of the oscillator to be in phase with the excitation force and with an amplitude proportional to the wave force. The ratio between the velocity and excitation force magnitudes can be tuned in real-time for performance and constraint handling. The reference velocity is then imposed on the system by a low-level controller, which applies a feedforward action through the PTO force.

The controller is based on the simplifying assumption of a harmonic sea, which is not always verified, so that the approach is sub-optimal in general. Stationarity of the waves, however, is not assumed and the instantaneous frequency, as well as the amplitude information, is tracked in real-time with the EKF. As a result of the stated assumption, the proposed controller is very simple to implement, once an estimation of the excitation force is available, and it only relies on

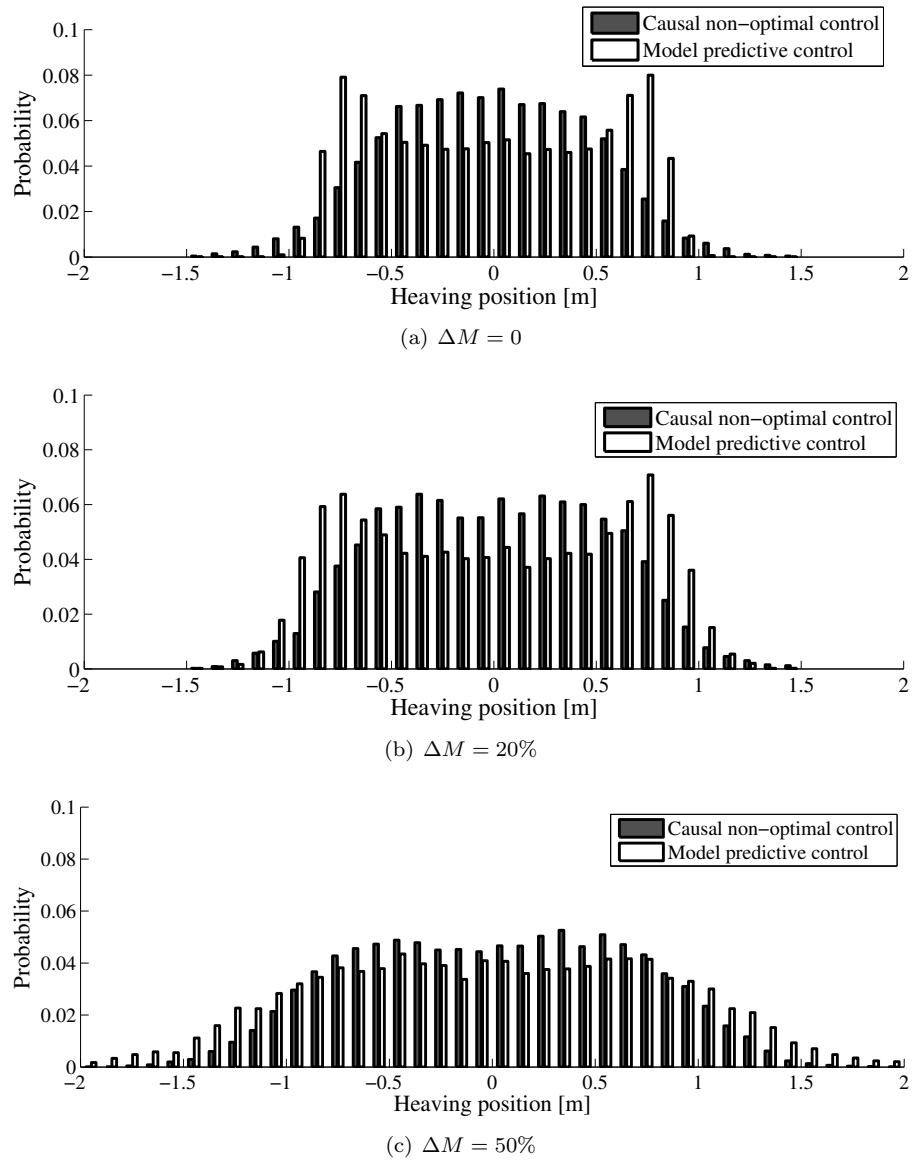


Figure 7.26: Detail of the distribution of the heaving position of some of the points of Fig. 7.25(b). The increase in performance is due to a violation of the constraints.

non-expensive computations (no predictions and no optimisation involved), which make it ideal for real-time applications.

In Section 7.7.1, it was shown, via simulations over different stochastic sea conditions, that, when constraints are not taken into account, the proposed controller achieves energy captures that are very close to the optimum predicted by complex-conjugate control, particularly in narrow-banded and single-peak sea states, that are close to the harmonic assumption. At the same time the controller seems to be relatively robust to wide-banded and double-peaked seas, where the performance is reasonably good. No significant advantage was experienced with a non-causal implementation of complex-conjugate control, based on predictions of the wave-excitation force, with reference to the study proposed in Chapters 5 and 6.

The constraint handling ability was also verified, in Section 7.7.2, where the proposed method was shown to approach the performance obtained with an optimisation-based controller such as MPC. In contrast to MPC, the proposed controller does not require predictions of the excitation force and, when operating in the constrained region, does not rely heavily on a model of the system for the calculation of the optimal motion. In addition, unlike MPC, the resulting motions and forces are linear with respect to the excitation force, giving velocities and forces which follow the same harmonic behavior as waves, with benefits in terms of long-term survivability and longevity of the WEC equipment. At the same time, a significant gain in computational simplicity is achieved, since the resolution of an optimisation problem at each time step is not required.

Performance with real wave data was also assessed in order to validate the general results, calculated with simulated stochastic waves in order to have more flexibility in the choice of the operating conditions (spectral peaks, bandwidth, central frequency,...). The results, shown in Section 7.7.3, confirmed the hypothesis derived from simulations with synthetic data.

An analysis of the robustness of the proposed controller was also carried out, in Section 7.7.4. The performance achieved in the presence of variations to the main parameters of the system, mass and hydrostatic stiffness, is very similar to MPC. In particular, the controllers are able to cope with variation of up to 10 % of the either of the parameters, while a significant drop in performance is experienced for larger variations. It was also shown how an increase of performance could also be experienced at wave frequencies where the model is under-estimated, due to a violation of the constraints by the controller. However, it was highlighted that the proposed controller can be modified to increase the robustness, trading off some performance, by adding feedback at the low-level control. Such a topic will be further investigated in Chapter 8.

While ideal efficiency in the bi-directional energy flow of the PTO mechanism was assumed, it was highlighted how the nature of the controller allows the possibility of including the efficiency information. The high-level control strategy could take into account losses in the reverse of energy flow at the PTO in the adaptive law for tuning the ratio between the velocity and the excitation force. The absorbed power, in fact, is proportional to the velocity but also to the amount of reactive power required, so that a straightforward compromise could be achieved. Finally, note that an additional parameter may be introduced, which is the phase-lag between oscillation velocity and excitation force. The phase parameter adds an additional degree of freedom resulting in a amplitude and phase controller, which can be very flexible in achieving a desired balance between high power absorption and reduced inverse energy flow. Such a possibility has not been studied here and would be of interest for further investigations.

Chapter 8

Robust design of the low-level controller for velocity-tracking

Abstract

A novel strategy for the control of a WEC, consisting of an oscillating body, was introduced in Chapter 7. The high-level component of the control system produces a reference velocity for the body's oscillation such that an effective wave energy transfer from the waves to the PTO is realised, within given motion constraints. The reference velocity is then imposed on the system through a low-level controller, by acting on the PTO force.

Since the focus of Chapter 7 was on the high-level control, a simplistic approach to the low-level controller was adopted, based on the plant inversion, with filtering for physical controller realisability. In practice, such a controller would be not acceptable, because it can be extremely sensitive to model uncertainties, measurement noise and other unknown disturbances, resulting in performance degradation as well as constraint violations. This Chapter focuses on the possibility of adding feedback to the low-level controller, for an improved robustness in the presence of model uncertainties. An approach based on the concept of Internal model control (IMC), that integrates well with the feedforward controller discussed earlier allows, with an intuitive design, the achievement of a significant improvement of the robustness.

The author is well aware that the proposed solution is not the only answer to the problem, and many other approaches could be adopted. The present Chapter is meant to make a contribution towards the completeness of the work started in Chapter 7, rather than an exhaustive study in the field of velocity tracking control for wave energy devices. At the same time, the separation into a unique Chapter permits a sharper focus to be maintained, which will hopefully help the clarity of the exposition.

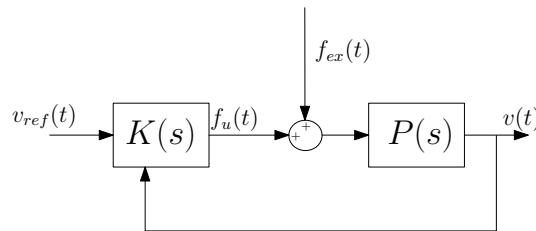


Figure 8.1: General structure of a feedback control that imposes a desired velocity of oscillation on a floating body, under the influence of the wave excitation force.

8.1 Control specifications

The control problem under study is the set-point tracking of a reference signal by a given plant. An external stochastic disturbance is acting linearly at the input of the system. The reference signal is possibly generated by a higher-level control logic.

In the specific case of a WEC consisting of a single body constrained to move in one degree of freedom, as modelled in Section 3.3, the block scheme of Fig. 8.1 applies. A reference velocity, $v_{ref}(t)$, needs to be followed by the system for an effective wave power absorption. The controller, namely $K(s)$, can manipulate the load force provided by the PTO in order to affect the dynamics of the WEC and impose the desired velocity. The system is persistently excited by the wave excitation force, $f_{ex}(t)$, which is modelled as a disturbance at the input of the system.

The reference velocity can be generated following the causal or non-causal approaches proposed in Chapter 7. Alternatively, an optimisation-based solution, such as MPC, could be utilised for the production of a reference signal. In any case, the desired velocity has a direct impact on the wave power absorption from the device and it is fundamental that the low-level controller is able to accurately impose it on the WEC. In Chapter 7, a simplistic solution for the velocity-tracking controller was proposed, designed as a feedforward action based on an approximation of the system inverse.

An important issue, however, was not dealt with in Chapter 7, in order to maintain the focus on the high-level controller. In particular, the feedforward action can be sensitive to model uncertainties. An analysis of the behavior of the controller in the case of parametric uncertainties, in Section 7.7.4, has shown that perturbations in the system can cause large deviations in the expected behavior, resulting in performance drops (wave energy absorption) and/or violation of the constraints. Stability was not an issue in that specific situation since the system is always stable and no feedback was introduced. In this Chapter, feedback is added to the controller specifically to handle the robustness issues.

One possibility is to follow an approach based on IMC. Such a solution would clearly separate the design of the feedforward component for the achievement of the desired performance, as already proposed in Section 7.6, from the design of the feedback component for robustness to given uncertainties. IMC was already effectively implemented in wave energy, for dealing with non-linearities in the model of the WEC [98, 193, 100]. Stability and robustness in the presence of structured or unstructured uncertainty, however, was not considered in the mentioned references.

A multi-step design procedure for IMC is detailed in [192], for the case that uncertainty information is available in the form of frequency-dependent bounds:

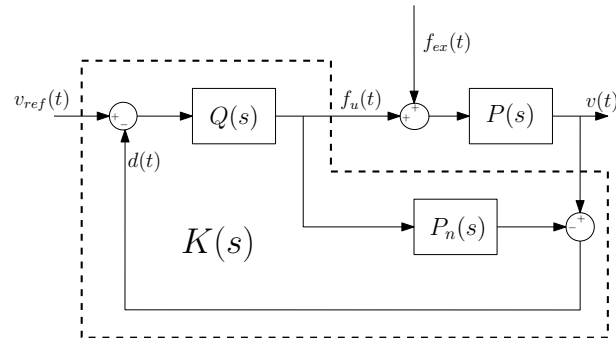


Figure 8.2: Block diagram of the IMC [192].

1. A feedforward controller, based on the plant inversion, is designed to achieve the desired performance on the nominal model.
2. Robust stability in the presence of uncertainty is ensured by augmenting the controller with a filter that conveniently shapes the sensitivity function.
3. Based on the IMC structure, the feedback controller is directly obtained from the feedforward component and the robustifying filter.

The design of the controller is described in Section 8.2. In Section 8.3, simulations show the improved robustness achieved under the proposed design, when model uncertainties are applied. Final remarks and conclusions are discussed in Section 8.4.

8.2 Design of the controller

The low-level controller, for imposing the desired velocity on the WEC system, has an IMC structure, as shown in Fig. 8.2. A model of the system, $P_n(s)$, is utilised to determine the expected output from a given control input, which is the PTO force, $f_u(t)$. The difference between the real output and the expected output, namely $d(t)$, represents the feedback signal. In the absence of the disturbance, $f_{ex}(t) = 0$, and with a perfect model, $P_n(s) = P(s)$, the feedback goes to zero. IMC exploits the idea that if a process and all its inputs are known perfectly, there is no need for feedback control or, in other words, that, for stable processes, feedback control is only needed because of uncertainty [192].

The overall controller, $K(s)$, is separated into two different components, one being the nominal model of the system, $P_n(s)$, and the other being a filter $Q(s)$. The design of the IMC is therefore reduced to the design of the filter $Q(s)$, which can address performance and robustness issues. Conditions for the stability and performance of the closed loop system are converted in conditions on the filter $Q(s)$, which simplifies the design. A convenient multi-step procedure for the choice of $Q(s)$ was proposed in [192] and it is adopted here.

In the following, Section 8.2.1 discusses the model of the WEC and the uncertainty. The controller design is then outlined in Section 8.2.2.

8.2.1 WEC model and uncertainty

The system under study is a WEC consisting of a floating cylinder oscillating in the heave direction only, schematised in Fig. 7.1 and with a geometry as specified in Section 7.2. As usual, the model is described by the following linear relation between the output velocity, $v(t)$, and the input force, which is a superposition of the controllable PTO force, $f_u(t)$, with the wave excitation force, $f_{ex}(t)$:

$$j\omega mV(\omega) + Z_r(\omega)V(\omega) + \frac{K_b}{j\omega}V(\omega) = F_{ex}(\omega) + F_u(\omega). \quad (8.1)$$

In (8.1), m is the mass of the system, K_b is the constant of buoyancy and $Z_r(\omega)$ is the radiation impedance, modelling the relation between velocity and radiation force. For a full derivation of (8.1), and for a more detailed explanation of the terms, the reader is directed to Section 3.3.

The nominal model of the system, already derived in Section 7.2, is given by the following transfer function:

$$P_n(s) = \frac{1.8 \times 10^{-6} \cdot s(s^2 + 1.1s + 0.4)(s^2 + 1.6s + 1.8)}{(s^2 + 1.2s + 0.4)(s^2 + 1.4s + 1.6)(s^2 + 0.1s + 1.5)}. \quad (8.2)$$

Note that $P_n(s)$, in (8.2), is stable and proper with a relative degree of 1. Due to the presence of the zero at $s = 0$, the plant has a non-minimum phase. The other zeros are always stable. Such properties are retained in general by rigid floating bodies (at least with a convex geometry), when only the heaving mode of motion is considered: the zero at $s = 0$ is due to the spring term arising from the equilibrium between buoyancy and gravity (refer to Section 3.3 for more details about the derivation of the model); the other zeros are always stable, since they represent the poles of the radiation of the system, which can be clearly verified from (7.4).

It is supposed, here, that the nominal model, $P_n(s)$, is only an approximation of the real system, $P(s)$, and that the source of uncertainty lies in the coefficient of the spring term, K_b . The definition of the constant of buoyancy, given in (3.122), is based on quite a rough approximation that considers small oscillations of the floating body around the mean water level and, at the same time, calm sea. Under such conditions, the wet surface of the body does not change significantly. In practice, however, the wet surface changes instantaneously with the motion of the body and with the variation in the water level due to the incident wave. As a result, the hydrostatic forces are highly non-linear and, particularly for relatively large oscillations, such as in wave energy, the linear model in (8.1) may be inaccurate. Another reason for our specific choice of the source of uncertainty is that the considered system has a resonant behavior with relatively low damping, which is quite sensitive to variations in the spring term.

The non-linearity of the hydrostatic force has been studied by a number of researchers, who implemented time-domain simulations with a time-varying wet surface, through Computational fluid dynamics (CFD) [194, 195, 196] or Boundary element methods (BEMs) [197, 198]. A non-linear parametric model for a more accurate representation for the hydrostatic force, however, is not available and, for the purposes of the present study, it is simply assumed that the coefficient of buoyancy undergoes unknown variations, $K_b + \Delta K$, in the range $\Delta K \in [-10\%, +10\%]$.

Figure 8.3(a) shows the magnitude and phase response of the nominal plant against a model

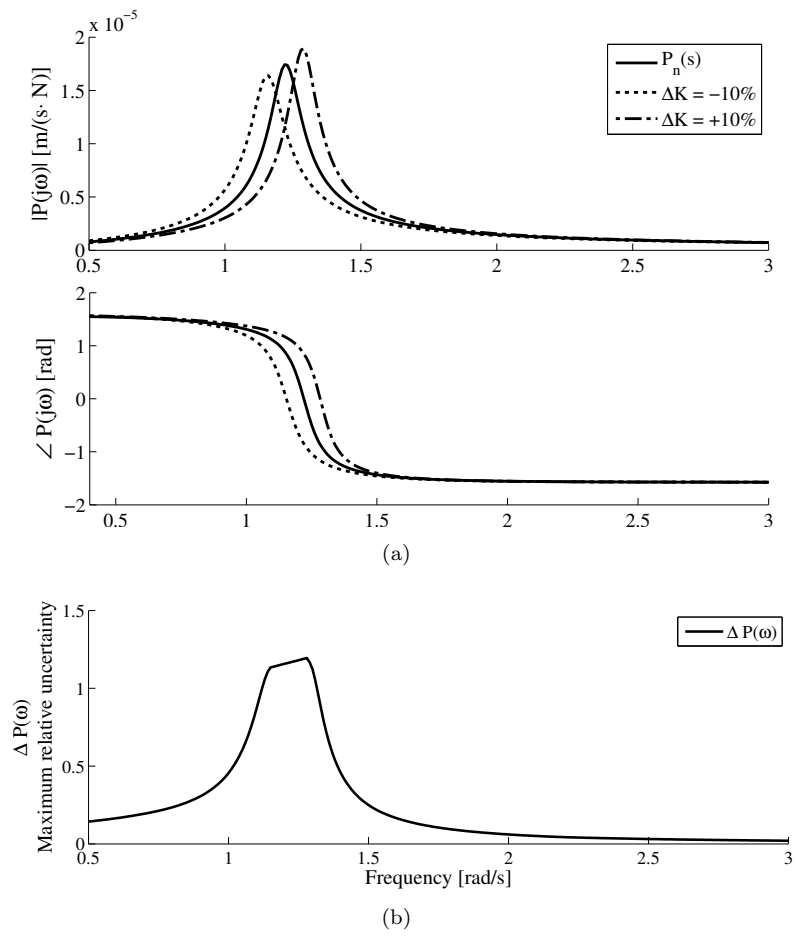


Figure 8.3: Uncertainty in the model. Largest parametric variation is $\Delta K = \pm 10\%$.

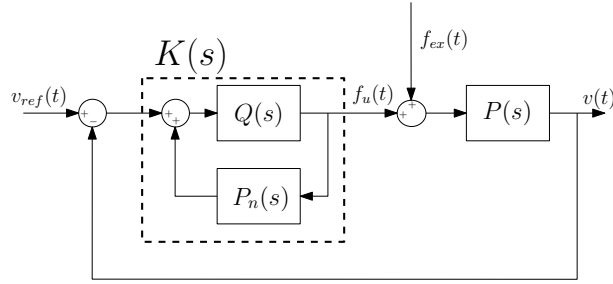


Figure 8.4: Equivalent block diagram of the IMC [192].

in which extreme variations $\Delta K = \pm 10\%$ are applied. In order to have an useful information for implementing a controller that is robust to such parametric variation, the uncertainty is modelled as a frequency domain bound, $\Delta P(\omega)$, defined as:

$$\frac{|P(j\omega) - P_n(j\omega)|}{|P_n(j\omega)|} \leq \Delta P(\omega) \quad (8.3)$$

The uncertainty bound, $\Delta P(\omega)$, is shown in Fig. 8.3(b) and it is important to notice that it can be quite conservative, depending on where the real parameter, K_b , lies within the specified range of uncertainty. Clearly, from Fig. 8.3, the uncertainty is quite significant around the resonance frequency of the device.

8.2.2 Controller design

The general structure of IMC, shown in the illustrative block scheme of Fig. 8.2, highlights the fact the actual controller is made of two components, which are the nominal model of the system, $P_n(s)$, and a filter, $Q(s)$. The equivalent block scheme of Fig. 8.4 clarifies the relation between the components of the IMC and the actual controller of a classical feedback scheme. In particular, the feedback controller, namely $K(s)$, which is what will have to be implemented in practice, is given by the following expression:

$$K(s) = \frac{Q(s)}{1 - P_n(s)Q(s)}. \quad (8.4)$$

The following relation exists between the output, $v(t)$, and the inputs, $v_{ref}(t)$ and $f_{ex}(t)$:

$$v = \frac{PQ}{1 + Q(P - P_n)} v_{ref} + \frac{1 - P_n Q}{1 + Q(P - P_n)} P f_{ex}, \quad (8.5)$$

where the dependence on the complex variable, s , has been dropped for brevity.

The sensitivity function, $S(s)$, and the complementary sensitivity function, $T(s)$, are defined

[192] as:

$$S \triangleq \frac{1 - P_n Q}{1 + Q(P - P_n)} = \frac{v}{P f_{ex}} \quad (8.6)$$

$$T \triangleq \frac{PQ}{1 + Q(P - P_n)} = \frac{v}{v_{ref}}. \quad (8.7)$$

The sensitivity function expresses the response of the feedback system to the input disturbance filtered by the plant, namely $P(s)f_{ex}(t)$. The complementary sensitivity indicates the tracking ability of the closed-loop system, as well as the sensitivity to measurement disturbances [192]. Ideally one would set $S = 0$ and $T = 1$ (perfect control), but this is not possible, in general, due to the presence of measurements noise, model disturbances and other issues related to the practical realisability of the controller, $K(s)$, so that the conditions are only approximated in a range of frequencies.

It is interesting to note that, in the case of a perfect WEC model, $P = P_n$, the relations in (8.5) simplify to:

$$v = T v_{ref} + S f_{ex} = P Q v_{ref} + (1 - P_n Q) P f_{ex}, \quad (8.8)$$

where the filter, $Q(s)$, has a direct meaning in terms of sensitivity (robustness to plant variations, disturbance rejection) and complementary sensitivity (tracking performance and measurement noise rejection). Through the IMC parametrisation, the controller component $Q(s)$ is related to $T(s)$ and $S(s)$ in a very simple manner which makes the design of $Q(s)$ relatively straightforward [192], as it will emerge throughout the present Section.

An important property of IMC, that is immediately verified from (8.8), is that, in the case of a perfect model, $P(s) = P_n(s)$, the closed-loop system is internally stable if and only if the process, $P(s)$, is stable and the function $Q(s)$ is stable. Such a consideration simplifies the design of the controller, $K(s)$, since it is sufficient to choose a stable filter $Q(s)$ in order to ensure the stability of the feedback system, provided that $K(s)$ is calculated from (8.4). Unfortunately such a statement is not usable in practice, since the model of the system is not known with complete accuracy.

However, a very convenient necessary and sufficient condition, for the internal stability of the closed-loop system, can be utilised in the case of model mismatch.

Theorem 8.1. [192] *Assume that all the plants, $P(s)$, in the family Π*

$$\Pi = \left\{ P(s) : \frac{|P(j\omega) - P_n(j\omega)|}{|P_n(j\omega)|} \leq l_m(\omega) \right\}, \quad (8.9)$$

have the same number of stable poles and that a particular controller, $K(s)$, stabilises the nominal plant, $P_n(s)$. Then, the closed-loop system is robustly stable with the controller $K(s)$ if and only if the complementary sensitivity function for the nominal plant, $T_n(s)$, satisfies the following condition:

$$\|T_n(j\omega)\Delta P(\omega)\|_\infty \triangleq \sup_\omega |T_n(j\omega)\Delta P(\omega)| < 1. \quad (8.10)$$

In the case of a controller, $K(s)$, based on the IMC structure, condition (8.10) provides a very convenient condition on the filter $Q(s)$. Based on the equivalence in (8.8), the complementary sensitivity function for the nominal plant is $T_n(s) = Q(s)P_n(s)$ and the robust stability is ensured if and only if:

$$\sup_{\omega} |Q(j\omega)P_n(j\omega)\Delta P(\omega)| < 1. \quad (8.11)$$

The IMC parametrisation reduces the design of a feedback controller, $K(s)$, to the design of a filter, $Q(s)$, that is directly related to the performance and disturbance rejection properties, through (8.8), and to the robust stability of the system, through (8.11). Based on such considerations, a step-by-step procedure was proposed in [192], where $Q(s)$ is firstly designed for performance on the nominal plant and then adjusted to ensure robust stability. Although being suboptimal, the procedure has the advantage of simplicity, where each design choice has a straightforward impact on some fundamental characteristics of the closed-loop system. The two important steps in the procedure are described next.

Step 1 - Nominal performance

The ideal choice for the filter $Q(s)$, when the plant coincides with the nominal model, is:

$$Q(s) = P_n^{-1}(s). \quad (8.12)$$

Under condition (8.12), perfect control is achieved, that is $S = 0$ (perfect disturbance rejection) and $T = 0$ (perfect reference tracking). However, it is not always possible to invert the plant, because $P_n(s)$ may be strictly proper (the inverse being non-realizable) or it may be non-minimum phase (the inverse being unstable).

The model of the WEC, given in (8.2), is strictly proper, with relative degree of 1, and it is non-minimum phase, with a zero in $s = 0$. The filter $Q(s)$ needs to be augmented as:

$$Q(s) = F(s)P_n^{-1}(s), \quad (8.13)$$

where $F(s)$ should be proper with relative degree of at least 1, for physical realizability. In addition, $F(s)$ should have a zero at $s = 0$, in order to remove the unstable pole at $s = 0$ appearing from the inversion of the plant.

Observing such constraints, $F(s)$ can be shaped such that the desired performance is achieved within the range of frequencies of interest. In particular, the complementary sensitivity function for the nominal plant, $T_n(s) = Q(s)P_n(s)$, should approach unity for good tracking and disturbance rejection properties. In our specific case, the filter $F(s)$ can be chosen as already proposed and discussed in Section 7.6, based on the consideration that the reference signal, as well as the disturbance, are only significant in a well known frequency range $[0.3, 2]$ rad/s. The lower limit of the range is set by the lowest frequency of typical ocean waves, that exceeds 0.3 rad/s (period nearly 20 seconds), except in the case of extreme events (when typically the WEC would operate in safety mode rather than in production mode). The upper limit is determined, through the filter $H_{ex}(\omega)$, defined in (3.114), by the geometry of the floating body, that filters out high-frequency

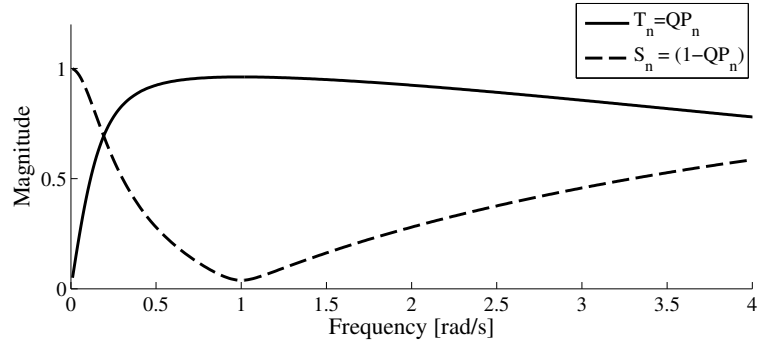


Figure 8.5: Sensitivity, $S_n(s)$, and complementary sensitivity, $T + n(s)$, in the case of nominal plant.

waves.

The filter, $F(s)$, is therefore designed as in (7.36):

$$F(s) = \frac{s}{(s + 0.2)} \cdot \frac{5}{s + 5}, \quad (8.14)$$

that is a band-pass filter with a magnitude of approximately one over the frequency range $[0.3, 2]$ rad/s. At the same time, a zero at $s = 0$ cancels the unstable pole due to the plant inversion (not a problem since $F(s)$ is not implemented directly, but $K(s)$ is, as already explained in Section 7.6). The resulting complementary sensitivity function and sensitivity function, assuming nominal plant, are shown in Fig. 8.5.

As already discussed in Section 7.6, the choice in (8.14) is not optimal and a numerical procedure could be implemented for fine tuning the filter $F(s)$, as proposed in [192]. Such optimisation goes beyond the scope of the present Chapter, which is more focused on the structure of the controller and on the possibility of dealing with robustness to model uncertainties.

Step 2 - Robust stability and performance

The information of the plant uncertainty is available in the form of a frequency-dependent maximum variation, $\Delta P(\omega)$, as defined in (8.3). Based on theorem 8.1, robust stability for any plant within the uncertain region is guaranteed, if and only if condition (8.11) is satisfied. The condition is easily verifiable since it only depends on the nominal plant, $P_n(s)$, the filter $Q(s)$, designed for performance in (8.13), and the uncertainty, $\Delta P(\omega)$.

Figure 8.6 shows that the condition for robust stability is not satisfied within a certain range of frequencies where the uncertainty of the system is quite large. Such a band of frequencies is right in the centre of the region of interest, $[0.3, 2]$ rad/s, where maximum sensitivity is desired. Due to the nature of the parametric uncertainty (refer to Section 8.2.1), in fact, a relatively large inaccuracy is expected around the resonance frequency of the device.

The usual approach, as proposed in [192], is to augment the filter $Q(s)$ with an additional low-pass filter that rolls off the complementary sensitivity above a certain frequency. Typically, in fact, the uncertainty of a plant increases at high frequencies, while it may be reasonably assumed that the model is accurate at low frequencies. In the specific case under study, the uncertainty

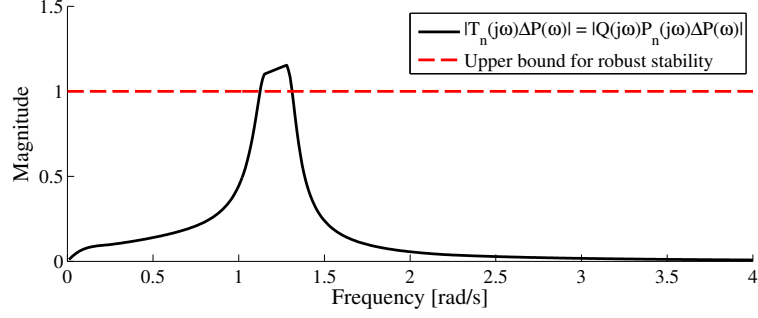


Figure 8.6: The condition for robust stability is not verified by $Q(s)$ chosen at step 1, from (8.13).

is maximum around the centre of the region where high sensitivity would be desired and, at the same time, it decreases at higher frequencies.

In order to achieve a better compromise between the drop in sensitivity and improved robustness, the filter $Q(s)$ is augmented with a notch filter, as proposed in [199]:

$$Q(s) = F(s)P_n^{-1}(s)N(s), \quad (8.15)$$

where

$$N(s) = \frac{s^2 + 2M\chi\omega_0 + \omega_0^2}{s^2 + 2\chi\omega_0 + \omega_0^2}. \quad (8.16)$$

In (8.16), ω_0 specifies the frequency of maximum attenuation (centre of the notch), χ determines the bandwidth of the attenuation (wideness of the notch) and M is directly related to the maximum attenuation.

Based on such a parametrisation, the notch filter required in order to push down the complementary sensitivity, such as to ensure robust stability, can be easily designed. As it can be seen from Fig. 8.6, the peak of the complementary sensitivity is centred at $\omega \approx 1.28$ rad/s and its value is approximately 1.15. As a consequence, the notch filter is specified by $\omega_0 = 1.28$ rad/s and $M = 1/1.15 \approx 0.85$. The bandwidth parameter is chosen as $\chi = 0.9$, since the uncertainty peak is relatively broad.

Figure 8.7 shows the magnitude response of the chosen notch filter and the effect that it has on the complementary sensitivity function. Condition (8.11), for robust stability, is now verified. As a consequence, based on (8.4), the final feedback controller, $K(s)$, is designed as:

$$K(s) = \frac{Q(s)}{1 - P_n(s)Q(s)} = \frac{P_n^{-1}(s)F(s)N(s)}{1 - P_n(s)P_n^{-1}(s)F(s)N(s)}, \quad (8.17)$$

with $F(s)$ given as in (8.14) and $N(s)$ chosen as in (8.16), which ensures that the closed-loop system is robust to model variations in the range specified in (8.3).

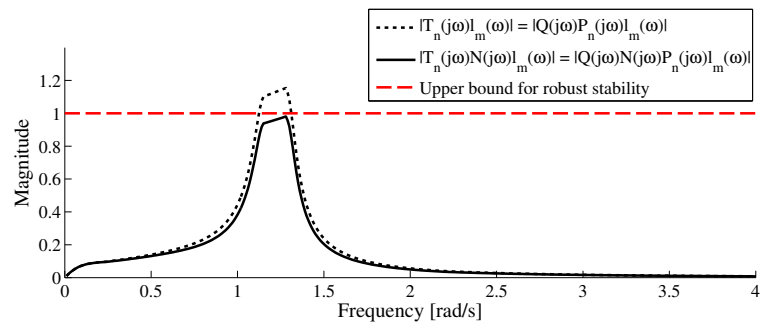
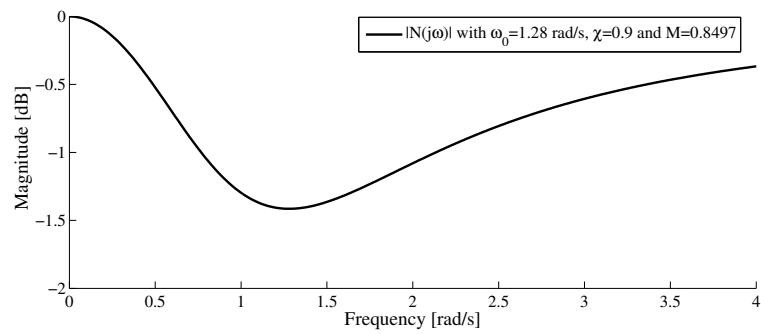


Figure 8.7: The complementary sensitivity function is lowered down with a notch filter so that the robust stability condition is satisfied: (a) Notch filter (magnitude expressed in dB to highlight the notch); (b) Modification of complementary sensitivity.

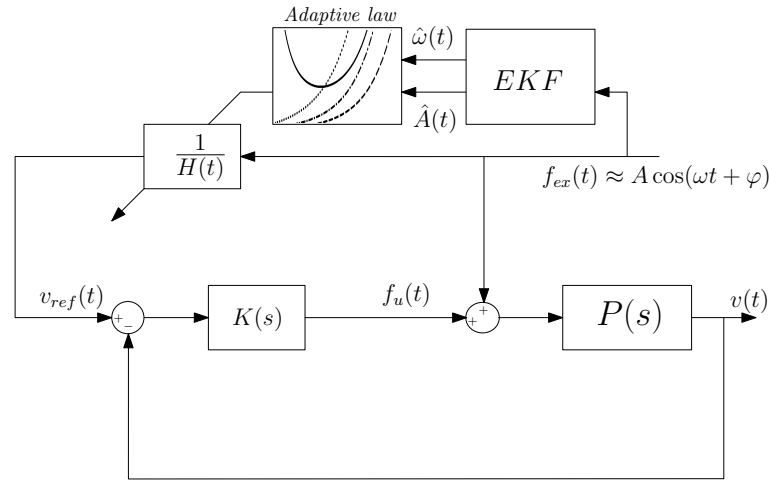


Figure 8.8: Complete control architecture. The high-level controller, designed in Chapter 7, produces a reference velocity, that is imposed on the system by a robust feedback controller, $K(s)$, designed in the present Chapter.

8.3 Results

The proposed low-level controller for tracking a desired velocity imposed on the WEC is implemented together with the high-level control logic proposed in Chapter 7. The improved robustness is verified against the case where the simplistic feedforward control, designed in Section 7.6, is utilised to impose the desired velocity. Fig 8.8 shows the block scheme of the overall control system, including high-level and low-level controllers.

The controller, $K(s)$, is designed based on an IMC structure, according to the methodology outlined in Section 8.2. As discussed in Section 8.2.1, a parametric uncertainty in the range $\Delta K \in [-10\%, +10\%]$, for the buoyancy coefficient, is assumed for the real model of the WEC, with respect to the nominal model, $P_n(s)$. Details about the nominal model and the geometry of the system can be found in Sections 7.2 and 8.2.

Simulations are run with the system being excited by irregular waves following a single-peak Ochi spectral distribution, generated according to the methodology outlined in Section 7.7. The spectral distribution, an expression for which was given in (7.37), is parameterised with different peak frequencies, $\omega_p \in [0.3, 1.2]$ rad/s (wave period about 5 to 22 seconds), a constant narrowness factor, $\lambda = 2$, and a constant significant wave height, $H_s = 1$ m.

The high-level controller optimises the operation of the WEC (for maximum wave energy absorption) by producing a reference velocity that is in phase with the wave excitation force and such that the vertical motion is constrained within $\pm X_{lim} = \pm 0.8$ m. A sensitivity analysis, carried out in Section 7.7.4, highlighted the effects that model uncertainties can have on the performance, when not properly handled (which is the case with a feedforward controller). In particular, depending whether the model was under- or over-estimated, a drop in performance (caused by the imposed velocity being lower than the desired one) or a significant violation of the motion constraints (resulting, in the simulation, in a higher energy capture) was experienced.

Figure 8.9 compares the results obtained with the robust controller proposed in this Chapter against the results calculated with the simple feedforward control, when the largest possible model

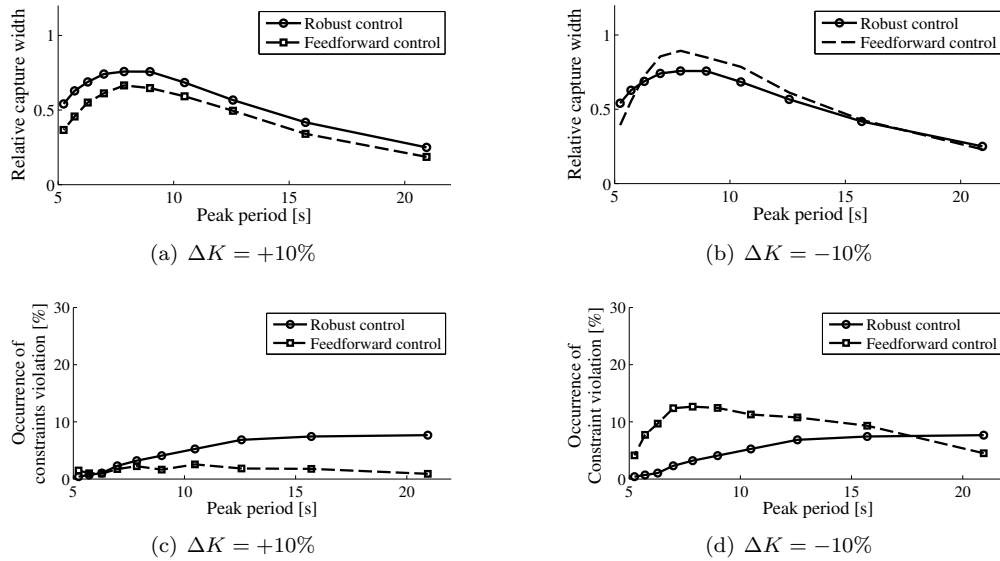


Figure 8.9: Performance of proposed robust controller against feedforward controller when the largest parametric variation, $\Delta K = \pm 10\%$, is applied: (a)-(b) Relative capture width; (c)-(d) Percentage of occurrence of motion constraints violation, due to the model inaccuracy.

variations, $\Delta K = \pm 10\%$ are applied. In particular, Fig. 8.9(a) (variation $\Delta K = +10\%$) and Fig. 8.9(b) (variation $\Delta K = -10\%$) show the RCW achieved through the two controllers when the incident waves are centred at different peak frequencies. Clearly, the robust controller seems not to suffer from the model uncertainty and offers similar performance for both the extreme variations. On the other hand, the feedforward controller is quite sensitive to the parametric variations and the performance increases or decreases according to whether the model is over- or under-estimated (which depends on the parametric variation and on the frequency, refer to Fig. 8.3). The higher performance of the feedforward control at certain frequencies is only due to a more frequent violation of the constraints, that is particularly evident in the case $\Delta K = -10\%$, shown in Fig. 8.9(d) (already discussed in Section 7.7.4).

Note that the robust control seems to violate the motion constraints almost 10% of the time for very long waves (peak period more than 15 seconds, peak frequency below 0.41 rad/s). Such violation, however, is not due to the behavior of the low-level controller, since the model uncertainty is not significant at such frequency. The problem, in this case, lies in the reference-generation strategy, that needs to include some safety margin for long waves, as also discussed in Chapter 7.

Additional evidence of the robustness of the proposed controller is given in Fig. 8.10, which shows the capture width achieved with the robust controller and with the feedforward controller, for different values of the parametric uncertainty in the range $\Delta K \in [-50\%, +50\%]$. An irregular wave train centred at a peak frequency $\omega_p = 1.22$ rad/s was utilised, since the largest uncertainty always appears at such frequency (it is approximately the resonance frequency of the system).

Again, the RCW achieved with the robust control system is quite insensitive to the proposed variations (which are relatively large). The feedforward control, as already verified in Section 7.7.4, is otherwise strongly and negatively affected by parametric variations in the buoyancy coefficient. Another interesting fact can be noticed, in Fig. 8.10, with reference to the performance in the

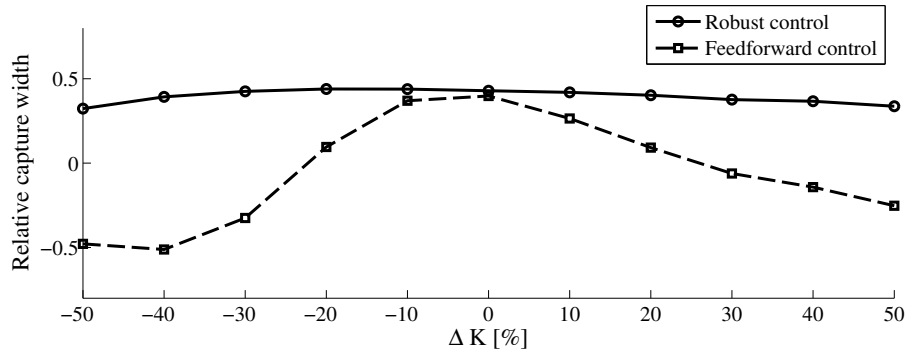


Figure 8.10: Sensitivity of robust control and feedforward control to variations in the buoyancy coefficient, ΔK . The incident wave is centred at a frequency $\omega_p = 1.22$ rad/s, that is the resonance frequency of the device, where the uncertainty is the largest.

case of a perfect model, that is $\Delta K = 0\%$. As discussed in Section 8.2, the design of the robust controller trades performance against robustness: an increase in robustness to model uncertainties requires a more conservative control and therefore a drop in performance in nominal conditions. In this specific case, however, the robust controller performs as well as the feedforward controller and the price paid for the robustness is quite small. The reason behind such behavior can be explained by the range of uncertainties utilised in the design, but also in the notch-type of shape chosen for the robustifying filter, which offers a good compromise for the given uncertainty model.

8.4 Conclusion

An important property which is required of control systems is robustness to uncertainties, such as unknown disturbances, unknown (or un-modelled) system dynamics or time-varying characteristics of the system (e.g. due to ageing or change of operating conditions). Particularly in wave energy, it is widely acknowledged that the typical linear models utilised for control design are unable to capture the correct behavior. Unlike most classical control problems, the motion of a WEC is controlled to be as extreme as possible (within given constraints) in order to maximise the wave energy capture. As a consequence, non-linearities can be significant.

This Chapter proposed a possible approach to the design of a robust low-level controller that manipulates the PTO force in order to effectively impose a desired velocity on a WEC. The reference velocity may be generated by a higher-level control logic, such as the one proposed in Chapter 7 or the more popular MPC methodology. By employing a structure based on IMC, it is shown how the design of the low-level controller can be separated into steps that intuitively address the performance and the robustness to model variation issues. While being a sub-optimal procedure, simulation results showed that the resulting system has a significantly reduced sensitivity to parametric uncertainties, even when they cause a significant variation in the expected response of the system, within the range of frequencies of interest (where most wave energy is).

The design of the low-level controller completes the work proposed in Chapter 7, focused on the high-level control. It is not meant to offer a complete coverage of the different possibilities

available in the field of robust control. The work presented through this Chapter, however, highlights the potential and the importance of considering model uncertainties, in the field of wave energy. Particular attention, in the author opinion, should be focused, in the immediate future, on understanding the main inaccuracies in the current models of wave-energy conversion systems. Experimental testing and computational fluid dynamics could be particularly helpful in producing appropriate models for the uncertainty. Many techniques from the field of control theory, such as the one proposed here (but not only), can then be called upon for appropriately addressing the robust control issue.

Chapter 9

Conclusion

This Chapter reports the main conclusions that are derived from the research work presented in this thesis, in Section 9.1. Some notes regarding possible directions for future research are also documented, in Section 9.2.

9.1 Overall conclusions

Wave energy represents a significant resource of renewable energy and can make an important contribution to the development of a more sustainable solution in support of the contemporary society, which is becoming more and more energy intensive.

As explained in Chapter 2, high levels of penetrations of intermittent energy sources strongly increase the requirement of surplus capacity from conventional and controllable thermal plants, that, as a cause, are operated at much lower efficiencies to ensure the stability of power systems. Therefore, it is fundamental that the mix of renewable energy sources is as diverse as possible in order to exploit the non-correlation between different (could be geographic diversity) variable sources such that variability of the generated power is reduced. At a time when offshore wind systems are receiving much attention, wave energy offers the opportunity to introduce the right mix of renewable generation, with important benefits in terms of reduced variability and improved predictability of the power supply. The analysis proposed in Chapter 2, in fact, demonstrated that in certain situations ocean waves and wind present very small correlation. This is particularly true at sea locations which are exposed to large swell waves that have travelled a long distance after being generated by remote storms. A numerical analysis based on wind and wave measurements collected at different locations around the coast of Ireland, showed that significant potential exists, off the West and Shout-West coasts, to reduce the variability of the power generation by deploying mixed farms with wind and wave energy devices.

Given the potential of wave energy, however, the technology for the generation of electricity from ocean waves is not mature yet. In order to raise the economic performance of Wave energy converters (WECs), still far from being competitive, a large scope exists for the improvement of their capacity factor through more intelligent control systems. In particular, the efficiency of WECs, of the oscillating type, can be significantly increased through an automatic control that

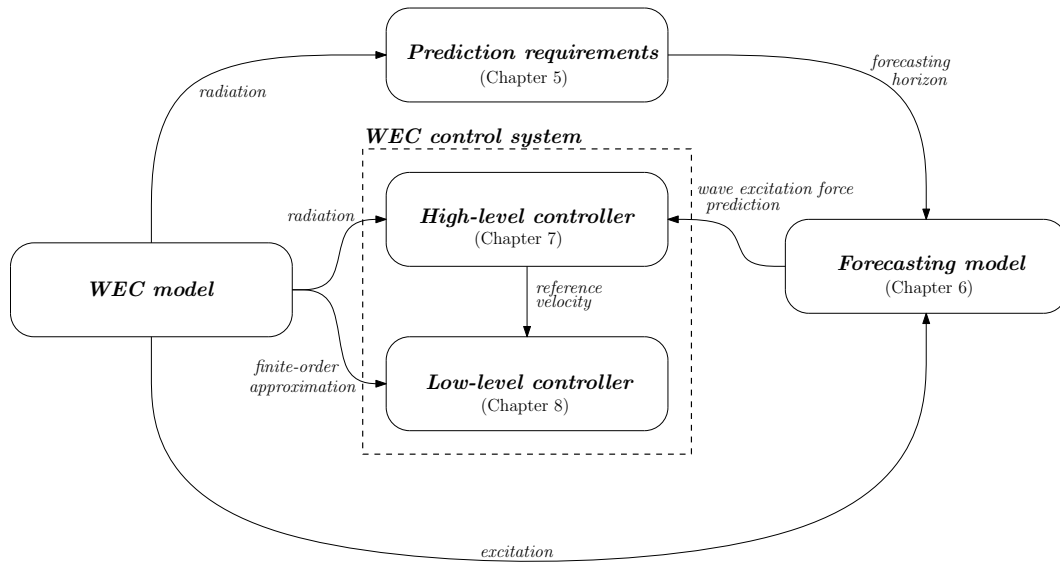


Figure 9.1: Logic structure of the thesis.

tunes their oscillation to the incident wave elevation, in such a way to improve the power transfer from the ocean to the system.

The review proposed in Chapter 4 highlighted the fact that most control solutions proposed in the literature, for the enhancement of the power absorption of WECs, require future knowledge of the wave elevation or wave excitation force. With this thesis, the author has attempted to analyse the non-causality of the existing control solutions and to investigate the possibility of solving such non-causality by integrating the control system with predictions of the excitation force. Figure 9.1 summarises the logical structure of this thesis, by highlighting the main lines of research that have been followed and how they are inter-connected. In particular, Chapter 5 analysed the non-causality of complex-conjugate control and put it in relation with the radiation properties of the floating body. Based on this quantification of the prediction requirements, Chapter 6 studied the possibility of producing the predictions of the wave excitation force by following a stochastic approach, where future values are estimated only from current and past measurements by exploiting the correlation within the ocean waves. A relation between the excitation properties of the floating body and the achievable prediction horizon was found. Then, in Chapter 7, the integration of the predictions within a WEC control system was studied. A hierarchical structure was investigated, where a high-level controller (Chapter 7) produces a reference velocity and a low-level controller (Chapter 8) imposes such velocity on the oscillating system, while ensuring robustness to uncertainties in the WEC model.

The starting point of the research work in this thesis is the analysis of the prediction requirements: how long into the future is it necessary to predict for? The focus, in Chapter 5, was put on the non-causality of the unconstrained optimal conditions for maximum wave energy absorption, that are named complex-conjugate control. This allowed an analytical treatment of the problem and the identification of the link between fundamental properties of the radiation of the floating body and the non-causality of complex-conjugate control. Numerical results, calculated for WECs with a simple geometry (cylinder and sphere), confirmed the link between system radiation

and prediction requirements. It was found that a prediction horizon ranging between as low as 10 seconds up to more than 1 minute would be necessary with the considered geometries. By introducing some knowledge about the waves, particularly their typical frequency distribution, a manipulation of the solution of complex-conjugate control was also proposed, in order to reduce the non-causality, with a minor penalty on the achievable energy capture. In absolute terms, the manipulation of complex-control allowed the reduction of the prediction requirements to 10-20 seconds (1 to 2 typical wave periods) for all the considered geometry.

Based on the identified requirements, Chapter 6 demonstrated, with real wave data, that the problem of short-term forecasting of the wave excitation force can be effectively solved by following a purely stochastic approach. The correlation within ocean waves, in fact, allows the achievement of accurate predictions for 1 or 2 wave periods into the future, only from past measurements. Prediction algorithms based on remote sensing of the wave elevation around the device, which require complex models taking into account multi-directionality, radiated waves and non-linearities in the wave propagation, can therefore be avoided, at least for the purposes of real-time control. In particular, linear Autoregressive (AR) models are able to implicitly capture the harmonic nature of the waves and, given the relative simplicity of their estimation, can be easily adapted in real-time to variations in the sea state. Besides, a numerical analysis of real wave data, in Section 6.3, confirmed that the typical waves of interest for wave energy conversion (low-frequency swell or fully developed wind waves) present weak non-linearities and follow a nearly-Gaussian distribution around the mean free-surface water level. Another interesting outcome of Chapter 6 was the identification of a link between the excitation properties of the floating body and the predictability of the wave excitation force. Useful indications in terms of controllability of a WEC can therefore be derived, at design stage, by looking at its radiation (prediction requirements) and excitation (achievable prediction) properties.

The implementation of non-causal complex-conjugate control, by using predictions of the wave excitation force, was then studied in Chapter 7. The controller was structured as a high-level component, producing the desired oscillation velocity for the WEC, based on predictions of the wave excitation force, followed by a low-level velocity-tracking controller. The achieved performance, in terms of power capture, is very close (above 90% in most cases) to the theoretical optimum. Some difficulties are encountered with mixed seas, characterised by a multi-peaked spectral distribution, for which the prediction model is not adequate. The occurrence of such sea states, though, is not frequent at highly-energetic sea locations.

While the issue of the non-causality of complex-conjugate control is solved, its implementation in practice is still prohibitive due to the extremely large oscillations and forces required to the WEC and its Power take-off (PTO) equipment (it is indeed an unconstrained optimum). Based on the assumption that the wave excitation force is a non-stationary and narrow-banded harmonic process, a simple and effective extension of the proposed controller, for the treatment of motion constraints, is proposed. The reference velocity is simply calculated as proportional to the wave excitation force, the constant of proportionality being effectively tuned for performance and constraint handling. The non-causality is removed and predictions are not required (the controller implicitly assumes that the future wave excitation force is sinusoidal). In practice, deviations from the validity of the assumption (harmonic excitation) make the proposed controller sub-optimal. However, simulations in (synthetic and real) irregular waves, in Chapter 7, demonstrate that the solution allows the

achievement of levels of power capture that are very close to non-causal complex-conjugate control, in the unconstrained case, and Model predictive control (MPC), in the constrained case. At the same time, the following benefits are achieved:

- No need of predictions. However, a real-time estimate of the frequency and amplitude of the excitation force is required, for example using the Extended Kalman filter (EKF).
- Motion constraints are handled without the resolution of an optimisation problem at each time step.
- Produced motions and forces follow the same harmonic behavior as waves, with benefits in terms of long-term survivability and longevity of the WEC equipment.
- When operating in the constrained region, the high-level controller does not rely on the model of the system for the calculation of the optimal motion, with possible benefits in terms of robustness.

With regards to the latter point, the hierarchical structure of the controller makes it possible to deal with model uncertainties at the low level velocity-tracking loop. Particularly in wave energy, it is widely acknowledged that the typical linear models utilised for control design are unable to capture the correct behavior. Unlike most classical control problems, in fact, the motion of a WEC is controlled to be as extreme as possible in order to maximise the wave energy capture, with the consequence that non-linearities can be significant. Chapter 8 proposed one possibility for the design of a robust low-level controller, if a model of the uncertainty, in the form of frequency-dependent bounds, is available. The solution is based on Internal model control (IMC), which is not new to wave energy applications. A multi-step procedure is applied, where the controller is firstly designed for nominal performance and then adjusted for ensuring robust stability. Robust performance in the presence of model variations, with minor reductions of energy capture and non-violation of the constraints, is also achieved.

9.2 Notes on possible future research

Several directions for further research emerged throughout this thesis. Future possibilities on very detailed aspects of the different research topics studied in Chapters 5 to 8 were outlined in the specific conclusive Sections. In this Section, the author points out some more general perspectives on the topics that he thinks can make a significant contribution towards the advancement of research in the field of control of wave energy devices.

A first major comment regards the assumption, throughout the thesis, that the wave excitation force acting on the floating body is known. As discussed in Section 6.6.1, such an assumption is not realistic since the excitation force is only a mathematical convenience (it is the force produced by the incident wave when the body is assumed to be at the equilibrium) and is not measurable. It is crucial that the problem of estimating of the excitation force, from available sensor measurements, is addressed.

An important effort needs to be made, in the wave energy community, in order to extend the knowledge about the hydrodynamic model of the wave energy conversion systems. The extreme motions required to the system make the conventional linear model, that was adopted in this thesis, not always adequate. As demonstrated in Chapter 8, at least a non-parametric quantification of the non-linearities of the floating system (e.g. through *wet* experiments) can serve the purposes of the design of a robust control system, though conservative in performance.

A final comment regards the focus of this thesis on WECs in one degree of freedom. It would be interesting to extend the analysis of the prediction requirements and the proposed control design to more general multi-body and multi-degree-of-freedom oscillating systems.

Appendix A

Model-order reduction based on Hankel singular values

A.1 State-space balanced realisation and Hankel singular values

Given the state space representation of a linear system:

$$\begin{cases} \dot{x}(t) = Ax(t) + Bu(t) \\ y(t) = Cx(t) \end{cases}, \quad (\text{A.1})$$

and a real a non-singular transformation matrix P , the system defined by the matrices $(\bar{A} = PAP^{-1}, \bar{B} = PB, \bar{C} = CP^{-1})$ is equivalent to the system (A, B, C) , that is they have the same set of eigenvalues and the same input-output transfer function.

For any state-space representation as in (A.1), the controllability Gramian matrix, W_c , and the observability Gramian matrix, W_o , are defined such that [72]:

$$AW_c + W_cA^T = -BB^T \quad (\text{A.2})$$

$$A^TW_o + W_oA = -C^TC. \quad (\text{A.3})$$

The matrices W_c and W_o are important because their product, W_cW_o , is similar (same determinant and eigenvalues, among other properties) to the product $\bar{W}_c\bar{W}_o$, corresponding to an equivalent state-space representation $(\bar{A}, \bar{B}, \bar{C})$. Furthermore, the product W_cW_o is similar to the Hankel matrix:

$$\Sigma = \text{diag}\{\sigma_1, \sigma_2, \dots, \sigma_n\}, \quad (\text{A.4})$$

where n is the dimension of the state and the elements $\sigma_1 \geq \sigma_2 \geq \dots \geq \sigma_n \geq 0$ are the Hankel singular values of the system, which represent a quantification of the energy of each state component [72].

A state space realisation of a system, (A, B, C) , is balanced when $W_c = W_o = \Sigma$ [72].

A.2 Model reduction based on Hankel singular values

The properties of a balanced state-space realisation and the Hankel singular values can be exploited in order to isolate the dominant dynamics of a system. If the state space model in (A.1) is decomposed as follows:

$$\begin{cases} \begin{bmatrix} \dot{x}_1(t) \\ \dot{x}_2(t) \end{bmatrix} = \begin{bmatrix} A_{11} & A_{12} \\ A_{21} & A_{22} \end{bmatrix} \begin{bmatrix} x_1(t) \\ x_2(t) \end{bmatrix} + \begin{bmatrix} B_1 \\ B_2 \end{bmatrix} u(t) \\ y(t) = \begin{bmatrix} C_1 & C_2 \end{bmatrix} \begin{bmatrix} x_1(t) \\ x_2(t) \end{bmatrix} \end{cases}, \quad (\text{A.5})$$

and the Hankel matrix is accordingly decomposed as:

$$\Sigma = \text{diag} \{ \Sigma_1, \Sigma_2 \}, \quad (\text{A.6})$$

then the subsystem (A_{11}, B_1, C_1) is a good approximation of the original system (A, B, C) if the singular values in Σ_1 are much bigger than the singular values in Σ_2 .

Appendix B

State estimation with the Kalman filter

B.1 The Kalman filter

The Kalman filter is a recursive algorithm providing the optimal estimation of the state of a linear dynamical system driven by Gaussian white noise [153].

Consider the following state-space representation of a linear system in discrete time:

$$\begin{cases} x[k+1] = A[k]x[k] + B[k]w[k] \\ y[k] = C[k]x[k] + D[k]n[k] \end{cases}, \quad (\text{B.1})$$

where x, u and y are, respectively, the state, the input and the output of the system. The state disturbance, $w[k]$, and the output noise $n[k]$ are Gaussian, white and statistically independent from each other, with known covariance matrices, given by:

$$E \{w[i]n[k]^T\} = 0 \quad \forall i, k \quad (\text{B.2})$$

$$E \{w[i]w[k]^T\} = \begin{cases} 0 & \forall i \neq k \\ M[k] & i = k \end{cases} \quad (\text{B.3})$$

$$E \{n[i]n[k]^T\} = \begin{cases} 0 & \forall i \neq k \\ N[k] & i = k \end{cases}. \quad (\text{B.4})$$

Probabilistic information about the initial state $x[0]$ is also assumed to be known:

$$E \{x[0]\} = X_0 \quad (\text{B.5})$$

$$E \{[x[0] - X_0][x[0] - X_0]^T\} = P_0. \quad (\text{B.6})$$

The Kalman gives the *optimal* estimate, $\hat{x}[k|k]$, of the state $x[k]$, based on all the available

observations $Y_k = \{y[0], \dots, y[k]\}$. The solution assumes the following recursive form:

$$P[k+1|k] = A[k]P[k|k]A[k]^T + B[k]W[k]B[k]^T \quad (\text{B.7})$$

$$K(k+1) = P[k+1|k]C[k]^T (C[k]P[k+1|k]C[k]^T + D[k]N[k]D[k]^T)^{-1} \quad (\text{B.8})$$

$$\hat{x}[k+1|k+1] = A[k]\hat{x}[k|k] + K[k+1](y[k+1] - C[k]A[k]\hat{x}[k|k]) \quad (\text{B.9})$$

$$P[k+1|k+1] = (I - K[k+1]C[k+1])P[k+1|k], \quad (\text{B.10})$$

where it can be noted how $\hat{x}[k|k]$ is calculated as the *prediction* $\hat{x}[k+1|k] = A[k]\hat{x}[k|k]$ plus a correction consisting of the *innovation* from the new available information, $(y[k+1] - C[k]A[k]\hat{x}[k|k])$, weighted by the Kalman gain, $K[k]$. In (B.7) to (B.10), $P[k|k]$ and $P[k+1|k]$ are the covariance matrices of the optimal estimate and of the one-step-ahead prediction, respectively.

Bibliography

- [1] J. Cruz, *Ocean wave energy. Current status and future perspectives*. Springer-Verlag, 2008.
- [2] Sea Power Ltd., “Wave Energy.” [Online]. Available: <http://www.seapower.ie/wave-energy/> (Accessed:23-02-2012)
- [3] G. Hagerman, “Wave energy resource and economic assessment for the state of Hawaii,” SEASUN Power Systems, Tech. Rep., 1992.
- [4] M. E. McCormick, *Ocean wave energy conversion*. John Wiley & Sons Inc., 1981.
- [5] C. C. Mei, *The applied dynamics of ocean surface waves*. World Scientific Publishing Co. Pre. Ltd., 1989.
- [6] J. Falnes, *Ocean waves and oscillating systems*. Cambridge University Press, 2002.
- [7] D. V. Evans, “Maximum wave-power absorption under motion constraints,” *Applied Ocean Research*, vol. 3, no. 4, pp. 200–203, 1981.
- [8] J. Hals, J. Falnes, and T. Moan, “A Comparison of Selected Strategies for Adaptive Control of Wave Energy Converters,” *Journal of Offshore Mechanics and Arctic Engineering*, vol. 133, no. 3, pp. 03110–1.12, 2011.
- [9] U. A. Korde, “On control approaches for efficient primary energy conversion in irregular waves,” in *Proceedings of OCEANS '98 Conference*, no. ii, 1998, pp. 1427–1431.
- [10] J. Ringwood and S. Butler, “Optimisation of a Wave Energy Converter,” in *Proceedings of the Sixth IFAC Conference on Control Applications in Marine Systems (CAMS)*, Ancona, Italy, 2004, pp. 155–160.
- [11] J. Falnes, “A review of wave-energy extraction,” *Marine Structures*, vol. 20, pp. 185–201, Oct. 2007.
- [12] A. Babarit and A. H. Clément, “Optimal latching control of a wave energy device in regular and irregular waves,” *Applied Ocean Research*, vol. 28, pp. 77–91, 2006.
- [13] J. Hals, J. Falnes, and T. Moan, “Constrained Optimal Control of a Heaving Buoy Wave-Energy Converter,” *Journal of Offshore Mechanics and Arctic Engineering*, vol. 133, no. 1, p. 011401, 2011.
- [14] F. Fusco and J. V. Ringwood, “A Simple and Effective Real-time Controller for Wave Energy Converters,” *IEEE Transactions on Sustainable Energy*, vol. Submitted, 2012.

- [15] F. Fusco and J. V. Ringwood, "A Study on the Prediction Requirements in Real-Time Control of Wave Energy Converters," *IEEE Transactions on Sustainable Energy*, vol. 3, no. 1, pp. 176–184, 2012.
- [16] F. Fusco and J. V. Ringwood, "Short-Term Wave Forecasting for Real-Time Control of Wave Energy Converters," *IEEE Transactions on Sustainable Energy*, vol. 1, no. 2, pp. 99–106, Jul. 2010.
- [17] F. Fusco, G. Nolan, and J. V. Ringwood, "Variability reduction through optimal combination of wind/wave resources An Irish case study," *Energy*, vol. 35, no. 1, pp. 314–325, Jan. 2010.
- [18] F. Fusco and J. V. Ringwood, "A Model for the Sensitivity of Non-Causal Control of Wave Energy Converters to Wave Excitation Force Prediction Errors," in *Proceedings of the 9th European Wave and Tidal Energy Conference (EWTEC)*, Southampton, UK, 2011.
- [19] F. Fusco and J. V. Ringwood, "Quantification of the Prediction Requirements in Reactive Control of Wave Energy Converters," in *Proceedings of the 18th IFAC World Congress*, no. 1, Milano, Italy, 2011, pp. 11 483–11 488.
- [20] F. Fusco and J. V. Ringwood, "Suboptimal Causal Reactive Control of Wave Energy Converters Using a Second Order System Model WEC," *Proceedings of the Twenty-first International Offshore and Polar Engineering Conference*, pp. 687–694, 2011.
- [21] F. Fusco, J.-C. Gilloteaux, and J. V. Ringwood, "A Study on Prediction Requirements in Time-Domain Control of Wave Energy Converters," in *Proceedings of the Eight IFAC Conference on Control Applications in Marine Systems (CAMS)*, no. 1, Rostock-Warnemünde, Germany, 2010, pp. 405–410.
- [22] F. Fusco and J. V. Ringwood, "Short-Term Wave Forecasting with AR models in Real-Time Optimal Control of Wave Energy Converters," in *Proceedings of the IEEE International Symposium on Industrial Electronics*, Bari, Italy, 2010, pp. 2475–2480.
- [23] F. Fusco and J. Ringwood, "A Study on Short-Term Sea Profile Prediction for Wave Energy Applications," in *Proceedings of the 8th European Wave and Tidal Energy Conference*, Uppsala, Sweden, 2009.
- [24] The European Parliament, "Directive of the European Parliament and of the Council on the promotion of the use of energy from renewable sources amending and subsequently repealing directives 2001/77/ec and 2003/30/ec." Tech. Rep. March, 2009.
- [25] SEAI, "Renewable Energy in Ireland 2010," Tech. Rep., 2010.
- [26] EirGrid, "Annual Report 2010: Securing Ireland's Electricity Supply," Tech. Rep., 2010.
- [27] Eirgrid, "Generation adequacy report 2009-2015," Tech. Rep., 2008.
- [28] ESB National Grid, "Impact of Wind Power Generation In Ireland on the Operation of Conventional Plant and Economic Implications," no. February, pp. 1–42, 2004.

- [29] Eirgrid, “Quarterly review of the Irish electricity system - Autumn 2008,” Tech. Rep. 24, 2008.
- [30] H. Lund, “Renewable energy strategies for sustainable development,” *Energy*, vol. 32, no. 6, pp. 912–919, Jun. 2007.
- [31] H. Lund and B. V. Mathiesen, “Energy system analysis of 100% renewable energy systems The case of Denmark in years 2030 and 2050,” *Energy*, vol. 34, pp. 524–531, May 2009.
- [32] M. Grubb, “Value of variable sources on power systems,” *IEE Proceedings-C*, vol. 138, no. 2, pp. 149–165, 1991.
- [33] L. Freris and D. Infield, *Renewable energy in power systems*. John Wiley & Sons Inc., 2008.
- [34] H. Lund, “Large-scale integration of optimal combinations of PV, wind and wave power into the electricity supply,” *Renewable Energy*, vol. 31, no. 4, pp. 503–515, Apr. 2006.
- [35] N. Duić and M. D. G. Carvalho, “Increasing renewable energy sources in island energy supply: case study Porto Santo,” *Renewable and Sustainable Energy Reviews*, vol. 8, pp. 383–399, Aug. 2004.
- [36] P. A. Østergaard, “Reviewing optimisation criteria for energy systems analyses of renewable energy integration,” *Energy*, vol. 34, pp. 1236–1245, Sep. 2009.
- [37] J. Widén, “Correlations Between Large-Scale Solar and Wind Power in a Future Scenario for Sweden,” *Power*, vol. 2, no. 2, pp. 177–184, 2011.
- [38] E. K. Hart, , E. D. Stoutenburg, and M. Z. Jacobson, “The Potential of Intermittent Renewables to Meet Electric Power Demand : Current Methods and Emerging Analytical Techniques,” *Proceedings of the IEEE, accepted for publication*, 2011.
- [39] B. S. Kallesøe, F. H. Dixen, H. F. Hansen, and A. Køhler, “Prototype test and modeling of a combined wave and wind energy conversion system,” in *Proceedings of the 8th European Wave and Tidal Energy Conference*, Uppsala, Sweden, 2009, pp. 453–459.
- [40] E. D. Stoutenburg, N. Jenkins, and M. Z. Jacobson, “Power output variations of co-located offshore wind turbines and wave energy converters in California,” *Renewable Energy*, vol. 35, no. 12, pp. 2781–2791, Dec. 2010.
- [41] C. De Boor, *A practical guide to splines*. Springer-Verlag, 1978.
- [42] P. Nørgaard and H. Holttinen, “A Multi-Turbine Power Curve Approach,” in *Nordic Wind Power Conferece*, no. March, Chalmers University of Technology, 2004, pp. 1–5.
- [43] M. Gibescu, A. J. Brand, and W. L. Kling, “Estimation of Variability and Predictability of Large-scale Wind Energy in The Netherlands,” *Wind Energy*, vol. 12, pp. 241–260, 2009.
- [44] M. K. Ochi, *Ocean waves: the stochastic approach*. Cambridge University Press, 1998.

- [45] X. Hong and S. A. Billings, "Time Series Multistep-ahead Predictability Estimation and Ranking," *Journal of Forecasting*, vol. 18, pp. 139–149, 1999.
- [46] C. E. Shannon, "A mathematical theory of communication," *The Bell System Technical Journal*, vol. 27, pp. 379–423, 1948.
- [47] A. Costa, A. Crespo, J. Navarro, G. Lizcano, H. Madsen, and E. Feitosa, "A review on the young history of the wind power short-term prediction," *Renewable and Sustainable Energy Reviews*, vol. 12, pp. 1725–1744, Aug. 2008.
- [48] G. Kariniotakis, P. Pinson, N. Siebert, G. Giebel, and R. Barthelmie, "The State of the Art in Short-term Prediction of Wind Power - From an Offshore Perspective," in *Proceedings of 2004 SeaTechWeek*, Brest, France, 2004.
- [49] J. N. Newman, *Marine hydrodynamics*. The Massachusetts Institute of Technology (MIT) Press, 1977.
- [50] V.I. Smirnov, *A course of higher mathematics*. Addison-Wesley, 1964.
- [51] T. Perez, *Ship Motion Control. Course Keeping and Roll Stabilisation Using Rudder and Fins*. Springer-Verlag London Limited, 2005.
- [52] M. K. Ochi and E. N. Hubble, "Six-parameter Wave Spectra," *Proceedings of the 15th International Conference on Coastal Engineering*, 1976.
- [53] Karl J. Astrom, *Introduction to Stochastic Control Theory*. Academic Press, 1970.
- [54] J. Figwer, "A new method of random time-series simulation," *Simulation Practise and Theory*, vol. 5, pp. 217–234, 1997.
- [55] A. P. French, *Vibrations and Waves*. W. W. Norton & Company Inc., 1971.
- [56] J. Falnes, "Wave-Energy Conversion Through Relative Motion Between Two Single-Mode Oscillating Bodies," *Journal of Offshore Mechanics and Arctic Engineering*, vol. 121, no. 1, pp. 32–38, 1999.
- [57] J. Falnes, "On non-causal impulse response functions related to propagating water waves," *Applied Ocean Research*, vol. 17, pp. 379–389, 1996.
- [58] W. E. Cummins, "The impulse response function and ship motion," in *Proceedings of the Symposium on Ship Theory*, Hamburg, Germany, 1962.
- [59] Wamit Inc., "WAMIT Vers. 6.4," 2008.
- [60] Wamit Inc., "WAMIT User manual," Tech. Rep., 2005.
- [61] H. D. Maniar, "A three dimensional higher order panel method based on B-splines," Phd Thesis, Massachusetts Institute of Technology, 1995.
- [62] A. V. Oppenheim and R. W. Schaffer, *Discrete-time Signal Processing*. Pearson Higher Education, Inc., 1989.

- [63] M. L. V. A. N. Blaricum and R. A. J. Mittra, "A Technique for Extracting the Poles and Residues of a System Directly from Its Transient Response," *IEEE Transactions on Antennas and Propagation*, vol. ap-23, no. 6, pp. 777–781, 1975.
- [64] G. R. de Prony, "Essai experimental et analytique: sur les lois de la dilatabilite de fluides elastiques et sur celles de la force expansive de la vapeur de lalkool, a differentes temperatures," *Journal de l'École Polytechnique Floréal et Plairial*, vol. 1, no. 22, pp. 24–76, 1795.
- [65] R. Taghipour, T. Perez, and T. Moan, "Hybrid frequency time domain models for dynamic response analysis of marine structures," *Ocean Engineering*, vol. 35, pp. 685–705, 2008.
- [66] T. Perez and T. I. Fossen, "Time- vs . Frequency-domain Identification of Parametric Radiation Force Models for Marine Structures at Zero Speed," *Model, Identification and Control*, vol. 29, no. 1, pp. 1–19, 2008.
- [67] A. P. McCabe, A. Bradshaw, and M. B. Widden, "A Time-domain model of a Floating Body Using Transforms," in *Proceedings of the Sixth European Wave and Tidal Energy Conference (EWTEC)*, no. 2, Glasgow, UK, 2005, pp. 281–288.
- [68] P. Beirão, D. Valério, and J. Sá da Costa, "Identification and Phase and Amplitude Control of the Archimedes Wave Swing using a PID and IMC," in *Proceedings of the Second International Conference on Electrical Engineering*, no. 1, Beirao2007, 2007, pp. 1–8.
- [69] E. Levy, "Complex Curve Fitting," *IRE Transactions on Automatic Control*, vol. 4, pp. 37–44, 1959.
- [70] B. r. Gustavsen, A. Semlyen, and L. Fellow, "Enforcing Passivity for Admittance Matrices Approximated by Rational Functions," *IEEE Transactions on Power Systems*, vol. 16, no. 1, pp. 97–104, 2001.
- [71] T. Perez and T. I. Fossen, "A Matlab Toolbox for Parametric Identification of Radiation-Force Models of Ships and Offshore Structures," *Model Identification and Control*, vol. 30, no. 1, pp. 1–15, 2009.
- [72] Chi-Tsong Chen, *Linear System Theory and Design*. Oxford University Press, Inc., 1999.
- [73] S. H. Salter, J. R. M. Taylor, and N. J. Caldwell, "Power conversion mechanisms for wave energy," *Proceedings of the I nstitute of Mechanical Engineers (IMEchE), Part M: J Engineering for the Maritime Environment*, vol. 216, no. 1, pp. 1–27, Sep. 2002.
- [74] B. Drew, a. R. Plummer, and M. N. Sahinkaya, "A review of wave energy converter technology," *Proceedings of the Institution of Mechanical Engineers, Part A: Journal of Power and Energy*, vol. 223, no. 8, pp. 887–902, Dec. 2009.
- [75] J. Hals, "Modelling and phase control of wave-energy converters," Ph.D. dissertation, National University of Science and Technology, Trondheim, Norway, 2010.
- [76] L. Cameron, R. Doherty, A. Henry, K. Doherty, J. Van t'Hoff, D. Kaye, D. Naylor, S. Bourdier, and T. Whittaker, "Design of the Next Generation of the Oyster Wave Energy Converter," in *Proceedings of the 3rd International Conference on Ocean Energy (ICOE)*, Bilbao, Spain, pp. 1–12.

- [77] J. Sá da Costa, P. Pinto, A. Sarmiento, and F. Gardner, "Modeling of an ocean waves power device AWS," *Proceedings of 2003 IEEE Conference on Control Applications*, pp. 618–623, 2003.
- [78] H. Polinder, B. Mecrow, A. Jack, P. Dickinson, and M. Mueller, "Linear generators for direct-drive wave energy conversion," *IEEE International Electric Machines and Drives Conference*, vol. 2, pp. 798–804, 2003.
- [79] H. Polinder, M. Damen, and F. Gardner, "Linear PM Generator System for Wave Energy Conversion in the AWS," *IEEE Transactions on Energy Conversion*, vol. 19, no. 3, pp. 583–589, Sep. 2004.
- [80] C. Bostrom and M. Leijon, "Operation analysis of a wave energy converter under different load conditions," *IET Renewable Power Generation*, vol. 5, no. 3, p. 245, 2011.
- [81] R. Waters, M. Stalberg, O. Danielsson, O. Svensson, S. Gustafsson, E. Stromstedt, M. Eriksson, J. Sundberg, and M. Leijon, "Experimental results from sea trials of an offshore wave energy system," *Applied Physics Letters*, vol. 90, no. 3, p. 034105, 2007.
- [82] M. Leijon, O. Danielsson, M. Eriksson, K. Thorburn, H. Bernhoff, J. Isberg, J. Sundberg, I. Ivanova, E. Sjostedt, and O. Agren, "An electrical approach to wave energy conversion," *Renewable Energy*, vol. 31, no. 9, pp. 1309–1319, Jul. 2006.
- [83] M. Mueller, "Electrical generators for direct drive wave energy converters," *IEE Proceedings - Generation, Transmission and Distribution*, vol. 149, no. 4, p. 446, 2002.
- [84] J. Xiang, P. Brooking, and M. Mueller, "Control requirements of direct drive wave energy converters," *Proceedings of the IEEE Region 10 Conference on Computers, Communications, Control and Power Engineering (TENCON), Beijing, China*, pp. 2053–2056, 2002.
- [85] J. K. H. Shek, D. E. Macpherson, and M. A. Mueller, "Control of Linear Electrical Generators for Direct Drive Wave Energy Conversion," in *Proceedings of the International Conference on Electrical Machines, Crete Island, Greece*, 2006.
- [86] H. Polinder, B. Mecrow, a.G. Jack, P. Dickinson, and M. Mueller, "Conventional and TFPM Linear Generators for Direct-Drive Wave Energy Conversion," *IEEE Transactions on Energy Conversion*, vol. 20, no. 2, pp. 260–267, Jun. 2005.
- [87] R. Costello, J. V. Ringwood, and J. Weber, "Comparison of Two Alternative Hydraulic PTO Concepts for Wave Energy Conversion," in *Proceedings of the 9th European Wave and Tidal Energy Conference (EWTEC), Southampton, UK*, no. 1, 2011.
- [88] D. J. Pizer, "Maximum wave-power absorption of point absorbers under motion constraints," *Applied Ocean Research*, vol. 15, pp. 227–234, 1993.
- [89] C. A. Desoer and Ernest S. Kuh, *Basic circuit theory*. McGraw-Hill, 1987.
- [90] D. G. MacMartin and S. R. Hall, "Structural Control Experiments using an Hoo Power Flow Approach," *Journal of Sound and Vibration*, vol. 148, no. 2, pp. 223–241, 1991.

- [91] J. Nocedal and S. J. Wright, *Numerical Optimization*. Springer Science+ Business Media, LLC, 2006.
- [92] S. Naito and S. Nakamura, “Wave Energy Absorption in Irregular Waves by Feedforward Control System 80,” in *International symposium on Hydrodynamics of ocean wave energy utilization*, 1986, pp. 269–280.
- [93] U. A. Korde, “Efficient primary energy conversion in irregular waves,” *Ocean Engineering*, vol. 26, pp. 625–651, 1999.
- [94] U. A. Korde, “Control System Applications In Wave Energy Conversion,” in *OCEANS 2000 MTS/IEEE Conference and Exhibition*, 2000, pp. 1817–1824.
- [95] U. A. Korde, M. P. Schoen, and F. Lin, “Time Domain Control of a Single Mode Wave Energy Device,” in *Proceedings of the Eleventh International Offshore and Polar Engineering Conference*, vol. I, Stavanger, Norway, 2001, pp. 555–560.
- [96] D. Valério, P. Beirão, and J. Sá da Costa, “Optimisation of wave energy extraction with the Archimedes Wave Swing,” *Ocean Engineering*, vol. 34, no. 17-18, pp. 2330–2344, Dec. 2007.
- [97] C. Maisondieu and A. Clement, “A realizable force feedback-feedforward control loop for a piston wave absorber,” in *8th International Workshop on Water Waves and Floating Bodies*, St John’s, Newfoundland, Canada, 1993, pp. 79–82.
- [98] J. Sá da Costa, P. Beirão, and D. Valério, “Internal Model Control Applied to the Archimedes Wave Swing,” in *16th International Conference on Control Systems and Computer Science (CSCS)*, Bucharest, Romania, 2007.
- [99] D. Valério, P. Beirão, and J. Sá da Costa, “Feedback linearisation control applied to the Archimedes Wave Swing,” in *Proceedings of the Mediterranean Conference on Control & Automation*, no. 1, Athens, Greece, 2007.
- [100] D. Valério, M. J. Mendes, P. Beirão, and J. Sá da Costa, “Identification and control of the AWS using neural network models,” *Applied Ocean Research*, vol. 30, no. 3, pp. 178–188, Jul. 2008.
- [101] D. Valério and P. Beirão, “Robustness Assessment of Model-Based Control for the Archimedes Wave Swing,” in *Proceedings of the European Control Conference*, Budapest, Hungary, 2009, pp. 3749–3754.
- [102] J. N. B. A. Perdigão and A. J. N. A. Sarmiento, “A Phase Control Strategy for OWC Devices in Irregular Seas,” in *The Fourth International Workshop on Water Waves and Floating Bodies*, Department of Mathematics, University of Oslo, 1989, pp. 205–209.
- [103] K. Budal, J. Falnes, L. C. Iversen, P. M. Lillebekken, G. Oltedal, T. Hals, T. Onshus, and A. S. Hoy, “The Norwegian Wave-power Buoy Project,” in *Proceedings of the The Second International Symposium on Wave Energy Utilization*, Trondheim, Norway, 1982, pp. 323–344.

- [104] A. Babarit, G. Duclos, and A. Clément, “Comparison of latching control strategies for a heaving wave energy device in random sea,” *Applied Ocean Research*, vol. 26, no. 5, pp. 227–238, Jul. 2004.
- [105] A. Babarit and A. H. Clément, “Method to the Control Application of the the Optimal optimal Command command method control of the the SEAREV Study on the Infl uence of SEAREV Wave wave Energy energy Converter converter : : A a study influence of Time time Constants ciency of the consta,” in *Proceedings of the European Control Conference*, 2009, pp. 3737–3742.
- [106] L. Pontryagin and R. V. Gamkrelidze, *The Mathematical Theory of Optimal Processes*. Gordon and Breach Science Publishers, 1986.
- [107] F. Kara, “Time domain prediction of power absorption from ocean waves with latching control,” *Renewable Energy*, vol. 35, no. 2, pp. 423–434, Feb. 2010.
- [108] A. F. D. O. Falcão, “Phase control through load control of oscillating-body wave energy converters with hydraulic PTO system,” *Ocean Engineering*, vol. 35, no. 3-4, pp. 358–366, Mar. 2008.
- [109] M. Lopes, J. Hals, R. Gomes, T. Moan, L. Gato, and A. O. Falcão, “Experimental and numerical investigation of non-predictive phase-control strategies for a point-absorbing wave energy converter,” *Ocean Engineering*, vol. 36, no. 5, pp. 386–402, Apr. 2009.
- [110] J. A. M. Cretel, A. W. Lewis, G. P. Thomas, and G. Lightbody, “A Critical Assessment of Latching as Control Strategy for Wave-Energy Point Absorbers,” in *Proceedings of the Twenty-first International Offshore and Polar Engineering Conference*, vol. 8, Maui, Hawaii, USA, 2011, pp. 680–686.
- [111] A. Babarit, M. Guglielmi, and A. H. Clément, “Declutching control of a wave energy converter,” *Ocean Engineering*, vol. 36, no. 12-13, pp. 1015–1024, Sep. 2009.
- [112] B. Teillant, J. C. Gilloteaux, and J. V. Ringwood, “Optimal Damping Profile for a Heaving Buoy Wave Energy Converter,” in *Proceedings of the Eight IFAC Conference on Control Applications in Marine Systems (CAMS)*, no. 2, Rostock-Warnemünde, Germany, 2010.
- [113] G. A. Nolan, J. V. Ringwood, W. E. Leithead, and S. Butler, “Optimal Damping Profiles for a Heaving Buoy Wave Energy Converter,” *Proceedings of the Fifteenth International Offshore and Polar Engineering Conference*, vol. 8, pp. 477–484, 2005.
- [114] J. A. Rossiter, *Model-based Predictive Control*. Boca Raton, FL, USA: CRC Press, 2004.
- [115] T. K. A. Brekken, “On Model Predictive Control for a Point Absorber Wave Energy Converter,” in *Proceedings of the IEEE PES PowerTech Conference*, Trondheim, Norway, 2011, pp. 1–8.
- [116] P. Gieske, “Model Predictive Control of a Wave Energy Converter: Archimedes Wave Swing,” Ph.D. dissertation, MS thesis, Delft University of Technology, Delft, The Netherlands, 2007.

- [117] J. A. M. Cretel and A. W. Lewis, "An Application of Model Predictive Control to a Wave Energy Point Absorber," in *Proceedings of the IFAC conference on Control Methodologies and Technology for Energy Efficiency (CMTEE)*, Vilamoura, Portugal, 2010.
- [118] J. A. M. C. G. Lightbody, "Maximisation of Energy Capture by a Wave-Energy Point Absorber using Model Predictive Control," in *Proceedings of the 18th IFAC World Congress*, no. 2002, Milano, Italy, 2011, pp. 3714–3721.
- [119] G. Bacelli, J.-C. Gilloteaux, and J. Ringwood, "A Predictive Controller for a Heaving Buoy Producing Potable Water," in *Proceedings of the European Control Conference*, Budapest, Hungary, 2009, pp. 3755–3760.
- [120] G. Bacelli, J. V. Ringwood, and J.-C. Gilloteaux, "A control system for a self-reacting point absorber wave energy converter subject to constraints," in *Proceedings of the 18th IFAC World Congress*, Milano, Italy, 2011, pp. 11 387–11 392.
- [121] P. R. Costa, P. B. Garcia-Rosa, and S. F. Estefen, "Phase control strategy for a wave energy hyperbaric converter," *Ocean Engineering*, vol. 37, no. 17-18, pp. 1483–1490, Dec. 2010.
- [122] U. Korde, "Systems of reactively loaded coupled oscillating bodies in wave energy conversion," *Applied Ocean Research*, vol. 25, no. 2, pp. 79–91, Apr. 2003.
- [123] J. K. H. Shek, D. E. Macpherson, M. A. Mueller, and J. Xiang, "Reaction force control of a linear electrical generator for direct drive wave energy conversion," *IET Renewable Power and Generation*, vol. 1, no. 1, pp. 17–24, 2007.
- [124] J. K. H. Shek, D. E. Macpherson, and M. A. Mueller, "Phase and Amplitude Control of a Linear Generator for Wave Energy Conversion," in *Proceedings of the 4th IET Conference on Power Electronics, Machines and Drives (PEMD)*, York, UK, 2008, pp. 66–70.
- [125] F. Wu, X. P. Zhang, P. Ju, and M. Sterling, "Optimal Control for AWS-Based Wave Energy Conversion System," *IEEE Transactions on Power Systems*, vol. 24, no. 4, pp. 1747–1755, Nov. 2009.
- [126] V. Gómez, R. Guanche, C. Vidal, and I. Eguinoa, "Numerical Simulation of a Submerged Wave Energy Converter under Irregular Wave Conditions," in *Proceedings of the IEEE OCEANS Conference*, Santander, Spain, 2011.
- [127] G. De Backer, M. Vantorre, R. Banasiak, J. D. Rouck, C. Beels, and H. Verhaeghe, "Performance of a point absorber heaving with respect to a floating platform," in *Proceedings of the Seventh European Wave and Tidal Energy Conference (EWTEC)*, Porto, Portugal, 2007, pp. 1–8.
- [128] M. Vantorre, R. Banasiak, and R. Verhoeven, "Modelling of hydraulic performance and wave energy extraction by a point absorber in heave," *Applied Ocean Research*, vol. 26, no. 1-2, pp. 61–72, Apr. 2004.
- [129] M. Stalberg, R. Waters, O. Danielsson, and M. Leijon, "Influence of Generator Damping on Peak Power and Variance of Power for a Direct Drive Wave Energy Converter," *Journal of Offshore Mechanics and Arctic Engineering*, vol. 130, no. 3, p. 031003, 2008.

- [130] M. Eriksson, R. Waters, O. Svensson, J. Isberg, and M. Leijon, “Wave power absorption: Experiments in open sea and simulation,” *Journal of Applied Physics*, vol. 102, no. 8, p. 084910, 2007.
- [131] A. F. D. O. Falcão, “Modelling and control of oscillating-body wave energy converters with hydraulic power take-off and gas accumulator,” *Ocean Engineering*, vol. 34, no. 14-15, pp. 2021–2032, Oct. 2007.
- [132] H. Yavuz, T. J. Stallard, a. P. McCabe, and G. a. Aggidis, “Time series analysis-based adaptive tuning techniques for a heaving wave energy converter in irregular seas,” *Proceedings of the Institution of Mechanical Engineers, Part A: Journal of Power and Energy*, vol. 221, no. 1, pp. 77–90, Jan. 2007.
- [133] M. P. Schoen, J. Hals, and T. Moan, “Wave Prediction and Fuzzy Logic Control of Wave Energy Converters in Irregular Waves,” in *Proceedings of the 16th Mediterranean Conference on Control and Automation*, Ajaccio, France, 2008, pp. 767–772.
- [134] M. P. Schoen, J. Hals, and T. Moan, “Robust Control of Heaving Wave Energy Devices in Irregular Waves,” in *Proceedings of the 16th Mediterranean Conference on Control and Automation*, no. 1, Ajaccio, France, 2008, pp. 779–784.
- [135] M. P. Schoen, S. Member, J. Hals, and T. Moan, “Wave Prediction and Robust Control of Heaving Wave Energy Devices for Irregular Waves,” *IEEE Transactions on Energy Conversion*, vol. 26, no. 2, pp. 627–638, 2011.
- [136] L. A. Sievers and A. H. von Flotow, “Comparison and Extensions of Control Methods for Narrow-Band Disturbance Rejection,” *IEEE Transactions on Signal Processing*, vol. 40, no. 10, 1992.
- [137] L. A. Sievers and A. H. von Flotow, “Linear Control Design for Active Vibration Isolation of Narrow Band Disturbances,” in *Proceedings of the 7th Conference on Decision and Control*, Austin, Texas, USA, 1988, pp. 1032–1037.
- [138] D. W. Miller, S. R. Hall, and A. H. von Flotow, “Optimal control of Power Flow at Structural Junctions,” in *Proceedings of the American Control Conference*, Pittsburgh, PA, USA, 1989, pp. 212–221.
- [139] A. J. Connolly, M. Green, J. F. Chicaro, and R. R. Bitmead, “The Design of LQG & Hoo Controllers for use in Active Vibration Control & Narrow Band Disturbance Rejection,” in *Proceedings of the 34th Conference on Decision & Control*, no. December, New Orleans, LA, USA, 1995, pp. 2982–2987.
- [140] D. G. MacMartin and S. R. Hall, “Control of Uncertain Structures Using an Hoo Power Flow Approach,” *Journal of Guidance*, vol. 14, no. 3, pp. 521–530, 1991.
- [141] W. J. O’Connor, F. RamosadelaFlor, D. J. McKeown, and V. Feliu, “Wave-based control of non-linear flexible mechanical systems,” *Nonlinear Dynamics*, vol. 57, no. 1-2, pp. 113–123, Sep. 2008.

- [142] W. J. OConnor and A. Fumagalli, “Refined Wave-Based Control Applied to Nonlinear, Bending, and Slewing Flexible Systems,” *Journal of Applied Mechanics*, vol. 76, no. 4, pp. 1–9, 2009.
- [143] B. Widrow, J. R. J. Glover, H. M. McCool, J. Kaunitz, C. S. Williams, R. H. Hearn, J. R. Zeidler, E. J. Dong, and R. C. Goodlin, “Adaptive Noise Cancelling : Principles and Applications,” *Proceedings of the IEEE*, vol. 63, no. 12, pp. 105–112, 1975.
- [144] S. Kuo and M. Ji, “Development and analysis of an adaptive noise equalizer,” *IEEE Transactions on Speech and Audio Processing*, vol. 3, no. 3, pp. 217–222, May 1995.
- [145] S.-J. Chen and J. Gibson, “Feedforward adaptive noise control with multivariable gradient lattice filters,” *IEEE Transactions on Signal Processing*, vol. 49, no. 3, pp. 511–520, Mar. 2001.
- [146] J. T. Scruggs and S. M. Lattanzio, “Optimal Causal Control of an Ocean Wave Energy Converter in Stochastic Waves,” in *Proceedings of the 9th European Wave and Tidal Energy Conference (EWTEC)*, Southampton, UK, 2011.
- [147] A. A. E. Price, D. I. M. Forehand, and A. R. Wallace, “Time-Span of Future Information Necessary for Theoretical Acausal Optimal Control of Wave Energy Converters,” in *Proceedings of the European Control Conference*, Budapest, Hungary, 2009, pp. 3761–3766.
- [148] F. Fusco and J. V. Ringwood, “Linear Models for Short-term Wave Forecasting,” in *Proceedings of the 10th World Renewable Energy Congress (WREC X)*, no. 2, Glasgow, Scotland, 2008, pp. 1030–1035.
- [149] M. Belmont, J. Horwood, R. Thurley, and J. Baker, “Filters for linear sea-wave prediction,” *Ocean Engineering*, vol. 33, no. 17-18, pp. 2332–2351, Dec. 2006.
- [150] J. Tedd and P. Frigaard, “Short term wave forecasting, using digital filters, for improved control of Wave Energy Converters,” in *Proceedings of the Seventeenth International Offshore and Polar Engineering Conference*, Lisbon, Portugal, 2007, pp. 388–394.
- [151] V. Voronovich, B. Holmes, and G. P. Thomas, “A Preliminary Numerical and Experimental Study of Wave Prediction,” in *Proceedings of the Sixth European Wave and Tidal Energy Conference (EWTEC)*, Glasgow, UK, 2005, pp. 535–542.
- [152] P. Frigaard and M. Brorsen, “A time-domain method for separating incident and reflected irregular waves,” *Coastal Engineering*, vol. 24, no. 3-4, pp. 205–215, Mar. 1995.
- [153] R. E. Kalman, “A New Approach to Linear Filtering and Prediction Problems,” *Transactions of the ASME - Journal of Basic Engineering*, vol. 82, no. Series D, pp. 35–45, 1960.
- [154] M. R. Belmont, “A lower bound estimate of the gains stemming from quiescent period predictive control using conventional sea state statistics,” *Journal of Renewable and Sustainable Energy*, vol. 1, no. 6, pp. 063 104–1/8, 2009.

- [155] M. Belmont, “Increases in the average power output of wave energy converters using quiescent period predictive control,” *Renewable Energy*, vol. 35, no. 12, pp. 2812–2820, Dec. 2010.
- [156] H. Kautzt, “Transient Synthesis in the Time Domain,” *Transactions of the IRE Professional Group on Circuit Theory*, vol. 1, no. 3, pp. 22–39, 1954.
- [157] A. A. E. Price and A. R. Wallace, “Non-linear methods for next wave estimation,” in *Proceedings of the Seventh European Wave and Tidal Energy Conference (EWTEC)*, Porto, Portugal, 2007.
- [158] C. Barrera, E. Azevedo, M. Rueda, M. Gelado, and L. O., “Real-time monitoring network in the Macaronesian region as a contribution to the Coastal Ocean Observations Panel (COOP),” *Journal of Operational Oceanography*, vol. 1, pp. 59–69, 2008.
- [159] E. Azevedo and M. Rodrigues, “Projectos CLIMAAT\CLIMARCOST Clima e Meteorologia dos Arquipélagos Atlânticos, Clima Marítimo e Costeiro,” in *Workshop Intenacional sobre Clima e Recursos Naturais nos Países de Língua Portuguesa, WSCRA08*, Cabo Verde, Portugal, 2008.
- [160] R. Esteves, A. Valente, M. Costa, F. Reis, and E. Azevedo, “Dados Direcciones DE agitação marítima nos Açores (projecto CLIMAAT-CLIMA e meteorologia dos Arquipélagos Atlânticos),” in *6 Jornadas Portuguesas de Engenharia Costeira e Portuária, PIANC*, Funchal, Portugal, 2009.
- [161] G. Nolan, J. V. Ringwood, and B. Holmes, “Short Term Wave Energy Variability off the West Coast of Ireland,” in *Proceedings of the Seventh European Wave and Tidal Energy Conference (EWTEC)*, vol. 2, no. 4, Porto, Portugal, 2007.
- [162] S. Massel, “Wavelet analysis for processing of ocean surface wave records,” *Ocean Engineering*, vol. 28, no. 8, pp. 957–987, Aug. 2001.
- [163] G. Stokes, “On the theory of oscillatory waves,” *Transactions of the Cambridge Philosophical Society*, vol. 8, pp. 441–455, 1847.
- [164] M. K. Ochi, *Applied probability and stochastic processes*. Wiley Interscience, 1990.
- [165] H.-P. Bernhard, “A tight upper bound on the gain of linear and nonlinear predictors for stationary stochastic processes,” *IEEE Transactions on Signal Processing*, vol. 46, no. 11, pp. 2909–2917, 1998.
- [166] D. S. Jones, *Elementary Information Theory*. Oxford Clarendon Press, 1979.
- [167] A. Dionisio, R. Menezes, and D. Mendes, “Mutual information: a measure of dependency for nonlinear time series,” *Physica A: Statistical Mechanics and its Applications*, vol. 344, no. 1-2, pp. 326–329, Dec. 2004.
- [168] A. C. Harvey, *Forecasting, structural time series and the Kalman filter*. Cambridge University Press, 1989.

- [169] P. C. Young, D. J. Pedregal, and W. Tych, "Dynamic harmonic regression," *Journal of Forecasting*, vol. 18, no. 6, pp. 369–394, Nov. 1999.
- [170] G. E. P. Box, G. M. Jenkins, and G. C. Reinsel, *Time Series Analysis: Forecasting and Control*. Prentice-Hall, 1994.
- [171] D. S. Shook, C. Mohtadi, and S. L. Shah, "Identification for long-range predictive control," *Control Theory and Applications, IEE Proceedings D*, vol. 138, no. 1, pp. 75–84, 1991.
- [172] S. Bittanti, *Identificazione dei modelli e controllo adattativo*. Pitagora Editrice, Bologna, 2000.
- [173] G. Kreisselmeier, "Stabilized least-squares type adaptive identifiers," *IEEE Transactions on Automatic Control*, vol. 35, no. 3, pp. 306–310, Mar. 1990.
- [174] S. Gunnarsson, "Combining tracking and regularization in recursive least squares identification," *Proceedings of 35th IEEE Conference on Decision and Control*, vol. 3, no. December, pp. 2551–2552, 1996.
- [175] B. Quine, J. Uhlmann, and H. Durrant-Whyte, "Implicit Jacobian for linearised state estimation in nonlinear systems," *Proceedings of 1995 American Control Conference - ACC'95*, vol. 3, no. 12, pp. 1645–1646, 1995.
- [176] M. Norgaard, O. Ravn, N. Poulsen, and L. Hansen, *Neural Networks for Modelling and Control of Dynamic Systems*. Springer, 2000.
- [177] B. M. Wilamowski, "An Algorithm for Fast Convergence in Training Neural Networks," in *Proceedings of International Joint Conference on Neural Networks*, no. 1, Washington, DC, USA, 2001, pp. 1778–1782.
- [178] D. J. C. Mackay, "Introduction to Gaussian processes," in *Neural Networks and Machine Learning*. Springer-Verlag, 1998.
- [179] D. J. Leith, M. Heidl, J. V. Ringwood, and S. Member, "Gaussian Process Prior Models for Electrical Load Forecasting," in *Proceedings of the 8th International Conference on Probabilistic Methods Applied to Power Systems*, Ames, Iowa, USA, 2004.
- [180] N. J. Gordon, D. J. Salmond, and A. F. M. Smith, "Novel approach to nonlinear/non-Gaussian Bayesian state estimation," *Radar and Signal Processing, IEE Proceedings F*, vol. 140, no. 2, pp. 107–113, 1993.
- [181] A. Doucet and A. M. Johansen, "A Tutorial on Particle Filtering and Smoothing : Fifteen years later," in *The Oxford handbook of nonlinear filtering*. Oxford University Press, Oxford, 2009, no. December.
- [182] R. Isermann, *Fault-Diagnosis Systems: An Introduction from Fault Detection to Fault Tolerance*. Springer, 2006.
- [183] H. Akaike, "A new look at the statistical model identification," *IEEE Transactions on Automatic Control*, vol. 19, no. 6, pp. 716–723, Dec. 1974.

- [184] G. Schwarz, “Estimating the Dimension of a Model,” *The Annals of Statistics*, vol. 6, no. 2, pp. 461–464, 1978.
- [185] A. F. D. O. Falcão, P. A. P. Justino, J. C. C. Henriques, and J. M. C. S. André, “Reactive versus Latching Phase Control of a Two-body Heaving Wave Energy Converter,” in *Proceedings of the European Control Conference*, Budapest, Hungary, 2009, pp. 1–6.
- [186] D. O’Sullivan, J. Griffiths, M. G. Egan, and A. W. Lewis, “Development of an electrical power take off system for a sea-test scaled offshore wave energy device,” *Renewable Energy*, vol. 36, no. 4, pp. 1236–1244, Apr. 2011.
- [187] E. Tedeschi, M. Carraro, M. Molinas, and P. Mattavelli, “Effect of Control Strategies and Power Take-Off Efficiency on the Power Capture From Sea Waves,” *IEEE Transactions on Energy Conversion*, vol. 26, no. 4, pp. 1088–1098, Dec. 2011.
- [188] P. Ricci, J. Lopez, M. Santos, P. Ruiz-Minguela, J. Villate, F. Salcedo, and A. Falcao, “Control strategies for a wave energy converter connected to a hydraulic power take-off,” *IET Renewable Power Generation*, vol. 5, no. 3, p. 234, 2011.
- [189] P. E. Gill, W. Murray, M. A. Saunders, and M. H. Wright, “Procedures for Optimization Problems with a Mixture of Bounds and General Linear Constraints,” *ACM Transactions on Mathematical Software*, vol. 10, no. 3, pp. 282–298, 1984.
- [190] B. Boashash and S. Member, “Estimating and Interpreting The Instantaneous Frequency of a Signal-Part 1 : Fundamentals,” *Proceedings of the IEEE*, vol. 80, no. 4, pp. 520 – 538, 1992.
- [191] B. Boashash and S. Member, “Estimating and Interpreting the Instantaneous Frequency of a Signal-Part 2 : Algorithms and Applications,” *Proceedings of the IEEE*, vol. 80, no. 4, pp. 540 – 568, 1992.
- [192] M. Morari and E. Zafriou, *Robust Process Control*. Prentice-Hall, Inc., 1989.
- [193] P. Beirão, M. J. Mendes, D. Valério, and J. Sá da Costa, “Control of the Archimedes Wave Swing using Neural Networks,” in *Proceedings of the Seventh European Wave and Tidal Energy Conference (EWTEC)*, Porto, Portugal, 2007.
- [194] O. Dalane, F. F. Knutsen, and S. Løset, “Nonlinear Coupled Hydrostatics of Floating Conical Platforms,” in *ASME 28th International Conference on Ocean, Offshore and Arctic Engineering (OMAE)*, Honolulu, Hawaii, USA, 2009, pp. 793–802.
- [195] A. Babarit, A. Mouslim, and A. Clement, “On the numerical modelling of the non linear behaviour of a wave energy converter,” in *ASME 28th International Conference on Ocean, Offshore and Arctic Engineering (OMAE)*, Honolulu, Hawaii, USA, 2010, pp. 1045–1053.
- [196] Y. Cao, G. Tahchiev, and F. Zhang, “Effects of Hydrostatic Nonlinearity on Motions of Floating Structures,” in *ASME 29th International Conference on Ocean, Offshore and Arctic Engineering (OMAE)*, Shanghai, China, 2010, pp. 257–267.

- [197] J.-C. Gilloteaux, “Mouvements de grande amplitude dun corps flottant en fluide parfait. Application à la récupération de lénergie des vagues,” Ph.D. dissertation, Ecole Centrale de Nantes, France, 2007.
- [198] J.-C. Gilloteaux, G. Bacelli, and J. V. Ringwood, “A non-linear potential model to predict large-amplitudes-motions: application to a multi-body wave energy converter,” in *Proceedings of the 10th World Renewable Energy Congress (WREC X)*, Glasgow, Scotland, 2010.
- [199] H. Procházka and I. D. Landau, “Pole placement with sensitivity function shaping using 2nd order digital notch filters,” *Automatica*, vol. 39, no. 6, pp. 1103–1107, Jun. 2003.